THE THEORY AND SIGNIFICANCE OF RETAINED AUSTENITE IN STEELS

By

Harshad Kumar Dharamshi Hansraj Bhadeshia

Darwin College, Cambridge.

A dissertation submitted for the degree of

Doctor of Philosophy

at the University of Cambridge, September 1979.

PREFACE

This dissertation is submitted for the degree of Doctor of Philosophy in the University of Cambridge. The work described herein was carried out between October 1976 and September 1979 in the Department of Metallurgy and Materials Science, Cambridge.

The contents of this thesis do not exceed 60,000 words and result from my own work; they include nothing which is the outcome of work done in collaboration. Except where appropriately referenced, the work presented in this dissertation is original. No part of this dissertation has already been, or is being concurrently, submitted for any other degree, diploma or any other qualification at any other university.

The work was financially supported by RARDE, Fort Halstead, who also kindly supplied many of the alloys used. I am sincerely grateful to Professor R.W.K. Honeycombe for the opportunity to work in his Alloy Steels Research Group and for the provision of laboratory facilities. The research was carried out under the supervision of Dr. D.V. Edmonds.

I owe an especial debt to Dr. Barry Muddle for so many inspiring discussions on the subject of martensite crystallography. His patience and rigorous approach never ceases to amaze me. I should like to express my gratitude to Professors H.I. Aaronson, J.W. Christian, R.F. Hehemann and C.M. Wayman for brief, and yet fruitful and exciting, discussions on bainite. My friend Gillian Smith carefully reviewed the script, and made several useful (and often very witty) comments. I am extremely concious of the numerous discussions with my colleagues in the Alloy Steels group, which must have contributed to the development of this work.

I warmly acknowledge the delightful encouragement and interest that I have always received from my family, and especially from my little sister Sunita. My wife Chanda put up with a lot in the final year of this work, and her comments do no end of good when morale is low.

Finally, it seems to me that I owe so much to my parents that to express my gratitude in words would surely lead me to exceed the 60,000 word quota!

H.D. Bhadeshia

Harshad K.D.H. Bhadeshia

September 1979

CONTENTS

THE THEORY AND SIGNIFICANCE OF RETAINED AUSTENITE IN STEELS

Harshad K.D.H. Bhadeshia

Abstract

The processes leading to the retention of small quantities of austenite following the bainite and martensite phase transformations have been examined, together with the influence of retained austenite on the properties of low alloy steels.

It was found that the upper and lower bainite transformations are separate reactions, although both involve a displacive transformation mode. Growth seems to occur by the repeated nucleation of martensitic sub-units, and this leads to an apparently slow growth rate. The partitioning of carbon from bainitic ferrite into residual austenite was thermodynamically proven to occur subsequent to transformation, and was shown to be directly responsible for the 'incomplete reaction phenomenon'. The nature of sympathetic nucleation and of the limited size of bainitic sub-units was rationalised in terms of the relatively low driving force available for bainite transformations.

It was shown that the retention, stability and morphology of austenite could be directly derived from the basic transformation mechanism. Under certain circumstances, the bainitic retained austenite conferred exceptional strength/toughness properties to silicon steels; these were shown to be superior to the properties associated with tempered martensite microstructures. Using thermodynamics, a model was established which could predict the toughness behaviour of silicon steel bainites simply from a knowledge of the composition.

The tempered martensite embrittlement phenomenon was not found to be directly linked to the decomposition of retained austenite films, but to the coarsening of inter- or intra-lath carbides. In dislocated martensites, it was found that the distribution and quantity of retained austenite could be rationalised in terms of the degree of accommodation between adjacent martensite variants. The incipient twins generally observed in lath martensites were shown to be accommodation defects such that the extent of twinning was the greatest when adjacent martensite units had twin-related lattices. The thermodynamics of dislocated martensites have been briefly examined.

The inhomogeneous deformation behaviour of dual-phase steels has been analysed in terms of available models.

GENERAL INTRODUCTION

This work is concerned with retained austenite in low-alloy steels, when present in association either with martensite or with bainite.

At the time the project was conceived, retained austenite seemed to be a panacea for unresolved issues in the field of ultra-high strength steels. Research on high-alloy steels had indicated that the presence of austenite could be beneficial towards mechanical properties. Thus, when retained austenite was discovered in low-alloy directly-quenched steels and in isothermally transformed bainitic steels, there was a natural tendency to extrapolate the earlier findings in order to rationalise the new observations on low-alloy steels. This was in spite of the fact that only very small quantities of retained austenite could be detected in low-alloy steels.

Hence, the conclusion was reached that the films of retained austenite found in low-alloy steels confer beneficial properties. Research in this area immediately intensified, and references to the films of austenite cropped up with notorious frequency in contemporary literature. Often, direct evidence connecting the presence of retained austenite with specific mechanical properties seemed lacking, and the significance of many structure-property correlations was not obvious.

Recently, however, there seems to have been a swing in the opposite sense - retained austenite in high-strength steels appears to have fallen from favour. The 'general' consensus seems to be that the mechanical or thermal instability of film retained austenite causes embrittlement, and that certain morphologies of bainitic retained austenite can reduce the general yield stress.

It was in this context that the project was initiated, and the aim was to try and understand the mechanisms for the retention of austenite but also to clarify its influence on the bulk properties of high-strength steels. It was thus essential to understand the mechanisms of the transformations which do not reach completion, thereby leaving residual austenite; this was taken to be the starting point of the present work.

Although the theory of phase transformations is interesting in its own right, in this thesis I have tried, wherever possible, to use the theory to form the basis of improved heat treatment procedures and steel design, and to minimise the degree of empiricism involved in structure - property work.

Of the four chapters (Ch.I-IV) concerned with the bainite reactions, the first two are devoted to the mechanisms involved and the rest to the understanding of mechanical properties as a function of these mechanisms.

The work on dislocated martensites (Ch.V-VII) is less complete and should be regarded as a part of a long term program to resolve this problem. The role of retained austenite in certain embrittlement phenomena is dealt with in Ch.V, while Ch.VI & VII are concerned with the crystallographic characteristics of dislocated martensites and their significance with respect to the retention of austenite.

The purpose of the work presented in Ch.VIII is to evaluate two available deformation models using a simple two-phase microstructure, the ultimate aim of this work being to apply the models to the more complex bainites discussed in the earlier chapters.

Throughout this thesis, the term 'residual austenite' refers to austenite remaining untransformed at the transformation temperature, whereas 'retained austenite' denotes austenite remaining untransformed at ambient temperature. The following abbreviations have also been used in this thesis:

TTT	= Time-Temperature-Transformation	WQ	= Water quenched
BCC	= Body Centered Cubic	AC	= Air cooled
FCC	= Face Centered Cubic	OQ	= Oil quenched
BCT	= Body Centered Tetragonal	IBQ	= Iced-brine quenched
TRIP	= Transformation Induced Plasticity		
θ	= Cementite		
TME	= Tempered Martensite Embrittlement		
GBLB	= Grain Boundary Nucleated Lower Bainite		

Lists of nomenclature are provided at the end of each chapter in which the use of specific nomenclature is extensive.

THE MECHANISM OF THE BAINITE TRANSFORMATION IN STEELS

(I.1) Introduction

The bainite transformation remains the least understood of all the decomposition reactions of the high temperature austenitic phase in steels. The complexities of its formation mechanism and kinetics, and the apparent diversity in its microstructural appearance, even create disagreement in identifying its correct definition (1,2). However, the well known difference in carbide distribution between bainite formed at high and low temperatures, viz., intralath and interlath, respectively, appears to exist in a majority of steels and makes the classical nomenclature of upper and lower bainite useful, both in describing the microstructural appearance and in classifying the overall reaction mechanism (3-9). In this respect, these terms are used in the present work.

Since bainite forms in the temperature range dividing the reconstructive ferrite/pearlite reactions and the displacive martensitic reaction, there has been a natural desire to relate bainite to one or other of these phases, which has led to much controversial debate concerning the mechanism of its formation (1,10-14).

One school of thought considers that the ferritic component of bainite develops over the whole bainitic temperature range by a diffusional ledge mechanism analogous to the proposals made to account for the formation of widmanstätten proeutectoid ferrite (1). The carbon content of this ferrite is considered to be between the $\alpha/\alpha+\theta$ and the extrapolated $\alpha/\alpha+\gamma$ phase boundaries, and bainitic carbides are considered to form primarily at the austenite/ferrite interface (1). Recent detailed electron diffraction studies of the carbide precipitation reactions have been interpreted to give support to this hypothesis (13). A solute drag model is invoked to explain the bay in the TTT curve at the B_s temperature (15). The incomplete reaction characteristic of the bainite transformation (1,16) is claimed not to be a general phenomenon (1).

The opposing school of thought considers the bainite reaction to be a displacive transformation (involving an atomic correspondence) controlled essentially by the rate at which composition change is accomplished by carbon removal to the surrounding austenite, or by some other rate controlling process such as

strain energy relaxation (1,10,11,16). It is expected that the austenite/ferrite interface should exhibit the same characteristics as in the martensitic transformations. The ferritic component of bainite is thus thought to form with a carbon supersaturation (10,16,17) which in lower bainite is essentially relieved by carbide precipitation within the ferrite. This reaction is thus analogous to autotempered martensite. The existence of a metastable eutectoid reaction controlling the carbide precipitation event has also been postulated (16). This concept is also extended to support the idea of a discontinuous change from upper to lower bainite at a temperature of 350°C virtually independent of the steel composition. The B_s temperature is considered to be due to the intersection of two separate C-curves for reactions (i.e. widmanstätten ferrite and upper bainite) occurring by fundamentally different mechanisms(1,18).

The present chapter describes a study of the bainite reaction in a steel containing deliberate additions of Mn and Si. The importance of the silicon addition in this respect is that it inhibits the formation of cementite, which is the critical event in the progress of the bainite reaction since it removes carbon from the austenite or ferrite. Thus, despite being classified as a ferrite forming element, the presence of Si during the bainite reaction leads to incomplete transformation. The further addition of Mn to the alloy helps to stabilise the untransformed austenite at room-temperature, and also to impart sufficient hardenability for heat treatment. The presence of retained austenite and the slower progress of the overall bainite reaction allows a more thorough study of the transformation mechanism.

(I.2) Experimental Procedures

A 65g melt of the experimental alloy was prepared from pure constituents in an argon-arc furnace, and the final chemical analysis was Fe-0.43C-3.00Mn-2.12Si wt. pct. The ingot was sealed in a quartz capsule under a partial pressure of argon and homogenised for three days at 1250°C, before hot-swaging to 3mm diameter rod.

Austenitising treatments (generally 5mins. at 1200°C) were carried out with the specimen sealed in a quartz capsule. Subsequent isothermal heat treatments were carried out by fracturing the quartz and quenching into a tin bath covered with a layer of active charcoal.

Thin foil specimens for transmission electron microscopy were

prepared from 0.25mm thick discs slit from the heat-treated 3mm diameter rod under conditions of flood lubrication. The discs were subsequently thinned and electropolished in a twin-jet polishing unit using a 5% perchloric acid, 25% glycerol and 70% ethanol mixture at room temperature and 55 volts. The foils were examined in a Philips EM300 transmission electron microscope operated at 100kV.

Dilatometric analysis was carried out on a Theta Industries high-speed vacuum dilatometer using a 20mm by 3mm diameter tube specimen with a 1.5mm diameter bore to facilitate fast cooling. Quenching to the isothermal transformation temperature was achieved by an automatically controlled high-pressure helium jet directed both radially and axially at the specimen. No significant decarburisation occurred.

X-ray analysis was carried out on 1.5mm thick flat-rolled specimens which had been chemically thinned to remove approximately 0.3mm of material from the surface subsequent to heat treatment. A Philips horizontal diffractometer with Co radiation and a LiF crystal monochromator in the diffracted beam was used.

(I.3) Results and Discussion

(i) Reaction Kinetics

Dilatometry combined with optical and electron microscopy was used to determine the bainite TTT curve. Figure I.1 shows the 5% transformation curve; the dashed lines indicate the scatter obtained and it is thought that this scatter is real since it exceeds the estimated experimental errors. Since transformation was usually incomplete, calibration for the total length change due to 100% transformation was obtained by first transforming to upper bainite at 350°C followed by a temper at 500°C in order to decompose the retained austenite. The two length changes measured were then added, after allowing for thermal expansion, in order to obtain the length change due to 100% transformation. Separate C-curves were indicated for upper and lower bainite*, and this is

* Throughout this study upper bainite is defined as an aggregate of bainitic ferrite and high-carbon retained austenite without any carbide precipitation due to the influence of the high level of silicon in the experimental alloy. Lower bainite is defined as an aggregate of bainitic ferrite with little retained austenite and, distinctively, intralath precipitation of sheet-like cementite particles in the ferrite. Justification for these definitions will become evident in the section on microstructural observations.

considered further below.

Electron microscopy revealed that the upper and lower bainite reactions did not go to completion despite prolonged periods of holding at the isothermal transformation temperature (significant amounts of retained austenite were detectable in all cases).

It was found that near the B_s temperature only a very limited amount of austenite transformed to bainite despite holding at the isothermal transformation temperature for 32 hours. Dilatometry indicated an initial limited amount of rapid transformation followed by an asymptotic termination. Figure I.2 shows a specimen isothermally transformed at 452°C for 32 hours and it is clear that only a small amount of upper bainite has formed and that eventually the pearlite reaction has taken over.

The temperature dependence of the 'incomplete reaction' was investigated by measuring the length change from zero time to a time when the reaction rate was negligible ($dL/dt = 7.6 \times 10^{-6}$ cm s^{-1}). This data is plotted as a function of the isothermal transformation temperature in fig.I.3. It is clear that the extent of transformation is a sensitive function of the incomplete reaction phenomenon (16). This data is considered to be particularly relevant since there is no interference from carbide precipitation during the upper bainitic ferrite reaction in this alloy. Any precipitation of carbide would naturally reduce the carbon content of the enriched austenite, thereby promoting further transformation.

The extra bays indicated by high-speed dilatometry in the bainite TTT diagram between the upper and lower bainite reactions, and between the lower bainite and martensite reactions have not been detected before and required further confirmatory studies. Quenching into a tin bath held at the required isothermal transformation temperature failed to reveal metallographically the lower part of the upper bainitic curve due to the onset of the lower bainite reaction. However, it was found that when helium quenching was used (in the dilatometer) the lower part of the upper bainitic curve was well defined (e.g. figure I.1), and metallography specified a temperature region where either upper bainite or lower bainite formed but never a mixture of the two. This indicated a dependence of the transformation product (upper or lower bainite) on the quench rate to the isothermal transformation temperature. It appeared that upper bainite would form when the quench rate was relatively slow. Step

quenching experiments were conducted to verify this. Following austenitisation, specimens were quenched to the metastable bay (500°C) above the B_s temperature and held for 30 seconds before quenching into a tin bath at a temperature in the lower range of the upper bainitic C-curve (283°C). This treatment effectively reduces the quench rate to the isothermal transformation temperature. Very little transformation to a typically feathery upper bainite product was recorded, and electron microscopy confirmed upper bainite consisting of bainitic ferrite and retained austenite in a bulk matrix of martensite (figure I.4). The existence of a separate C-curve for the upper bainite reaction was therefore confirmed in detail and a quench rate effect was noted such that upper bainite was obtained at low quench rates (to isothermal transformation temperature) in the region of overlap of the upper and lower bainite reactions.

Isothermal transformation at 247°C revealed the lower part of the lower bainitic curve; very little transformation was detectable metallographically despite relatively long periods at the isothermal transformation temperature (figure I.5). It is noted that the dilatometrically determined M_s temperature of this alloy is 220°C. It was found that a significant slowing down of reaction kinetics corresponding to the upper part of the lower bainitic C-curve could not be detected with confidence.

By the kinetic definition the bainite reaction has its own C-curve; as the maximum temperature of this curve (the so-called kinetic B_s temperature) is approached, the proportion of bainite formable decreases (ideally) to zero (1). In alloy steels there is usually a well defined bay at the B_s temperature above which austenite will not transform by the bainitic mode. The present results are consistent with this definition and, because of the agreement between the dilatometry and optical and electron microscopy, also indicate that the kinetic definition is directly equivalent to the microstructural B_s. The existence of separate reaction curves for the upper and lower bainitic transformations is also observed.

Based on kinetic observations of an Fe-Mo-C alloy, Aaronson concludes that the kinetic-B_s is only a manifestation of the special effect of alloying elements on the growth kinetics of proeutectoid ferrite (1,2) i.e. the minimum in growth kinetics is interpreted in terms of a drag effect produced by the segregation of certain alloying elements to the austenite/ferrite

interfaces. It is suggested that alloying elements which decrease the activity of carbon in austenite should exercise an enhanced drag effect relative to those that do not (2,15) and the absence of a bay in an Fe-C-1.0Mn a/o alloy is claimed to be consistent with the relatively small effect of Mn in reducing the carbon activity in austenite (15). It is further claimed that elements such as Si and Co which raise the activity of C in austenite should not give rise to the kinetic-B_s phenomenon (2). In plain carbon steels the kinetic features are not well defined although several other features of the bainite reactions are present. Depending on the theory subscribed to, diffusional ledges or displacive shear, this can be attributed either to observational difficulties (related to competition from the pearlite and proeutectoid ferrite reactions) (1) or to the absence of any substitutional solute elements to exert a drag on the transformation front (1).

According to Aaronson (2) the development of the bainite reaction below the B_s temperature can be visualised in terms of the competition between the reaction driving force and the approach to saturation of the solute drag effect.

The present results would appear to be inconsistent with the solute drag model which can only explain a single bay in the vicinity of the B_s temperature, and not the three observed in the present work. Recent work (19,20) has added the possibility that the so-called "solute drag effect" may simply be due to the influence of carbide precipitation on the dynamics of the austenite/ferrite interface in the region of the kinetic bay.

Based on available thermodynamic data (21) it is concluded that the composition of the present alloy merits a large increase in the activity of carbon in austenite. Despite this fact, a strong kinetic B_s is observed, in contradiction to the above solute drag model; furthermore, electron microscopy clearly shows the absence of any carbide precipitation at this temperature.

The alternative explanation is that the B_s temperature arises from a fundamentally different mechanism of the bainite reaction as compared to the formation of widmanstätten ferrite (1,10,14,16). Additionally, supporters of the theory that bainite forms by a displacive shear mechanism also postulate that it 'forms' by the repeated nucleation of substructural units that propagate rapidly to a limited size, and thus the incomplete nature of the

reaction can be attributed to a restriction on nucleation rather than on growth. Consistent with this observation is that upper bainite plates retain their lenticularity; they do not appear to thicken following their initial rapid formation. There is, however, only limited evidence for the existence of these substructural units, especially for the case of upper bainite (10) and the explanation of the incomplete reaction phenomenon in terms of a link between the relaxation of accommodation strains and the nucleation event is tenuous and unconvincing. Speich (22) points out that the major component of the accommodation strains would not be relieved by the partitioning of carbon - the latter would only lead to a volume contraction and not reduce the important shear component of the total shape strain. In the present work, evidence for the sub-units referred to above is presented for upper and lower bainite in the section on microstructural observations and an explanation of the incomplete reaction phenomenon is dealt with in detail in chapter two.

The two separate C-curves for upper and lower bainite observed in the present study are also thought to arise from two distinct transformations operating in each case and the lower parts of the two C-curves may then be attributed to the increasing difficulty of dissipating the carbon diffusion fields of the prior sub-units (this will become clear in the context of chapter two).

(ii) Microstructural Observations - Upper Bainite

Isothermal transformation in the upper bainitic temperature range (defined by dilatometry) always gave an aggregate of bainitic ferrite and retained austenite (figure I.6). There was no detectable carbide precipitation even after holding at 350°C for 74 hours. As indicated by previous investigators (23-25), this clearly results from the presence of Si. Si is known to inhibit cementite formation during the tempering reaction in steels (23-25). This is generally explained by the relative insolubility of Si in cementite requiring the diffusion controlled ejection of Si at the transformation front which in turn results in a Si concentration build-up during an early stage of growth. This locally increases the activity of carbon so that the carbon flux is reduced and further development of the cementite embryo is inhibited (23). However, it should be noted that even high resolution electron microscopy failed to reveal any carbide in the upper bainite involved in the present study.

Prevention of cementite formation correspondingly leads to a high concentration of carbon in austenite. Stabilisation of the austenite at room temperature indicates that at some stage during the bainite reaction the austenite becomes enriched with respect to carbon. Whether the bainitic ferrite forms with a supersaturation in carbon, and if so, at which stage of the reaction the partitioning of carbon to the austenite takes place, is a matter of keen dispute (e.g. ref.1). Furthermore, although carbon must play a vital role in the stability of this austenite, it is likely that other physical factors also contribute to this and to the overall extent of transformation; this point is dealt with further in the discussion of the X-ray diffraction experiments. For the purpose of a detailed metallographic study it was found that 30 minutes at 350°C allowed sufficient reaction, and hence adequate carbon enrichment to stabilise the austenite for subsequent room temperature examination. This does not imply that zero austenite is retained when the extent of transformation is low because regions of austenite which become totally surrounded by bainitic ferrite achieve the required carbon content (e.g. figure I.4).

The interwoven or branching nature of the bainitic ferrite/retained austenite aggregate is shown in figures I.4,6 and is characteristic of the upper bainite morphology in similar steels containing Si additions (13). It is interesting to speculate how bainitic 'plates' could have formed with internal films of austenite to give an irregular composite character to each individual macroscopic plate. Although interrupted by the austenite regions, the ferritic components of the plate are semi-continuous and in the same crystallographic orientation. It is clearly difficult to see how the plates could have thickened to this morphology by the progression of ledges along the planar interfaces parallel to the long direction of the plates. Rather, the regular partitioning of the plate along its length by the austenite fingers emanating from the main austenite lamellae is more suggestive evidence for the formation of bainitic ferrite by 'martensitic jumps' composed of smaller units. This aspect will be developed further in chapter two.

During the course of electron metallography it was observed qualitatively that the bainitic ferrite contained a high dislocation density, and that this was higher than that of the retained austenite. Clusters of dislocations could also be found associated with the austenite/ferrite interfaces (figure I.7a).

The retained austenite was also found to contain planar faults, very often with one dominant fault plane (figure I.7b). When the fault plane was approximately normal to the foil plane, the faults could be seen to terminate at slip steps in the austenite/ferrite interface (figure I.7c). It is attractive to suggest that these steps are indicative of accommodation slip on $\{111\}_\gamma$ planes in the austenite phase during a displacive transformation.

A series of specimens was given different austenitising treatments before transforming to upper bainite for 115 minutes at 350°C. Varying both the austenitising temperature and time gave a range of austenite grain sizes and also corresponding changes in austenite texture (due to selective grain growth). The isothermal treatment chosen allowed the bainite reaction to proceed to an extent sufficient to stabilise untransformed austenite at room temperature. The austenite levels were sufficient for accurate X-ray analysis (Table I.1).

The volume fraction of retained austenite was calculated from the X-ray intensities; texture effects were taken into account in accordance with the work of Dickson (26) by utilising the integrated intensities of a minimum of three ferrite and three austenite peaks. Experimentally determined lattice parameters were used in each case since these were expected to vary with the degree of transformation due to the partitioning of carbon into the austenite; different structure factors thus had to be calculated for each specimen. The accuracy of the lattice parameter calculations was maximized by the use of an extrapolation function (27).

The results of the analysis may be interpreted as follows: $P_{hkl} = 0$ corresponds to a random orientation, $P_{hkl} < 1$ shows that such $\{hkl\}$ planes are preferentially avoided and $P_{hkl} > 1$ means that these planes are preferentially oriented parallel to the plane of section** .

** $P_{hkl} = (I_{hkl}/R_{hkl})/\frac{1}{n} \sum^{n} (I/R)$

where I = integrated intensity of the reflection concerned,
and R = correction factor for each reflection as defined in ref.26.

The prior austenite grain diameter (d) was also measured by lineal analysis on the actual specimens used for the X-ray determinations. The correlation between the volume fraction of retained austenite and grain size proved to be rather poor

with the best correlation coefficient of 0.56 obtained against d^{-3}.

In view of this rather poor correlation the data was examined in greater detail and it was thought that texture was affecting the degree of transformation. To test this hypothesis, the pct. retained austenite was examined as a function of P_{111_γ} and d^{-3}. It was found that a drastically improved multiple correlation coefficient was obtained when the pct. retained austenite was plotted as a function of both the above variables. However, the multiple correlation coefficient was further increased to 0.981 when P_{110_α} was used instead of P_{111_γ}, (figure I.8). This is probably so because the textured austenite $\{111\}_\gamma$ planes are not necessarily faithfully replicated by the ferrite $\{110\}_\alpha$ planes during transformation.

In view of the excellent correlation, it is concluded that the texture of the $\{111\}_\gamma$ planes has a significant effect on the extent of transformation. Since the $\{111\}_\gamma$ planes are the most common slip planes in austenite, this effect is consistent with slip in the austenite during transformation; that its importance is revealed through a texture effect is probably because of a greater possibility of cooperative transformation between adjacent grains with an increase in the $\{111\}_\gamma$ texture. Certainly, in the initial nucleation event, irrespective of the final details of the transformation crystallography, the close-packed planes are considered to be of fundamental importance in generating the BCC lattice from the FCC lattice (28). One would thus expect a decrease in the amount of retained austenite with an increase in the degree of cooperative formation, as manifested by the P_{111_γ} and P_{110_α} values.

The strong correlation of P_{111_γ} with pct. retained austenite rather than any of the other low index austenite planes emphasises the importance of $\{111\}_\gamma$ planes in the upper bainite transformation. This is consistent with the previous observation of slip steps on $\{111\}_\gamma$ planes in the upper bainitic retained austenite.

The fact that such large variations in the extent of transformation can be attributed solely to physical effects stresses the need to refine thermodynamic theories of phase transformations which often ignore these variables.

Bainitic carbide precipitation is an integral part of the

overall bainite reaction, and in order to study this in the upper bainite reaction in the Si-steel it was necessary to induce decomposition of the retained austenite by tempering at a higher temperature. Tempering at 500°C for less than 30 minutes gave a microstructure consisting of bands of fine carbides separated by 'clean' ferrite (i.e. with a minimum of carbide precipitation), indicating that the carbides had mainly precipitated in the prior austenite regions (figure I.9a). The carbides had a thin plate-like morphology, and due to their extremely small size and close spacing, identification by conventional selected area electron diffraction proved impossible. However, using convergent beam electron microscopy several solvable diffraction patterns were obtained, an example of which is illustrated in figure I.9b. All the diffraction patterns could be consistently indexed to the following monoclinic structure:

$a = 8.096\ \text{Å},\ b = 10.41\ \text{Å},\ c = 7.00\ \text{Å},\ \beta = 107.2°$

It is thought that this phase is probably an iron-silicon-manganese carbide. The identification of this carbide is considered more fully in appendix one.

Further tempering at 500°C led to complete decomposition of the retained austenite (figure I.9c) and replacement of the above monoclinic carbide by cementite (figure I.9d) with the microstructure now appearing somewhat similar to conventional upper bainite. The cementite was concentrated at lath/sub-boundaries, and gave unusual orientation relationships (i.e. inconsistent with any known rational ferrite-cementite orientation relationships). It is thus probable that the cementite precipitated at the monoclinic-carbide/ferrite interfaces, in which case it would be energetically favourable for it to adopt an orientation giving low energy interfaces with both the monoclinic carbide and the ferrite. Since negligible intragranular precipitation occurred in the bainitic ferrite, it was concluded that the carbon content of the ferrite was of the order of 0.03 wt. pct. However, this only shows that the final upper bainitic ferrite is not supersaturated with respect to carbon and gives no indication as to whether it was supersaturated at some earlier stage in the reaction with carbon which subsequently partitioned into the surrounding austenite.

In order to examine the precipitation sites, hot stage electron microscopy was conducted on specimens which had first been transformed to upper bainite (i.e. a lamellar aggregate of

retained austenite and bainitic ferrite). This revealed (figure I.9e) that while some precipitation occurred totally within the austenite, the majority of carbides formed at the austenite/ferrite interface and grew into the austenite. Following this, the boundary pulled away from the line of carbides and this sequence continued repeatedly until the austenite had fully decomposed. In general, due to the thinness of the austenite lamellae, only one or two lines of carbide were observed before austenite decomposition was completed. These results indicate that the majority of upper bainitic carbides nucleate at the austenite/ferrite interface and grow into the austenite, resulting in its diffusional decomposition. It is thought that this sequence is representative of the full reaction to a bainitic ferrite/carbide aggregate in low-Si steels, but that in the latter case the decomposition events must occur virtually simultaneously. In the latter case the transition carbide would probably be epsilon carbide rather than the monoclinic carbide found in the present work. This would be consistent with the Isaichev orientation relationship generally observed between the cementite and bainitic ferrite in low-Si steels (29) since the crystallography of epsilon carbide/ferrite is closely related to that of cementite/ferrite when the latter corresponds to either the Isaichev or the Bagaryatski orientations (30). Hence, in steels where intermediate carbides are stabilised relative to cementite, there is a clear possibility that the final upper bainitic cementite is really the result of a sequence of carbide precipitation events. In other steels such a sequence would perhaps be too rapid to detect, if it existed at all.

(iii) Microstructural Observations - Lower Bainite

Isothermal transformation in the lower bainitic temperature range also resulted in an aggregate of ferrite and retained austenite, although the amount of retained austenite was very much lower than obtained in the upper bainite reaction. The lower bainite microstructure was, however, distinctly characterised by the presence of carbide precipitation within the bainitic ferrite plates (figure I.10a).

In contrast to upper bainite, the individual ferrite plates in the lower bainite are more regular. The dislocation content of the ferrite was higher than in the retained austenite, and also higher relative to upper bainitic ferrite. Furthermore, regular dislocation arrays were occasionally observed, with dislocation lines appearing parallel to the traces of the sheets of carbide

precipitates, implying, as will be seen later, that the dislocations could lie on $\{110\}_\alpha$ planes (figure I.10b).

The ferrite plates very occasionally showed twinning (figure I.10c) on a single variant of the twin plane which appears very similar to the twins observed in the martensite in this alloy. Studies of martensite in this alloy have shown that these martensitic twins are on $\{112\}_{\alpha'}$ planes (Ch.7). When the austenite-martensite matrix-martensite twin lattices are superimposed in the correct relative orientations, the $\{112\}_{\alpha'}$ planes correspond to different planes in the austenite lattice in different sets of data (the same variant of the correspondence is used in each case) which suggests mechanical twinning rather than transformation twinning (Ch.7). If they had been transformation twins they would all have corresponded to the same austenite plane. While a similar analysis has not yet been conducted for the lower bainitic twins, the morphology, probability of occurrence, and distribution are the same and it is tentatively concluded that they are also mechanical twins. This is considered to be an appropriate conclusion for a supersaturated lower bainitic ferrite; the carbon would be expected to raise the general flow stress relative to the twinning stress, thereby making twinning deformation more likely.

No apparent regularity in the dislocation structure of the retained austenite was detected. Furthermore, the lower bainitic retained austenite did not in general exhibit regular stacking fault arrays (figure I.10d), and the stacking fault density also appeared to be significantly lower relative to the upper bainitic retained austenite. These qualitative observations on the differences in the defect structures of upper and lower bainite provide further evidence for mechanistic differences between the two structures.

Despite the high level of silicon in the experimental alloy, the intragranular bainitic carbide was identified by transmission electron microscopy and electron diffraction to be cementite, even at the very earliest of transformation times (2 minutes at 300°C), and at the lowest of transformation temperatures (247°C). The cementite displayed a distinctive sheet like morphology (figure I.10e), similar to that often obtained in tempered martensites. It is noted that in this alloy there can be no confusion between auto-tempered martensite and lower bainite since electron microscopy revealed that the martensite did not contain

carbides, and negligibly small quantities of retained austenite were associated with the martensite obtained by direct quenching (figure I.11). (Additionally, the martensite in the present alloy tempers initially to epsilon carbide and subsequently to cementite (Ch.4) but the results that follow demonstrate that the starting precipitate in lower bainite is cementite.)

Epsilon carbide was not detected at any stage of the lower bainite reaction. This may be attributable to the high level of manganese in the experimental alloy, which would tend to stabilise cementite; manganese is very soluble in the cementite lattice and also forms Mn_3C which has a structure isomorphous with cementite (31). This result is also consistent with the dilatometric data which showed no contraction associated with the tempering of lower bainite; a contraction is expected if epsilon is present and is eventually replaced by cementite (16).

The absence of epsilon carbide is inconsistent with the interesting concept of a metastable $\gamma \rightleftharpoons \alpha + \varepsilon$ eutectoid reaction (16) proposed to explain the relative temperature insensitivity of the transition from upper to lower bainite to the carbon content of the steel. However, in view of the low diffusivity of Si in the lower bainite temperature range, the cementite must be supersaturated with Si and this leads to the possibility of another metastable equilibrium reaction, i.e. $\gamma \rightleftharpoons \alpha + \theta_{metastable}$. To examine this proposal step quenching experiments were carried out in accordance with the methods of (16). Specimens were partially isothermally transformed to lower bainite and were immediately up-quenched into the γ phase field (time periods up to 15 minutes and temperatures between 350°C and 500°C -i.e. above the alleged eutectoid temperature of 350°C), finally followed by a quench to room temperature. The existence of a metastable eutectoid reaction would require the dissolution of the carbide formed by cooling through the invariant temperature when the system is reheated rapidly to a phase field above that temperature (16). Subsequent examination by thin foil electron microscopy showed that the cementite did not redissolve, and consequently the possibility of a metastable eutectoid reaction based on cementite was also ruled out. Only small volume fractions of lower bainite were involved in the above experiments (0.05-0.10) in order to ensure that the lower bainite was readily in contact with residual austenite and hence allow the carbon resulting from the dissolution of metastable cementite to be easily dissipated into the

residual austenite.

The above results are also supported by the fact that the cementite/lower bainitic ferrite orientation relationship (to be discussed later) found in the present study is different from that observed generally when epsilon carbide is an intermediate phase relative to cementite (31). It can therefore be concluded that the metastable eutectoid, if it exists at all, cannot be a general phenomenon and therefore cannot alone account for the differences between the upper and lower bainite reactions.

Trace analysis showed the cementite precipitate habit plane to be in the vicinity of $\{011\}_\alpha$ in the majority of micrographs analysed although in two specific cases the results were unclear. Up to four different variants of the cementite habit plane have been observed in a single ferrite crystal (e.g. figure I.12a). Analysis of several electron diffraction patterns (an example is given in figure I.12b) revealed an uncommon orientation relationship between the cementite and ferrite matrix , viz.,

$$(011)_\theta \;//\; \{011\}_\alpha \qquad [122]_\theta \;//\; \langle 100\rangle_\alpha$$

However, it was not possible to obtain a rational three phase ($\gamma \succ \alpha \succ \theta \succ \gamma$) crystallography, given the experimentally observed Kurdjumov-Sachs orientation relationship between the austenite and bainitic ferrite. (It should be noted that when carbides precipitate at the interphase interface, a rational three phase crystallography is generally observed -ref. 32).

It was also observed that isothermal transformation for short periods showed a generally low precipitate density, and that often some of the lower bainitic ferrite did not contain detectable carbide precipitates at all (e.g. figure I.12c). This observation along with the multi-variant habit plane and orientation relationship is strong evidence for the hypothesis that the cementite precipitates from a supersaturated matrix. Thus, the often suggested possibility (1,33) that the lower bainitic carbides form at the austenite/ferrite interface is discounted.

The corollary to this argument is that the lower bainitic ferrite does form with a carbon supersaturation which is subsequently relieved by carbide precipitation. However, it may or may not form with a full supersaturation since enriched retained austenite is still obtained. This point will be dealt with in chapter two. From carbide volume fraction measurements the supersaturation is <u>estimated</u> to be 0.25-0.3 wt. pct. C.

It is clear that at the reaction temperatures involved the lower bainitic cementite formation could not possibly have involved any diffusion of iron atoms or of substitutional atoms. It is therefore believed that the cementite must initially form with a supersaturation of silicon so that the growth barrier posed by the build up of silicon at the cementite/ferrite interface does not arise. A detailed examination of the positions of iron atoms in the ferrite lattice and the cementite lattice (figure I.12d) for the observed orientation relation shows that only small atom shuffles are required to generate the cementite lattice from the ferrite lattice. Furthermore, the stacking sequence of the $\{110\}_\alpha$ planes is the same as for the $\{022\}_\theta$ planes after allowing for the shuffles. This is entirely consistent with the idea that cementite has formed with a supersaturation of silicon and with a sheet like morphology.

At low magnifications the cementite often appeared wavy. However, high resolution electron microscopy revealed that the individual cementite particles actually consisted of combinations of sheets on different variants of the habit plane (figure I.10e). These components of the individual particles are also in different crystallographic orientation, i.e. the whole particle is not illuminated in dark field imaging, but only those components that lie on the same habit plane. This is the reason why despite the absence of any coincident reflections between different cementite variants, one is able to image parts of precipitates on apparently different habits (figure I.12a). Considering the mechanism of cementite formation, the change in habit plane in individual precipitates could be due to effects of growth accommodation or minimization of carbon diffusion distances. The apparently wavy nature of the carbide phase has in the past been attributed to the consequence of ledge motion (13).

Some interesting observations were made on specimens partially transformed to give lower bainite in a matrix of martensite. Optical microscopy revealed two basic morphologies of bainitic ferrite, one associated with the grain boundaries and the other precipitated intragranularly (figure I.13a). It was found that the edges of the grain boundary phase corresponded to the habit plane traces of the intra-granularly nucleated phase (figure I.13b). Furthermore, the intragranular plates often formed from the grain boundary lower bainite in a morphology not far removed from that of widmanstätten sideplates associated with proeutectoid ferrite allotriomorphs.

The tips of the intragranular plates could be resolved by electron microscopy into a set of spikes (figure I.13c) of approximately 0.2 microns width. No superledges were observed on the planar edges of these plates. Often individual isolated spikes of approximately 0.2 microns width were also observed (figure I.13d); these exhibited all the carbide precipitation characteristics of the plates (i.e. more than one variant of cementite) although some spikes had none or only sporadic cementite precipitates due to the short transformation times involved. These spikes had the same habit plane trace as those at the tips of larger plates.

Spikes could also be associated with the grain boundary nucleated lower bainite (GBLB), as shown in figure I.13e, and again the width of these was ca. 0.2 microns. The traces of these spikes corresponded to the intragranular lower bainite traces (figure I.13b) so that the mechanism of their formation is not considered to be different in the two structures. In some cases all of the spikes terminated at the same position, giving a jagged, step-like appearance to the transformation front, with the width of these perturbations corresponding to ca. 0.2 microns, consistent with that of the isolated spikes (figure I.13f). It is noted that these cannot be mistaken for superledges since they are not on the habit plane but across the plate; the superledge mechanism requires a major component of the ledge motion to lie on the habit plane in order to generate the plate morphology (34).

It is suggested that the observation of spikes at the advancing transformation interfaces of lower bainitic plates provides strong metallographic evidence for the propagation of the lower bainitic reaction by the successive transformation of units of austenite by displacive shear. This proposal is also consistent with the constant width recorded for the shear units, whether on intragranular or grain boundary nucleated plates.

It is considered that the morphological differences in lower bainite arise because of the effect of the austenite grain boundaries in stimulating nucleation so that a larger number of shear units are nucleated adjacent to each other, giving rise to the GBLB structure.

(I.4) General Summary

The Si-containing steel examined in the present investigation was found to exhibit the upper and lower bainite microstructures,

essentially as described classically, although in the case of upper bainite carbide precipitation was prevented by silicon addition. Detailed dilatometry and electron metallography of this bainite provides further experimental evidence which is thought to be pertinent to the differentiation of the two most favoured models proposed for the reaction mechanism. Both the kinetic and structural results obtained appear inconsistent with a growth model based on a diffusional ledge mechanism (as applied more successfully to widmanstätten ferrite).

Separate bainite C-curves have been identified dilatometrically, with a B_s-temperature and incomplete reaction, which with microstructural observations indicated the overlap of separate C-curves for ferrite/pearlite and upper bainite, consistent with transformation by fundamentally different mechanisms. The existence of separate C-curves for upper and lower bainite gives rise to two further incubation bays in the transformation curve which are impossible to explain by special alloying element effects giving interfacial solute drag. Furthermore, the morphology of the upper bainite is difficult to reconcile with its formation by the migration of transformation ledges along the planar partially-coherent faces of the bainitic ferrite plates and is consistent with a displacive mechanism involving the propagation of the transformation by the successive nucleation of displacive sub-units.

The observation of lower bainitic ferrite growth by the apparent formation and coalescence of adjacently nucleated transformation spikes is also consistent with the hypothesis of growth by the repeated nucleation of shear units. Furthermore, the importance of the $\{111\}_\gamma$ slip planes, and the observed defect structures in the retained austenite suggest transformation slip in the parent austenite in upper bainite, whilst the high dislocation density (with some linear arrays parallel to $\{110\}_\alpha$ traces) and occurrence of mechanical twinning in the ferrite suggest accommodation in the product ferrite in lower bainite. These observations not only support formation of bainitic ferrite by a shear mechanism, but are also consistent with the existence of two separate C-curves for upper and lower bainite, and indicative of two fundamentally different mechanisms separated by a very narrow temperature range at approximately 350°C.

The retention of relatively large quantities of austenite and its stability (even in thin foils) suggest carbon enrichment of the parent austenite in both the upper and lower bainite

reactions. In upper bainite the enriched austenite decomposed during subsequent tempering to ferrite and carbide; carbide precipitation was shown to occur at the austenite/ferrite interface and grow into the austenite. This behaviour is consistent with the crystallography of austenite, ferrite and carbide phases found, and conforms to a generally agreed sequence for the upper bainitic carbide precipitation reaction. It was not possible to determine whether the upper bainitic ferrite was supersaturated with carbon at any stage of its formation. This was possible to deduce, however, in the case of lower bainitic ferrite. Firstly, because of the mechanical twinning which implies a higher yield stress conferred by carbon supersaturation, and secondly, because of structural observations made of the mode of intralath carbide precipitation. This carbide was not observed at very short transformation times, but then precipitated on more than one variant of the habit plane, and with a uniquely determined habit plane consistent with minimum energy precipitation from supersaturated solid solution.

The absence of epsilon carbide and the thermal stability of lower bainitic cementite during retrogression experiments showed that the lower bainite reaction cannot in general be considered as a product of a metastable eutectoid reaction.

Table I.1

Austenitising Treatment	Grain Size/μm	P_{022_α}	Retained Austenite(%)
955°C @ 15 mins	35	0.629	22
955°C @ 15 mins	35	0.798	22
955°C @ 66 mins	45	0.631	20
955°C @ 300 mins	62	0.366	15
955°C @ 715 mins	70	0.986	24
1100°C @ 5 mins	62	0.196	12
1280°C @ 15 mins	1000	0.563	16

Notes

1) All the specimens were isothermally transformed at 350°C for 115 mins after austenitising.
2) It should be noted that the above texture analysis and the regression determinations presented in the text should only be taken to apply to the specific set of specimens used here. Because the texture parameter (P_{022_α}) takes no account of three dimensional texture variation, the results are unlikely to be general. Hence the regression analysis based on the above data can only serve to illustrate the trends involved. It is likely that specimens with other hot working histories (towards the achievement of the final specimen shape) will exhibit different values for the above parameters with respect to the surface used in the X-ray analysis.

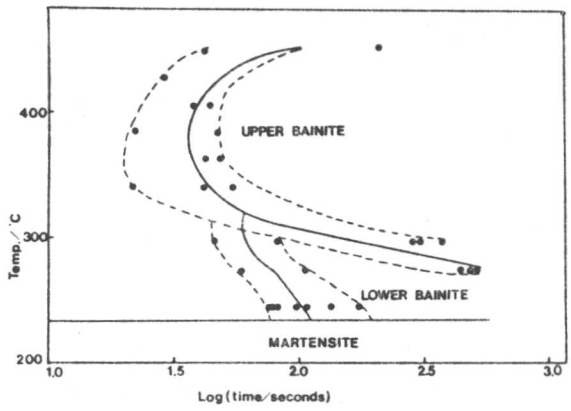

Figure I.1
Dilatometrically determined 5% transformation TTT curve.

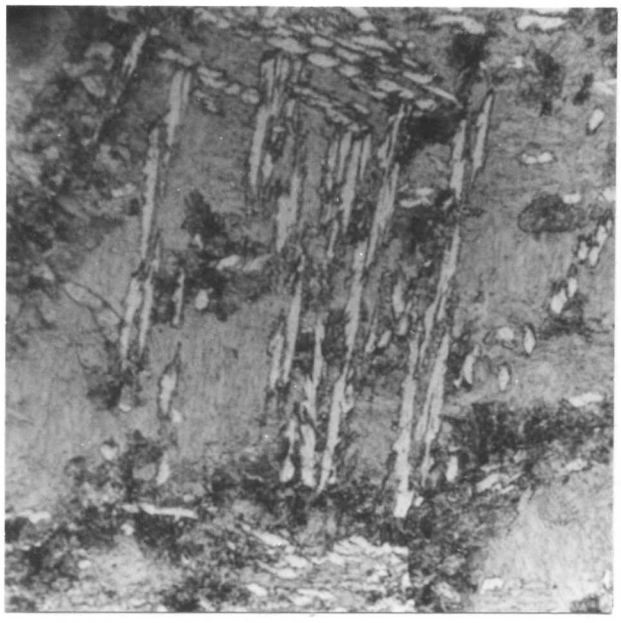

Figure I.2
Optical Micrograph showing the termination of the upper bainite reaction and the onset of pearlite formation after isothermal transformation at 452°C for 32 hours.

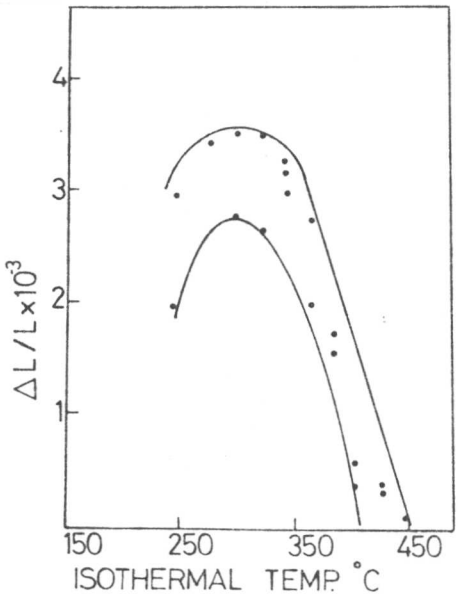

Figure I.3
Curve of dL versus isothermal transformation temperature showing temperature dependency of the 'incomplete reaction' phenomenon.

(a)

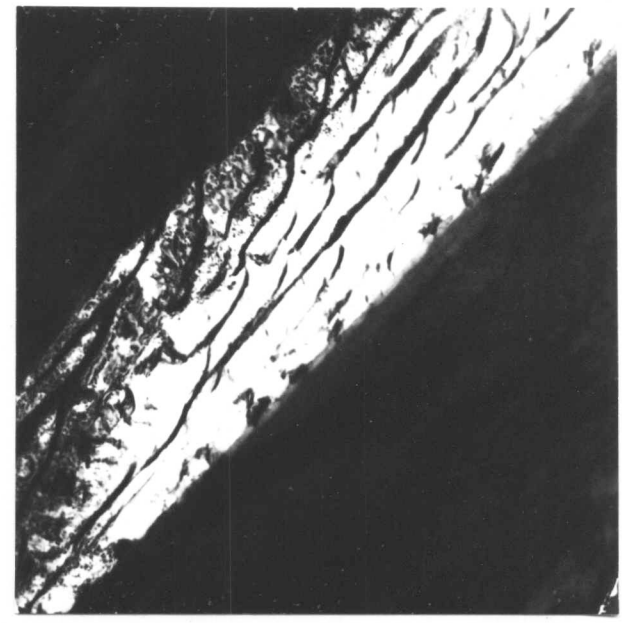

(b)

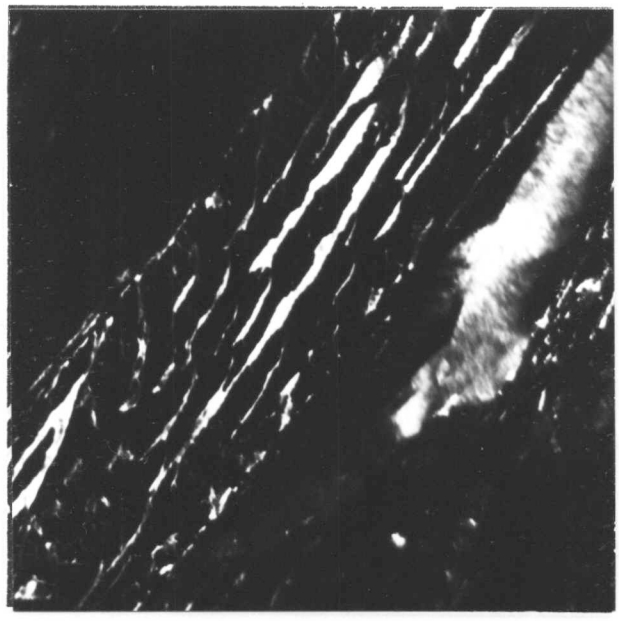

(c)

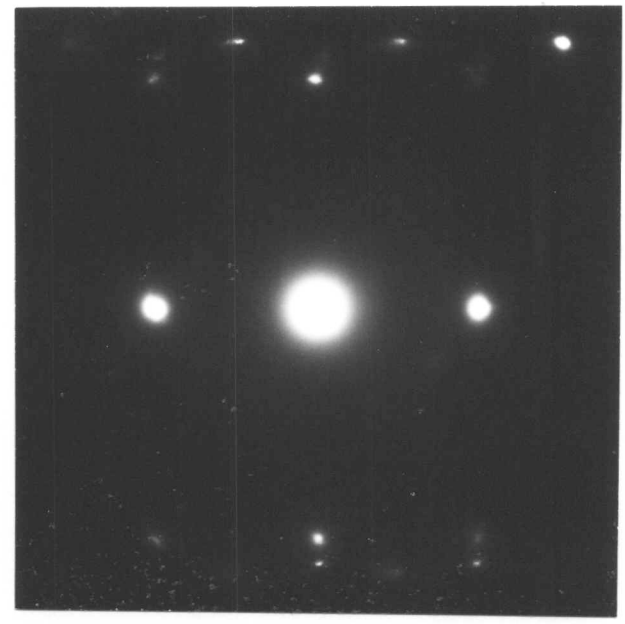

(d)

Figure I.4

Upper Bainite formed after isothermal transformation at 286°C for 30 minutes.

(a) Optical Micrograph.

(b) Transmission bright field image of a single 'plate'.

(c) Corresponding dark field image of retained austenite.

(d) Corresponding diffraction pattern.

(e) Interpretation of (d).

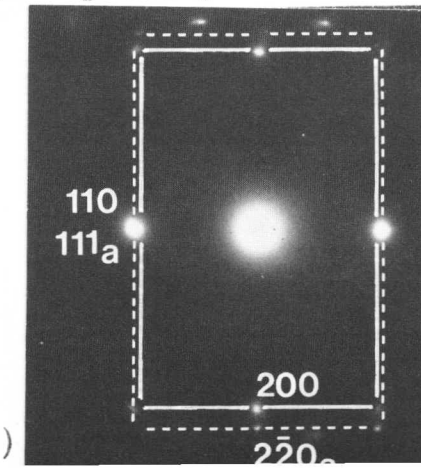

(e)

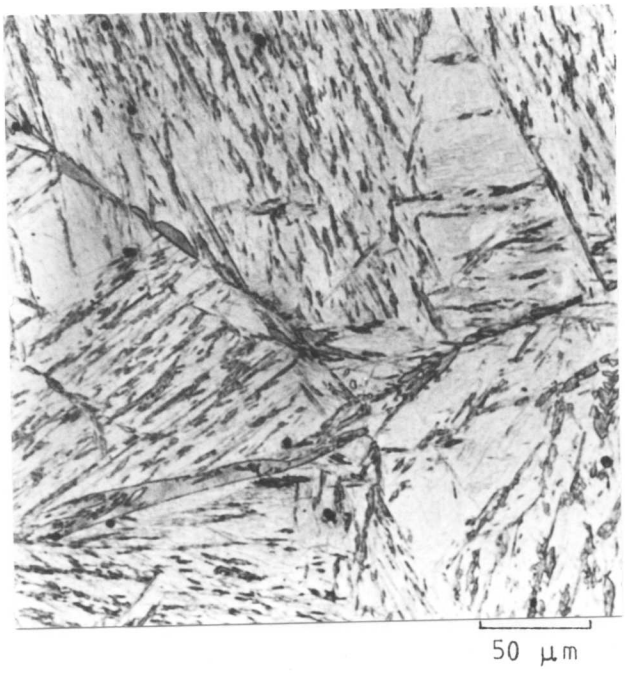

Figure I.5
Lower bainite formed after isothermal transformation at 246°C for 30 min.

Figure I.6
Upper bainite formed after isothermal transformation at 350°C for 205 min. The retained austenite is the grey phase.

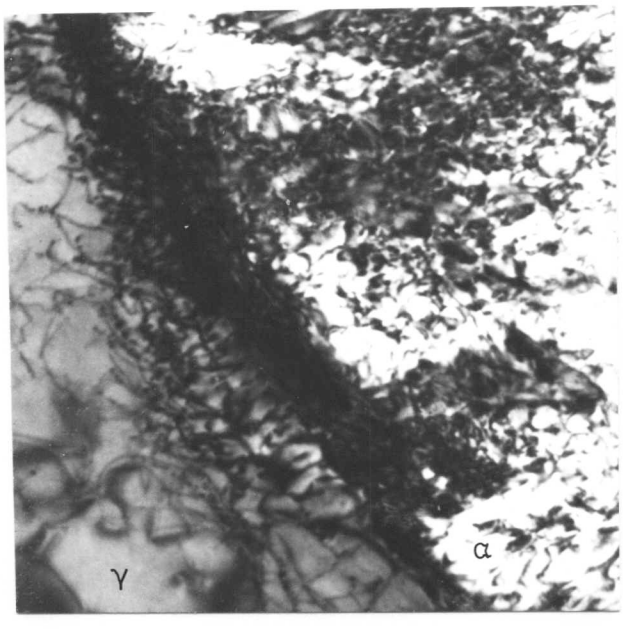

(a)

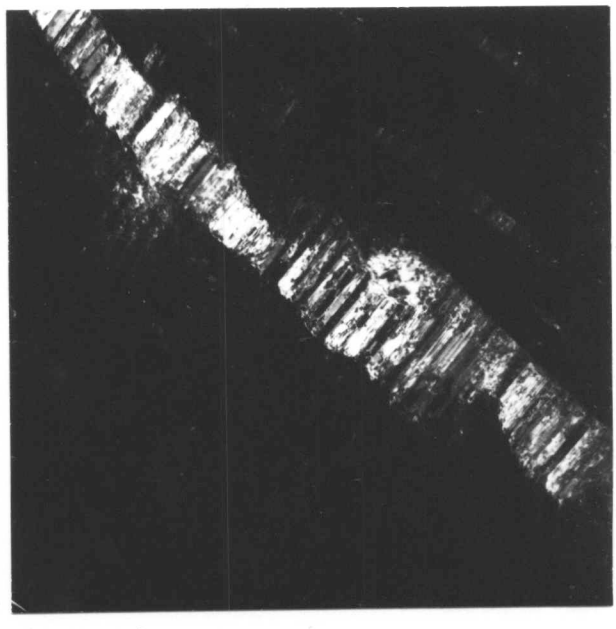

(b)

Figure I.7
Microstructural features of upper bainite formed after isothermal transformation at 350°C for 205 min.
(a) Dislocation clusters associated with the bainitic ferrite-retained austenite interface.
(b) Dark field image of upper bainitic retained austenite showing extensive faulting.

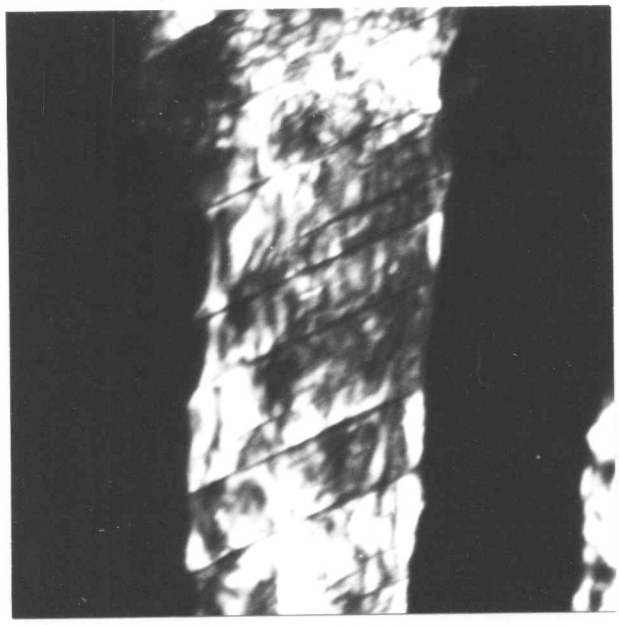

Figure I.7c
Dark field image of upper bainitic retained austenite showing accommodation slip steps. (Isothermally transformed at 350°C for 205 min.)

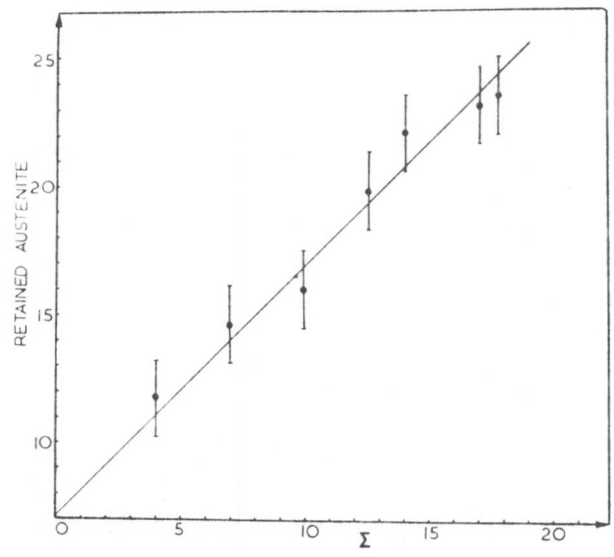

Figure I.8
The variation of upper bainitic retained austenite with the parameter Σ , where
$\Sigma = 17.5P_{022_\alpha} + (124000/d^3)$

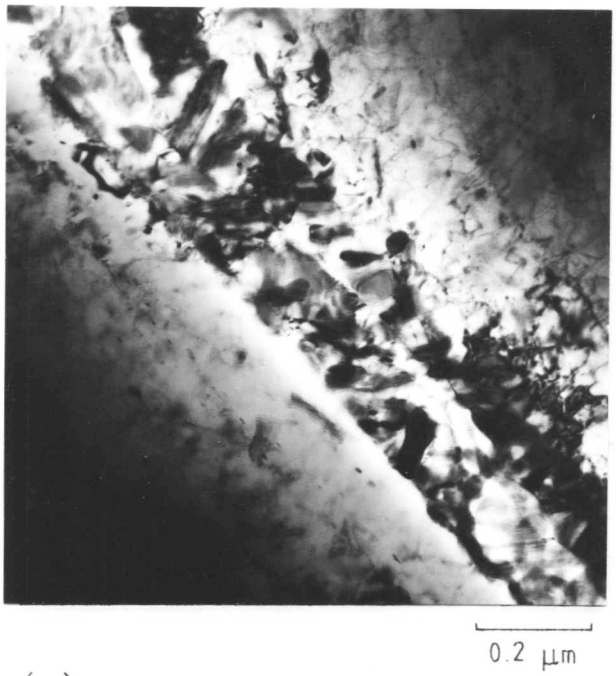

(a)

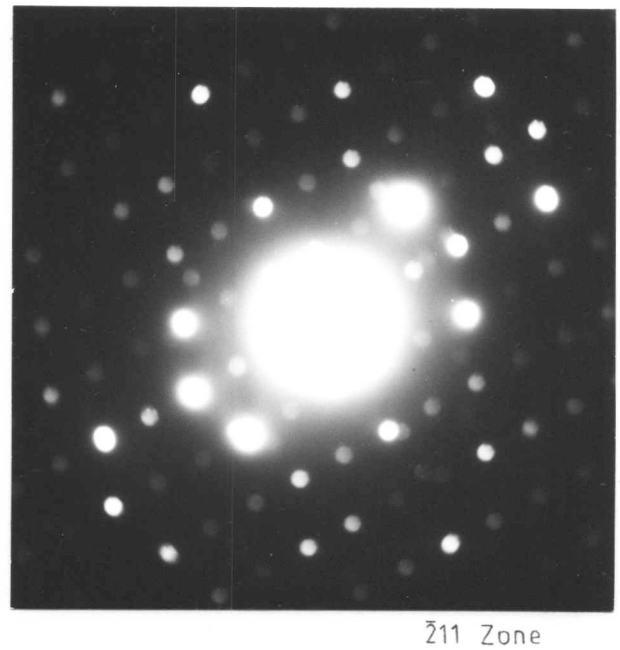

(b)

Figure I.9
Precipitation events resulting from the tempering of upper bainite formed after isothermal transformation at 350°C for 205 min.
(a) Tempered at 500°C for 30 min.
(b) Convergent beam diffraction pattern from monoclinic carbide of the type illustrated in (9a).

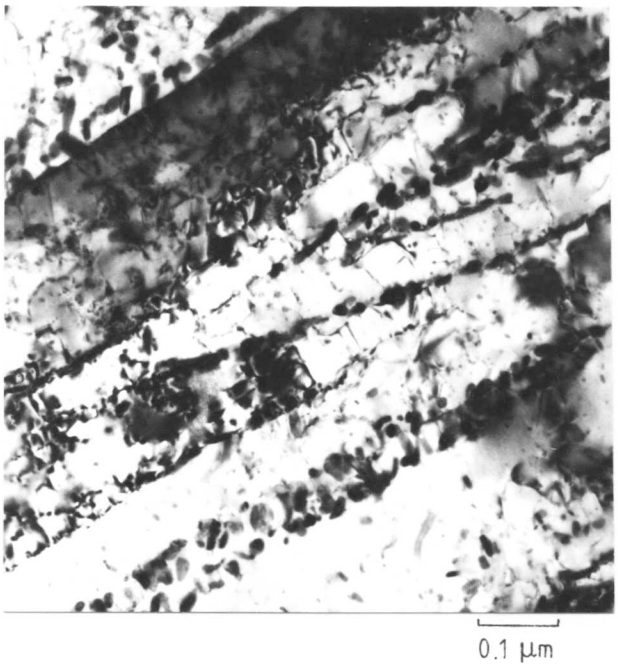

Figure I.9c
Tempered at 500°C for 60 min.

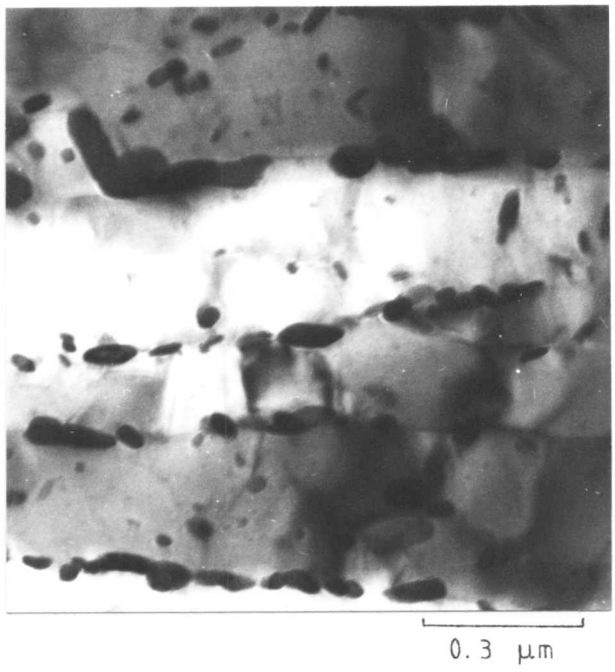

Figure I.9d
Tempered at 500°C for 120 min.

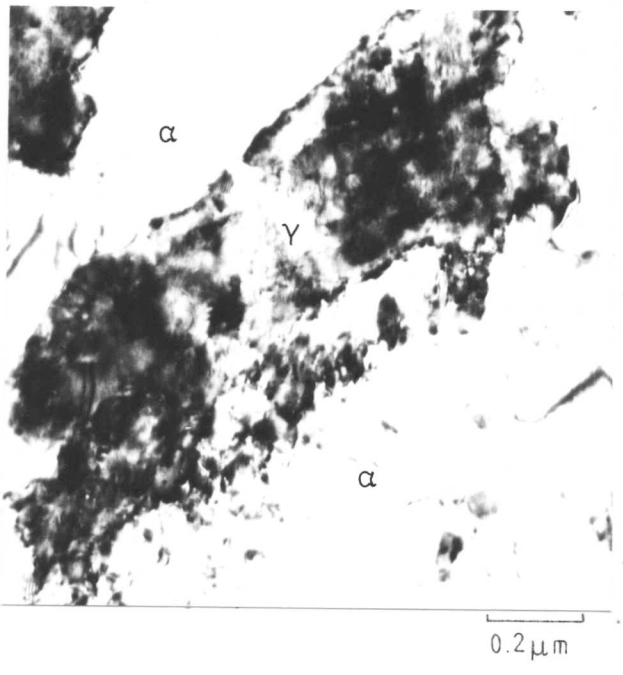

Figure I.9e
Hot stage electron micrograph showing decomposition of retained austenite at 500°C.

Figure I.10a
Typical lower bainitic microstructure after isothermal transformation at 300°C for 30 minutes.

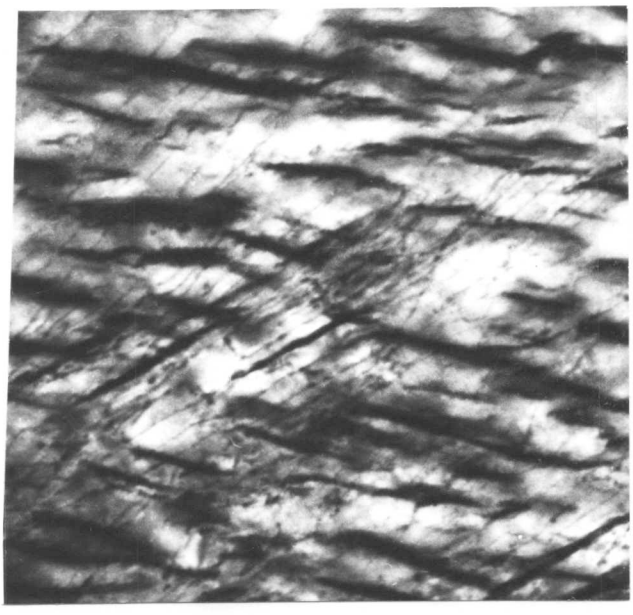

Figure I.10b
Dislocation arrays in lower bainitic ferrite formed after isothermal transformation at 247°C for 30 minutes.

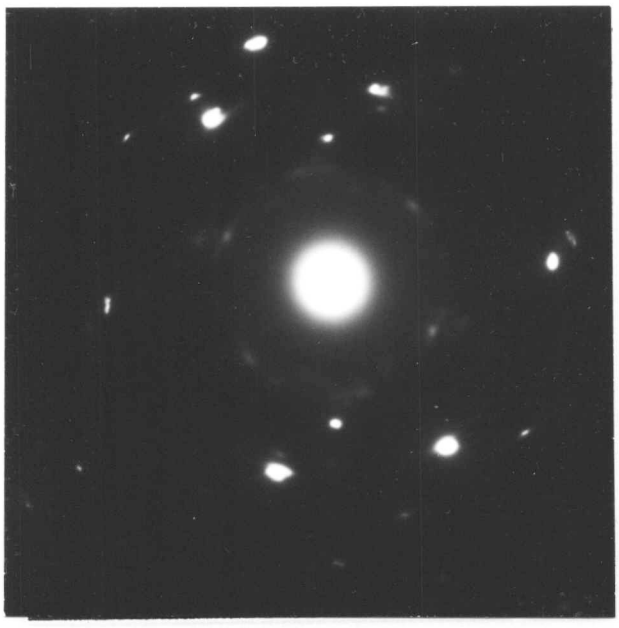

(i)

(ii)

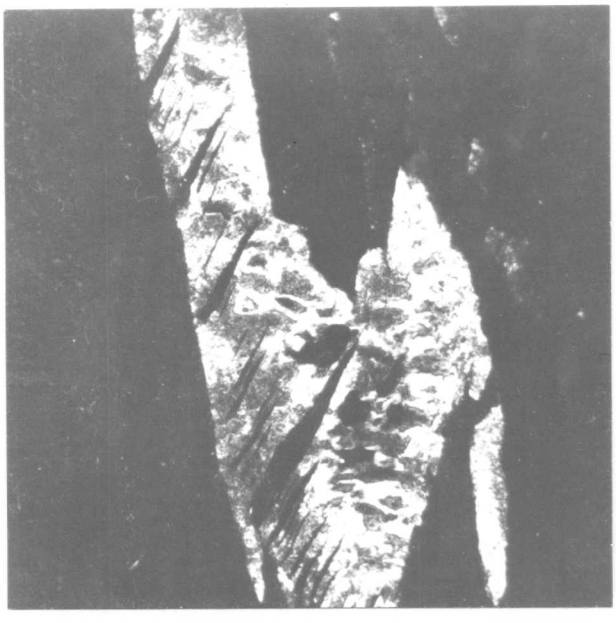

(iii)

(iv)

Figure I.10c

Mechanical twinning in lower bainite formed after isothermal transformation at 300°C for 30 minutes.

(i) Diffraction pattern.

(ii) Bright field image.

(iii) Matrix dark field image.

(iv) Twin dark field image.

(v) Interpretation of (i).

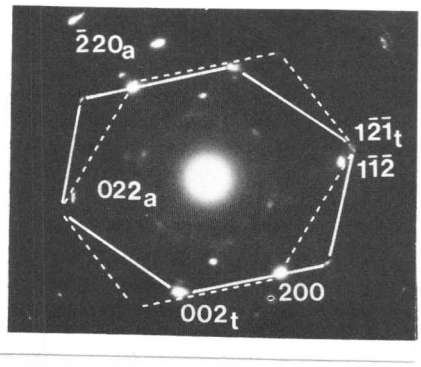

(v)

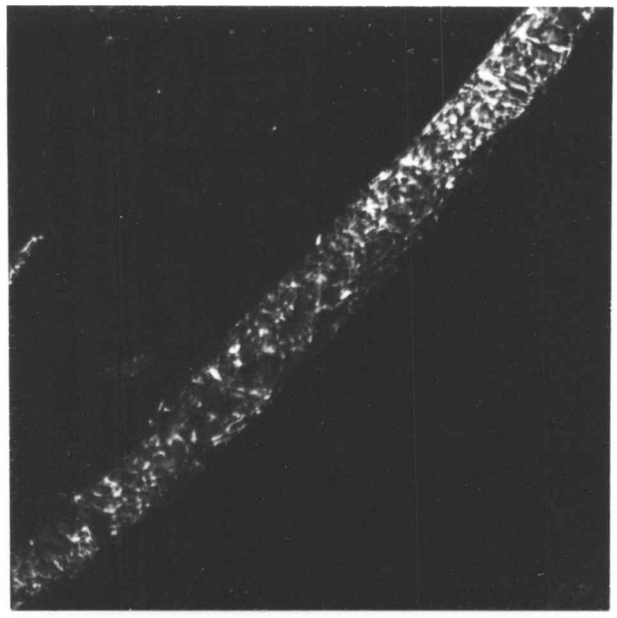

Figure I.10d
Structure of lower bainitic retained austenite after isothermal transformation at 300°C for 30 minutes.

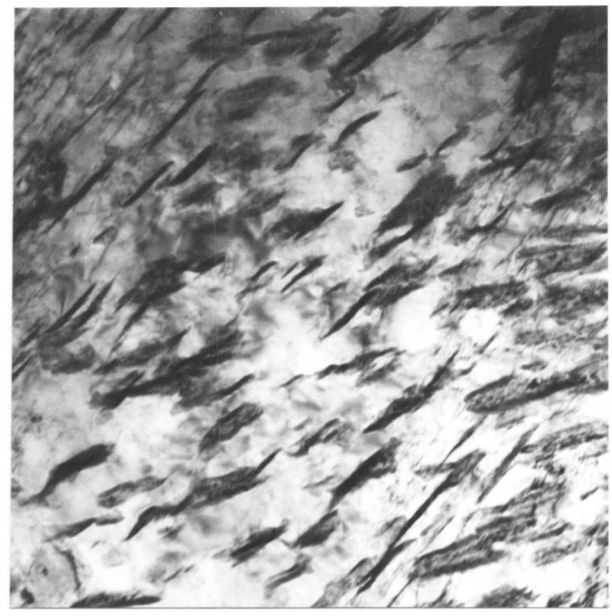

Figure I.10e
Morphology of lower bainitic cementite.

Figure I.11
Typical microstructure of lath martensite resulting from a direct quench following austenitisation.

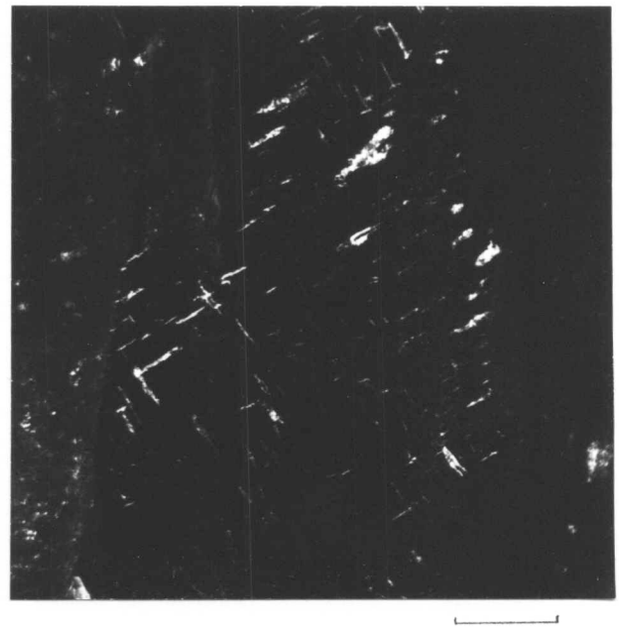

Figure I.12a
Dark field illumination of several cementite variants in a single ferrite crystal.

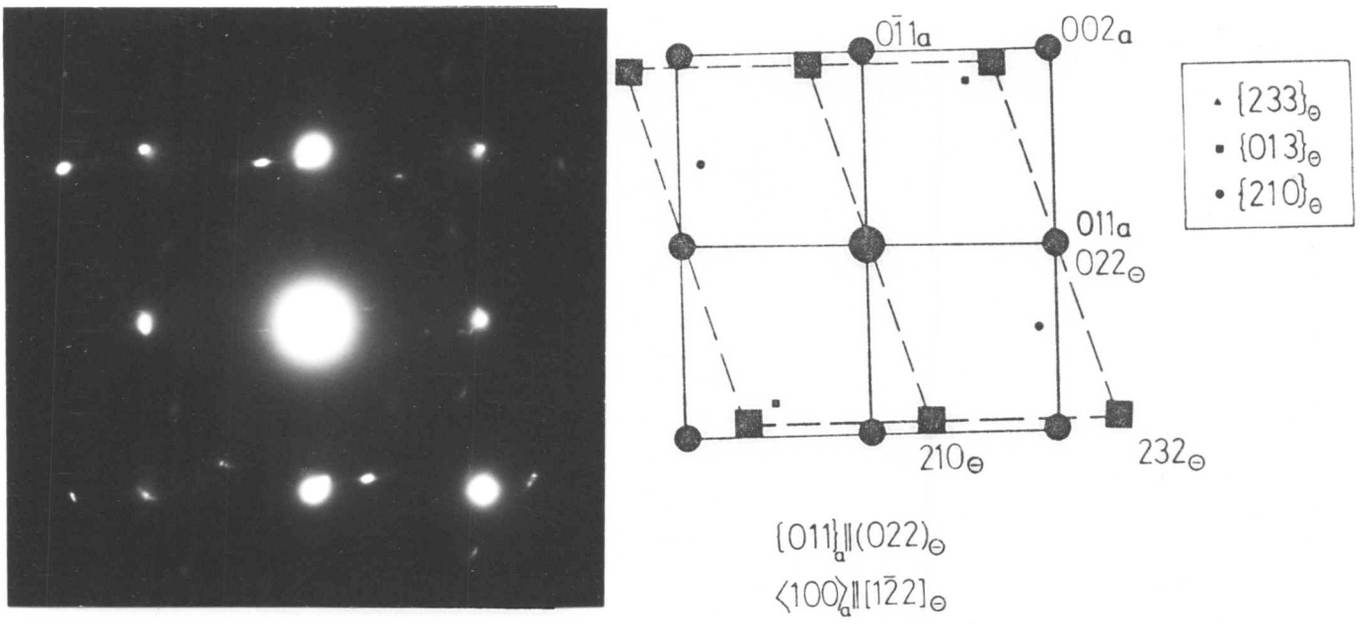

Figure I.12b
The orientation relationship between cementite and lower bainitic ferrite. It should be noted that $(011)_\Theta$ is essentially a missing reflection.

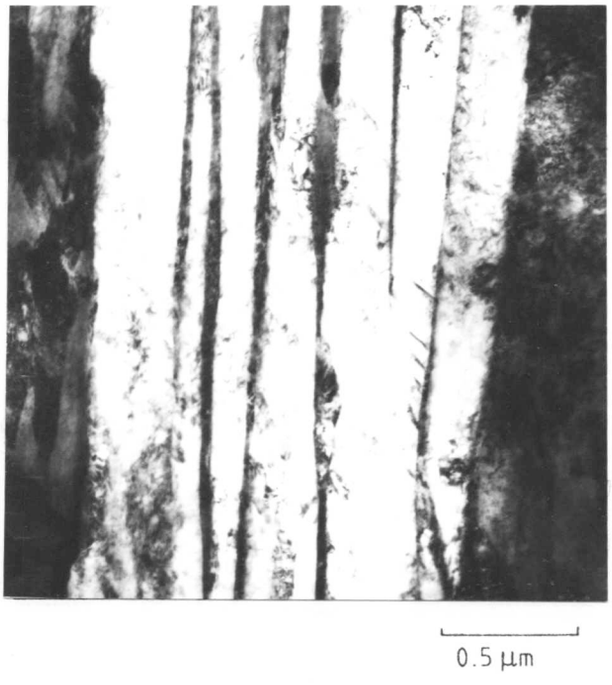

Figure I.12c
Incipient precipitation in lower bainite formed after isothermal transformation at 300°C for 4 minutes.

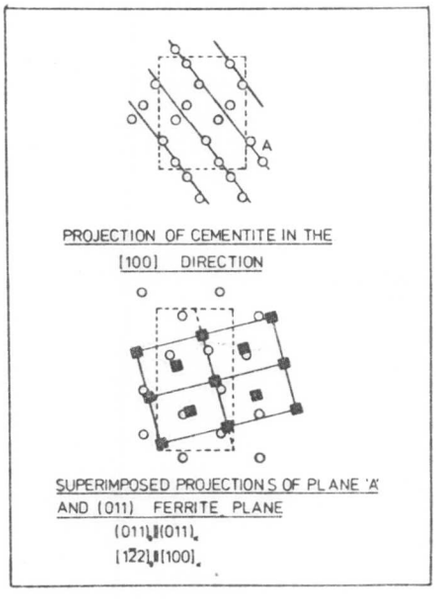

Figure I.12d
Superposition of iron atoms at the cementite-ferrite interface.

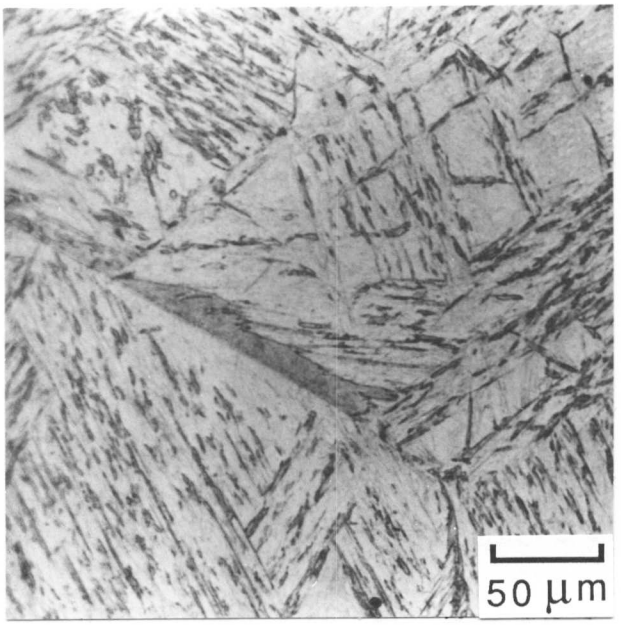

Figure I.13a
Grain boundary and intragranular lower bainite in a martensitic matrix after isothermal transformation at 246°C for 30 minutes.

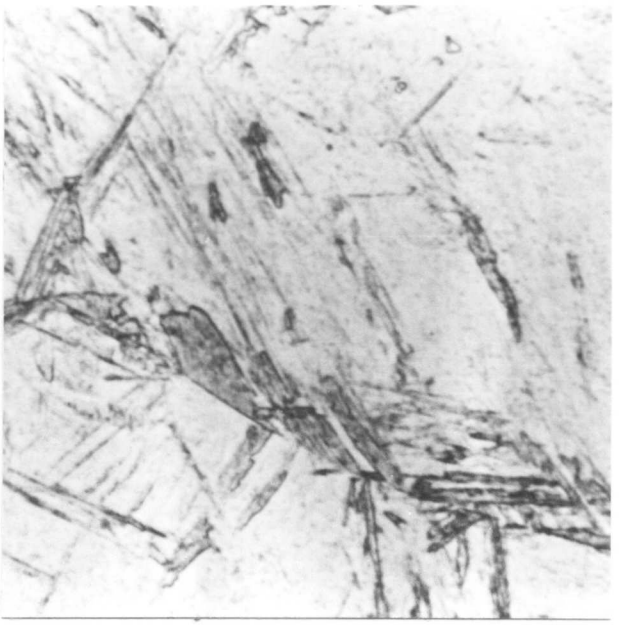

Figure I.13b
Parallelism of habit plane traces of grain boundary and intragranular lower bainite.

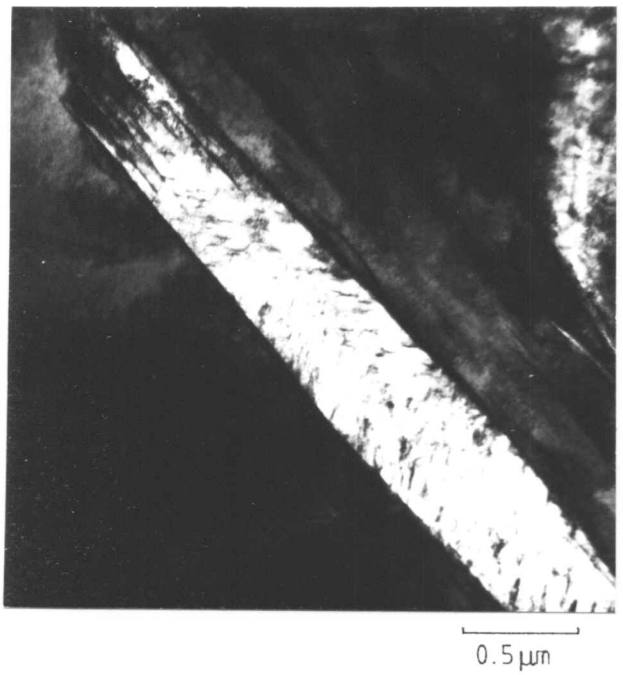

Figure I.13c
Structure of an intragranular plate tip; isothermally transformed at 257°C for 10 min.

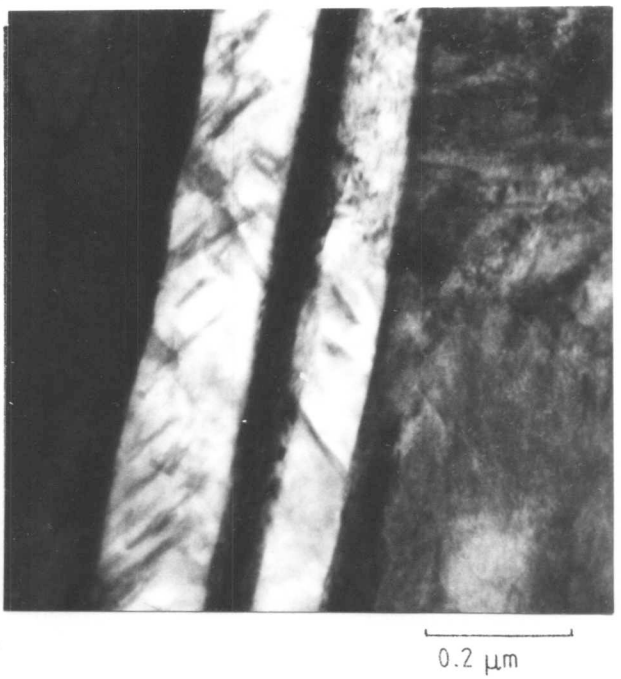

Figure I.13d
Individual spikes of lower bainite after isothermal transformation at 257°C for 5 min.

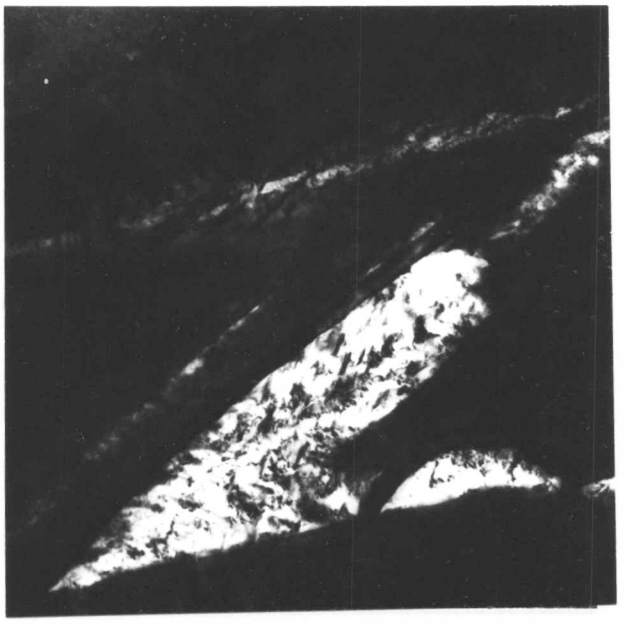

Figure I.13e
Spikes associated with grain boundary lower bainite formed during isothermal transformation at 257°C for 10 min.

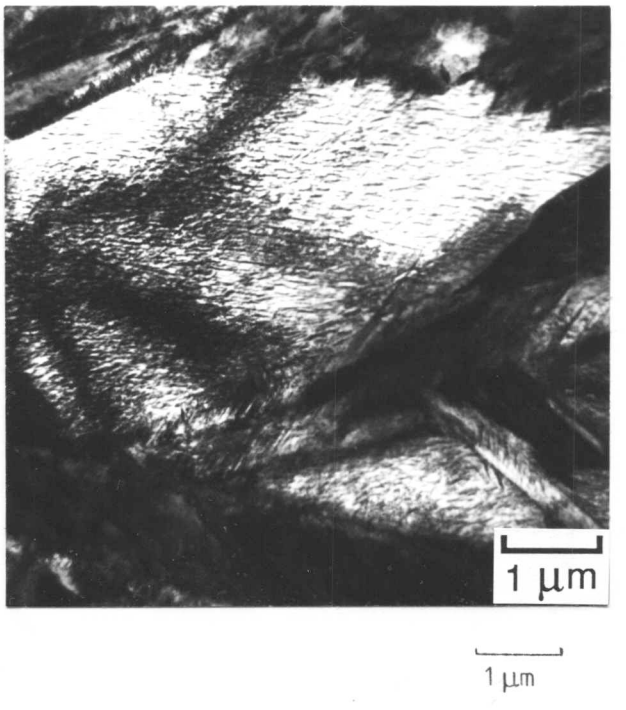

Figure I.13f
Grain boundary lower bainite formed during isothermal transformation at 247°C for 30 min.

CHAPTER TWO

THE THERMODYNAMICS OF BAINITE FORMATION IN STEELS

(II.1) Introduction

From the examination of the bainite transformations in a silicon steel (Ch.I), it was demonstrated that the sheaf of upper bainite apparently consists of displacive sub-units (ca. 0.2μm wide). The arrangement of sub-units was found to have the appearance of a plate on the scale of optical microscopy. Furthermore, it was shown that these sub-units could not possibly be confused with super-ledges since the individual sub-units were, for the most part of their interfaces, isolated by carbon-enriched retained austenite films. In the present chapter it is intended to show that the mechanism thought to be operative has a sound thermodynamic basis and to briefly consider other aspects of transformations below the B_s temperature in steels. It is, however, appropriate to outline the nature of the disputes concerning the mechanism of bainite formation within the context of the present chapter.

The conflict primarily arises in the choice between the displacive and reconstructive modes of solid state transformation. The former mechanism implies the existence of an atomic correspondence across the transformation interface whereas the latter allows diffusion controlled processes to destroy any such correspondence.

By the displacive mechanism (10), bainitic ferrite is considered to grow by the propagation of discrete martensitic sub-units, the aggregate of these sub-units constituting the classical sheaf of upper bainite. The sheaf itself has a plate like morphology and its formation involves sympathetic nucleation of successive sub-units. The bainitic ferrite is considered to form with a carbon supersaturation, with partitioning of the carbon into the residual austenite occurring immediately after formation. The width of the sub-units observed by Oblak and Hehemann (10) was ca. 0.5μm, with a length of ca. 10μm.

On the other hand, Aaronson and Kinsman (1) maintain that the observed sub-units are in fact ledges propagating along the broad faces of bainite plates. Based on thickening rates obtained from the in situ thermionic emission microscopy observations following the work of Rouze and Grube (35,36), they calculated an expected inter-ledge spacing of ca. 0.5μm which was claimed

to be consistent with the sub-unit size and with the 0.3-8.0μm ledges observed in the thickening of proeutectoid ferrite plates in the Fe-C system (37). They thus claimed a direct correspondence between ledges and sub-units. Additionally, they suggested that if the ledge mechanism is accepted, the apparent lengthening kinetics are consistent with a diffusion controlled growth mechanism. In some earlier work, Aaronson and Kinsman (38) presented a thermodynamic analysis which was claimed to invalidate the displacive sub-unit mechanism.

In the present chapter, it is hoped to deal with the problems outlined above with the help of new microstructural evidence together with a detailed thermodynamic analysis. The latter will be shown to support the displacive mechanism and will be further utilised in the evaluation of the details of the mechanism itself.

(II.2) Experimental

The alloy used was the same as that of chapter one, i.e. Fe-0.43C-3.00Mn-2.12Si wt.pct. Austenitising (1200°C for 10 mins) was carried out with the specimen sealed in a quartz capsule. Subsequent isothermal transformation was carried out by fracturing the quartz and quenching the specimen into a tin bath (286°C for 30 mins) covered with a layer of active charcoal before finally quenching into water.

Thin foil specimens for transmission electron microscopy were prepared from 0.25mm thick discs slit from the heat-treated 3mm diameter rod under conditions of flood lubrication. The discs were subsequently thinned and electropolished in a twin-jet polishing unit using a 25% glycerol, 5% perchloric acid and 70% ethanol mixture at room temperature. The foils were examined in a Philips EM300 transmission electron microscope operated at 100 kV.

(II.3) Results and Discussion

(i) Microstructural Observations.

It was decided to examine a complete sheaf of upper bainite using electron microscopy with the aim of observing the detailed mutual arrangement of sub-units within a given sheaf and to characterise the tip of the sheaf in order to be able to compare the events at the apparent transformation front with those near the original sheaf nucleation site. It was additionally hoped to gain information on the thickening of the sheaf, the nature

of sympathetic nucleation and to examine the morphology of individual sub-units.

The normal foil preparation technique had to be modified since the examination described above necessitated a very large electron transparent area on the thin foil. The conventional technique did not give sufficient thin area and also suffered from electron beam induced foil buckling. However, by adjusting the electropolishing conditions such that the bainite sheaf was preferentially attacked relative to the martensite matrix, it proved possible to examine a complete sheaf, with the relatively thicker martensite matrix providing foil support to prevent buckling.

Figure II.1 is a montage of electron micrographs of an isolated sheaf and the following points are to be noted:
1) The sheaf consists of an arrangement of sub-units such that the aggregate itself has a plate like morphology on a macroscopic scale, as is also obvious from the accompanying optical micrograph (inset).
2) Observation of a large number of thin foils indicated that the sub-units are themselves plate shaped.
3) The sub-units exhibit pronounced lenticularity, a feature most prominent near the edge of the sheaf, where their sharply pointed tips are also apparent.
4) Consistent with previous observations (Ch.1), the sub-units were found to be separated by films of retained austenite and are in the same crystallographic orientation relative to the austenite.
5) The width of the sub-unit at the tip of the sheaf is approximately the same as that near the original nucleation site.
6) Examination of the regions near the tip of the sheaf indicate that the new sub-units are sympathetically nucleated near the tips of the prior sub-units.

(ii) Thermodynamic Analysis

Assuming that the free energy surface of austenite can be reasonably extrapolated into the temperature regions where the austenite is not in thermodynamic equilibrium, a T_o temperature can be defined (39) such that stress free austenite and ferrite of the same composition (with respect to both the interstitial and substitutional alloying elements) are in metastable equilibrium. Thus, any displacive transformation involving a full supersaturation of carbon can occur only below the

appropriate T_o temperature. In the present work the data of chapter one is analysed using the thermodynamics delineated in refs. 38,40,41. The equations based on the treatment by Lacher (42) and Fowler and Guggenheim (43) are used since these resolve the problem of overlapping regions of influence of individual interstitial atoms and are considered to be the most reliable at low temperatures (40,41). Thus, when element partitioning does not apply, the T_o temperature is given by (38)

$$\Delta F^{\gamma-\alpha'} = 0$$

where,

$$\Delta F^{\gamma-\alpha'} = RT\Big| 6x \ln \frac{(\delta + 1 - 3x)}{(\delta - 1 + 3x)} -$$

$$6(1-x)\ln\frac{[1-2J+(4J\ 1)x-\delta]}{2J(2x-1)}$$

$$+\ 6x\ln x - 4(1-x)\ln(1-x)$$

$$+\ 5(1-2x)\ln(1-2x)\Big| + x[H - 10525$$

$$-\ (E+2.34)T - RT\ln 3] +$$

$$(1-x)\Big\| 141\sum_i y_i(\Delta T_{Mag_i} - \Delta T_{NM_i})$$

$$\Delta F^{\gamma-\alpha}\{\ T - 100\sum_i y_i\ \Delta T_{Mag_i}\}\Big\| \qquad \text{Equation II.1}$$

$$\delta = [1 - 2(1+2J)x + (1+8J)x^2]^{0.5}$$

$$J = 1 - \exp(\bar{w}/RT)$$

and $\bar{w}$ is evaluated using the procedure in (38) and the data presented in (41). The terminology involved in the above equations and the ones that follow is listed in table II.1. The T_o curve can thus be computed as a function of x. Since two sets of E and H are available, both were used so that two corresponding T_o curves were obtained.

The following equation from ref.40, again based on the Lacher-Fowler-Guggenheim treatments, was used to obtain the no-substitutional element partitioning Ae_3 curve:

$$141 \sum_i y_i \left(\Delta T_{Mag_i} - \Delta T_{NM_i}\right) + \Delta F^{\gamma-\alpha}\left\{T - 100 \sum_i y_i \Delta T_{Mag_i}\right\}$$

$$= 5RT \ln \frac{(1 - x)}{(1 - 2x)} +$$

$$6RT \ln \frac{1 - 2J + (4J - 1)x - [1 - 2(1+2J)x + (1+8J)x^2]^{0.5}}{2J(2x-1)}$$

Equation II.2

In both the above equations, values of $\Delta F^{\gamma-\alpha}$ were obtained from the data of ref.44.

Briefly, the above analysis can be understood as follows:

a) We begin with the experimentally determined free energy difference between austenite and ferrite in pure iron, i.e. $\Delta F^{\gamma-\alpha}$, as a function of temperature.

b) We then take account of the presence of carbon by considering its experimentally determined heat of solution together with the contributions via the entropy terms. In practice, only the positional entropy is calculable so that the other components of entropy are taken into account by fitting equations for the activity of carbon derived principally on positional entropy considerations to experimental information on these quantities. This procedure results in the adjustment of the parameter W .

c) Approximate account is then taken of the presence of substitutional alloying elements by allowing them to modify the magnetic and non-magnetic components of the fundamental free energy change for the austenite to ferrite transformation in pure iron and by further modifying W to allow for the influence of alloying elements on the activity of carbon. Experimental information on the variation of carbon activity with alloying element concentration is necessary for the latter modification.

d) As yet, no account can be taken of synergistic effects between substitutional alloying elements so that they are assumed to have additive effects, proportional to their concentrations.

The calculations were conducted for the alloy used and figure II.2 shows the results obtained. The B_s temperature was

found to fall below the T_o temperature at the general alloy carbon content, in agreement with the displacive mechanism for bainite formation.

The analysis was taken further in an attempt to understand the nature of the 'incomplete reaction phenomenon' (Ch.I). In this, the bainite reaction stops after a certain amount of transformation at a given temperature and ideally reaches zero transformation at the B_s temperature. In chapter one it was demonstrated that dilatometry backed by extensive optical and electron microscopy showed that the 0.43C-3Mn-2.12Si steel precisely exhibited the incomplete reaction phenomenon described above.

At 363°C, quantitative metallography showed a maximum of 52% bainitic ferrite. Using this as a calibration datum, the dilatometric data of chapter one was analysed as follows:

If $\Delta L/L$ is the length change accompanying transformation, then at 363°C, $\Delta L/L = 2.74 \times 10^{-3}$, with the volume fraction of bainitic ferrite, $V_{b-363} = 0.52$. Hence for any other temperature 'T', V_{b-T} is given by:

$$V_{b-T} = \frac{0.52(\Delta L/L)}{(2.74 \times 10^{-3})} \qquad \text{Equation II.3}$$

Since it has been shown (Ch.I) that the final carbon content of bainitic ferrite (s) is ca. 0.03 wt. pct., the carbon content of the austenite (x_γ) can be shown to be

$$x_\gamma = \bar{x} + \frac{V_b(\bar{x} - s)}{(1 - V_b)} \qquad \text{Equation II.4}$$

with $\bar{x} = 0.43$ and $s = 0.03$.

Using the above equations and the dilatometric data, the carbon content of the austenite at the termination of reaction is also plotted in figure II.2, as a function of the transformation temperature. It is clear that the reaction ceases as the carbon content of the austenite reaches a level such that a displacive mechanism is not allowed - i.e. bainite formation stops when the austenite carbon content transgresses the T_o curve. On the other hand, if the transformation did not involve full carbon supersaturation, there is no reason why the reaction should not proceed until the no-substitutional partitioning Ae_3 curve is reached. It can therefore be concluded that the bainite reaction does in fact involve growth of sheaves by the propagation of fully martensitic sub-units.

It is important to note that such an analysis is not valid for those bainite reactions involving carbide precipitation since the latter will necessarily reduce the carbon content of the system, thereby allowing further progress of the reaction by a displacive mechanism and rendering the incomplete reaction phenomenon undetectable. In general, the partitioning of carbon into the austenite and the precipitation of carbides (either subsequent precipitation at the interface as in upper bainite or precipitation from a supersaturated matrix as in lower bainite) are competitive processes, the relative rates depending on the alloy chemistry (in terms of carbide inhibitors for example) and transformation temperatures. In such cases the incomplete reaction analysis can only be applied if the carbide precipitation events can be quantitatively accounted for. This is clearly one of the reasons why the incomplete reaction effect is not well pronounced in steels where cementite precipitation dominates, as in plain carbon steels.

The above analysis shows that the martensitic sub-units form with a full carbon supersaturation, with the carbon being subsequently partitioned into the residual austenite. The latter reaction would be extremely rapid, of the order of a few milliseconds (38), at the temperature ranges over which bainite forms. In the incomplete reaction analysis it was implicitly assumed that the partitioned carbon is uniformly distributed throughout the residual austenite. Experimental observations show that this is not the case since austenite films entrapped between neighbouring sub-units have a higher carbon content than the islands of residual austenite resulting from the geometrical partitioning of the prior austenite grain by crystallographically different variants of bainite sheaves. This effect is reflected in the martensitic decomposition of the islands of residual austenite when quenching to room temperature from the isothermal transformation temperature whereas the entrapped films are fully retained (Ch.I). Thus, even with $V_b = 0.005$, the films of retained austenite have an X-ray determined carbon content of approximately 0.8 wt. pct. (Ch.III) despite the fact that eqn. II.4 would indicate an extremely small average austenite enrichment.

The effect of the inhomogeneous distribution of carbon would be to allow the transformation to proceed to an extent somewhat greater than that allowed by the T_o curves. It is estimated, however, that such an effect would be small since the probability of adjacent sub-unit formation is relatively small. Electron

microscopy indicates that the sub-units nucleate sympathetically near the tip of the prior sub-units. This would enable the growth of the new sub-unit to be essentially unaffected by the carbon diffusion field (arising from post-martensitic partitioning) of the previous sub-unit. Such growth into relatively lower carbon austenite would clearly be energetically more favourable. Indeed, the carbon concentration near the tip of the prior sub-unit would be lower than that near the broad faces since the shape lenticularity not only implies a higher interface to volume ratio at the tip, but the very geometry of the tip leads to a smaller carbon concentration per unit interface area. The latter effect originates from the fact that a positively curved surface will have a greater volume of austenite per unit distance from the interface compared to a relatively planar interface. It is only when the carbon pile ups at the broad faces level out that adjacent sympathetic nucleation becomes favourable and feasible. The latter would take a relatively longer time, thereby favouring tip nucleation and directly leading to the apparent plate morphology for the sheaf of sub-units as a whole.

(iii) Growth Termination Mechanism.

With respect to the limited size of the displacive sub-units, it is noted that a stress is required to drive the interface between the ferrite and austenite in order to accomplish the necessary transformation strain (45). This stress, τ, is the friction stress and the forces necessary to overcome τ during transformation are provided by the chemical free energy change. Under circumstances where the transformation is perfectly thermoelastic, τ does not increase with the progress of transformation. However, when the transformational shape change is plastically accommodated*, the elastic strain energy is relaxed

* In accordance with (46), plastic accommodation refers to all processes beyond those prescribed by the phenomenological theories to establish an invariant- plane condition, i.e. mainly complex slip.

and the frictional stress is greatly increased (45,46) due to interaction of the interface with accommodation defects to a point where the chemical free energy change will no longer be adequate to further drive the transformation. The interface is thus immobilised by extensive dislocation jamming (46). This is consistent with the electron micrograph presented in chapter one (figure I.7a) showing extensive dislocation tangles in the vicinity of the bainitic ferrite-austenite interface, thus

providing direct evidence for the above size limiting mechanism.

Additionally, the interfacial diffusion coefficient of carbon at the temperatures where bainite forms may be sufficiently high to allow interstitial atmospheres to exert a drag on the transformation interface. This could then stop, or at least hinder the transformation when some critical level of carbon concentration is achieved. The latter would not only pin the interface but would also locally increase the carbon content, thereby reducing the available chemical driving force. This would be consistent with the general observation that the sub-units are larger when the average carbon content of the alloy is lower (47) since the time taken to reach a critical concentration for immobilisation would be greater.

(iv) Strain and Interfacial Energy Contributions.

It is interesting to consider why, near the B_s temperature, only a small amount of undercooling is necessary (below the corresponding T_o temperature) prior to the onset of transformation. The calculated T_o temperature does not account for non-chemical components such as interfacial and strain energies. Certainly, in the case of martensite obtained on direct quenching, a substantial supercooling below T_o is necessary before the M_s is reached. In the case of the FCC to BCC martensite transformation, the $\Delta F^{\gamma-\alpha'}$ is approximately -1260 J mol^{-1} (48) before transformation actually commences. It appears that the high supercoolings below T_o prior to martensite formation are necessary in order to overcome the high strain and interfacial energies of the fault sequences associated with the spontaneous nucleation of martensite (48-51). However, this does not apply to the case of the bainite discussed above. The first sub-units to form martensitically nucleate at the prior austenite grain boundaries and subsequent sub-units, of course, nucleate sympathetically, thereby overcoming the relatively large nucleation barriers. Additionally, we note that at the relatively high temperatures at which bainite forms, a greater amount of thermal activation is available to overcome any nucleation barrier. Following the above considerations, the basis of the calculations below is that the strain and interfacial energy terms in the overall energy balance are the ones associated with the <u>final</u> platelet(sub-unit). The latter statement is equivalent to saying that initial nucleation at the prior austenite grain boundaries followed by sympathetic nucleation mitigates the energy barriers associated with martensite nucleation.

Considering the sub-unit as an oblate-spheroid of radius r and semi-thickness c, the strain energy per unit volume is given by Ac/r (ref.52) where A is of the order of 2090 J cm^{-3} (48,53) at 25°C, and since A is a linear function of the shear modulus of the matrix (54), we can calculate its magnitude at 470°C (i.e. B_s) on the basis that the shear modulus decreases by 0.03% per degree centigrade rise in temperature (55) to give A_{470} = 1815 J cm^{-3} or 12910 J mol^{-1}. The influence of the variation of the poissons ratio with temperature on the magnitude of A may be neglected over the temperature range being considered here according to the data presented in ref.56. Thus Ac/r = 260 J mol^{-1} when c ~ 10^{-7} μm and r ~ 5 x 10^{-6} μm. The latter dimensions were obtained directly from electron micrographs.

It is important to note that this figure could be significantly reduced if plastic relaxation of elastic strains occurs, (57), as is the case for bainite. The displacement of the transformation interface should, in principle, leave a defect free single crystal region (58) in the absence of periodic twinning or faulting associated with the relevant lattice invariant shears. Because of the ordered arrangement of the latter defects, the martensite containing such inhomogeneities may be regarded as a long period structure rather than as a crystal containing defects. Thus we do not expect the martensite to contain dislocations. Nevertheless, both bainitic ferrite and its associated retained austenite have high dislocation densities (Ch.I); the latter can only be attributed to plastic relaxation effects.

It can be shown that the interfacial energy contribution to the overall energy balance is small, as follows:

Taking the interfacial energy to be of the order of 0.2-1.0 J m^{-2} (48,59,60), and using the platelet dimensions quoted earlier, the interfacial energy contribution amounts to only 2-10 J mol^{-1}. Hence the strain and interfacial energy contributions would jointly amount to only about 270 J mol^{-1} and would lead to an undercooling requirement of only about 60°C below T_o. This is despite the fact that plastic relaxation, which would reduce the strain energy contribution, has not been taken into account. The experimental B_s in figure II.2 is consistent with this order of undercooling.

It is interesting to note that the M_s temperature in the present alloy is 220°C (Ch.I) so that the undercooling below T_o before the onset of the martensite transformation proper would

lead to a $\Delta F^{\gamma-\alpha'}$ of -1420 J mol^{-1}. The latter compares very well with the $\Delta F^{\gamma-\alpha'}$ values at the M_s temperatures of high alloy plate martensites (48). Such a large chemical free energy change facilitates the nucleation modes conventionally associated with martensites (49-51) so that the need for sympathetic nucleation does not arise. Thus the above results are consistent with a displacive mechanism operating throughout the temperature range $B_s - M_f$.

(v) The Nature of the Bainite/Austenite Interface.

The crystallographic theory of martensite is based on the postulate that the habit plane is an invariant plane relative to the macroscopic shape deformation. The parent/product mismatch at the habit plane is considered to be periodically corrected by discontinuities so that it does not accumulate over large distances (58). These structural discontinuities are needed only to correct the mismatch at the semi-coherent (in general) planar boundary. However, for lenticular plates (as observed in the present study) exhibiting a curved boundary this interface is glissile since the additional misfit regions (other than the structural discontinuities) arising from boundary curvature constitute the transformation dislocations of the martensite pole mechanism (61). Since the sub-units observed in the present work are indeed lenticular, their interfaces with austenite must also be glissile, in accord with a displacive transformation mechanism.

There are three possible criteria (62) for the selection of the interfacial array of mismatch dislocations under transformation conditions; a) minimum strain at the interface, b) minimum force required to displace the dislocation array, c) the array is such that it produces the required lattice invariant shear on displacement. These criteria are in general incompatible when considered on their own. However, we recall that the interfacial energy is only one aspect of the complete energy balance involved in transformation thermodynamics and a relatively small one at that. Hence the choice of any particular criterion must not be made solely on the basis of interfacial energy. It must be borne in mind that post-transformation examination of static interfaces need not be reliable in the case of high temperature transformations (as in the case of 63,64) as there will exist a driving force for any glissile transformation interface to equilibrate into an energy cusp orientation following transformation.

Such criticism also applies to geometrical modelling based solely on minimum interfacial energy considerations (63,64). Furthermore, it should be noted that the concept requiring an increase in interfacial energy in order to accomplish transformation is not alien to the ledge mechanism of growth. In the latter, the experimentally observed rates of transformation require the riser of the ledge to have a disordered structure, thus conferring the necessary mobility. However, if the ledge riser turns out not to have a disordered structure, Aaronson et.al. (65) suggest that higher order ledges or jogs must be formed on the risers to provide an interfacial structure which is sufficiently disordered to allow an adequately rapid net rate of transfer of atoms across the boundary. The ledge mechanism therefore permits an increase in interfacial energy within the context of a general reduction of free energy of the system due to the accompanying phase transformation.

(vi) The T_o Concept and the Lower Bainite Transformation.

In chapter one it was shown that lower bainite forms by the adjacent nucleation of sub-units which are not limited in size so that parallel growth occurs, giving rise to a plate with a spiked transformation tip (figure I.13c). Grain boundary nucleated lower bainite was also found to be composed of adjacently nucleated sub-units. Additionally, cementite precipitation was found to occur within the bainitic ferrite such that approximately 0.25 wt. pct. of the carbon content of the alloy could be attributed to carbide precipitation. These results can be rationalised in terms of the T_o concept because the lower bainite transformation occurs at higher undercoolings below T_o so that the amount of carbon partitioning tolerated by the austenite before the T_o curve is transgressed is very much higher. Additionally, the amount of carbon partitioned into the austenite is lower since cementite precipitation effectively allows the value of (s) in equation II.4 to reach 0.25. The above factors combine to make adjacent sympathetic nucleation feasible. Furthermore, since the lower bainite forms at high undercoolings below T_o (relative to upper bainite), sufficient driving force is available to keep up with the rise in friction stress with the progress in transformation so that the size of the lower bainite sub-units need not be limited, assuming that impingement does not occur. This is in fact the case, as shown in chapter one.

These considerations do not imply that the only difference

between upper and lower bainite is concerned with the nucleation sites, since evidence was presented in chapter one to suggest that the two bainites occur as fundamentally separate transformations It is possible for the upper and lower bainite and the martensite reactions to be simultaneously consistent with a displacive mechanism and yet differ crystallographically since the modes of lattice invariant shears could differ. However, this clearly requires further work to elucidate the details.

(II.4) Conclusions

It has been shown that the displacive sub-unit mechanism for bainite formation is in agreement with the expectations of thermodynamic analysis. Furthermore, the incomplete reaction phenomenon can only be understood in terms of the thermodynamics of displacive transformations, as can the morphology of bainite sheaves. The totality of evidence is inconsistent with a reconstructive growth mechanism.

TABLE II.1 Nomenclature

c	= Semi-thickness of the oblate spheroid representing a bainite sub-unit.
r	= Radius of the oblate spheroid representing a bainite sub-unit.
R	= Gas Constant, $8.313\ J\ K^{-1}mol^{-1}$.
T	= Absolute temperature.
T_o	= Equilibrium temperature for stress free austenite and ferrite of identical composition.
E	= Standard state constant for ferrite.
H	= Partial molar heat of solution of carbon in ferrite.
x	= Mole fraction of carbon in austenite.
$\bar{x}$	= Wt. pct. of carbon in alloy.
y	= Mole fraction of substitutional alloying element in the alloy, disregarding the presence of carbon.
$\bar{w}$	= Weighted average of the pairwise interaction energy of carbon atoms in alloyed austenite.
ΔT_{Mag_i} & ΔT_{NM_i}	= Displacement in the temperature at which the free energy change accompanying the austenite to ferrite transformation in pure iron is calculated in order to account for the changes (per atomic percent) due to alloying element effects on the magnetic and non-magnetic components of free energy change, respectively.
A	= Strain energy factor, such that Ac/r defines the strain energy per unit volume.
$\Delta F^{\gamma-\alpha}$	= Chemical free energy change accompanying the austenite to ferrite transformation in pure iron.
$\Delta F^{\gamma-\alpha'}$	= Chemical free energy change accompanying the austenite to ferrite transformation in alloyed steel, such that the austenite and ferrite have identical compositions.
V_{b-T}	= Volume fraction of bainitic ferrite obtained by isothermal transformation at temperature T.
τ	= Friction stress associated with the motion of the transformation interface.
$\Delta L/L$	= Length change per unit length, accompanying transformation.
s	= Wt. pct. of carbon remaining in the bainitic ferrite, either as carbides or in interstitial solution.
x_γ	= Wt. pct. of carbon in austenite

Note

The two sets of values of H and E used in the T_o calculations were:

$H_1 = 109532$ $H_2 = 83991$ $J\ mol^{-1}$

$E_1 = 40.8$ $E_2 = 17.3$ $J\ mol^{-1}\ K^{-1}$

from refs. 40,41

Figure II.1

Upper bainite formed by isothermal transformation at 286°C for 30min.

(a) Optical micrograph, as in fig.I.4a.

(b) & (c) Bright field and corresponding retained austenite dark field image respectively, as in fig.I.4b,c.

(d) Montage of electron micrographs of a sheaf of upper bainite.

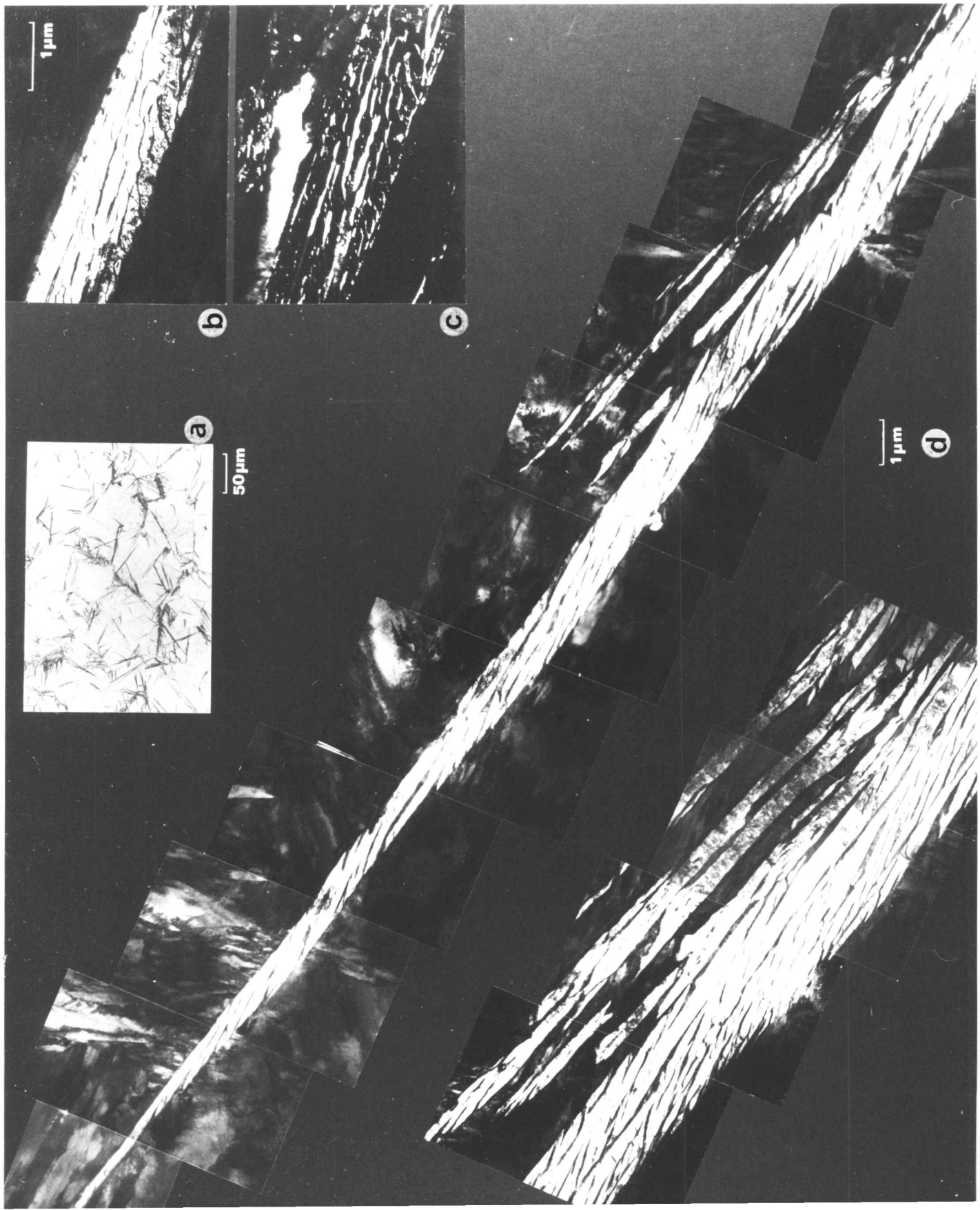

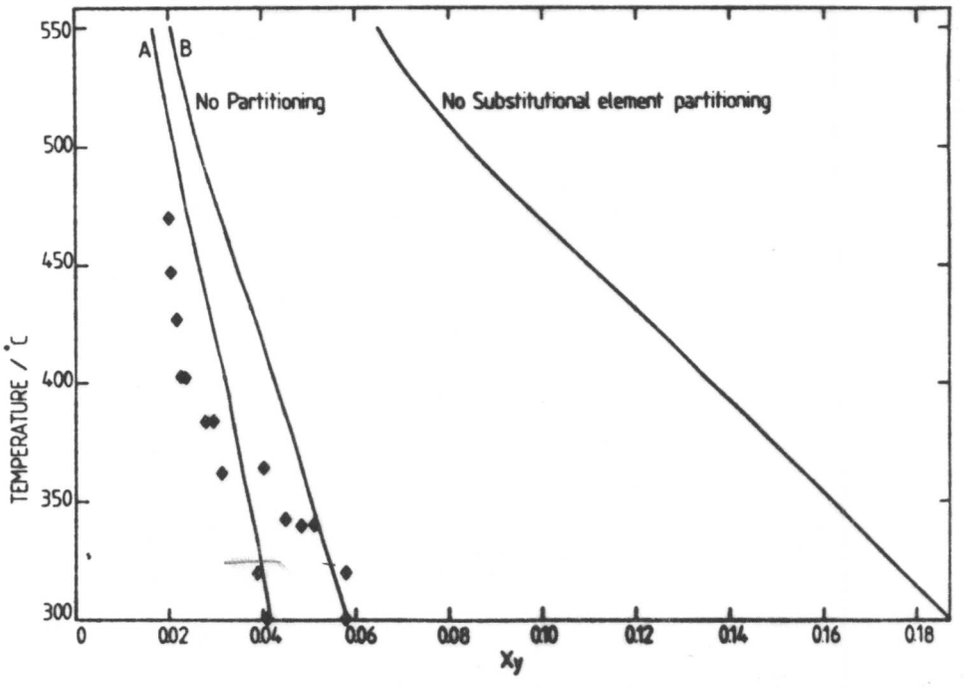

Figure II.2

Comparison of the experimental data with the calculated T_o curves. The curves marked 'A' and 'B' both represent no-partitioning, but have been calculated using different values of the partial molar enthalpy of solution of carbon in ferrite.

CHAPTER THREE

THE PROPERTIES OF MICROSTRUCTURES CONTAINING BAINITIC RETAINED AUSTENITE - PART 1

(III.1) Introduction

The majority of ultra-high strength steels are heat treated in one of two ways, by slow cooling or by quenching and tempering. However, isothermal heat treatments in the bainite temperature range have not found widespread application, partly due to the uncertainties associated with optimizing mechanical properties by such treatments and partly due to the difficulties of controlling such reactions. The overall confusion surrounding the mechanisms of the bainite transformations has meant that much of the development work has tended to be empirical. Additionally, the presence of undesirable carbides in conventional bainitic microstructures has tended to hinder their use.

The result of the above factors is that the ultra-high strength industry is almost completely dominated by quenched and tempered steels (66). Furthermore, much of the current research effort is directed towards the optimization of martensitic microstructures - other developments such as TRIP steels (67-69) tend to be too expensive for general usage. Present day technologists are demanding increased toughness in ultra-high strength steels but it seems that the research on martensite based microstructures is approaching the law of diminishing returns, assuming the absence of any surprising new developments.

However, a refreshing trend began with the basic work of Matas and Hehemann (70), Entin (71), Hehemann (16), Lyman and Troiano (72,73) and Davenport (74) who established that relatively large amounts of carbon enriched retained austenite could be found in association with bainitic transformations in alloy steels. This is particularly the case for steels containing cementite inhibitors such as Si or Al. Considerable effort (e.g. ref.75) was subsequently devoted to structure-property studies in such microstructures with the aim of exploiting any beneficial aspects of the associated retained austenite. Unfortunately, the general conclusion that emerged from such work is that carbon-enriched retained austenite is undesirable because of its mechanical instability, i.e. it decomposes under stress to give high carbon martensite, thereby causing embrittlement. Furthermore, austenite in the blocky morphology was found to reduce the overall yield stress (75).

Nevertheless, the basic approach of using retained austenite to enhance toughness seems to be sound, if the problem of stability can be overcome. It was decided to undertake an investigation of bainitic retained austenite with a view to establishing a model representing its influence on the properties of the steel concerned. Furthermore, it was hoped to link the model to the fundamental transformation mechanisms involved, as developed in the earlier chapters. Ideally, such a combination should help to minimise the empirical component of structure-property research in this field, and possibly predict the limitations or advantages of using bainitic retained austenite in ultra-high strength steels.

(III.2) Experimental

The alloys used in the present investigation are as follows:

	C	Mn	Si	S	P	Sb	As	Cu	Cr	Ni
a)	0.43	3.00	2.02	.002	.002	.001	.002	.004	.01	.01
b)	0.19	2.90	2.13							
c)	1.10	3	2							

The figures are expressed in wt. pct., and the analysis for alloy (c) is nominal except for the carbon content which was established by X-ray analysis of the martensite tetragonality. This alloy proved to be too difficult to machine into a form suitable for chemical analysis requirements. It should, however, be noted that the conditions of melting were such that minimal alloying element losses are expected.

Alloy (a) was prepared from high purity base materials as a 20 kg vacuum induction melt. The ingot was forged and hot rolled to 10 mm diameter rod followed by a hot swage reduction to 8 mm diameter rod.

Alloys (b) and (c) were prepared from pure constituents in an argon arc furnace as 65 g melts. The ingots were sealed in a quartz capsule under a partial pressure of argon and homogenised for three days at 1250°C, before hot reduction to 3 mm diameter rod.

Hardness testing was carried out on a Vickers pyramidal diamond indentation machine and the quantitative metallography was conducted on a Quantimet Image analyser.

X-ray analysis was done on a Philips horizontal diffractometer using the same procedure as outlined in Ch.I. Transmission

electron microscopy was carried out on a Philips EM300 microscope operated at 100 kV with the thin foils being prepared as in (I.2).

The impact specimens used were 8 mm in diameter and 45 mm long with a 1 mm deep notch. The notch was machined (prior to any heat treatment) with a standard Hounsfield notching tool but with the specimen supported in a jig with an eccentricity of 35 mm. In situ hot impact testing was facilitated by jets of furnace heated air directed at the specimen. A thermocouple attached directly to the specimen in the vicinity of the notch enabled the continuous monitoring of temperature.

During austenitising, the specimens were protected by a dynamic argon atmosphere together with a proprietary coating compound. Isothermal transformations were conducted in a molten-tin bath covered with a layer of active charcoal.

(III.3) Results and Discussion

(i) The carbon content of Bainitic Retained Austenite.

Using X-ray diffractometry and a standard extrapolation function (27), the lattice parameter of bainitic ferrite was determined to be 2.86(2) $\mp$ 0.01Å. The latter result applies to both upper and lower bainitic ferrite since the transformation times and temperatures were such that any excess carbon supersaturation of the latter phase is expected to be relieved by cementite precipitation in most cases. In any case, the errors due to the unavoidable presence of martensite have a significantly larger effect. Hence the lattice parameter determinations from specimens containing only small quantities of martensite were taken to be more reliable and the bainitic ferrite parameter was fixed at 2.860 $\mp$ 0.005 Å.

The determination of the lattice parameter of austenite presented a more formidable problem. Firstly, because of the low volume fractions of austenite present at room temperature, peak intensities were low and tended to be diffuse presumably due to the finely divided state of the austenite and also its transformation induced deformation structure. To mitigate the problem, the following procedure was devised:

The $\{002\}_\gamma$ and the $\{002\}_\alpha$ diffraction peaks are well separated from other austenite or ferrite peaks. Additionally, the diffracted intensities (or structure factors) of these peaks are adequately high. From Bragg's law it follows that the

separation of the $\{002\}_\gamma$ and $\{002\}_\alpha$ peaks (using twice the Bragg angle is given by

$$\psi = 2\left\{\sin^{-1}(\lambda/a_\alpha) - \sin^{-1}(\lambda/a_\gamma)\right\} \qquad \text{Equation III.1}$$

where

λ = wavelength of the X-radiation used,

a_γ = austenite lattice parameter,

a_α = ferrite lattice parameter.

We note that ψ is a function of a_γ, which in turn depends on the amount of carbon present in the austenite lattice (x_γ, wt.pct.). However, the latter dependence raises difficulties since its nature is not well defined. There are at least seven (76-82) different relationships between the lattice parameter of austenite and its carbon content. When all available data is simultaneously plotted, (83), two distinct relationships emerge:

$$a_\gamma = 3.555 + 0.044(x_\gamma) \qquad \text{(Ref. 79) Equation III.2}$$

$$a_\gamma = 3.\overset{5\,1\,8}{\cancel{753}} + 0.033(x_\gamma) \qquad \text{(Ref. 77) Equation III.3}$$

The reasons for the existence of two relationships is not clear except that one (Eqn.III.3) seems to represent 'equilibrium austenite' while the other is associated with austenite in the presence of large amounts of martensite (83). Nevertheless, since no explanation is available for the difference between the two relations, some of the data may be inaccurate and further work is clearly needed.

The consequence of the above confusion is that it is not possible to reliably quote absolute values of carbon content in austenite from lattice parameter measurements. However, differences in carbon contents certainly can be estimated; such differences would be manifested in the variation of ψ .

The carbon content of the residual austenite at the isothermal transformation temperature can be shown to be

$$x_\gamma = \bar{x} + \frac{V_b(\bar{x} - s)}{(1 - V_b)} \qquad \text{Equation III.4}$$

where

V_b = volume fraction of bainitic ferrite,

$\bar{x}$ = the average carbon content of the alloy,

s = the carbon 'tied up' in the ferrite, either as carbides or in solution.

The above set of equations can now be used to study the variations in carbon content of bainitic retained austenite.

Two sets of specimens were isothermally transformed at 363°C and 270°C respectively for various time periods prior to water quenching. Electron microscopy was used to confirm that the transformation product at the higher temperature was upper bainite while the lower transformation temperature gave lower bainite. The above heat treatments were designed to give specimens with different volume fractions of bainitic ferrite, martensite and retained austenite.

The volume fraction of retained austenite in each specimen was determined by X-ray diffraction, using the procedures given in chapter one. This also yielded the information on ψ . Quantitative metallography on a Quantimet image analyser enabled the volume fraction of bainitic ferrite to be determined. However, this method is known to overestimate the amount of bainitic ferrite (17) since the optical microscopy used in such analysis has insufficient resolution to account for the austenite films trapped between adjacent sub-units. However, a correction factor was used to overcome this problem. This factor was deduced by lineal analysis on electron micrographs such as the one presented in fig.III.1 and it was found that about 15% of the sheaf of bainite was composed of retained austenite. Hence any value of V_b obtained from the image analyser would be overestimated by a factor of 1.176. The corrected values of volume fractions of bainitic ferrite, retained austenite and martensite (obtained by difference) are given in table III.1.

As shown in figure III.2, the variation of ψ as a function of the extent of transformation to bainitic ferrite is very small, and can be taken to be negligible within the limits of experimental error. This is not, however, true for $V_b < 0.04$ and a large amount of scatter is observed. Also plotted on figure III.2 are the calculated curves based on Eqns. III.1-4 and the following assumptions:

a) The value of s = 0.03 for upper bainite, as estimated in Ch.I and confirmed by the data of ref.84.
b) The value of s = 0.27 for lower bainite. This was estimated to be 0.25 - 0.30 in Ch.I but calculation showed that s = 0.27 gave best agreement with the data of figure III.2, at $V_b > 0.6$.
c) Equation III.2 was used to represent the lattice parameter of the austenite so that the curves plotted in figure III.2 need only be accurate at high values of V_b, where the

difference between eqns.III.2 and III.3 becomes small. In any case, the curves are intended to represent trends- and these were found to be very similar, irrespective of the equation used.

The large scatter observed for the experimental data at $V_b < 0.04$ can essentially be understood in terms of the enhanced errors involved in measuring the peak separation when very small amounts of austenite are being detected. Nevertheless, the majority of points represent higher carbon contents in the retained austenite than expected intuitively from such low extents of transformation, since eqn. III.4 would predict only very limited carbon enrichment. This, coupled with the fact that there appears to be very little variation in the carbon content of the retained austenite (despite the predicted trends) leads to the following inferences.

Microstructural observations (figure I.4) demonstrate that the internal films of austenite are retained at room temperature even after small amounts of transformation to bainite, when the bulk matrix decomposes martensitically. This is in agreement with the above results since they both demonstrate that the films of austenite have a high carbon content at all degrees of transformation. Since such films are trapped between adjacent sub-units, the partitioned carbon would be confined within that region. However, in the case of the blocky austenite, the partitioned carbon would be distributed over a much larger volume. Since the X-ray measurements refer only to <u>retained</u> austenite, and since the blocky austenite would decompose martensitically at low V_b's, only the carbon content of the film morphology would be measured when the extent of transformation to bainite is small, thereby explaining the above results.

We may therefore conclude that the carbon content of the <u>retained</u> austenite does not vary significantly with the extent of transformation to bainite of the type observed in the present investigation.

(ii) Strength Analysis

Hardness tests were used to study the composite strength variations as a function of the volume fractions of retained austenite, bainitic ferrite and martensite. Tensile testing proved to be impractical for the present purpose since the specimens containing relatively large quantities of martensite

suffered from premature failure.

It was considered that the hardness contributions of the individual constituents could not be directly determined due to the fine scale of the microstructures involved. The hardness of the retained austenite was therefore obtained by measuring that of the Fe-3Mn-2Si-1.1C alloy, after austenitising and water quenching. Following the latter heat treatment, the specimen was found to be almost fully austenitic and the minimum hardness value observed (240 HV) was taken to be representative of the retained austenite associated with the bainite transformations. Care was taken to avoid the few plates of martensite that were present. The above procedure is thought to be justified since the carbon content of the bainitic retained austenite is expected to be of the same order as the above alloy. In any case, the strength of austenite is not sensitive to its carbon content (85). Furthermore, it was demonstrated in section (i) that the carbon content of the retained austenite is rather insensitive to the degree of transformation to bainite. It should, however, be noted that the above procedure fails to take account of the finely divided state of the bainitic retained austenite and also ignores the contribution from the defect structure of this austenite.

Following austenitising (1080°C for 10 mins) and water quenching, the hardness of the martensite in the 0.43C-3Mn-2.02Si steel was found to be 620-660 HV. However, this result cannot be used to represent the martensite formed from the residual austenite after quenching from the isothermal transformation temperature for the following reasons:

a) The martensite forms from the blocky regions of residual austenite, the carbon content of which is given by eqn.III.4. Thus, account has to be taken of the change in hardness of the martensite as a function of the extent of transformation to bainite.
b) The above hardness figures were obtained by directly quenching the specimen from the austenitising temperature, as opposed to quenching from the isothermal transformation temperature.

The latter effect was tested by step quenching from the austenitising temperature to temperatures between 370°C and 270°C (the M_s of this alloy is 220°C - Ch.I), holding for very short periods such that isothermal transformation was limited to less than 0.005 volume fraction, and immediately water quenching.

The small amount of isothermal transformation is not expected to significantly influence the martensite hardness. After allowing for the X-ray determined levels of retained austenite, the martensite hardness was found to be 795 HV.

The dramatic difference between the step-quenched and directly quenched hardness values is attributed to the relative abilities of the two treatments to eliminate thermal gradients within the specimens. The former specimens would have lesser gradients since they are effectively being quenched from a lower temperature. In the latter case the martensite would be expected to undergo an enhanced tempering treatment during the quench. Since electron microscopy failed to reveal any carbide precipitation in the directly quenched specimens (Ch.I), the influence of the above 'autotempering' on the structure of the martensite is thought to be connected with pre-precipitation events before the onset of detectable carbide formation. Such events would have to be consistent with the observed drop in hardness and their precise nature has not yet been resolved. For the purpose of the present strength analysis, a hardness figure of 795 HV is attributed to a martensite carbon content of 0.43 wt. pct. since all the specimens under investigation were quenched from the isothermal transformation temperature.

The variation of martensite hardness with carbon content was determined by measuring the hardness of martensite in the Fe-2.9Mn-2.13Si-0.19C steel using the step-quenching technique developed above. This gave a hardness value of 560 HV and comparison with the earlier result (assuming linear variation) gave a hardness change of 1020 HV per 1 pct. change in the carbon content of the martensite. It is interesting to note that the hardness of fully annealed martensite (600°C for 1 hr) in the 0.43C-3Mn-2.02Si alloy is 335 HV. Comparing the latter figure with the hardness of the martensite in the 0.19C alloy gives a change of 1190 HV per wt. pct. C, in good agreement with the previous value considering that the influence of recovery and carbide precipitation has not been taken into account.

The data on the constitution and hardness of the specimens used is listed in table III.1. The analysis was in terms of a simple composite model in which the total hardness is expressed as a linear combination of the contributions from the individual components, as follows:

$$H = V_{\acute{\alpha}} H_{\acute{\alpha}} + V_b H_b + V_\gamma H_\gamma \qquad \text{Equation III.5}$$

where the subscripts refer to martensite, bainitic ferrite and austenite respectively. V_x and H_x signify the volume fraction and the hardness of the component concerned.

As determined earlier,

$$H_\gamma = 240 \text{ HV}$$

and the martensite hardness, which is a function of the residual austenite carbon content can be shown to be

$$H_{\acute{\alpha}} = \frac{QV_b(\bar{x} - s)}{(1 - V_b)} + H_{\acute{\alpha}-x} \qquad \text{Equation III.6}$$

where

Q = the dependance of martensite hardness on carbon content, found to be 1020 HV/wt.pct.C

$H_{\acute{\alpha}-x}$ = the martensite hardness at a carbon content of (x), given by 795 HV in the present investigation.

The other terms have been previously defined.

When eqn. III.6 was evaluated using the data of table III.1, it was found that at some relatively high values of V_b, when partitioning of carbon into the austenite was extensive, unrealistic magnitudes of $H_{\acute{\alpha}}$ were obtained (sometimes reaching 1300 HV). Intuitively, it seems likely that the efficacy of carbon in hardening martensite must reach supersaturation when dislocation motion is 'completely' stopped. However, the point where such saturation may occur is unknown so that the following procedure was instituted.

Inspection of eqn. III.5 reveals that a plot of $(H - V_{\acute{\alpha}} H_{\acute{\alpha}} - V_\gamma H_\gamma)$ versus (V_b) would have a slope of H_b. Such plots were constructed using the data from table III.1, with the martensite hardness evaluated with eqn. III.6. However, a limit (N) was placed on the maximum value of hardness that the martensite can achieve so that $H_{\acute{\alpha}}$ is only allowed to vary below this limit. N was systematically varied (between 1500 and 500 HV) until the correlation coefficient relating $(H - V_{\acute{\alpha}} H_{\acute{\alpha}} - V_\gamma H_\gamma)$ and V_b was maximised, as shown in figure III.3. The point where correlation was maximised was at N = 800, when H_b = 480. The experimental data for N = 800 is plotted in figure III.4. The hardness of bainitic ferrite was therefore found to be 480 HV, and if it is assumed that yield stress and Vickers hardness are related by a factor of three, we get a bainitic ferrite yield stress as approx. 1440 MPa.

The calculated yield stress of 1440 MPa seems to be rather high since lath martensite of approximately the same carbon and manganese contents (86), after allowing for solid solution hardening due to silicon (with data from ref.87), has a yield strength of about 1000 MPa. However, this lath martensite forms as packets in which the individual laths are separated by very low angle boundaries (86) which would not be expected to act as very effective barriers to slip dislocations. On the other hand, the bainitic sub-units are separated by films of retained austenite whose interfaces with the ferrite are already jammed by formidable dislocation tangles (Ch.I). This would certainly make the transfer of slip very much more difficult.

Nevertheless, there are considerable errors involved in the analysis since it is based on data from both upper and lower bainite, the separate effects of which could not be resolved with confidence. If it is assumed that the dislocation density of lower bainitic ferrite is twice that of upper bainitic ferrite, the yield stress will only differ by some 70 MPa (86). The presence of cementite in the lower bainitic ferrite will lead to an increase in the yield stress of approximately 200 MPa, based on the quench ageing data of (88). Thus the yield stress of upper bainitic ferrite would probably be better represented by a value of 1150 MPa, while that of lower bainitic ferrite would be nearer 1440 MPa.

Examination of figure III.4 reveals that the linearity assumed for eqn. III.5 may not be justified and a more sophisticated model is clearly necessary. An attempt to use a more rigorous model is presented in chapter VIII, where a considerably simpler microstructure is analysed.

(iii) The Stability of Residual Austenite

The amount of residual austenite at the isothermal transformation temperature is given by $(1 - V_b)$. The fraction of this that decomposes to martensite on quenching to room temperature is calculable since the quantity of austenite retained can be determined by X-ray diffraction. Hence, the volume fraction of martensite is simply $V_\alpha = (1 - V_b) - V_\gamma$.

A suitable stability parameter for residual austenite would then be given by the ratio of the volume fraction of martensite to that of residual austenite at the isothermal transformation temperature, i.e. $V_{\acute{\alpha}}/(1 - V_b)$.

Figure III.5 is a plot of the stability parameter as a function of austenite carbon content, using the data from table III.1. The data for plain carbon steels was taken from (89).

For equivalent carbon contents, lower bainitic retained austenite was found to be marginally unstable relative to upper bainitic retained austenite. This could be understood if it is accepted that a lower degree of in situ stress relaxation occurs at the reduced transformation temperatures at which the former reaction occurs. However, the difference is not large.

On the other hand, the bainitic retained austenites are far more stable than the austenite of equivalent carbon content in plain carbon steel. In the latter case, the austenite is retained after a direct quench from the austenitising temperature. The extra stability cannot simply be attributed to the high manganese content of the steel under investigation, since this would only produce vertical shifts in the curves. It is interesting that the bainitic retained austenite becomes increasingly stable relative to the plain carbon steel as the degree of transformation to bainitic ferrite* becomes greater. This observation indicates that the enhanced stability arises from the finely divided state of the bainitic retained austenite. The sub-division of the prior austenite grains would increase with progress in transformation, and indeed, the three curves in figure III.5 converge as the amount of transformation to bainite tends to zero.

Two reasons could be advanced for the increase in stability with the fineness of residual austenite:

a) An increase in yield stress (associated with the finer 'grain size') of the austenite would make the martensite shear transformation more difficult.
b) The austenite would feel a greater degree of constraint when associated with a relatively rigid frame of bainitic ferrite.

---

* In the present context, the terms 'degree of transformation to bainitic ferrite' and 'austenite carbon content' are equivalent since they are related via equation III.4

(iv) Bainitic Retained Austenite and Toughness

Both bainitic and martensitic microstructures were examined* in an effort to isolate the influence of retained austenite on toughness properties. All austenitising treatments were carried out at 1080°C for a period of 10 minutes.

An 'upper bainitic' microstructure was obtained following isothermal transformation at 360°C for 115 mins (figure III.6). The microstructure was in fact a mixture of 42% bainitic ferrite, 27% retained austenite and 31% martensite, as determined by the techniques discussed in the earlier sections. At 360°C, and for the particular austenitising temperature used, the reaction essentially terminates at the above volume fraction of bainitic ferrite due to the T_o restrictions (Ch.II). This means that much of the austenite at the isothermal transformation temperature is present as a blocky morphology, delineated by crystallographic variants of bainite sheaves. The carbon content of this residual austenite is expected to be low, 0.74 wt. pct., (eqn. III.4). Furthermore, only about half of the residual austenite is predicted to be retained on quenching to room temperature according to figure III.5, and this is approximately the case, as indicated by the volume fractions given above.

The impact curves for the above microstructure and for martensite are presented in figure III.7. Caution must be exercised in drawing conclusions from these results since the microstructure of the 360°C upper bainite is in fact mixed, in the sense that it contains a large amount of martensite. It is therefore not clear as to which constituent, if any, exercises the controlling influence on the toughness properties. This factor has often not been taken into account in structure-property investigations on ultra-high strength steels even though the microstructure has been recognised to be mixed 'bainite-martensite'.

In the 360°C upper bainite being considered above, some indication can, however, be obtained as to which phase exercises control on toughness. In figure III.7 it is observed that at the highest of test temperatures, there is a fall off in the upper shelf energy. Such a fall off is also noticed in the virgin martensite* curve and has been attributed to the precipitation

---

* The martensite curves are reproduced from Ch.V. Virgin martensite refers to martensite without any detectable carbide precipitation using conventional transmission electron microscopy.

*Fe-0.43C-3Mn-2.02Si alloy

of epsilon carbide during the course of the high temperature impact tests. The impact energy falls off to a value given by the extrapolated tempered martensite curve, where the appropriate tempering treatment had induced epsilon precipitation before testing. Electron microscopy confirmed that carbide precipitation had occurred in the martensite phase of the 360°C upper bainite specimens which had been tested in the fall off region (figure III.8). No such precipitation was found in the specimens tested at room temperature. It therefore appears that the martensite is the controlling phase in determining the toughness of the isothermally transformed specimens. We note that the martensite results from the instability of the blocky austenite.

To overcome the above problem, it is necessary to promote further transformation to upper bainitic ferrite, so that the blocky morphology is reduced and at the same time the carbon content of the residual austenite is increased. Both these factors are expected to promote stability. However, the severity of the T_o restriction means that further transformation can only be achieved by lowering the isothermal transformation temperature, thereby allowing the residual austenite to tolerate more carbon before the T_o condition is transgressed.

Specimens were therefore isothermally transformed at 295°C for 115 minutes, giving an upper bainitic microstructure composed of about 68% bainitic ferrite, 22% retained austenite and 10% martensite. The hardness of this microstructure was found to be 447 HV. Due to the high degree of transformation, a greater proportion of the retained austenite was present as films between sub-units. The blocky morphology was still present, but was well dispersed and on a much finer scale compared to the 360°C upper bainite (figure III.9). The latter observation is further substantiated below.

It was previously determined that about 15 pct. of the optically resolved sheaf of bainite consisted of the film morphology of retained austenite. Using this information, it was estimated that close to half the X-ray determined retained austenite in the 295°C microstructure is of the film type, whereas for the 360°C microstructure only a fifth of the austenite was of the latter morphology.

The specimens isothermally transformed at 295°C not only showed good toughness, but this toughness exceeded that of <u>any</u> tempered martensite at equivalent or lower hardness levels.

The impact curves are presented in figure III.10. It is noted that holding at the isothermal transformation temperature for longer than 115 minutes has no effect on the toughness levels. This is consistent with the fact that the T_o condition has been achieved by isothermally transforming for 115 minutes. The above observation also indicates that little, if any, recovery occurs at 295°C.

Tempering the above microstructure at 397°C for 1 hour gave an increase in toughness performance (fig. III.11), with no detectable change in hardness. Electron microscopy revealed that the retained austenite was still intact (fig. III.12) although the small amount of martensite had been tempered. No signs of recovery were observed in the bainitic ferrite, and this is consistent with the observation that the hardness did not change significantly on tempering. The considerable toughness increment relative to the untempered microstructure can be attributed to the tempering of the martensite present in the microstructure.

On the other hand, tempering at 500°C for 1 hour led to a drastic fall in toughness (fig. III.11) despite a fall in the hardness value from 447 HV to 387 HV. Such tempering leads to the diffusional decomposition of high carbon retained austenite into bands of discretely nucleated carbides (Ch.I). It is important to note that the carbides have a monoclinic structure, they are discretely nucleated and the austenite does not decompose into continuous films of carbide. The microstructure following tempering is illustrated in fig. III.13.

Horn and Ritchie (91) examined an air-cooled 300M steel*

*300M steel is metallurgically very similar to the steel used in the present study, and is one of the most widely used 'cheap' ultra-high strength steels. Its basic composition is Fe-0.42C-0.8Mn-1.8Ni-0.4Mo-1.6Si-0.1V.

and found a microstructure very similar to the upper bainite of the present study. However, they claimed that the embrittlement found on tempering above 450°C could be associated with the change from epsilon carbide to cementite and with the decomposition of retained austenite to give films of cementite at the lath boundaries. These observations are not in agreement with the present work, and it is likely that the micrograph presented by (91) was unrepresentative of the air-cooled condition and the

microstructure probably contained a large amount of martensite in addition to upper bainite. We further note that Horn and Ritchie used extraction replicas to identify the carbides present, in which case it would be difficult to recognise the base structure (bainite or martensite) from which the carbides originated. Additionally, experimental data on the identification analysis was not presented so that it is not possible to determine whether the data can be ambiguously interpreted.

It is essential to stress the above uncertainties since it has been suggested (91,92) that the formation of continuous films of cementite at lath boundaries leads to embrittlement by inter-lath failure, although the overall failure would be transgranular with respect to the prior austenite grains. Examination of nickel plated fracture surfaces of tensile (to be discussed later) and impact specimens revealed the failure mode to be trans-lath, figure III.14. Additionally, comparative fractography between the tempered and untempered specimens in the ductile failure mode revealed a much smaller void size in the former case, figure III.15. These observations demonstrate the void nucleation role of carbides, rather than one of providing an easy fracture path. It should be noted that the room temperature tested impact specimens of the 500°C tested specimens still had a small component of ductile failure and that the embrittlement observed in the present study relates to a reduction in the energy of ductile failure rather than a change from ductile to cleavage failure, as observed by (91). Again, this could be due to the presence of a substantial amount of martensite in the air-cooled 300M microstructure.

Tempering the isothermally transformed microstructure at 615°C for 79 minutes led to a final structure of discrete cementite particles uniformly distributed at the prior austenite-ferrite boundaries, figure III.16. Extensive recovery was evident and was accompanied by a hardness fall to 319 HV. Although the toughness resulting from this heat treatment was better than the 500°C tempered condition (due to the lower hardness of the former microstructure), it was still poor relative to the as-transformed condition, figure III.11. This is despite the fact that the 295°C upper bainite has a considerably higher strength (447 HV) and the difference can be attributed to the presence of carbides in the tempered microstructure together with the possible beneficial influence of retained austenite in the untempered condition.

Figure III.11 also suggests that the impact transition temperature of the 615°C tempered specimens is well defined and higher than that of the 500°C specimens. This can be explained by the fact that the cementite in the former microstructure is considerably coarser than the monoclinic carbides in the latter (cf. figs. III.13,16).

Lower bainite obtained by isothermal transformation at 243°C for 24 hours was also examined. The favourable characteristics of the lower bainite transformation include the high degree of transformation permissible by the T_o condition and its inherently high strength (hardness = 520 HV). Hence the blocky morphology of retained austenite is minimised, as is the quantity of martensite obtained on quenching to room temperature. The impact properties are presented in figure III.17 and it is clear that tempering at 400°C for 1 hour makes no significant contribution to the toughness properties. The hardness level following the tempering treatment remained at about 520 HV. Electron microscopy revealed that the retained austenite was once again intact following the above tempering treatment. It is possible that the insensitivity to tempering treatment arises due to the generally high hardness level of the microstructure (V_b= 0.79, V_α= 0.1, V_γ = 0.11) so that the tempering of the small quantity of martensite makes an insignificant overall contribution.

Comparison of the lower bainite impact transition curve with those of the tempered martensites (all of which have lower hardness levels - table III.2) clearly demonstrates that the retained austenite has a strong and beneficial influence on the properties of the base microstructure. The comparison is particularly valid because the tempered martensite microstructure is equivalent to the lower bainite microstructure apart from the presence of retained austenite in the latter. Both the microstructures contain widmanstatten arrays of cementite precipitates and are morphologically similar. Furthermore, the significance of the comparison is enhanced by the fact that the tempered martensites have lower hardness values.

It is thought that the diminished shelf energies of the lower bainite compared with the 295°C upper bainite can be attributed to the presence of cementite in the former structure.

(v) The Mechanical Stability of Bainitic Retained Austenite

Tensile specimens were isothermally transformed to the 295°C upper bainite, water quenched and finally annealed at 400°C for 1 hour. The purpose of this treatment was to temper the martensite formed during the quench from the isothermal transformation temperature so that it could subsequently be distinguished from the martensite formed due to the application of stress.

No attempt is made in the present work to distinguish between stress and strain induced martensite. It is common to refer to the transformation as strain-induced when it occurs after yielding of the austenite and stress-induced when it occurs before yielding of the austenite.

The tensile specimens (Standard Hounsfield No.11) were stressed to various levels without fracture or necking and were then examined by transmission electron microscopy. The foils were removed such that the tensile axis was normal to the foil plane. Following stressing to 1000 MPa, it was found that much of the austenite was intact. The thin films of austenite between the bainitic ferrite sub-units had remained untransformed while thicker or irregular blocky austenite had decomposed martensitically, figure III.18. In addition, the defect structure of the retained austenite appeared more intense compared with the as transformed condition, indicating that the austenite had undergone some plastic deformation (fig.III.18e). Thus the film type of retained austenite was found to be stable to high levels of stress.

Some tensile specimens were stressed, without failure, to 1100 MPa in order to promote more extensive stress induced austenite decomposition. Thin foils for transmission electron microscopy were removed as described above and electron diffraction patterns were obtained from the martensite formed under the influence of stress. The patterns were taken at zero tilt, so that the electron beam direction (approximately equivalent to the diffraction zone axis) corresponded to the tensile axis. From basic stress analysis, the poles of the planes of maximum shear stress would lie on a right circular cone (of semi-apex angle 45°) whose axis is the tensile axis. When the martensite zone axis was plotted on a stereogram with a 45° small circle described about the zone axis (corresponding to the cone referred to above) it was invariably found that

{112} martensite poles could be associated with these circles, figure III.19. The {112} martensite plane is the most common plane of lattice invariant shear in ferrous martensites, and it is therefore concluded that the above results are consistent with the martensite forming in a manner compatible with the externally applied stress.

The blocky morphology of retained austenite was also studied in these experiments. Optical microscopy (fig.III.20) on Ni plated fracture surfaces of impact specimens (295°C upper bainite) indicated that the blocks of austenite often absorbed considerable deformation prior to martensitic decomposition. This was inferred from the observation that bainite sheaves adjacent to the prior austenite blocks had undergone substantial plastic strain near crack surface. However, there was no apparent loss of cohesion or signs of cracking at the interfaces between the blocky austenite and bainite sheaves. The austenite must therefore have undergone simultaneous deformation, before transforming to martensite. Had the transformation occured first, the resulting martensite would not be expected to permit such high plastic strains as are evident at the fracture surface, at least not without substantial cracking. It is therefore considered that the blocky morphology of austenite positively contributes to the toughness (for the 295°C upper bainite) not only by transformation, but also by considerable plastic deformation prior to transformation.

In order to test the influence of stress-induced martensite on the impact properites, some tensile specimens (8 mm diameter and 60 mm gauge length) were isothermally transformed at 295°C for 115 minutes and then stressed to 995 MPa without failure or necking. The exact stress histories involved are listed in table III.3. Impact specimens were subsequently machined from the gauge lengths and tested as indicated in table III.3. These indicated no deterioration in toughness, a result that is consistent with the observation that the islands of austenite are not the controlling features of the 295°C treatment and that the films of austenite remain stable to such stresses.

(III.4) General Summary

The partitioning of excess carbon into residual austenite following the displacive formation of supersaturated bainitic ferrite results in the austenite being retained on quenching to room temperature. However, in most cases, the practically simultaneous precipitation of carbides relieves the build up of carbon in the austenite so that little, if any, of the FCC phase remains untransformed at room temperature. This problem can be overcome by adding appropriate amounts of silicon, and bainites in such steels are henceforth referred to as silicon bainites.

The present work shows that under favourable circumstances the events described above can be advantageously exploited to give unique combinations of toughness and strength. The reasons for the exceptional properties of silicon bainites can be summarised as follows:

a) Silicon bainites have an ultra-fine operative grain size, resulting from the displacive nature of the transformation. The resulting lenticular plates are essentially separated by films of stable retained austenite. Such an arrangement leads to high strength and additionally it breaks up the path of a propagating crack since the crack not only has to traverse interphase interfaces and varying crystal structures but its motion can also be dampened by transformation at the crack front.
b) In silicon bainites, carbide precipitation can be totally avoided, thereby making crack and void nucleation all the more difficult.
c) A further strengthening component arises due to the transformation induced defect structures in both the bainitic ferrite and the retained austenite.
d) The strengthening of ferrite is not obtained by interstitial hardening (which is very detrimental to toughness) despite the high overall carbon content that can be tolerated in the base alloy.
e) The retained austenite can be designed to be stable to high stresses (> 1000 MPa) and to a wide temperature range (400°C to -196°C).

A number of restrictions apply to the achievement of good properties. The restrictions are thermodynamic in origin since only a limited amount of isothermal transformation is

permissible for a given temperature. If the allowed degree of transformation happens to be small, the properties will be poor despite the retention of relatively large quantities of austenite. This is because the austenite is found to occur in two morphological variants - blocky and film type. The former originates from the geometrical partitioning of the prior austenite grain whereas the latter is confined between bainitic sub-units. The carbon content (and hence the stability with respect to the quench from the isothermal transformation temperature) of the blocky austenite depends on the amount of transformation to bainitic ferrite, whereas that of the film austenite is essentially independent of V_b because it is isolated by the surrounding ferrite.

It is found that the blocky morphology must be avoided since its descendent martensite is undesirable as far as toughness is concerned. The condition for good toughness can be approximately expressed as follows:

Let $V_{\gamma-f}$ = Volume fraction of retained austenite of the film morphology,

$V_{\gamma-r}$ = Volume fraction of residual austenite at the isothermal transformation temperature,

$V_{\gamma-B}$ = Volume fraction of retained austenite of the blocky morphology.

Since $V_{\gamma-f} \simeq 0.15V_b$

and $V_{\gamma-r} = (1 - V_b)$,

it follows that

$$V_{\gamma-B} \simeq V_{\gamma-r} - V_{\gamma-f} - V_{\alpha'}$$
$$= (1 - 1.15V_b - V_{\alpha'}).$$

The ratio of the film to blocky morphology is given by

$$\frac{V_{\gamma-f}}{V_{\gamma-B}} = \frac{0.15V_b}{(1 - 1.15V_b - V_{\alpha'})} \qquad \text{Equation III.7}$$

Using the data from the 295°C upper bainite, we find that the above ratio must have a value of at least 0.9 and that the volume fraction of martensite must not exceed about 0.1 for good toughness, so that eqn. III.7 becomes

$$\frac{V_{\gamma-f}}{V_{\gamma-B}} = \frac{V_b}{(6 - 7.7V_b)} > 0.9 \qquad \text{Equation III.8}$$

Equation III. 8 thus becomes the criterion for good toughness in silicon bainites.

It is exciting to note that since V_b can be directly calculated using thermodynamics, the toughness behaviour of silicon bainites can, in principle, be estimated from a knowledge of the composition and without recourse to any experimental work!

It is anticipated, however, that an additional opposing condition must also apply; there has to be a certain (unknown) minimum amount of carbon in the alloy, if the films of austenite are to effectively separate the bainite sub-units. This becomes clear when we exaggerate the situation by letting x_γ tend to zero. The austenite films would initially become shorter and more discontinuous and would ultimately vanish altogether, leaving no barrier to continuous crack propagation across the remaining low-angle inter-sub unit boundaries.

Finally, the economic significance of the silicon bainite microstructure is clear - it uses carbon in a most elegant manner, enabling the existence of a duplex steel based on the cheapest and most effective austenite stabilizer known. At the same time it avoids the detrimental aspects of carbon in steels, i.e. the crack and void nucleation role of carbides and the embrittlement due to the presence of substantial quantities of interstitially dissolved carbon in ferrite.

Table III.1

Heat Treatment	V_b	V_γ	$V_{\alpha'}$	s	HV
363°C for 2015 min	0.46	0.27	0.27	0.03	433
363°C for 1070 min	0.52	0.33	0.15	0.03	420
363°C for 160 min	0.39	0.27	0.34	0.03	428
363°C for 80 min	0.48	0.27	0.25	0.03	492
363°C for 20 min	0.02	0.11	0.87	0.03	750
363°C for 10 min	0.004	0.084	0.912	0.03	759
363°C for 5 min	0.007	0.10	0.893	0.03	710
270°C for 5 min	0.044	0.082	0.874	0.27	756
270°C for 23 min	0.003	0.065	0.932	0.27	754
270°C for 80 min	0.22	0.10	0.68	0.27	590
270°C for 160 min	0.63	0.14	0.23	0.27	554
270°C for 1730 min	0.64	0.15	0.21	0.27	492
270°C for 6060 min	0.75	0.15	0.10	0.27	516

Notes

a) The austenitising temperature used was 1200°C for 7 min, with the specimens protected by a dynamic argon atmosphere and a proprietary coating compound.

b) About 0.5 mm of the surface of the specimen was removed by chemical polishing before any tests. The final specimen dimensions were 15 mm x 30 mm x 4 mm.

c) Some of the data in the above table has been quoted to three decimal places. This may not necessarily be justified, but it is felt that a greater error would have resulted following rounding off.

d) The hardness test were conducted before hot mounting the specimens in plastic since this treatment was found to reduce the hardness by approximately 80 HV. The quoted hardness value results from the average of ten indents. A 50 Kg load was used for all the hardness tests.

Table III.2

Heat Treatment**	Hardness / HV50
WQ + 247°C for 15 min, WQ	623
WQ + 347°C for 4 hr, WQ	483
WQ + 508°C for 1 hr, WQ	436
WQ + 597°C for 1 hr, WQ	334
360°C for 115 min, WQ	430
295°C for 115 min, WQ	447
295°C for 115 min, WQ, 397°C for 1 hr, WQ	461
295°C for 115 min, WQ, 500°C for 1 hr, WQ	387
295°C for 115 min, WQ, 615°C for 79 min, WQ	319
243°C for 24 hr, WQ	520
243°C for 24 hr, WQ, 400°C for 1 hr, WQ	520

** All the specimens were austenitised at 1080°C for 10 min, and the hardness results represent an average of ten determinations.

Table III.3

Impact energies of pre-stressed upper bainite (290°C) specimens.

Stress History	Test Temp./°C	Impact Energy/J
1) Stressed to 995 MPa	120	65
2) Cyclically stressed to 995 MPa five times	120	65
3) Cyclically stressed to 995 MPa twenty times	80	31

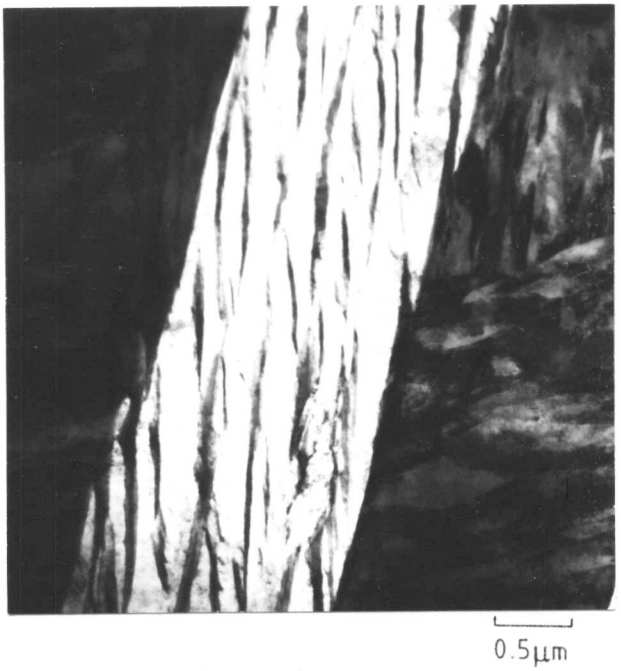

Figure III.1
Microstructure of a 'plate' of upper bainite showing the films of retained austenite between bainitic sub-units.

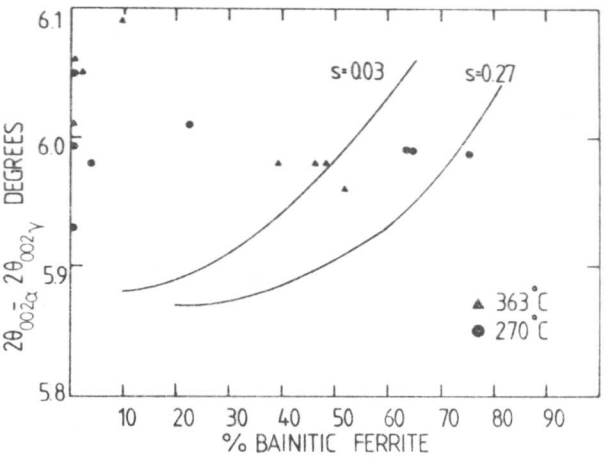

Figure III.2
Plot of the parameter ψ as a function of the volume fraction of isothermal transformation to bainitic ferrite.

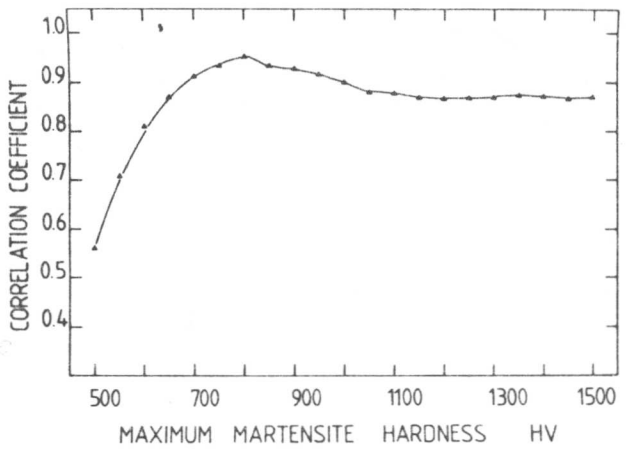

Figure III.3
Plot of the correlation coeff. relating $(H - V_\gamma H_\gamma - V_{\alpha'} H_{\alpha'})$ and V_b as a function of (N), the limiting hardness of martensite.

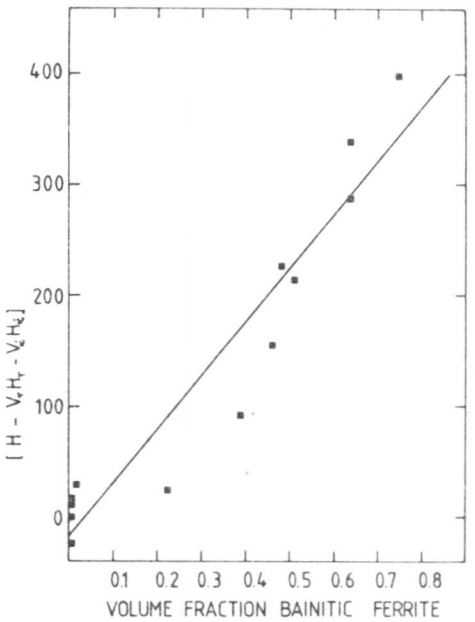

Figure III.4
Plot of $(H - V_\gamma H_\gamma - V_{\alpha'} H_{\alpha'})$ vs. V_b when the value of (N) is taken to be 800HV.

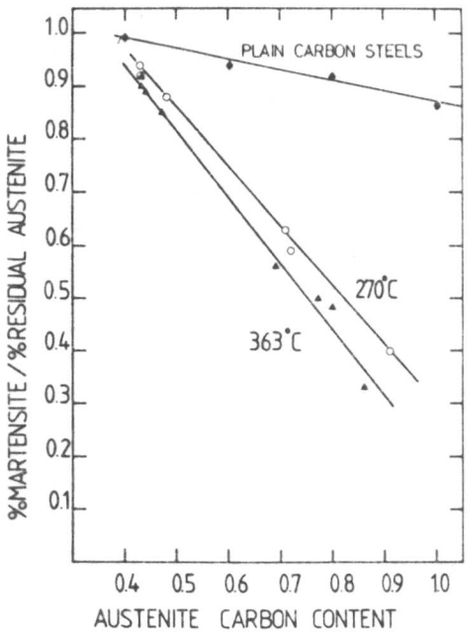

Figure III.5
Plot of the instability of bainitic residual austenite vs. the austenite carbon content.

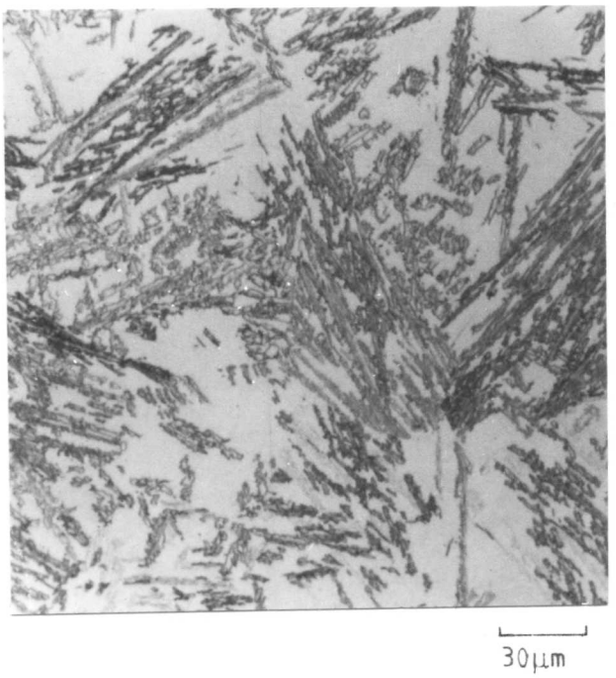

Figure III.6
Optical micrograph showing the blocky austenite following isothermal transformation at 360°C for 115 minutes.

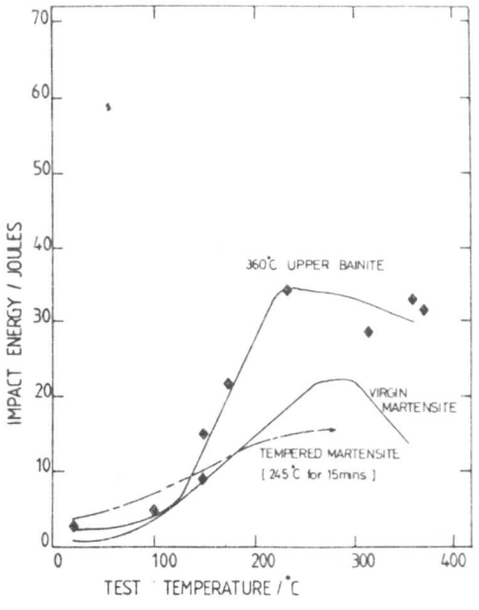

Figure III.7
Impact transition curves of virgin martensite, martensite with ε carbide, and the 360°C upper bainite.

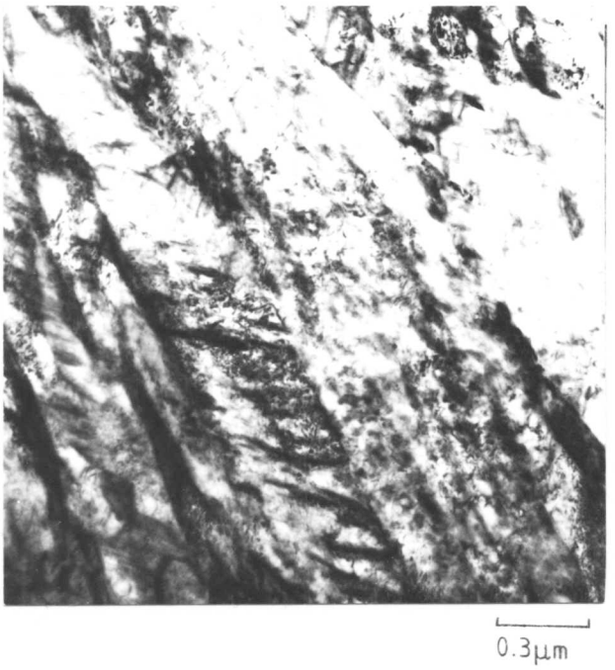

Figure III.8
Carbide containing martensite in a specimen tested in the 'fall off' region. The specimen was in the isothermally transformed (360°C) condition prior to impact testing.

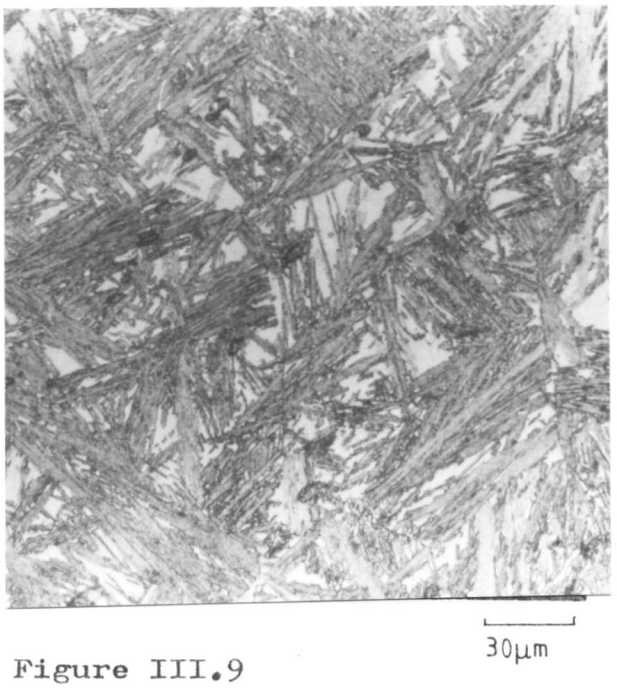

Figure III.9
Optical micrograph showing the blocky austenite following isothermal transformation at 295°C.

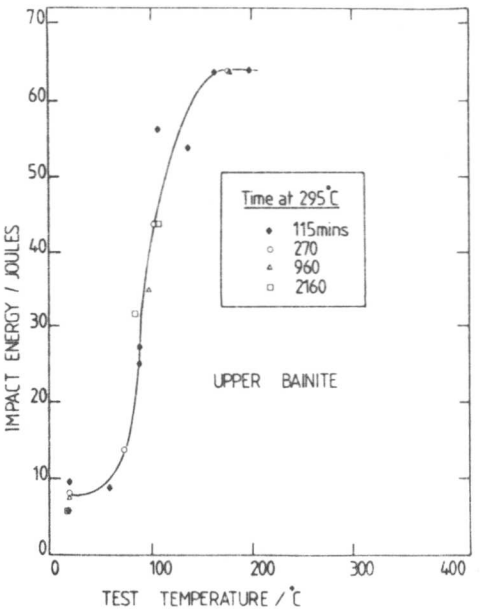

Figure III.10a
Impact transition curve for upper bainite formed by isothermal transformation at 295°C.

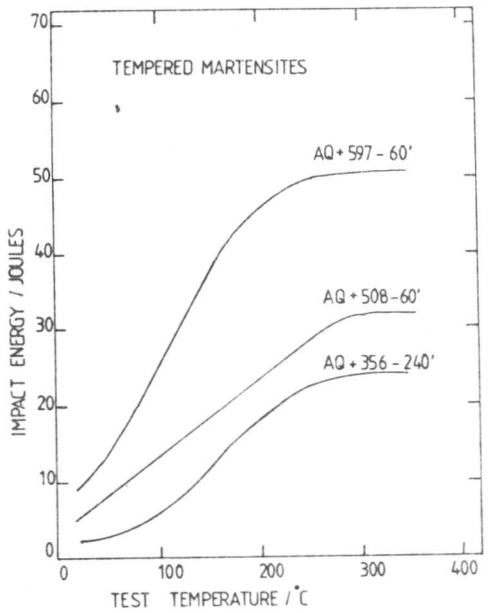

Figure III.10b
Impact transition curves for tempered martensites.

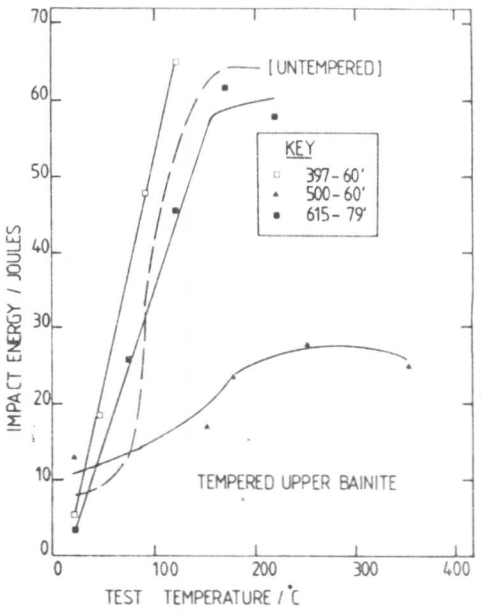

Figure III.11
Impact transition curves for the 295°C upper bainite following various tempering treatments.

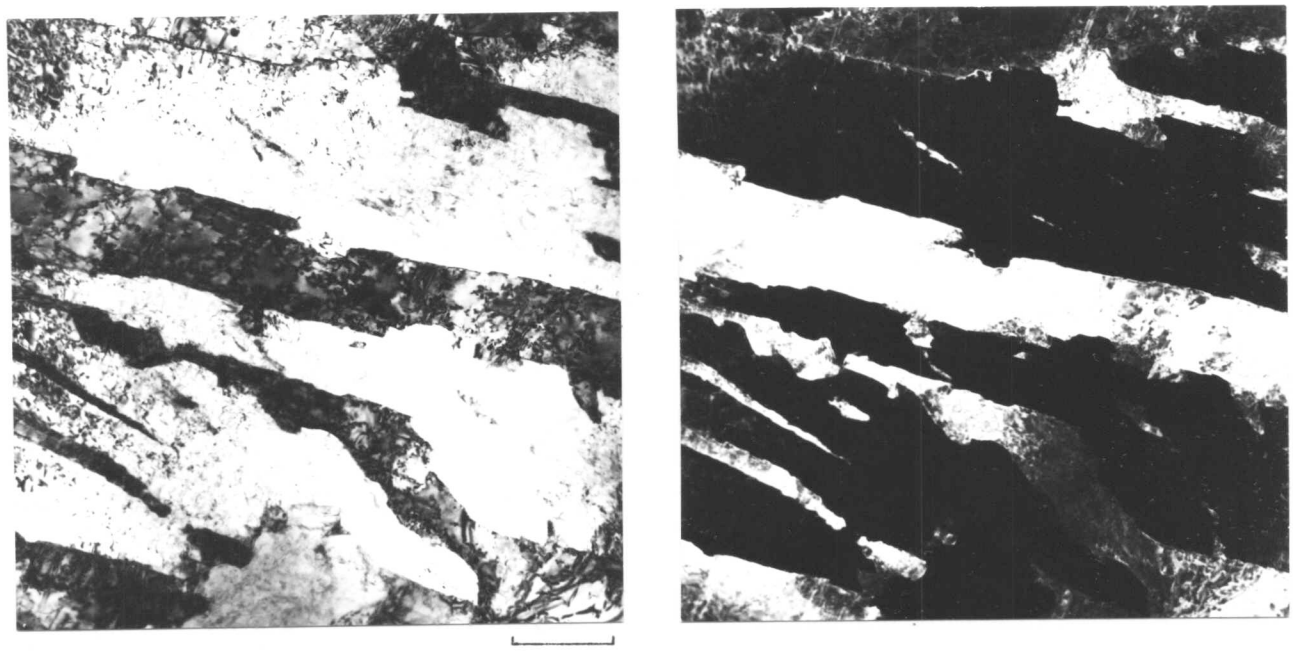

(a) (b)

Figure III.12

Electron micrographs illustrating the microstructure of 295°C Upper bainite after tempering at 397°C for 1 hour.

(a) Bright field image.

(b) Retained austenite dark field image.

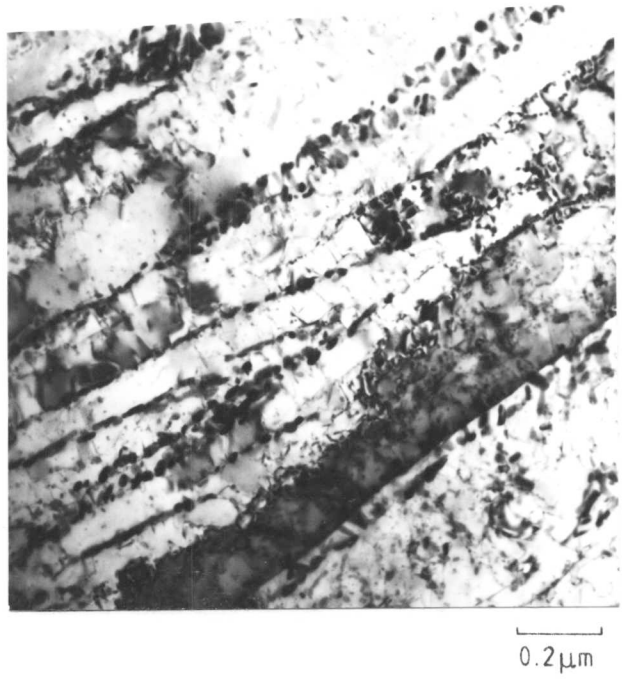

Figure III.13

Electron micrograph of 295°C upper bainite after tempering at 500°C.

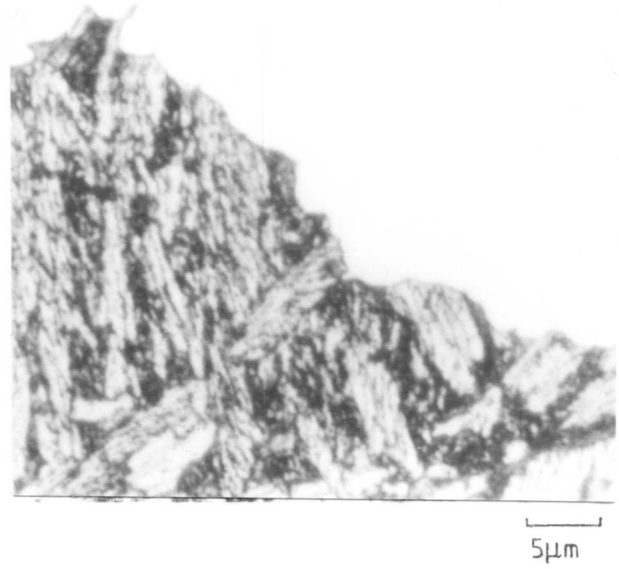

Figure III.14

Nickel plated fracture surface from the 295°C upper bainite after tempering at 500°C and impact testing at 250°C.

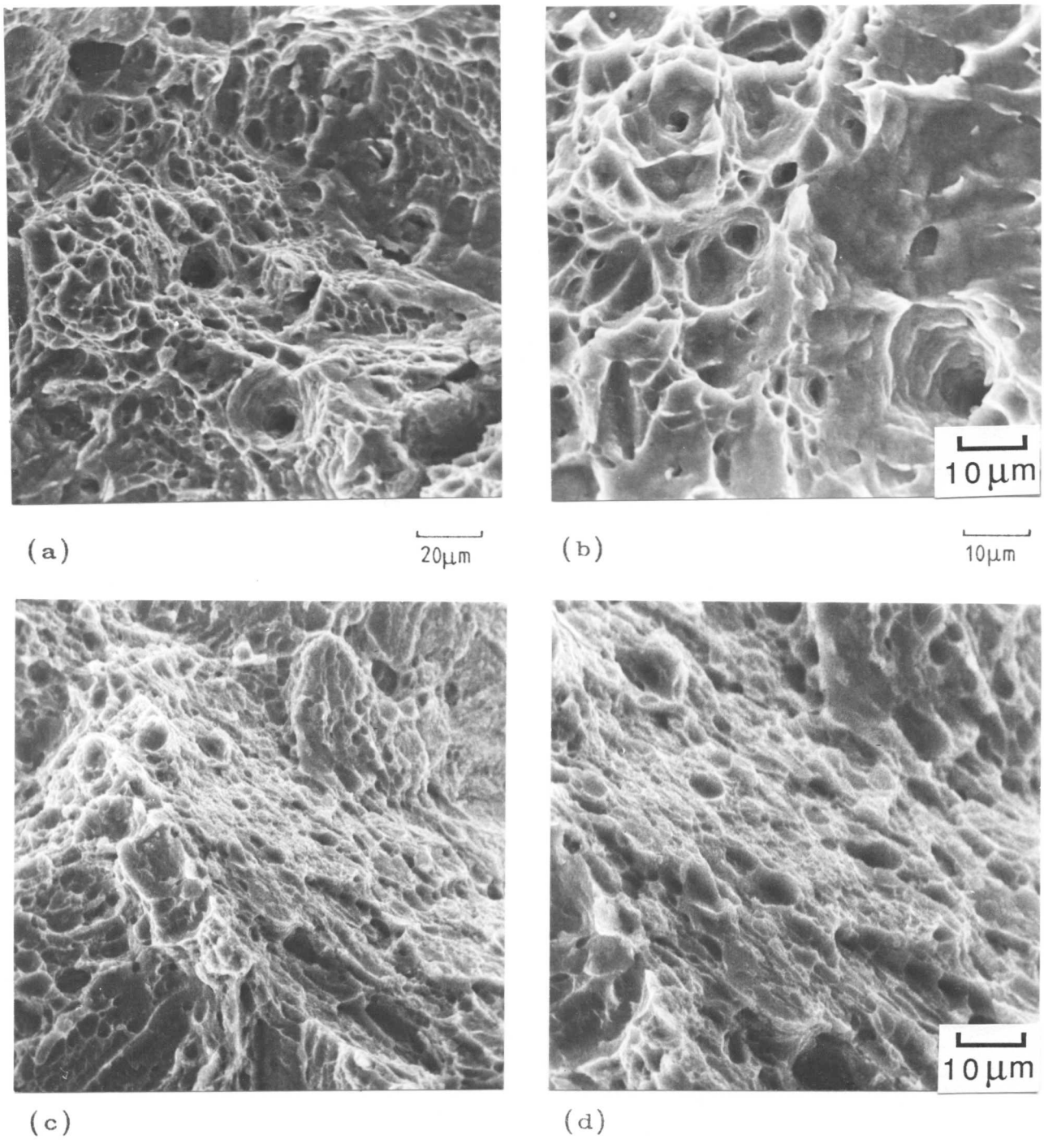

Figure III.15

(a) & (b) Fractographs from the 295°C upper bainite, taken from specimens tested in the ductile failure region of the impact transition curves.

(c) & (d) As above, but the specimens were tempered at 500°C for 1 hour before impact testing.

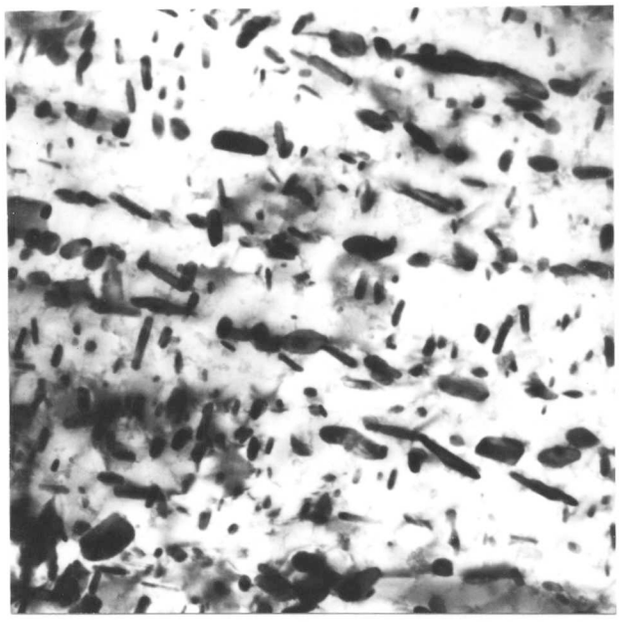

Figure III.16
Electron micrograph of upper bainite (295°C) after tempering at 615°C for 79 minutes.

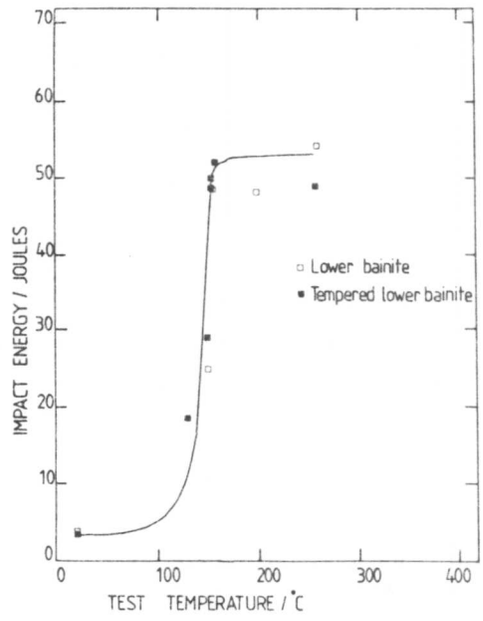

Figure III.17
Impact transition curve for lower bainite and for tempered lower bainite.

(a)

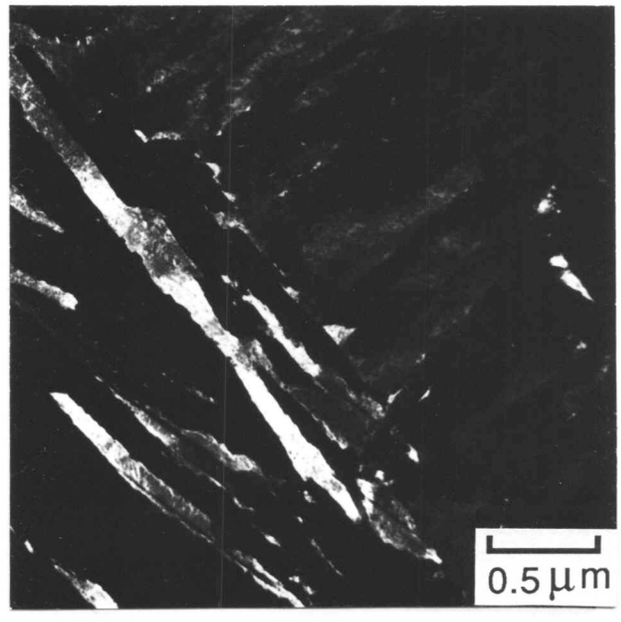

(b)

Figure III.18(a-e)
Electron micrographs illustrating the microstructures resulting from the application of stress to the 295°C upper bainite.
(a) Bright field image, specimen stressed to 850 MPa.
(b) Corresponding retained austenite dark field image. It should be noticed that the larger areas of austenite have decomposed martensitically.

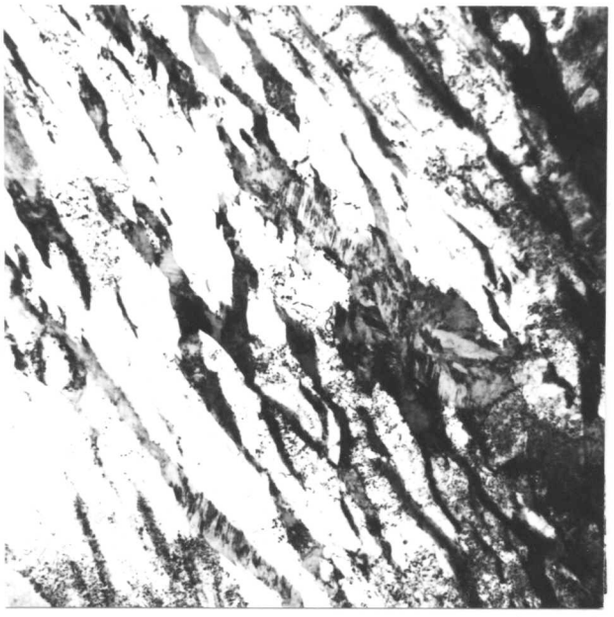

Figure III.18c

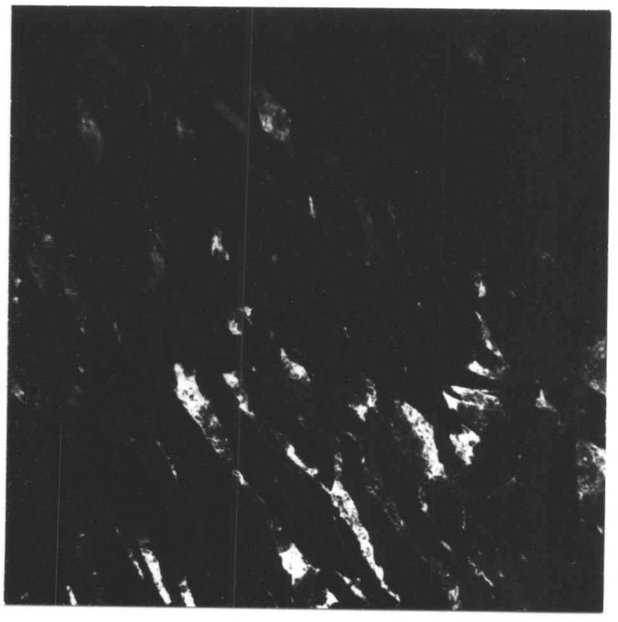

Figure III.18d

(c) Bright field image, specimen stressed to 1180 MPa.

(d) Corresponding retained austenite dark field image.

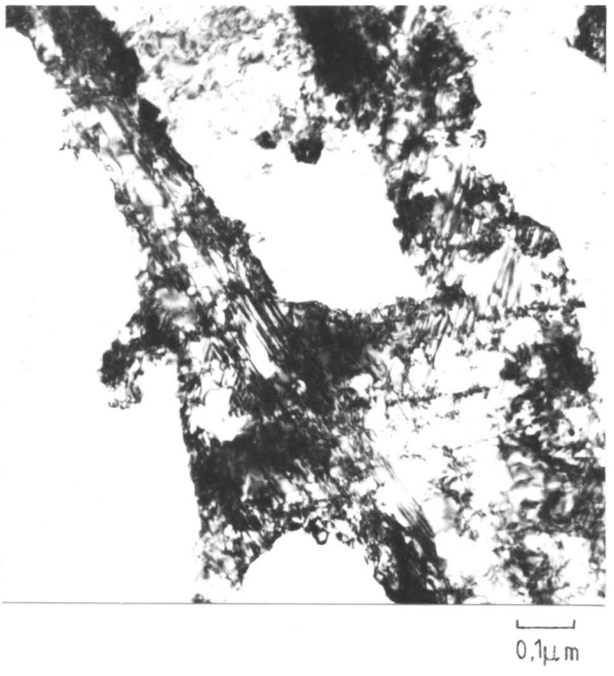

Figure III.18e

Electron micrograph illustrating the deformation structure of retained austenite after stressing to 850 MPa

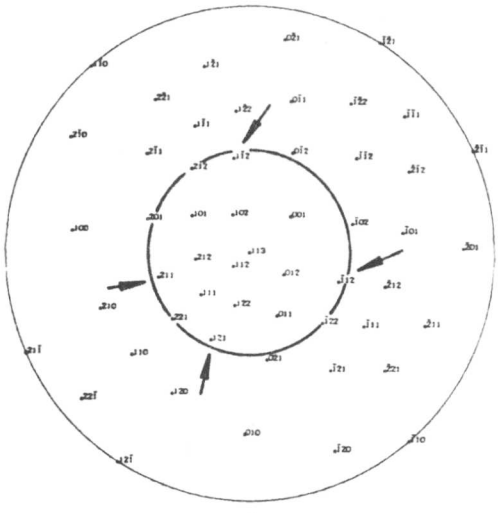

Tensile axis approximately corresponds to ⟨113⟩ martensite

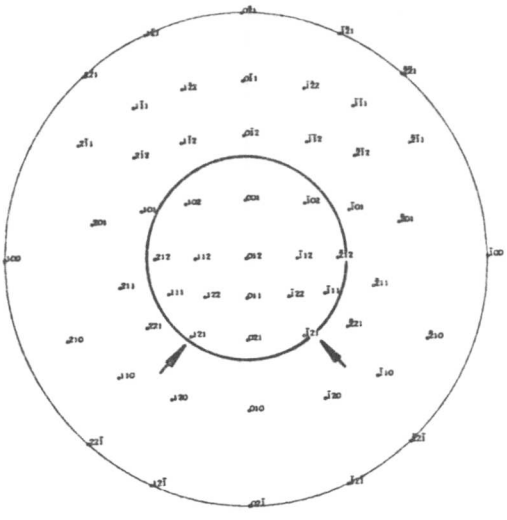

Tensile axis approximately corresponds to ⟨012⟩ martensite. In this instance, two twin related ⟨012⟩ zones were present.

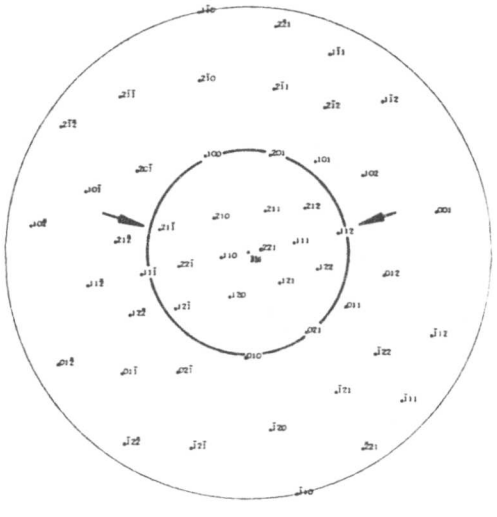

Tensile axis approximately corresponds to ⟨331⟩ martensite.

Figure III.19

Small circle analysis of stress induced transformation of retained austenite, as discussed in the text. The stereograms are centered on the approximate direction of the tensile axis so that the poles of the planes consistent with the planes of maximum shear stress lie on the small circles.

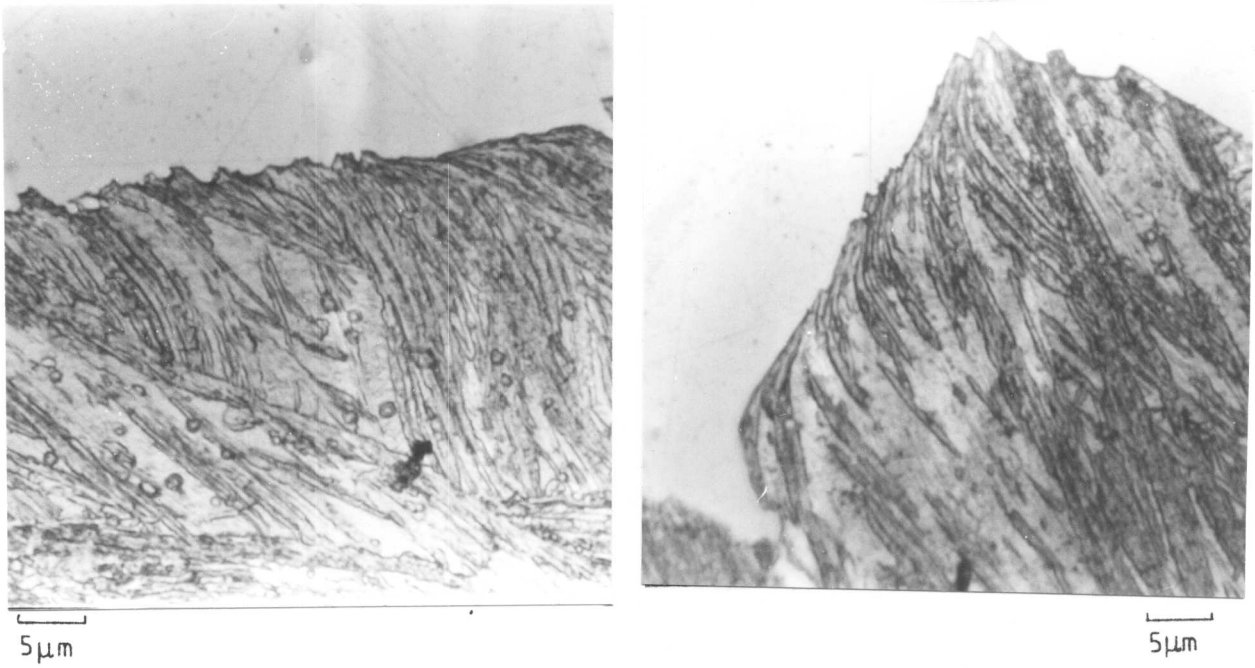

Figure III.20
Optical micrographs of nickel-plated fracture surfaces from the 295°C upper bainite, following tensile fracture. The deformation of the islands of prior austenite is deduced from the absence of decohesion or cracking relative to the obviously deformed bainitic ferrite.

CHAPTER FOUR

THE PROPERTIES OF MICROSTRUCTURES CONTAINING BAINITIC RETAINED AUSTENITE - PART 2

(IV.1) Introduction

The principal steel investigated in the experiments of chapter three (i.e. 0.43C-3Mn-2.02Si) was found to exhibit optimum strength and toughness in the bainitic condition. Nevertheless, the absolute toughness levels encountered even with the bainitic microstructures are inadequate, as is evident from the high transition temperatures of the impact curves presented in figures III.10,17. It is therefore clear that further toughness improvements must be made if such bainitic microstructures are to provide a viable basis for ultra-high strength steels.

From the results of chapter three, it was concluded that the blocky morphology of retained austenite is detrimental to toughness and is unstable relative to the film morphology of retained austenite. The stability of the two morphologies of retained austenite can be compared under two distinct circumstances, as follows:

a) Following isothermal transformation in the bainitic temperature range, to an extent less than that allowed by the T_o condition, the blocky austenite is unstable relative to the film austenite and can undergo martensitic transformation during the quench from the isothermal transformation temperature. This is not only because the former austenite has a lower carbon content than the film austenite (Ch.III), but it is also less refined and hence experiences less constraint from its ferritic environment.

b) Following the termination of reaction at the isothermal transformation temperature (i.e. when V_b reaches the maximum value beyond which displacive transformation is thermodynamically impossible), the carbon content of all forms of austenite is expected to be the same. Nevertheless, the blocky austenite turns out to be unstable to applied stress, presumably due to its larger size and the lower degree of constraint it experiences.

Since all the toughness tests were done on specimens which had been transformed till reaction termination, the latter situation is more relevant to the problems considered in the present chapter.

It is the instability of the blocky austenite that leads to

poor toughness, and eqn.III.8 effectively acknowledges this and states that toughness control by the blocky austenite is relinquished when a certain degree of transformation is achieved. This does not, however, imply that such austenite ceases to have any influence on the toughness behaviour once the criterion in eqn.III.8 is exceeded. Clearly, a lot depends on how the toughness is influenced by the austenite stability and understanding the link between the two parameters raises difficulties. It is known (93) that in general only FCC metals have good ductility at low temperatures. A good toughness response may therefore necessitate the presence of an FCC phase which remains stable to martensitic transformation at low temperatures and despite extensive deformation of the kind associated with the plastic zone of a crack tip. On the other hand, if transformation does occur, it may or may not enhance toughness. If martensite formation occurs in close proximity to the crack tip, it can be expected to form in a manner which would relieve the crack tip stresses, thereby hindering or stopping crack propagation. If the transformation occurs well ahead of the crack tip, it is not difficult to imagine the resulting high carbon martensite fracturing in a brittle manner under the influence of increasing levels of stress due to the advancing crack tip stress field. On balance, however, it seems advantageous to increase the austenite stability and expect a corresponding increase in toughness.

The stability problem, of course, reduces to that of increasing the degree of isothermal transformation permitted (by the T_o condition) at any given temperature within the bainitic transformation range. This would not only promote the further partitioning of carbon into any residual austenite, but would also refine and reduce the quantity of blocky austenite. Both these factors would contribute to the required stability. The mechanistic details resolved in the earlier chapters immediately suggest two methods of achieving further transformation:

a) By reducing the overall carbon content of the alloy concerned so that the critical concentration in the austenite at which displacive transformation becomes impossible is reached at a later stage in the transformation.

b) By modifying the substitutional alloying elements such that the T_o curves are shifted to higher austenite carbon contents.

The purpose of the present study was to evaluate these possibilities.

(IV.2) Experimental

The experimental details are essentially the same as in (III.2) and are not restated here. The steels used were prepared from high purity base materials as 20 Kg vacuum induction melts and were hot worked to 8 mm diameter rod. The final compositions are as follows:

Alloy A	Fe-0.22C-3.00Mn-2.03Si	wt. pct.
Alloy B	Fe-0.39C-4.09Ni-2.05Si	wt. pct.

The reasons for the choice of these particular compositions will become clear in (IV.3).

(IV.3) Results and Discussion

(i) T_o Calculations

With the notable exception of having a lower carbon content, alloy A has essentially the same composition as the 0.43C-3Mn-2.02Si steel used for the toughness evaluations of chapter three. The amount of carbon partitioned into the austenite per sub-unit of bainitic ferrite would therefore be relatively reduced, since the parameter ($\bar{x}$) in eqn. III.4 would be smaller. Hence the critical concentration of carbon in austenite beyond which bainitic transformation becomes impossible would be reached at a higher value of V_b, thus accomplishing the required increase in the degree of isothermal transformation. The T_o curves for alloy A are plotted in figure IV.1.

On the other hand, the calculation of T_o curves for the Ni containing alloy presents difficulties due to the rather erratic values of the interaction parameter W given in (41). Depending on the temperature of evaluation, the ratio W/T was found to vary considerably, even though the basic thermodynamic model of (41) allows for no such variation. It was therefore decided to derive W from some more recent data (94,95) relating the activity of carbon in austenite to the amount of nickel in solid solution. The procedure used was the same as in (40) and involved the plotting of $\ln(a_\gamma)$ versus

$$\ln \left\| \frac{\left(\left[1-2(1+2J)x+(1+8J)x^2\right]^{0.5}-1+3x\right)^6 (1-2x)^5 \exp(w/RT)}{\left(\left[1-2(1+2J)x+(1+8J)x^2\right]^{0.5}+1-3x\right)^6 x^5} \right\|$$

until the value of W (which was systematically varied) gave a regression slope equal to the theoretical slope of unity. a_γ refers to the activity of carbon in austenite, and the other terms have been previously defined (Ch.II). Hence, for the concentration of nickel in alloy B, the value of W that gave the correct slope was found to be 1960 J. This, together with some data from (40,41), was subsequently used to calculate the T_o curves of alloy B (figure IV.1) using the procedure of (38,40,41). From figure IV.1, it is clear that the nickel based alloy is capable of sustaining a greater amount of carbon in austenite before the termination of isothermal transformation compared with the Mn containing alloys. This means that a greater degree of bainitic transformation can be attained at any given temperature, thereby fulfilling the requirements of improved toughness.

(ii) The Influence of Austenitising Temperature

The toughness evaluation of the 0.43C-3Mn-2.02Si alloy (Ch.III) had been carried out with specimens austenitised at 1080°C for 10 mins (a temperature well above the estimated Ae_3 temperature) in order to allow the maximum degree of isothermal transformation* to upper bainite, in accordance with the texture/grain size analysis presented in (Ch.I).

---

* It should be noted that texture or other effects can only limit the degree of transformation <u>below</u> that specified by the T_o condition, since the latter specifies a thermodynamic maximum in the absence of any additional physical restrictions.

In fact, it was found that for isothermal transformation to upper bainite (at 295°C for 115 mins), the use of a lower austenitising temperature (880-900°C for 10 mins) results in a lower degree of isothermal transformation compared with the specimens austenitised at the higher temperature. Hence the hardness of the final microstructure increased from 477 HV (austenitised at 1080°C) to 530 HV (austenitised at 880-900°C) despite the fact that all specimens had undergone identical isothermal transformation treatment. This result is consistent with the texture/grain size analysis of (Ch.I). The effect of the above hardness increase was to reduce the general toughness levels (figure IV.2), although it was evident that the impact energy absorbed below the transition temperature (i.e. in the cleavage fracture mode) was significantly improved. This could possibly be due to the reduced prior austenite grain size and

lower degree of grain growth induced texturing associated with the lower austenitising temperature. Both of these factors can be expected to provide for increased resistance to cleavage crack propagation since the crack would have to follow a more tortuous path.

It follows that if the degree of transformation can be made sufficiently large such that the extra contribution due to physical effects(such as texture) becomes negligible, the use of a low austenitising temperature may be advantageous as far as the low temperature toughness is concerned. Hence, for the modified alloys used in the present investigation, the impact specimens were austenitised at 880°C for 10 minutes. This procedure turned out to be justified since use of the higher austenitising temperature (1080°C) seemed to make little difference to the impact properties, presumably due to the already high level of bainitic transformation (figure IV.3). The hardness values of the final microstructures obtained following the above two austenitising treatments were not found to differ significantly, consistent with the fact that physical effects do not seem to be important when V_b is high.

(iii) Microstructural Examination and Retained Austenite Determinations

The purpose of the microstructural examination was simply to verify that classical silicon upper bainite (as defined in Ch.I) was obtained following appropriate isothermal transformation of alloys A and B. Figure IV.4 shows the microstructures obtained after transformation at 340°C and it is clear that these do belong to the class of silicon upper bainite since they only consist of bainitic ferrite and carbon enriched retained austenite.

X-ray analysis was used to determine the time periods necessary for the effective termination of transformation at 340°C, and to get an idea of the quantities of retained austenite involved. Specimens from each alloy were isothermally transformed at 340°C for various time periods before finally water quenching. These were subsequently analysed using X-ray diffraction and the results are presented in figure IV.5. From this it is clear that alloy A requires 30 mins and alloy B requires 60 minutes in order to achieve maximum transformation at 340°C.

(iv) Evaluation of Toughness

The impact curves obtained from the specimens isothermally transformed at 340°C are presented in figs. IV.3,6 for alloys A and B respectively. It is clear that a drastic improvement in toughness has been obtained in both cases, compared with the 290°C upper bainite of the 0.43C-3Mn-2.02Si alloy (Cf.fig. III.10). This improvement is very significant because of the fact that the strength has remained essentially unchanged - all the above microstructures were found to have a hardness of about 450 HV. The results are rationalised below in terms of the mechanism of the bainite transformation (Ch.I-III).

It was earlier noted (Ch.II) that two T_o curves can be generated for a given alloy since two values of H (the partial molar heat of solution of carbon in ferrite) are quoted in the published literature. Either of the T_o curves can, however, be adopted for the present purposes since the underlying trends will not be altered if the procedure used below is followed in a self-consistent manner. Hence, the more restrictive T_o curve based on the higher value of H was used to generate some of the data listed below. In fact, the agreement with the measured values of V_b for the 0.43C-3Mn-2.02Si alloy is better if the latter curve is used.

Table IV.1

Alloy	Isothermal Temp./°C	V_b	V_γ	$V_{\gamma-f}$	$V_{\gamma-B}$	$V_{\alpha'}$	x_γ
0.43C-Mn-Si	295	0.68*	0.22*	0.11	0.11	0.10	0.92
0.43C-Mn-Si	360	0.42*	0.27*	0.06	0.21	0.31	0.79
0.22C-Mn-Si	340	0.84	0.16*	0.16	-	-	0.82
0.39C-Ni-Si	340	0.74	0.18*	0.11	0.07	0.08	1.02

*Experimentally determined values. The rest of the data is calculated using fig.IV.1, eqn.III.4 and eqn.III.7.

From the above data, it is clear that variations in the carbon content of the retained austenite cannot account for the improved toughness observed in alloys A and B. However, the results are consistent with the enhancement of toughness expected when the amount of blocky austenite and martensite are reduced, and in general, when the ratio $V_{\gamma-f}/V_{\gamma-B}$ is increased (eqn.III.8).

(v) Tensile Tests

The tensile specimens used were of the standard Hounsfield No.11 design with a 3 mm diameter but a 50 mm gauge length. These were heat treated after machining, in precisely the same manner as the impact specimens of section (iv), i.e. austenitisation at 880°C for 10 mins followed by isothermal transformation (in a molten tin bath) at 340°C for either 30 mins (Alloy A) or 60 mins (Alloy B) prior to quenching to room temperature. During austenitisation, the specimens were protected with a dynamic argon atmosphere and a proprietary coating compound. The results obtained are as follows:

Table IV.2

	0.22C-Mn-Si	0.39C-Ni-Si
Ultimate Tensile Strength/MPa	1420	1610
0.2% Proof Stress/MPa	1060	1350
Reduction of area/pct.	52	56
Elongation, $5.65\sqrt{A}$/pct.	22	12

It is probable that the higher strength of the nickel based alloy is due to the presence of some martensite and blocky austenite in its microstructure (table IV.1). It was earlier noted (IV.3.iv) the hardness of both the above alloys in the given condition was found to be about 450 HV, and yet the proof stresses seem to differ considerably. It is possible that this could be due to differences in the strain hardening behaviour, although this requires further investigation. It should be noted that the above results represent an average of two tests.

The data of table IV.2 is encouraging since the high strengths obtained enable the steels to be classified as ultra-high strength steels. Additionally, the considerable ductility and high tensile strength to proof stress ratios suggest good fatigue strength (96).

(vi) X-ray Analysis of Fracture Surfaces

These experiments were aimed at detecting any austenite remaining untransformed at the exposed fracture surfaces of impact specimens. The idea was to obtain some indication of the stability of retained austenite in the vicinity of the crack

tip. X-ray diffraction experiments were conducted with the beam directed at the unmodified fracture surfaces. The use of such a technique can be justified as follows:

In experiments using diffractometers, the penetration of X-rays into the surface of iron is given by

$$G_z = 1 - \exp(-2\varsigma z/\sin\theta) \qquad \text{Equation IV.1, ref.27}$$

where

G_z = Fraction of the total diffracted information that originates from the surface layer of depth z

ς = Absorption coefficient of iron, when using CoKα radiation

θ = Bragg angle of the diffracted peak concerned, in the present case the $\{111\}$ austenite peak.

Substitution into the above equation shows that 50% of the diffracted intensity originates from a layer of depth 3μm while 95% comes from a depth of 14μm. These depths are sufficiently small to have been considerably influenced by the events at the crack tip.

Another problem which needs to be considered is whether the presence of any tetragonal martensite introduced by the decomposition of high carbon retained austenite can interefere with the $\{111\}_\gamma$ peak, since the latter was found to be the only austenite peak that could be detected with confidence. The signal to noise ratio was found to be rather poor due to the small size of the exposed fracture surfaces involved. Additionally, the expected high degree of deformation at the fracture surface must inevitably cause considerable line broadening. The combination of these factors meant that only the high structure factor $\{111\}_\gamma$ peak could be detected.

Making the reasonable assumption that the austenite has a carbon content of approx. 0.9 wt. pct., and assuming the validity of eqn.III.2 (since we are only concerned with differences in lattice parameters) allows the position of the $\{111\}_\gamma$ peak to be calculated at $2\theta = 51.1°$, using CoKα radiation.

The martensite parameters can be approximated by the following equations (97):

$$a_{\acute{\alpha}} = 2.868 - 0.0019x_\gamma \qquad \text{Equation IV.2}$$

$$c_{\acute{\alpha}} = 2.868 + 0.024x_\gamma \qquad \text{Equation IV.3}$$

so that the tetragonal $\{110\}_{\acute{\alpha}}$ peak would be expected to appear at $2\theta = 52.2°$ (the other $\{110\}$ martensite and bainitic ferrite

peaks are similarly expected at $2\theta = 52.4°$). These calculations suggested that it would be possible to distinguish the 111 peak if other factors such as line broadening did not impair the resolution.

The experiments were conducted using impact specimens (which had been fractured at different temperatures) from the 0.43C-Mn-Si and the 0.39C-Ni-Si alloys. The results are given in figure IV.7, where the truncated peak is the main bainitic ferrite peak. For both the alloys used, it appears that the 111 peak (at $2\theta = 51°$) becomes increasingly significant as the temperature at which the impact test had been conducted increases. This is not surprising since the austenite is expected to become more stable relative to deformation induced martensite transformation as the temperature increases. However, comparison of the two alloys indicates that the stability of the austenite in the nickel containing alloy extends to lower temperatures compared with the case for the manganese containing alloy. This effect cannot be attributed to the slightly higher carbon content (table VI.1) of the former since the difference is not large enough.

The results can, however, be understood when it is considered that about half the retained austenite in the as-transformed upper bainite of the manganese containing alloy is of the blocky morphology while much of the austenite of the nickel containing alloy is of the film morphology (table IV.1). The blocky austenite is relatively unstable to stress induced transformation (III.3.v). It is also likely that not all of the film austenite remains stable in the vicinity of the crack tip. Hence the diffracted intensity from the specimens tested at low temperatures will be from the surviving film austenite. If the starting quantity of film austenite is low (as in the Mn containing alloy), the diffracted intensity from the fractured specimen will be relatively low, and probably undetectable in the type of experiments discussed above.

Thus the observed effects can be attributed to the differences in the blocky to film austenite ratios for the two alloys rather than to any difference in the stability of the film type retained austenite.

(IV.4) General Conclusions

It has been demonstrated that the model (Ch.III) based on the mechanism of bainite transformations (Ch.I,II) can be successfully used in the design of strong and tough steels. It can be tentatively concluded that the possibility of exploiting the silicon bainite microstructure as a superior and viable alternative to tempered martensite based steels seems to be on firm foundations.

It should be noted that the present experiments were not intended to provide a commercially usable ultra-high strength steel, but to establish and test the predictions of the basic model which resulted from the work presented in the earlier chapters. In fact, it is considered that further improvements in toughness and strength could be readily realised by means of additional modifications, the details of which are dealt with in appendix two.

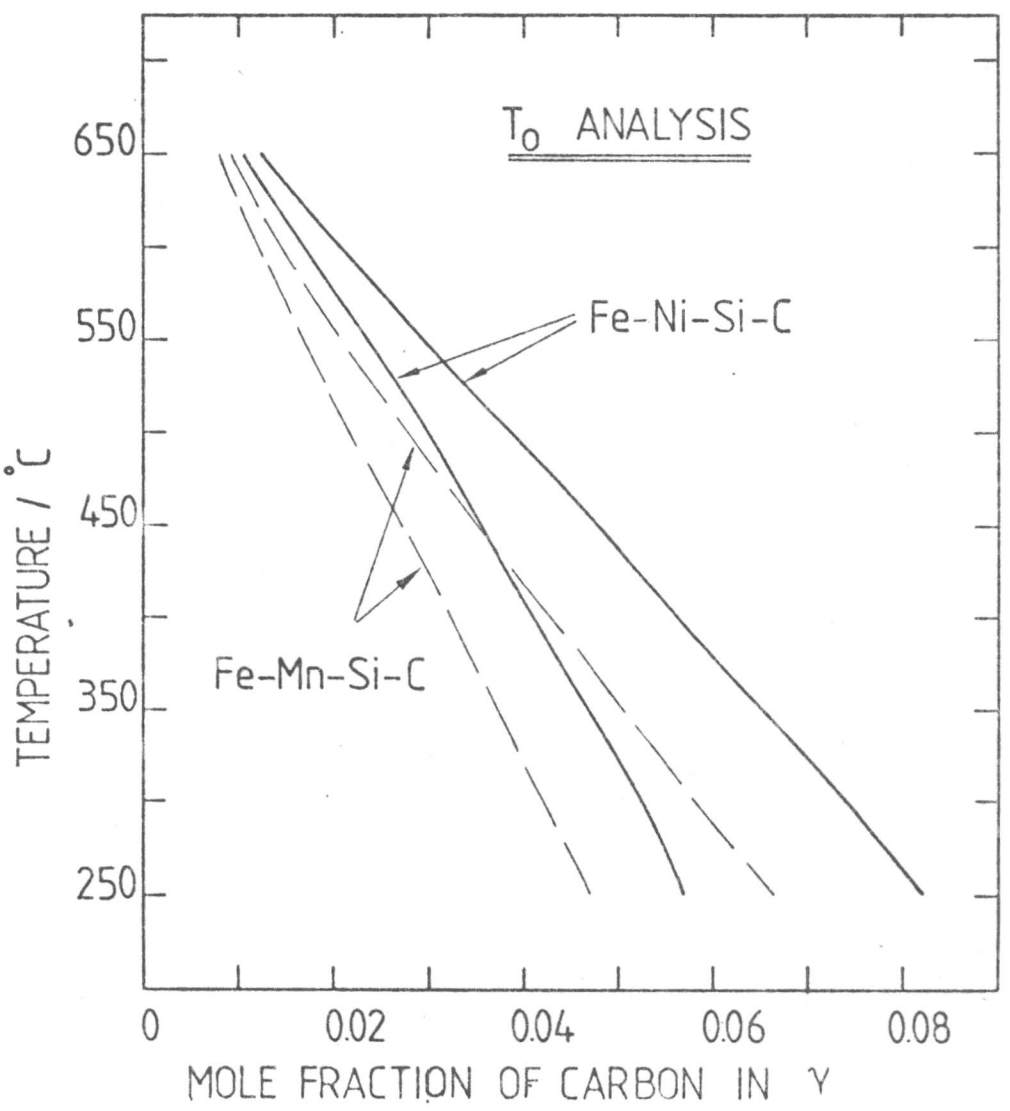

Figure IV.1

T_o curves for the Fe-3Mn-2.03Si-C and Fe-4.09Ni-2.05Si-C alloys. Two curves are plotted for each alloy since two values of the partial molar heat of solution of carbon in ferrite are available in published literature.

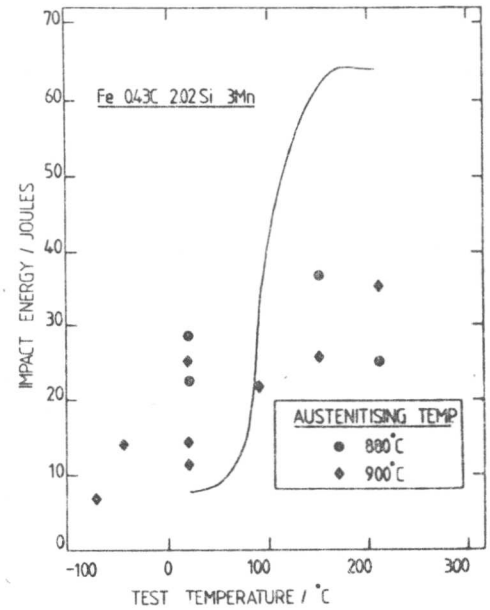

Figure IV.2

The results of impact tests on the Fe-0.43C-3Mn-2.20Si alloy following isothermal transformation at 295°C for 115 minutes. The austenitising temperatures used are as indicated in the figure. The curve represents specimens austenitised at 1080°C and is reproduced from fig.III.10. All specimens were austenitised for 10 minutes.

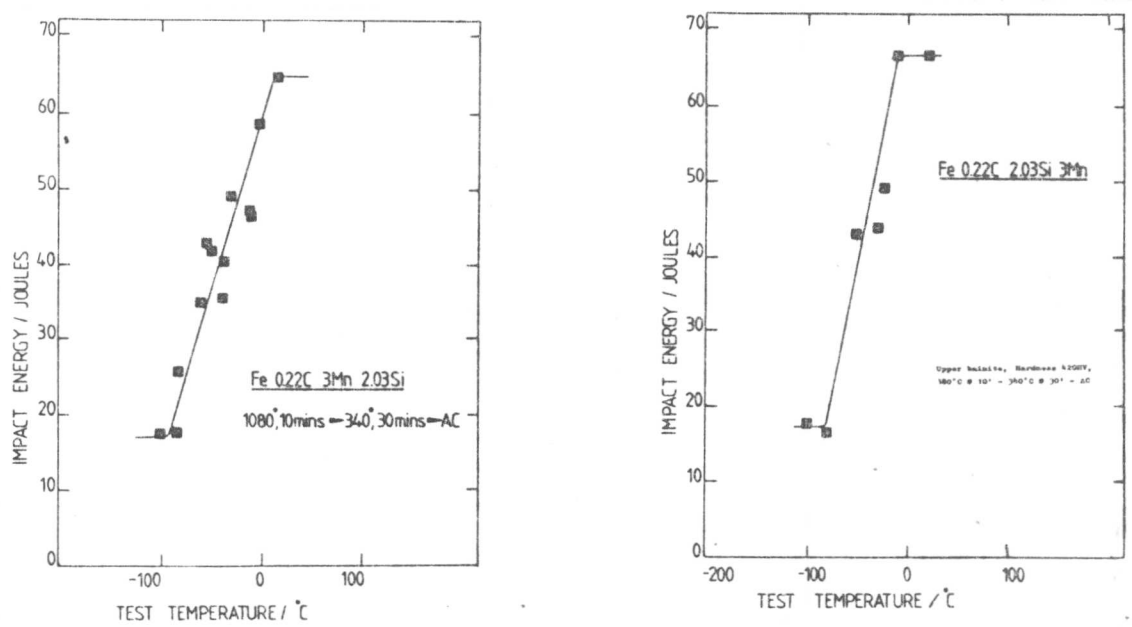

(a) (b)

Figure IV.3

Impact test results using the Fe-3Mn-2.03Si-0.22C alloy after isothermal transformation at 340°C for 30 minutes.

(a) Austenitising conditions = 1080°C for 10 minutes.

(b) Austenitising conditions = 880°C for 10 minutes.

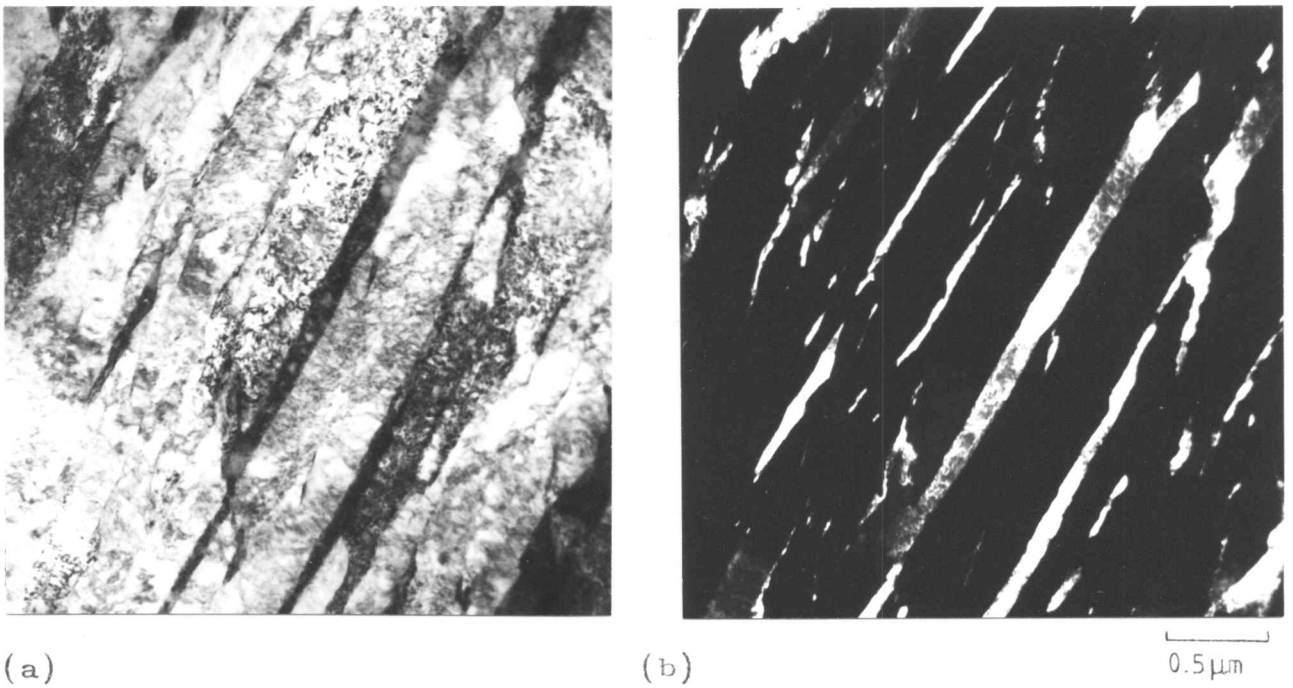

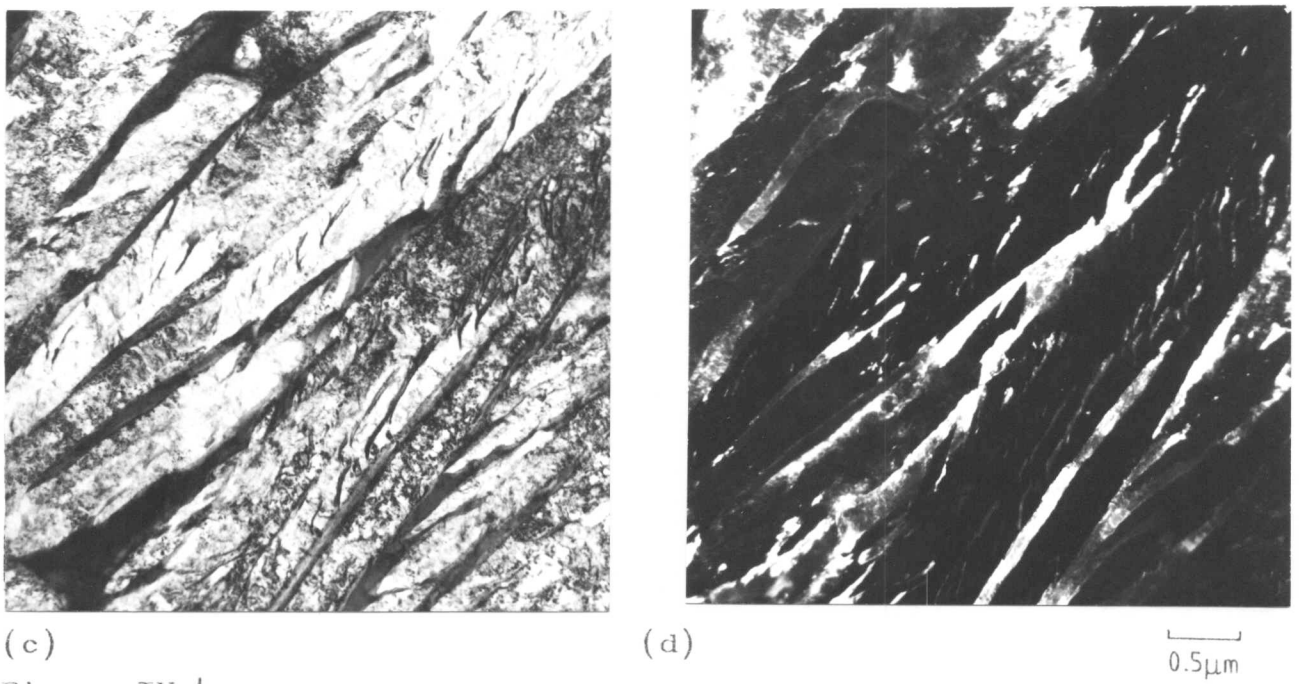

Figure IV.4

Typical upper bainitic microstructures.

(a) Fe-3Mn-2.03Si-0.22C alloy, bright field image of an isothermally transformed (340°C for 30 min.) specimen.

(b) Corresponding retained austenite dark field image.

(c) Fe-4.09Ni-2.05Si-0.39C alloy, bright field image of an isothermally transformed (340°C for 60 min.) specimen.

(d) Corresponding retained austenite dark field image.

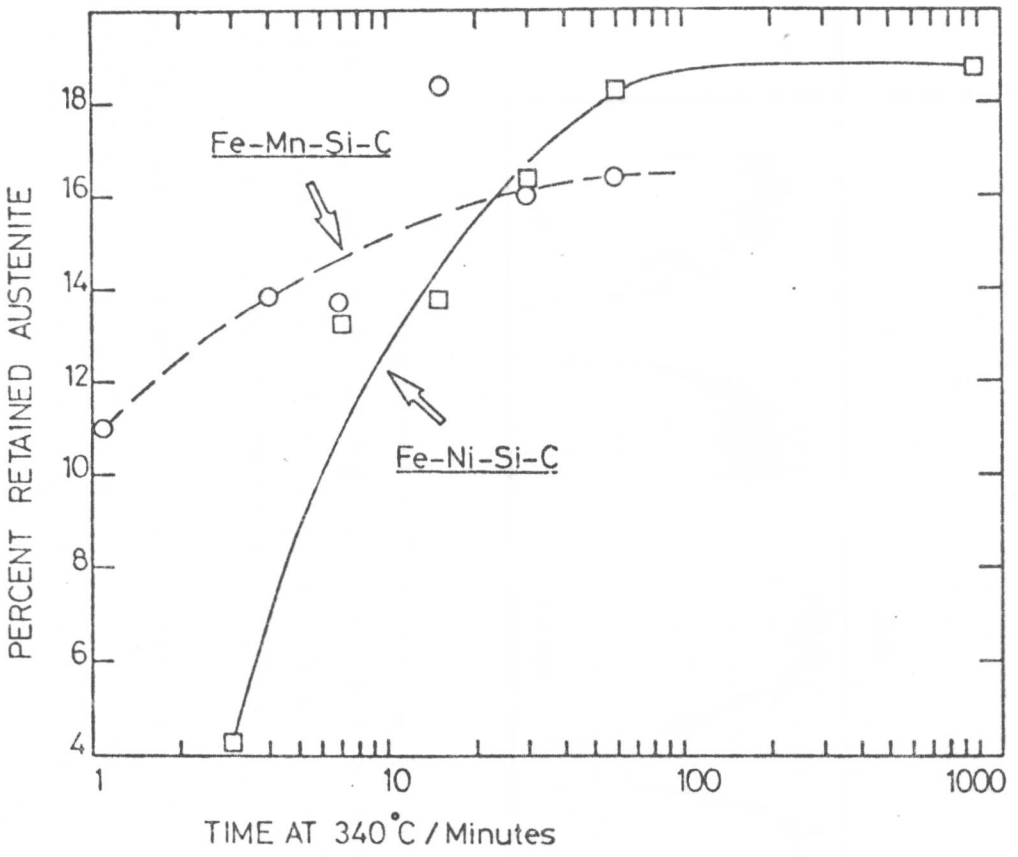

Figure ,IV.5

Plot of percent retained austenite as a function of time at the isothermal transformation temperature of 340°C.

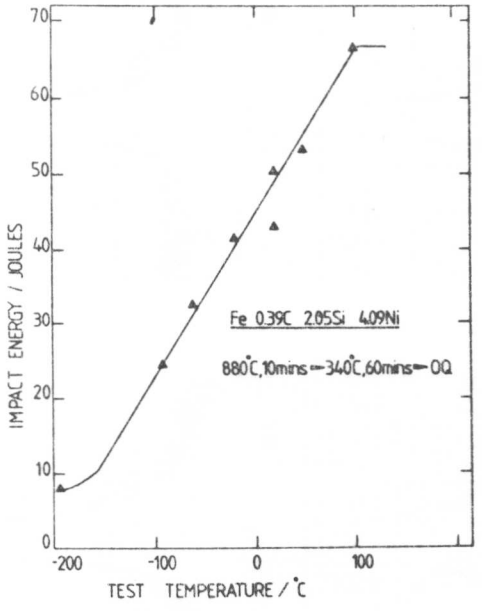

Figure IV.6

Impact transition curve for the Fe-4.09Ni-2.05Si-0.39C alloy in the isothermally transformed condition (340°C for 60 min.).

CHAPTER FIVE

TEMPERED MARTENSITE EMBRITTLEMENT: THE ROLE OF RETAINED AUSTENITE AND CEMENTITE

(V.1) Introduction

Tempered martensite embrittlement (TME) is characterised by a loss in toughness accompanying the tempering of martensitic structures at temperatures generally in the vicinity of 350°C, (91,92,98). TME is not conceptually connected to any of the more usual temper embrittlement phenomena involving impurity segregation; failure is distinctively transgranular with respect to the prior austenite grains (91,92,99,100). McMahon and Thomas (98) first correlated the thermal decomposition of interlath retained austenite (and resultant formation of interlath cementite films) with a drop in toughness upon tempering. Thomas (92) further considered that the thermal instability of interlath austenite is a fairly general cause of TME and showed that the failure to detect any interlath retained austenite in Fe-Mo-C alloys (92,101) correlated with the apparent absence of TME in these steels. Horn and Ritchie (91) have extended this idea by proposing that TME in pure steels (i.e. embrittlement not impurity controlled) is caused by the combined effect of both the thermal and mechanical instability of interlath retained austenite. Meanwhile, King et.al. (100) obtained TME in a plain carbon steel when the fracture mode was transgranular cleavage over a range of tempering temperatures and attributed TME simply to the coarsening of interlath cementite.

There is also some controversy as to the exact role of the interlath cementite in the embrittlement process. Rao and Thomas (99) consider the fracture path during TME in pure steels to be interlath along the cementite films resulting from the thermal decomposition of retained austenite; Horn and Ritchie (91) also support the possibility of interlath failure, although in both cases little metallographic evidence has been presented. On the other hand, there appears to be ample evidence for failure which is transgranular with respect to both the prior austenite grains and the martensite laths (100,102-105).

The purpose of the present study was to attempt to resolve some of the above uncertainties surrounding recent studies of TME, with the particular aim of understanding the role of retained austenite.

(V.2) Experimental Procedure

The experimental alloys used were prepared from high-purity base materials as 20 kg vacuum induction melts. The ingots were forged and hot rolled to 10 mm diameter rod followed by a hot-swage reduction to 8 mm diameter rod. The final compositions are listed below.

Table V.1

	C	Mn	Si	Mo	V	S	P
Fe-Mn-Si-C	0.43	3.00	2.02	-	-	0.002	0.002
Fe-V-C	0.25	-	-	-	1.08	0.012	0.004
Fe-4Mo-C	0.18	-	-	3.90	-	-	-
Fe-2Mo-C	0.20	-	-	2.00	-	-	-

Dash indicates not determined.

The Fe-Mo-C and Fe-V-C steels were austenitised at 1200°C for 15 min, while the Fe-Mn-Si-C alloy was austenitised at 1080°C for 10 min prior to quenching into water at ambient temperature. Austenitising and tempering treatments were carried out in tube furnaces. The specimens were protected by a proprietary coating together with a dynamic argon atmosphere.

The impact specimens were prepared and tested as in (III.2). Fractography was conducted on a Cambridge Stereoscan scanning electron microscope operated at 30 kV.

Transmission electron microscopy was carried out using a Philips EM300 microscope operated at 100 kV. Thin foils were prepared directly from discs machined from impact specimens such that the foil plane was normal to the axis of the swaged rod. Foil preparation was as in (I.2).

Retained austenite determinations were carried out on a Philips horizontal X-ray diffractometer using Co radiation and with a LiF monochromator in the diffracted beam. The X-ray lines used to determine the proportion of austenite were $\{022\}_\gamma$, $\{113\}_\gamma$, $\{112\}_\alpha$, and $\{022\}_\alpha$.

(V.3) Results and Discussion

(i) Fe-Mo-C alloys

Detailed electron microscopy and electron diffraction analysis

revealed retained austenite in both Fe-2Mo-C and Fe-4Mo-C directly quenched alloys (figures V.1,2). The austenite was found to be stable even after refrigeration at -196°C for 1 hour (figure V.3). It is estimated that the volume fraction of retained austenite is less than 0.02 since X-ray analysis failed to detect convincingly any austenite. These results disagree with those of Clark and Thomas (92,101) who did not detect any retained austenite in Fe-Mo-C alloys of similar composition. This disagreement possibly reflects the difficulties associated with the detection of films of retained austenite in thin foils of as-quenched samples. Thomas (92) has delineated several of these difficulties. However, other factors may also be involved. The fact that thin films of retained austenite are observed in a variety of high M_s temperature alloys is surprising at first sight, particularly since there is no partitioning of carbon into this austenite (106). Furthermore, the observations are in thin foils where the austenite would be expected to be even more unstable because of the removal of bulk constraints. Hence, if it is assumed that further transformation of the film austenite would involve movement of extant martensite/austenite interfaces, then a possible stability criterion could be that a major component of the martensite transformation displacement vector must lie in the foil plane such that a significant constraint effect is still experienced by the austenite.

Hence, the foil orientation with respect to the displacement direction concerned may be of importance. The influence of bulk crystallographic texture may then also be of relevance to the stability of the austenite, not only in bulk specimens , but also in thin foils. This would be consistent with the texture effect observed in (I.3). It is therefore possible that such variations might account for the detection differences between the specimens examined in the present work (from 8 mm swaged rod) and in that of Clark and Thomas (from 13 mm rolled plate).

Using the Fe-4Mo-C alloy, impact tests were carried out over a range of testing temperatures (figure V.4) and it was found that there was an almost monotonic decrease in toughness relative to the as-quenched specimens with increasing tempering temperature. This is despite the continuous decrease in hardness with increasing tempering temperature (figure V.5). It is therefore clear that an embrittling mechanism is operating even though a well defined TME trough is not obvious.

Transmission electron microscopy revealed considerable intralath cementite precipitation in the specimen tempered at 190°C (figure V.6a). The lath boundaries did not reveal any cementite precipitation although retained austenite could be detected readily (figure V.6b,c). Consequently, as the toughness was reduced by this tempering treatment it can only be concluded that in this alloy it is the intralath cementite that is responsible for the embrittling effect.

Raising the tempering temperature to 295°C led to the decomposition of the interlath retained austenite to give cementite films. However, the cementite films appeared to be discontinuous (figure V.7), which is not surprising in view of the fact that they arise from austenite films only a few hundred angstroms thick. The cementite probably nucleates at several positions of the austenite/martensite interface (as in the decomposition of upper bainitic retained austenite - Ch.I) so that the final decomposition product is small discrete cementite particles at the interlath boundary. Figure V.7 also shows that the interlath cementite adopts an orientation relationship with the martensite matrix which is equivalent to one of the intralath cementite variants. This is consistent with the formation of cementite in contact with both martensite and austenite at the interface, such that the orientation variant which is favoured is the one with low energy orientations with respect to both austenite and martensite.

Hence, during the earlier stages of tempering when retained austenite has not yet decomposed to interlath cementite, TME is clearly controlled by intralath cementite. Even at 295°C, the initial interlath cementite resulting from the thermal decomposition of retained austenite (i.e. prior to the onset of significant coarsening) is less coarse relative to intralath carbides. At a tempering temperature of 420°C, coarsening of interlath cementite was observed (figure V.8) and it is possible that this could then exercise control of TME. The overall tempering behaviour is therefore consistent with the wide TME trough found. Indeed, even the as-quenched martensite may not be at optimum toughness due to slight autotempering.

Of the specimens tested at -76°C, scanning electron microscopy revealed that only the as-quenched specimen had any ductile component of failure, while all specimens tested at -106°C exhibited cleavage fracture (figure V.9). Despite this fact,

embrittlement (relative to the as-quenched specimen) is still observed and this is consistent with a cementite coarsening mechanism for TME (100). The fact that there is no rise in impact energy at -106°C at the highest tempering temperatures is probably an indication of the possible insensitivity of the cleavage strength to the plastic yield strength, indicating that little localized plastic deformation must be occurring in association with cleavage in this alloy.

Optical examination of a nickel-plated fracture surface of a specimen in the most brittle condition revealed that the main cleavage fracture path (and that of internal secondary cracks) was, in general, translath (figure V.10). The internal cracks examined were near the fracture surface and approximately parallel to the main fracture path. The benefit of examining secondary cracks, as well as the main crack, is that the microstructure on both sides of the crack can be observed. These observations indicate the crack nucleation role of cementite rather than the provision of an easy fracture path.

At first sight, the present embrittlement results contradict those of Clark and Thomas, (92,101), who claim an absence of any TME effect (or retained austenite) in Fe-Mo-C steels. However, closer examination of the toughness results for their alloy designated C-198 (Fe-0.18C-0.38Mn-0.15Si-3.85Mo, Ref.101) shows that specimens tempered at 400°C have a lower toughness than as-quenched specimens, despite their lower yield stress.

(ii) Fe-1.08V-0.25C alloy

Tests similar to those on the Fe-Mo-C alloy were carried out on the Fe-V-C alloy which is known to exhibit interlath films of retained austenite (107), figures V.11a,b. Figures V.11c,d illustrate the results obtained. It is clear that the TME trough in this steel is well defined as compared to the Fe-Mo-C steel, although it is noted that the test temperature ranges are different, owing to the differing impact transition temperatures. The Fe-V-C alloy contains about 5pct. interlath retained austenite, as indicated by X-ray analysis. Upon tempering the quenched structure at 290°C transmission electron microscopy showed that the austenite had decomposed into laths of cementite at the martensite boundaries (figures V.12a,b). At 350°C, well within the TME trough, limited coarsening of the interlath cementite was detectable (figure V.12c). Despite the fact that

the retained austenite had decomposed completely at 290°C, the impact curves show that this treatment does not fully embrittle the steel; the embrittlement is more complete after tempering at 350°C. Since the interlath cementite is coarser than the intralath cementite in this steel (presumably because of the relatively large amount of retained austenite) it is concluded that it is the coarsening of interlath cementite that is responsible for TME rather than the decomposition of the retained austenite itself.

While the fracture mode (at room temperature) was mainly quasi-cleavage following the 350°C tempering, the as-quenched and 420°C tempered specimens showed large amounts of dimpled rupture as well (figures V.12d-f). Furthermore, in this alloy where interlath cementite controls TME, the nickel-plated fracture surface of the specimen in the most brittle condition revealed translath failure (figure V.12g), indicating once again the crack nucleation role of cementite rather than the provision of any easy fracture path. It should be noted that the mechanical instability of retained austenite has no role in either of the above steels examined since not only is embrittlement present in the absence of retained austenite (following tempering) but the embrittled toughness values fall below those of the as-quenched specimens.

(iii) Fe-0.43C-3.0Mn-2.02Si

The low M_s temperature (dilatometrically measured to be 220°C) and the high silicon content of the Fe-Mn-Si-C steel give carbide-free supersaturated martensite when directly quenched from the austenitised condition (Ch.I). The tempering of this martensite is easy to follow, partly because of the effect of silicon in retarding cementite precipitation. Tempering results predominantly in a fine dispersion of intralath carbides. Additionally, almost no retained austenite was detectable in the as-quenched condition, either by X-ray diffraction or by transmission electron microscopy. This is despite the fact that several different foil orientations (with respect to the hot working direction) were examined by machining discs from hot-rolled or hot-swaged specimens.

The results of impact tests on this alloy in the as-quenched and tempered condition are illustrated in figure V.13. Curve A represents the as-quenched martensite. The specimens of curve B contain martensite with ε-carbide positively identified by electron

diffraction (figure V.14) following tempering at 245°C for 15 min. Comparison with as-quenched martensite shows that there is a small but significant decrease in toughness of the tempered martensite in the region of ductile failure (upper shelf). This effect is also reflected in the fall-off of the as-quenched transition curve at the highest testing temperatures since tempering of the specimen occurs during impact testing. This toughness loss, despite the reduced hardness of the tempered martensite, is probably caused by an increased capacity for void nucleation in the specimens containing ε-carbide. After tempering at 355°C for 4 hours, the ε-carbide was replaced by cementite (figure V.15) but this in itself has clearly caused no TME. Further tempering led to complete precipitation of cementite with the concurrent elimination of ε-carbide. The cementite dispersion is noticeably refined by the silicon addition. The results show that there is no characteristic TME in this steel of a form similar to that in Fe-Mo-C or Fe-V-C alloys. This is entirely consistent with the absence of any coarse cementite or interlath retained austenite (with its attendant decomposition product of interlath cementite).

(V.4) General Summary

By the critical examination of a selected series of steels it proved possible to characterize the TME phenomenon in terms of the detailed microstructural changes accompanying tempering, and in particular, to distinguish between the various controlling factors in different steels.

In the Fe-Mo-C steels less than 2% retained austenite was detected together with an extensive embrittlement effect relative to the as-quenched specimens. It was, however, found that the coarser intralath cementite exercised the controlling influence on TME, and not the retained austenite or its subsequent decomposition product, i.e. a finer dispersion of interlath cementite.

The Fe-V-C steel contained substantially more retained austenite (about 5%) and in this case the TME could be attributed to the coarsening of interlath cementite formed during decomposition of this austenite. With this embrittlement mechanism the TME trough was well defined. Failure in both of these cases was found to be translath and this is consistent with the crack nucleation role of cementite in TME.

In the Fe-Mn-Si-C steel where the almost complete absence of retained austenite gave a structure containing only intralath carbides (which were extremely fine because of the high silicon level) no TME was detected and this is consistent with a TME mechanism based on the coarsening of cementite. Furthermore, no embrittlement could be attributed per se to the transition from ε-carbide to cementite.

With regard to the influence of silicon on carbide precipitation it would be of interest to modify the Fe-Mo-C and Fe-V-C steels with silicon in order to enhance tempering resistance.

The extent of the TME effect with respect to tempering temperature is important since there are conflicting requirements of a low tempering temperature (consistent with high strength requirements) and the need to be beyond the TME trough. While ideally TME should be eliminated, another approach might involve modifications such that the TME trough would be extremely narrow and well defined. In this respect, the interlath dependence of TME is more desirable, as in the Fe-V-C steel.

0.3 μm

(a)

(b)

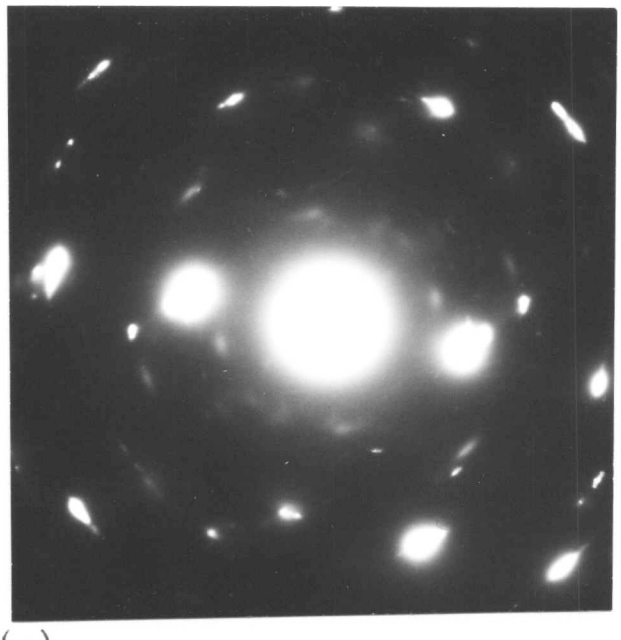

(c)

Figure V.1

Transmission electron micrographs of austenitised and quenched Fe-2Mo-C alloy.

(a) Bright field image.

(b) Retained austenite dark field image.

(c) Corresponding electron diffraction pattern.

(d) Interpretation of (c).

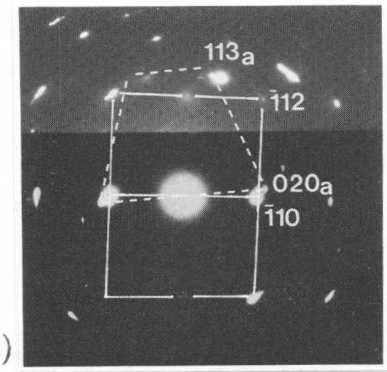

(d)

(a)

1μm

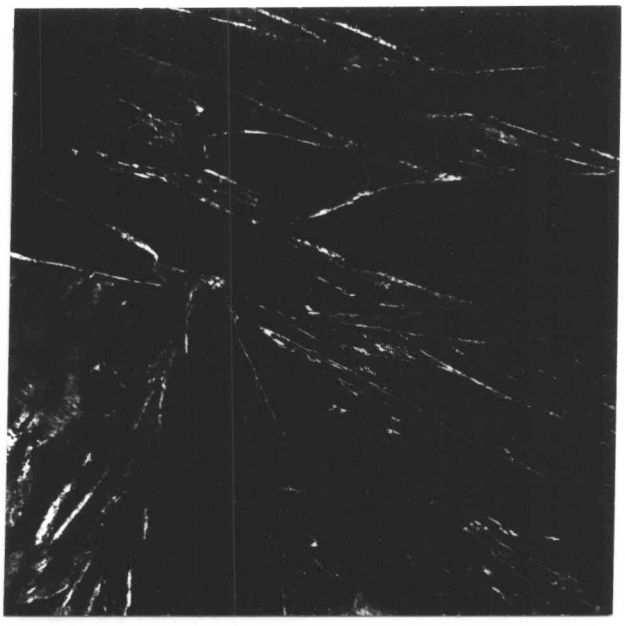

(b)

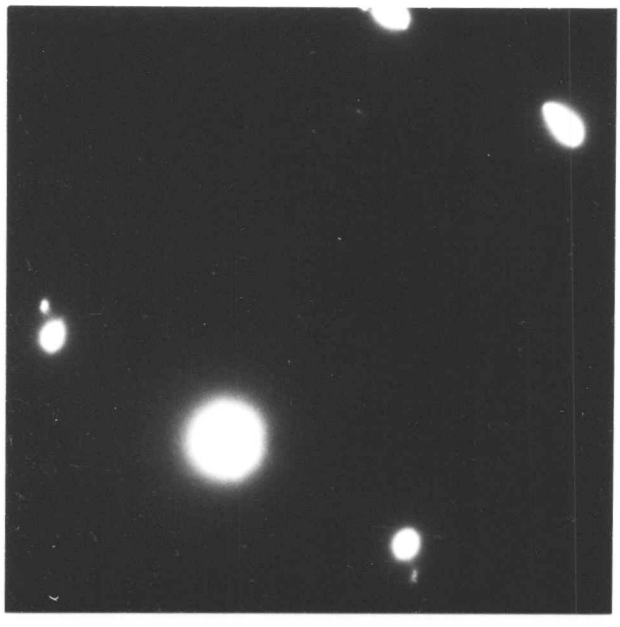

(c)

Figure V.2

Transmission electron micrographs of austenitised and quenched Fe-4Mo-0.2C alloy.

(a) Bright field image.

(b) Retained austenite dark field image.

(c) Corresponding diffraction pattern.

(d) Interpretation of (c).

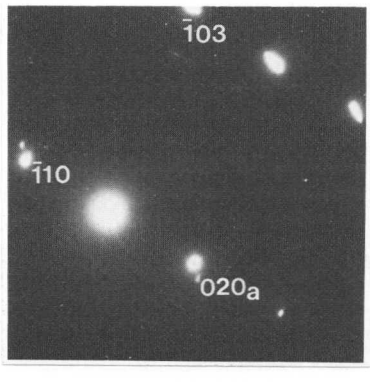

(d)

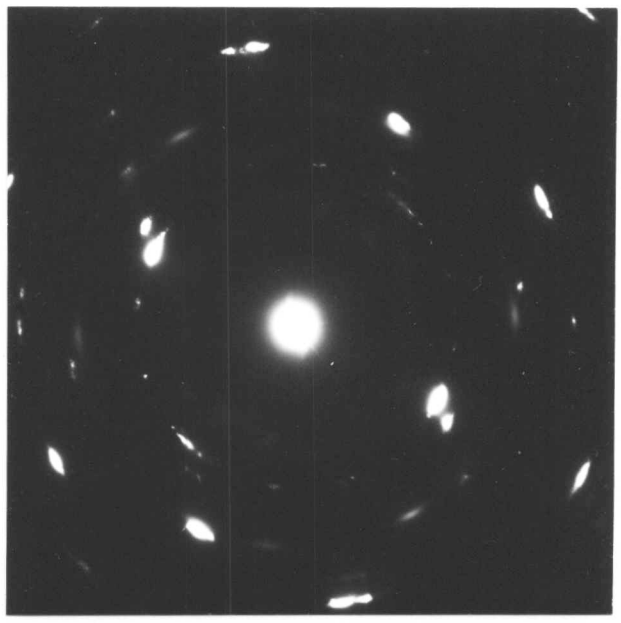

0.3 μm

(a) (b)

Figure V.3

Austenitised and quenched Fe-4Mo-0.2C alloy, following refrigeration at -196°C for 1 hour.

(a) Retained austenite dark field image.

(b) Corresponding diffraction pattern.

(c) Interpretation of (b).

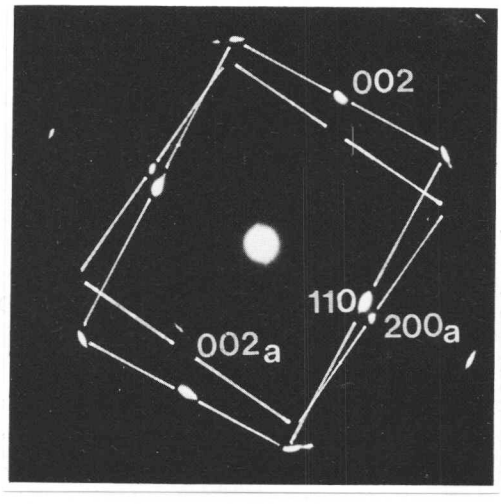

(c)

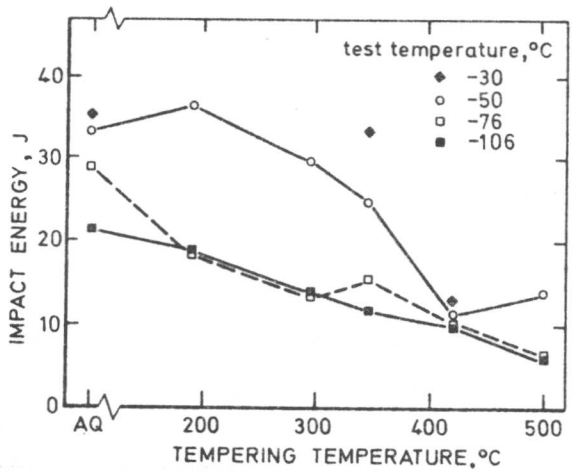

Figure V.4
Results of impact tests on Fe-4Mo-0.2C alloy.

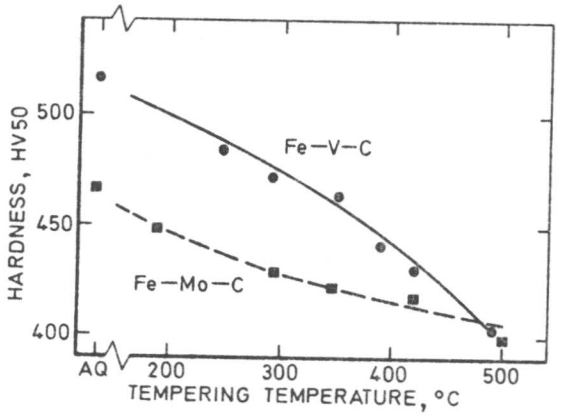

Figure V.5
Variation of hardness with tempering temperature for the Fe-4Mo-0.2C and Fe-1V-0.2C alloys.

(a)

0.5μm

(b)

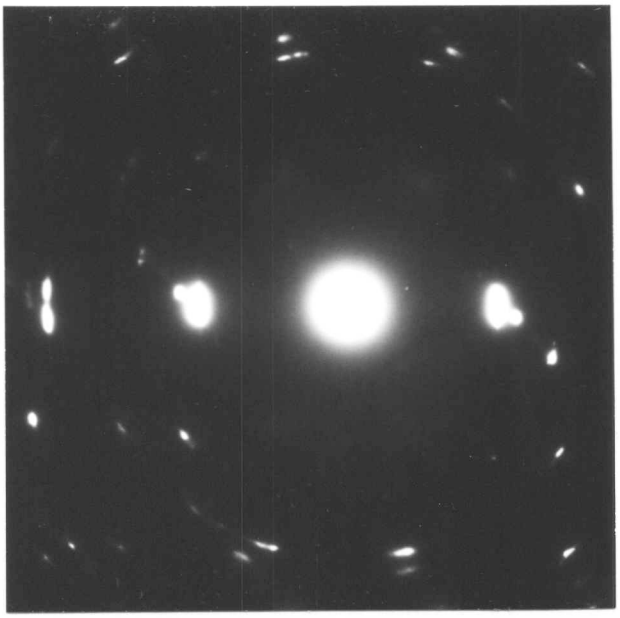

(c)

Figure V.6

Transmission electron micrographs of Fe-4Mo-0.2C alloy after quenching and tempering at 190°C for 1 hour.

(a) Bright field image.

(b) Retained austenite dark field image.

(c) Corresponding diffraction pattern.

(d) Interpretation of (c).

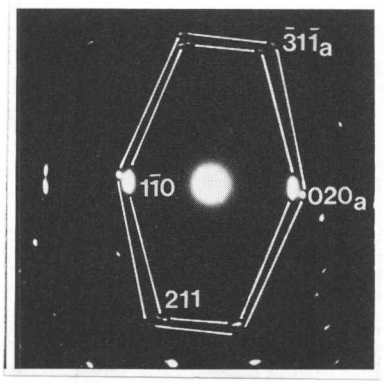

(d)

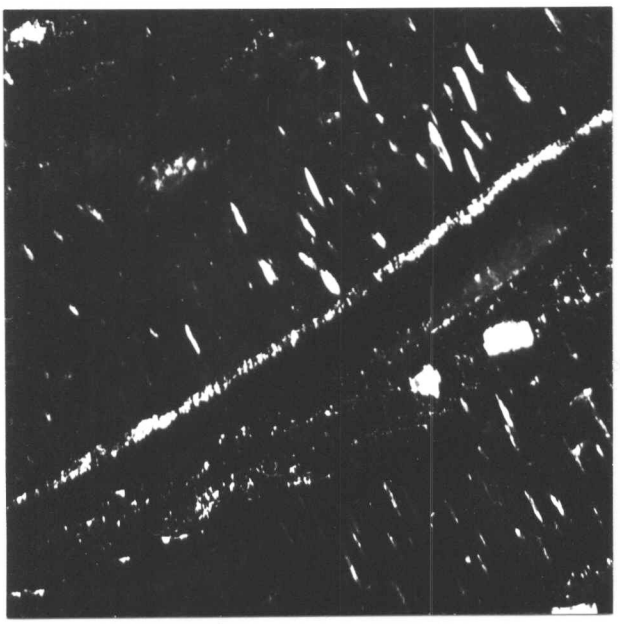

Figure V.7
Cementite dark field image using $(103)_\theta$ reflection from Fe-4Mo-0.2C alloy after quenching and tempering at 295°C for 1 hour.

0.3μm

Figure V.8
Transmission electron images of quenched Fe-4Mo-0.2C alloy after tempering at 420°C for 1 hour.

(a) Bright field image.

0.5μm

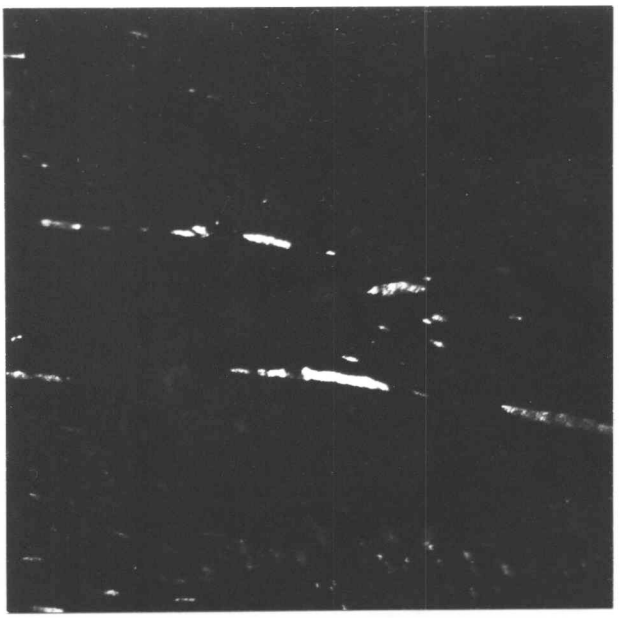

(b) Cementite dark field image using $(113)_\theta$ reflection.

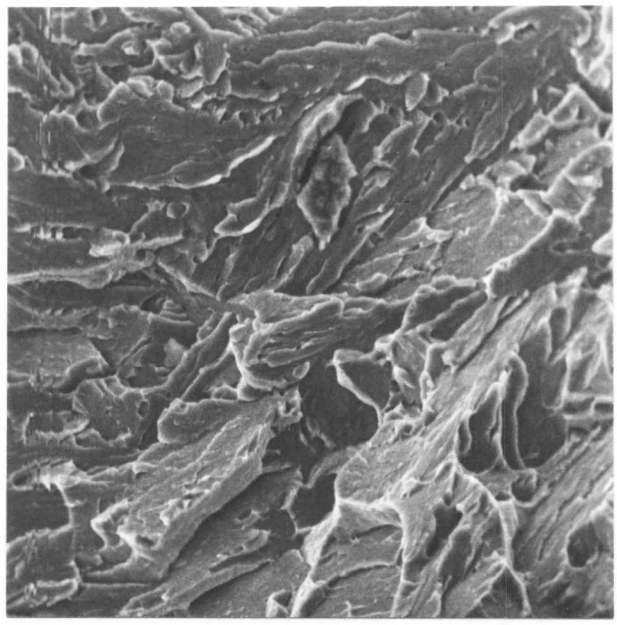

(a)

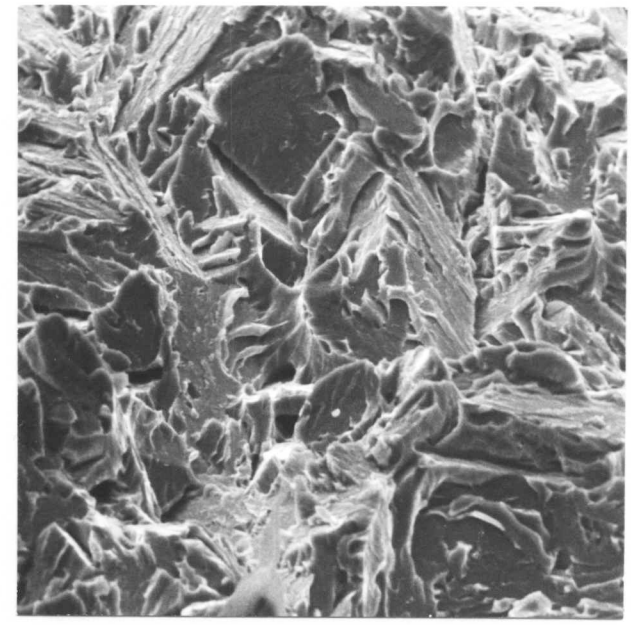

(b)

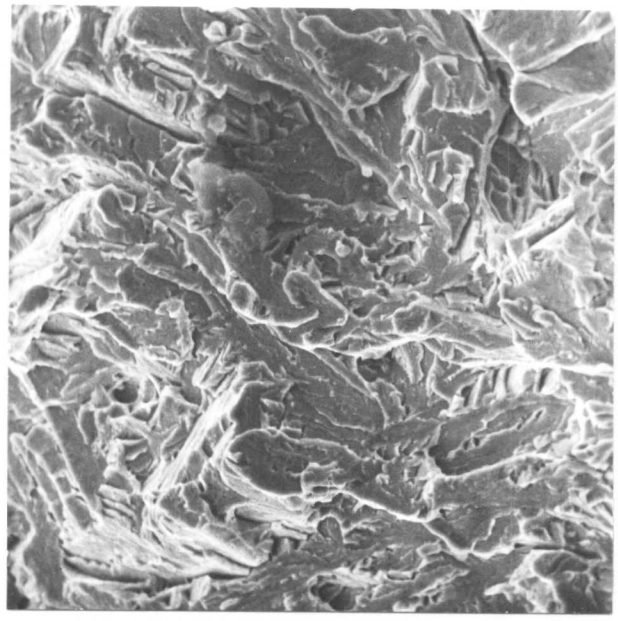

(c)

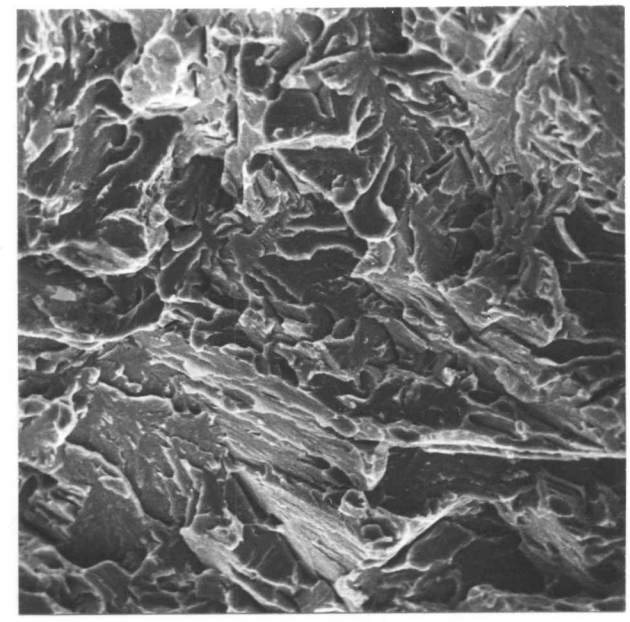

(d)

Figure V.9

Typical fractographs showing cleavage fracture following impact tests at -106°C in Fe-4Mo-0.2C alloy.

(a) As-quenched.

(b) Quenched and tempered at 190°C for 1 hour.

(c) Quenched and tempered at 295°C for 1 hour.

(d) Quenched and tempered at 420°C for 1 hour.

20μm

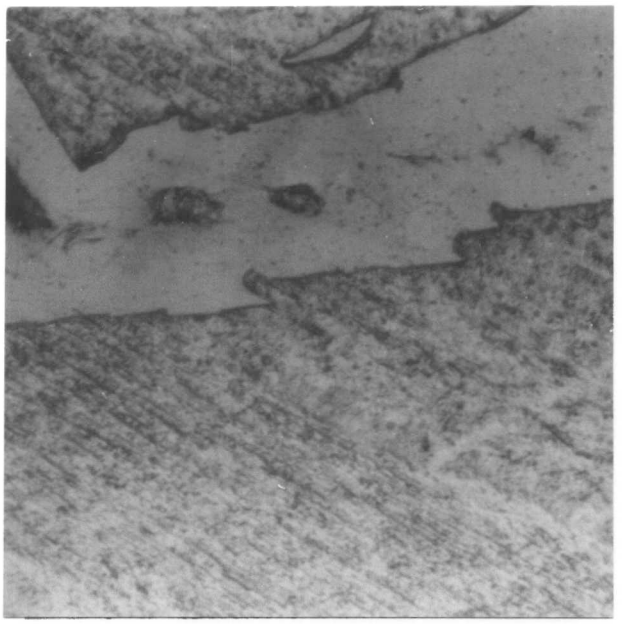

10μm

(a)

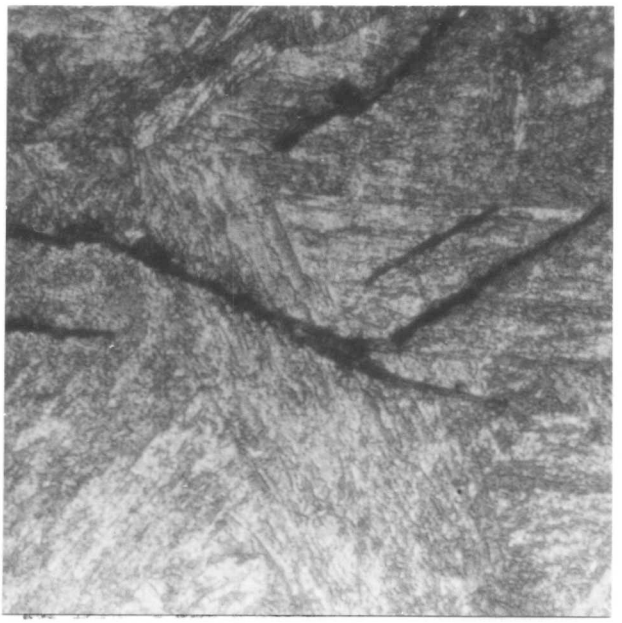

20μm

(b)

Figure V.10

Fe-4Mo-0.2C alloy quenched and tempered at 420°C followed by impact fracture at -106°C.

(a) Optical micrograph of nickel-plated fracture surface.

(b) Optical micrograph of internal secondary cracks.

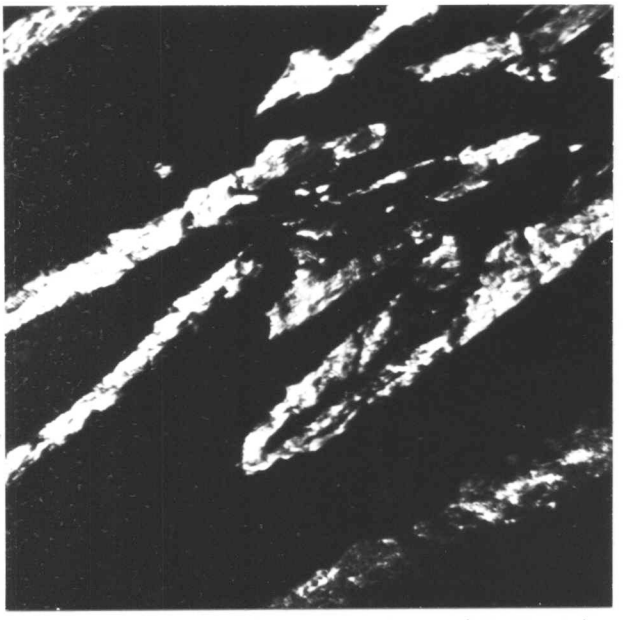

0.2μm

(a)

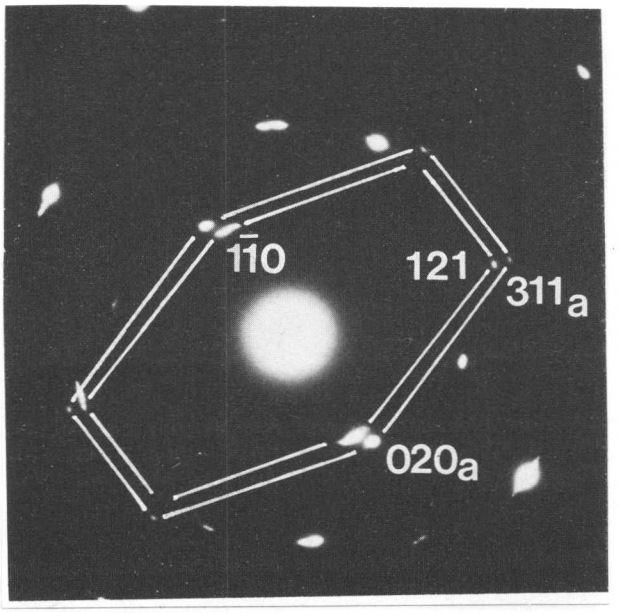

(b)

Figure V.11

(a) Retained austenite dark field image from Fe-1V-0.2C steel in the directly quenched condition.

(b) Corresponding diffraction pattern.

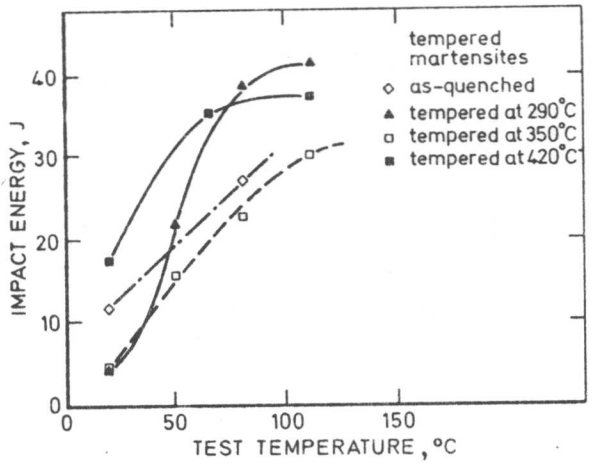

Figure V.11c

Results of impact tests on Fe-1V-0.2C steel.

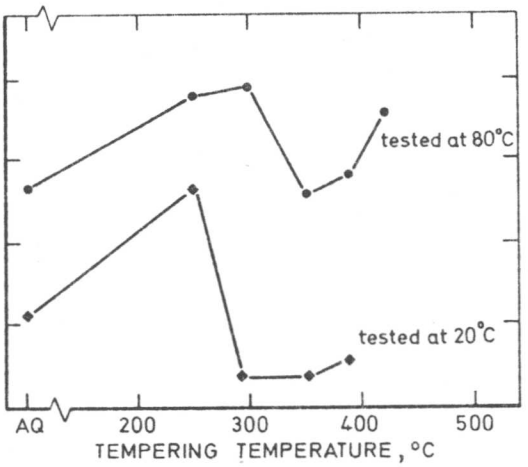

Figure V.11d

Further results of impact tests on Fe-1V-0.2C steel.

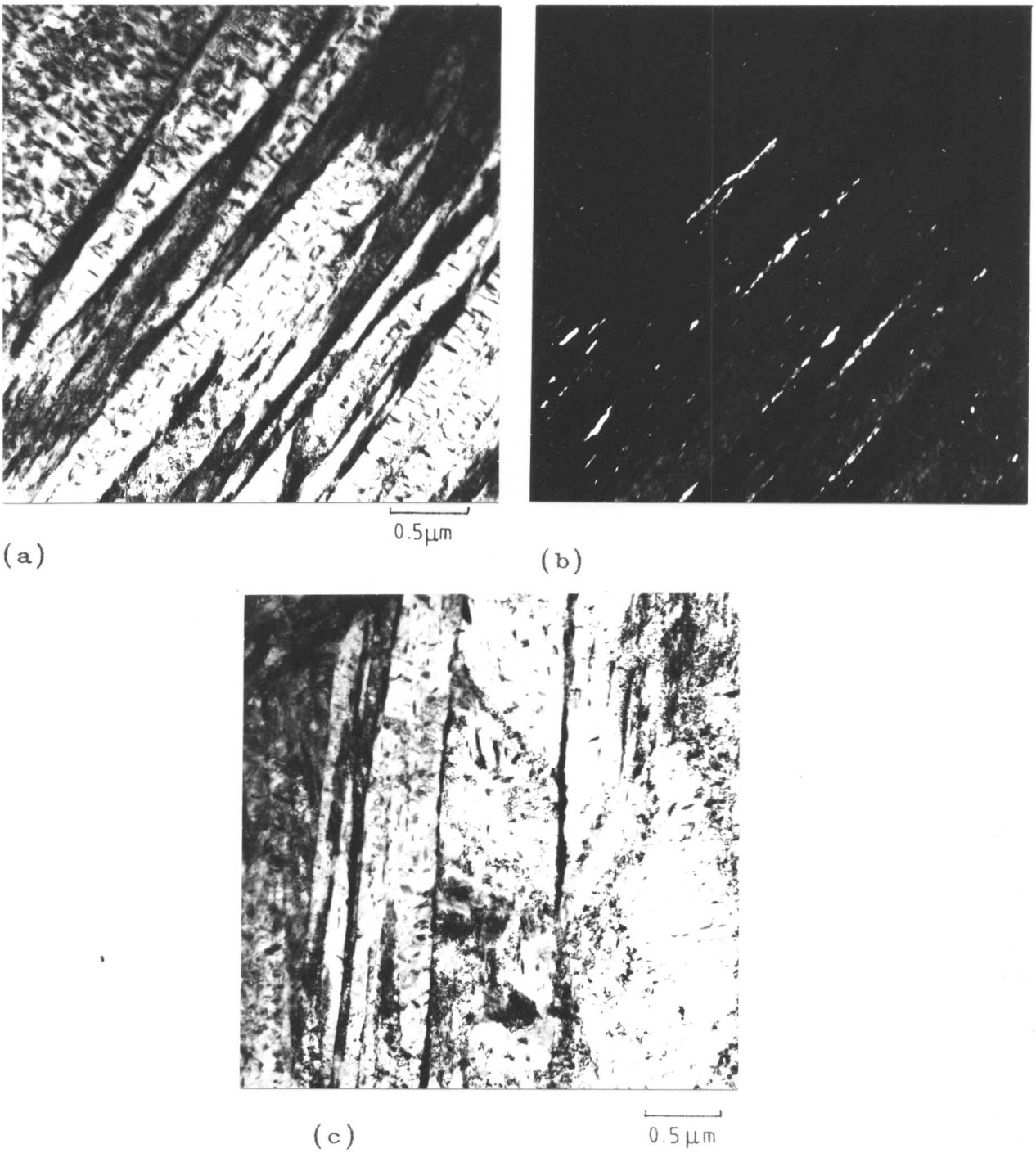

Figure V.12

(a) Fe-1V-0.2C alloy, quenched and tempered at 290°C for 1 hr. Bright field image.

(b) Corresponding cementite dark field image.

(c) Fe-1V-0.2C alloy, quenched and tempered at 350°C for 1 hr. Bright field image.

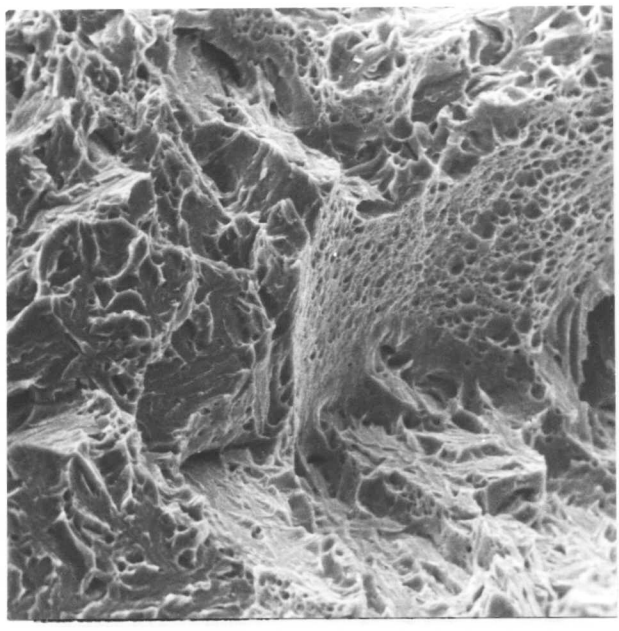

(d)

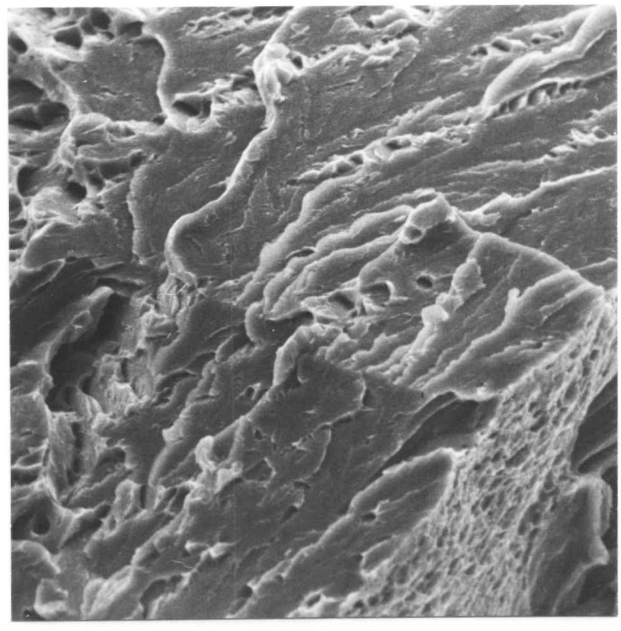

(e)

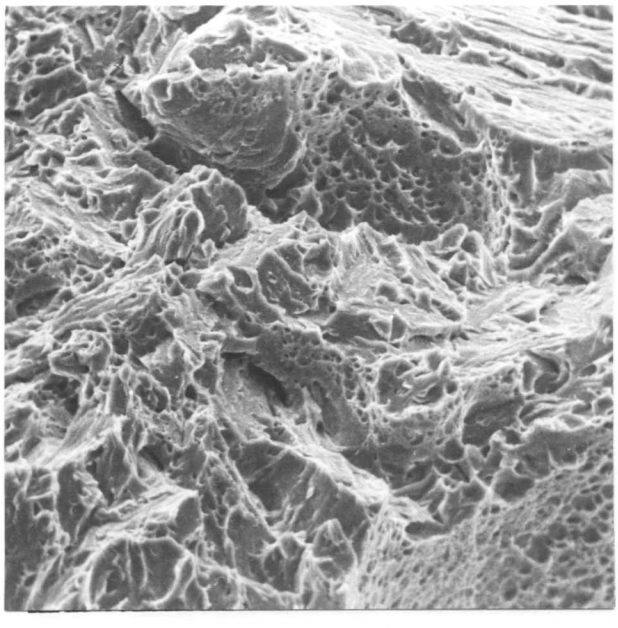

(f)

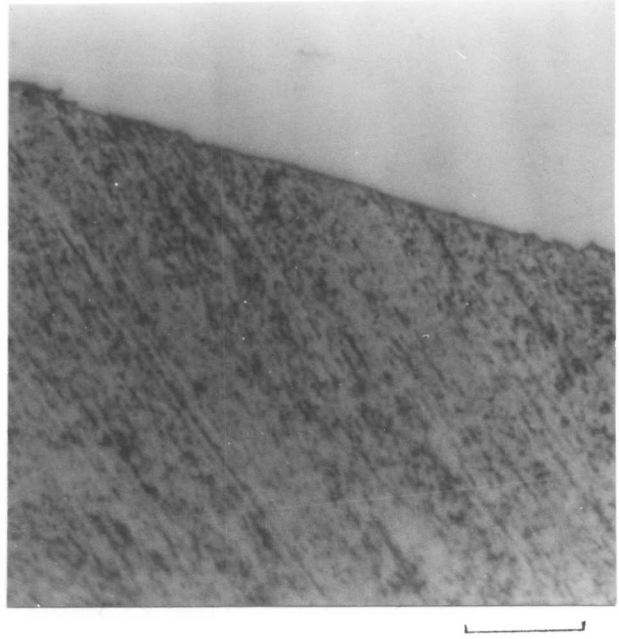

(g)

Figure V.12

(d)-(f) Fractographs of room temperature impact failures:
(d) direct quench, (e) quenched and tempered at 350°C for 1 hr.,
(f) quenched and tempered at 420°C for 1 hr.
(g) Optical micrograph of nickel-plated fracture surface from specimen quenched and tempered at 350°C for 1 hr. followed by impact failure at room temperature.

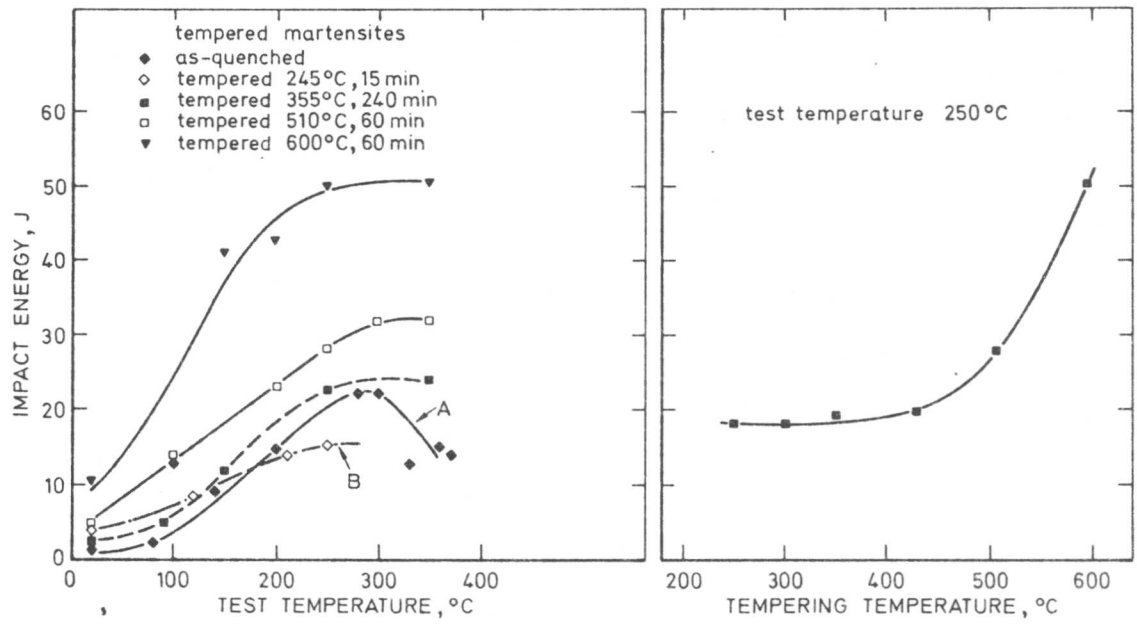

Figure V.13

Results of impact tests on Fe-Mn-Si-C alloy.

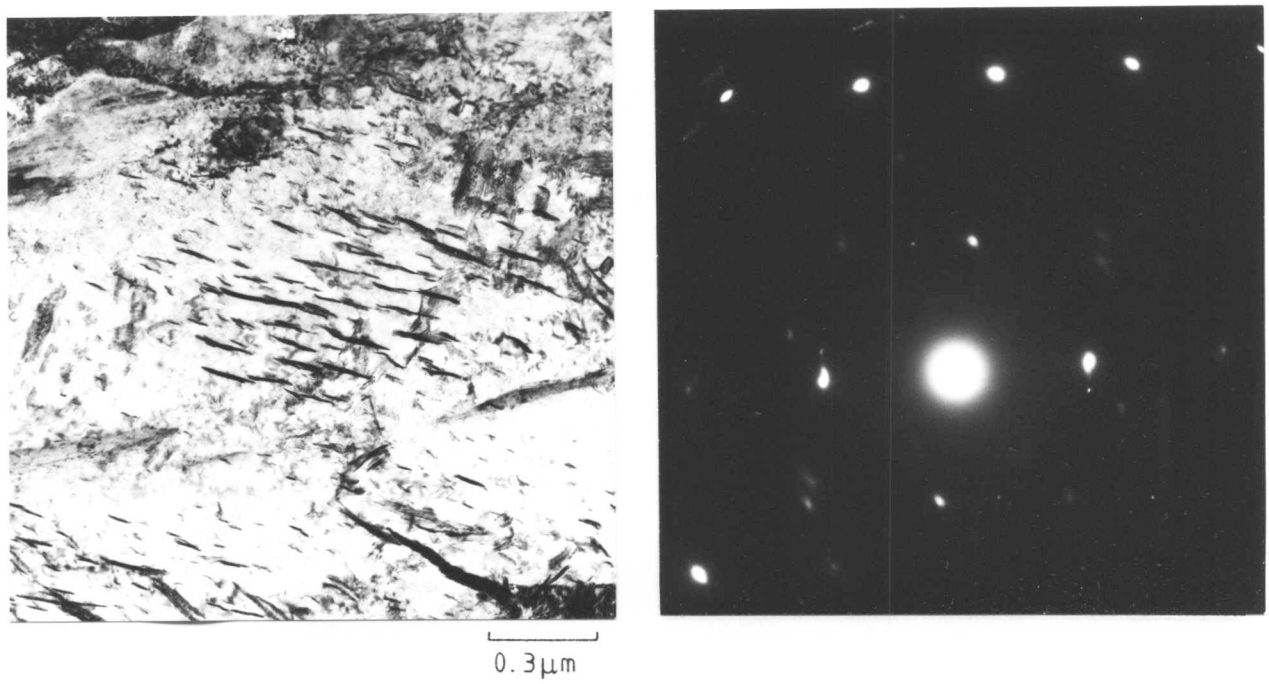

(a) (b)

Figure V.14

(a) Transmission electron micrograph of quenched Fe-Mn-Si-C alloy after tempering at 245°C for 15 min.

(b) Corresponding diffraction pattern.

(c) Interpretation of (b).

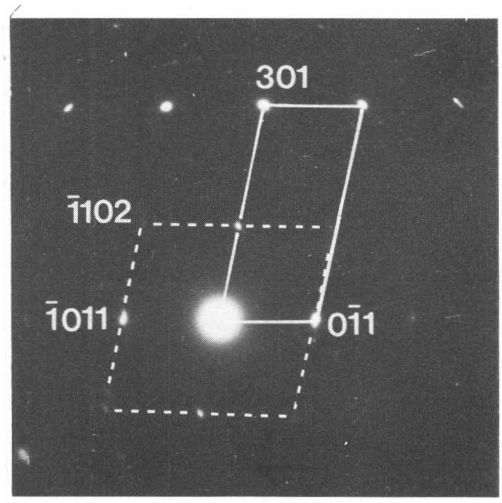

(c)

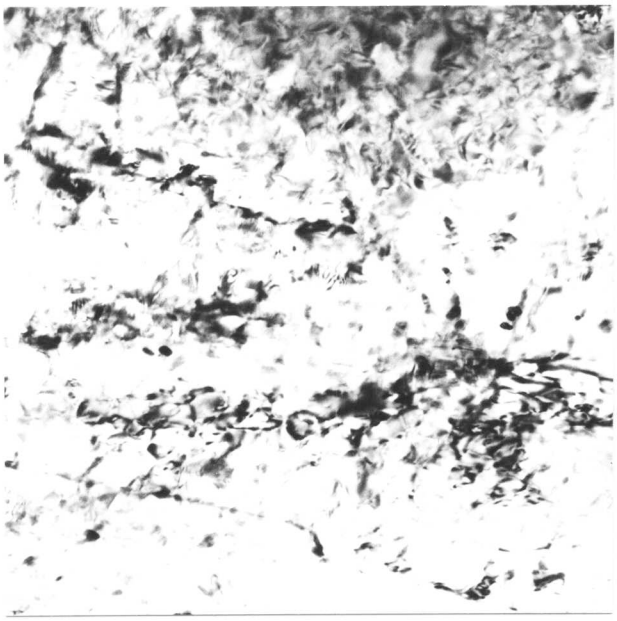

(a)

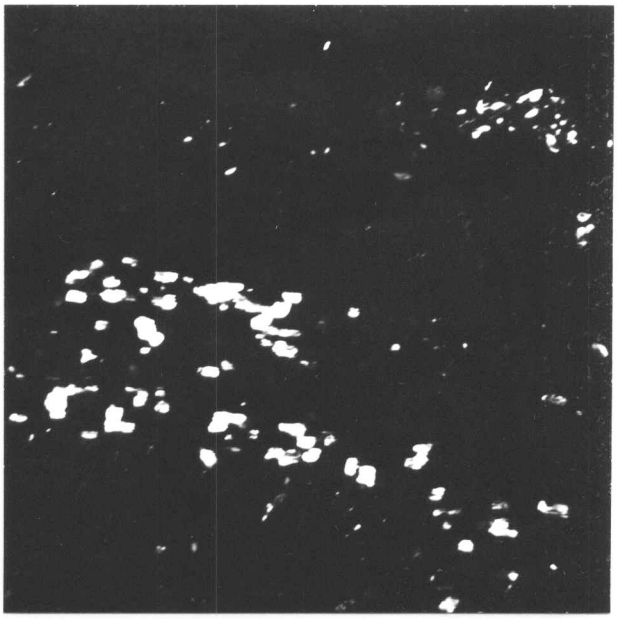

(b)

0,2µm

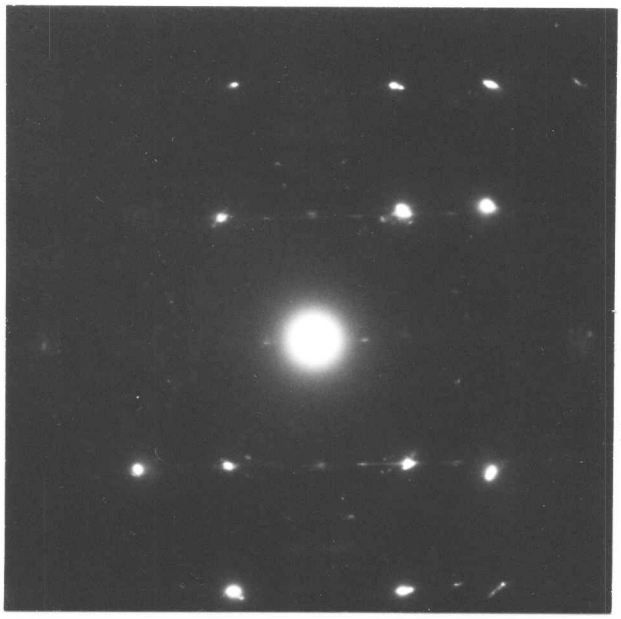

(c)

Figure V.15

(a) Transmission electron micrograph of quenched Fe-Mn-Si-C alloy after tempering at 355°C for 4 hours.

(b) Corresponding cementite dark field image.

(c) Corresponding diffraction pattern.

(d) Interpretation of (c), showing cementite (small figures) simultaneously in Bagaryatski orientation with adjacent twin-related martensite variants.

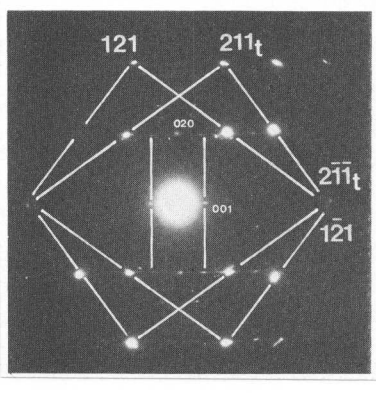

(d)

CHAPTER SIX

THE CORRELATION OF CRYSTALLOGRAPHY WITH THE RETENTION OF AUSTENITE IN LOW-ALLOY STEELS

(VI.1) Introduction

The most obvious feature of a martensite transformation is the change in shape, or shape deformation, which reveals itself in the form of a well defined surface distortion when a pre-polished crystal of austenite is allowed to transform to martensite. This macroscopically homogeneous shear strain will induce a large shear stress in the surrounding austenite; there will also be hydrostatic stresses due to the volume expansion or contraction accompanying the change in crystal structure during the martensite transformation.

In addition to the elements that characterise the shape deformation, a habit plane which is the interface plane between the austenite and martensite can also be identified. The induced shear stress in the austenite can be resolved with respect to further potential martensite habit plane variants, enabling the prediction of the most likely martensite plates which can form by optimum coupling with the induced stress system. In this respect, the operative stress system surrounding a martensite plate can be assumed to be disc shaped (108) so that those plates which form with their respective habit plane variants as parallel to each other as the crystallography concerned will allow, while at the same time minimising the total shape deformation involved, will have optimum coupling between their stress fields, thus resulting in a minimisation of strain energy. The autocatalytic burst phenomenon in certain martensite transformations is essentially a manifestation of such coupling.

The role of strain energy in the martensite transformation is clearly critical - indeed, the various features of the transformation can be predicted on a self consistent basis by the principle of strain energy minimisation (57,109). This is also reflected in the general application of the Bain correspondence in the phenomenological theory of martensite. This correspondence is by no means a unique correspondence between the austenite and martensite lattices but appears to be the one involving the minimum displacement of atoms during the transformation. In physical terms the role of strain energy is easy to understand when it is realised that the extent of

the shape deformation strain can be orders of magnitude greater than the local strain arising due to the residual stresses at a dislocation pile-up (108).

It should be noted that if the induced stresses in the austenite reach a magnitude greater than the local flow stress, plastic relaxation must follow. Indeed, it has been shown that the agreement with theory is optimum when account is taken of both the elastic and plastic components of strain (57).

It is clear that the ease of formation of martensite and conversely, the difficulty of retaining austenite will depend to some extent on the strain situations involved. The latter is a function of the martensite crystallography, and it was with this in mind that the present work was undertaken.

(VI.2) Theoretical Considerations

The prevalent orientation relationships describing the austenite and martensite disposition after transformation can be listed as follows:

Kurdjumov-Sachs (KS)	$(111)_\gamma$ // $(011)_{\acute{\alpha}}$ $[\bar{1}01]_\gamma$ // $[\bar{1}\bar{1}1]_{\acute{\alpha}}$	Reference 110
Greninger-Troiano (GT)	$(111)_\gamma$ 0.2° from $(011)_{\acute{\alpha}}$ $[\bar{1}01]_\gamma$ 2.7° from $[\bar{1}\bar{1}1]_{\acute{\alpha}}$	Reference 111
Nishiyama-Wasserman (NW)	$(111)_\gamma$ // $(011)_{\acute{\alpha}}$ $[1\bar{1}0]_\gamma$ // $[100]_{\acute{\alpha}}$	Reference 112

The KS and NW relationships are related by a rotation of 5.26° about the $[0\bar{1}1]_{\acute{\alpha}}$ axis. At first sight this appears to be a very small difference, but it will be shown later that it has a profound influence on the martensite-martensite crystallography.

The GT relationship generally refers to BCT martensite, but can also be found with FCC to BCC transformations (113).

Considering the KS orientation relationship first, we note that 24 independent crystallographic variants of martensite can be obtained within a single crystal of austenite. These are listed in table VI.1. The KS relationship has the special property that its variants can be twin related in pairs (114). Speich and Swann (115) elegantly illustrated that six independent variants can be obtained simply by rotation about the pole of

$(011)_{\alpha'}$ // $(111)_{\gamma}$, fig.VI.1. Hence, a group of six variants can be assigned to each of the four independent $\{111\}_{\gamma}$ planes in a given austenite crystal, (table VI.1), thereby generating the 24 variants. Using the terminology of table VI.1, Speich and Swann (115) listed the axis-angle pairs required to obtain variants (2-6) from variant (1) and showed that these could be divided into three pairs of twin-related variants. However, they did not consider the 18 other variants so that it is not known whether additional twin related variants might arise by choosing pairs of KS variants airsing from different groups, as listed in table VI.1. It is important to resolve this problem since it will be shown later that the formation of twin-related variants may be significant to the retention of austenite. The relationships between all 24 variants of KS were computed using Euler's theorem, as quoted in (116).

Euler's theorem states that any displacement of a rigid body which leaves one of its points fixed may be produced by a rotation of the body through an angle of 180° or less about an axis passing through that point. Letting the position of the body be specified by the position of the fixed point "O" and two other points "P" and "Q", such that O,P and Q are not colinear, the initial and final positions of these points (the latter being generated by the rotation operation) can be defined as O,P_1,Q_1 and O,P_2,Q_2 respectively such that

$$OP_1 = \underline{p}_1$$
$$OQ_1 = \underline{q}_1$$
$$OP_2 = \underline{p}_2$$
$$OQ_2 = \underline{q}_2$$

Euler's theorem then gives

$$\frac{(\underline{q}_2 - \underline{q}_1) \times (\underline{p}_2 - \underline{p}_1)}{(\underline{q}_2 + \underline{q}_1) \cdot (\underline{p}_2 - \underline{p}_1)} = \hat{\underline{u}}(\tan[\xi/2])$$

where $\hat{\underline{u}}$ is a unit vector parallel to the axis of rotation, and ξ is the amount of rotation about the axis $\hat{\underline{u}}$.

Considering variant (1) in table VI.1 as the reference variant and assuming that we wish to obtain the axis-angle pair relating variants (1) and (12), we have

$(011)_{\alpha_1}$ // $(111)_{\gamma}$	$[\bar{1}\bar{1}1]_{\alpha_1}$ // $[\bar{1}01]_{\gamma}$	Variant (1)
$(011)_{\alpha_{12}}$ // $(\bar{1}\bar{1}1)_{\gamma}$	$[1\bar{1}1]_{\alpha_{12}}$ // $[011]_{\gamma}$	Variant (12)

However, before Euler's theorem can be applied, both sets of indices must have a common reference frame, and for the present purposes the indices of variant (12) may be transformed to those of variant (1) via the common austenite lattice. Using the KS relationship**, we find that the $(\bar{1}\bar{1}1)_\gamma$ plane which lies parallel to the $(011)_{\acute{\alpha}12}$ is also parallel to $(-.0865\ -.8996\ .4282)_{\acute{\alpha}_1}$ and similarly, $[1\bar{1}1]_{\acute{\alpha}12}$ corresponds to $[-.5244\ .4065\ .7482]_{\acute{\alpha}1}$.

$$**(hkl)_\gamma = (hkl)_{\acute{\alpha}} \begin{vmatrix} .90825 & -.81650 & -.09175 \\ .79588 & .90825 & -.20412 \\ .20412 & .09175 & 1.20413 \end{vmatrix}$$

$$(hkl)_{\acute{\alpha}} = (hkl)_\gamma \begin{vmatrix} .60550 & .53058 & .13608 \\ -.54433 & .60550 & .06117 \\ -.06117 & -.13608 & .80275 \end{vmatrix}$$

Thus,

$$\underline{p}_1 = 0,1,1 = 0,\ .7071,\ .7071$$
$$\underline{q}_1 = -1,-1,1 = -.5774,\ -.5774,\ .5774$$
$$\underline{p}_2 = -.0865,\ -.8996,\ .4282$$
$$\underline{q}_2 = -.5244,\ .4065,\ .7482$$

and Euler's theorem can be applied to yield the result given in table VI.2. From table VI.2 it is clear that twin related variants cannot be obtained by choosing variants from different groups.

Considering the NW orientation relationship next, an examination of fig. VI.2 immediately reveals that twin-related variants of NW cannot arise. This follows from the fact that the $\{001\}_{\acute{\alpha}}$ poles of a BCC matrix coincide with poles of the $\{122\}_{\acute{\alpha}_t}$ form in the BCC twin. In the NW orientation relationship an $\{001\}_\alpha$ is parallel to an $\{011\}_\gamma$ but there is no $\{122\}_{\acute{\alpha}}$ pole also parallel to another $\{011\}_\gamma$ so that twin related martensite variants are impossible. In fact, figure VI.3 shows that the slightest departure (β) from parallelism of close packed directions (while maintaining parallelism of closest packed planes) leads to a condition where twin related variants cannot arise. A similar conclusion applies to the GT orientation relationship and we can conclude that no orientation relationship in the Bain orientation region other than KS can lead to the formation of twin related variants of martensite.

Having established the crystallographic necessities, some of the work given below is based on the hypothesis that the formation of twin related variants involves a high degree of mutual accommodation, such that the propensity to retain inter-lath

films of retained austenite is reduced. It will become evident (from the work to be presented below, and from the results of Ch.7) that this hypothesis is firmly based. Moreover, Kelly (117) examined alpha martensite in a high alloy stainless steel and found that the observed crystallographic elements are consistent with twin related laths having shear components of their shape strains that can cancel each other (assuming that the high value of the dilatation parameter he used can be justified).

(VI.3) The Distribution and Stability of Inter-Lath films of Retained Austenite

In recent years, the study of retained austenite films associated with martensite in low alloy steels has assumed new significance, primarily due to its apparent influence on the mechanical properties of commercially used quenched and tempered ultra-high strength steels (75,92,118). Due to the relatively high M_s temperatures of low alloy martensites, only thin films of inter-lath austenite are retained at room temperature (thickness ~500 Å, ref.107). However, the reasons for the lack of complete transformation are not clear - even cooling to -196°C often fails to finish the transformation (119, Ch.5). Since the films of austenite are, in general, found to be stable even in the thin foils used in transmission microscopy, the problem cannot simply be attributed to constraint effects, although these clearly do have some role (Ch.5).

Since refrigeration fails to give a significant decrease in the amount of retained austenite, Rao et. al. (119) proposed that chemical or thermal stabilisation could be ruled out as possible reasons for the anomalous stability of these films. As far as chemical stabilisation is concerned, we do not expect any partitioning of carbon when martensite is formed by directly quenching from the austenitised condition, since the transformation products reach ambient temperature in a very short period of time. The Mossbauer spectroscopy results of Azevedo and Da Silva (106) confirm that enrichment of austenite does not occur during the quench. In view of these factors, and by a process of elimination, it is thought that mechanical stabilisation could be responsible for the stability of the austenite films (119). The purpose of the present work was to examine this possibility and a number of steels were investigated.

(i) Fe-0.4C-4.0Ni

A microstructure of dislocated lath martensite was obtained on water quenching following austenitisation at 1200°C for 10 min. Examination of over 60 electron micrograph/diffraction pattern pairs revealed that approximately 55% of adjacent martensite units had twin related lattices. The structure appeared to be partitioned by large platelets, with finer martensite in the partitioned areas (figure VI.4). The twin related martensite was found mainly in the partitioned regions and occurred in two distinct formations. In one situation, the adjacent platelets alternated in twin orientation and formed as clearly defined packets and it was found that retained austenite could not be imaged within these regions (figure VI.5). When irregular groups of platelets with only some adjacent martensite units being twin related were observed, retained austenite could be imaged between units in the same crystallographic orientation but only to a very limited extent at the interfaces between twin related units (figure VI.6).

In all cases the retained austenite films were rather discontinuous and it is estimated that the quantity of retained austenite involved is less than 1% . The inhomogeneous distribution of retained austenite can be rationalised if it is considered that the twin related martensite units form in a mutually accommodating manner. In this case, mechanical stabilisation of austenite (which essentially involves the jamming of the austenite-martensite interface by accommodation defects) is expected to be mitigated relative to the situation where adjacent variants form in the same crystallographic orientation, when their shape deformations would be expected to be additive rather than mutually compensating**.

** When the laths constituting a packet are in the same orientation, it is likely that the shape deformation of each unit within the packet is identical. There is only one case where the habit plane and orientation relationship of adjacent units can be the same, and yet the shape deformations involved can be different. This occurs in the FCC to HCP transformation where a degeneracy exists so that the operation of any one of a set of three Shockley partials on a given $\{111\}_\gamma$ habit plane generates the HCP lattice. Irrespective of which of the three partials operates, the final lattice obtained will be crystallographically indistinguishable, except for the shape deformation (61). No such degeneracy exists for the FCC to BCC transformation.

Clearly, the compensating effects would be maximised when the twin related platelets can form in regular groups with alternating units. The formation of twin related variants in the regions partitioned by the larger platelets is consistent with the above arguments since such regions would be under the constraint of an already formed rigid frame of martensite. This last point is illustrated in figure VI.7, which is a surface relief image of a pre-polished and transformed specimen (taken using scanning electron microscopy). We notice that the total surface relief is minimised in the regions partitioned by the larger units.

(ii) Fe-0.18C-3.9Mo

Considerable quantities of inter-martensite retained austenite films could be imaged and it was found that the martensite platelets tended to be in the same crystallographic orientation in space (over distances of approximately 10 martensite units at least), figure V.2. It is probable that very little mutually compensating accommodation is involved in the formation of such groupings so that the residual austenite would be deformed to a greater extent by the resultant unaccommodated strains. This could lead to mechanical stabilisation. However, the films of retained austenite proved to be too fine to be able to easily characterise their microstructure.

(iii) Fe-0.08C-1.1Mn-0.2Si-5.5Ni-14.5Cr-2.1Mo-0.7Nb-1.9Cu

With this alloy the martensite groups again formed in the same crystallographic orientation and the high alloy content allowed the retention of larger quantities of austenite (fig.VI.8). The microstructure of this austenite could be clearly resolved and it was interesting to note that the austenite was heavily faulted, with a dominant fault plane aligned with respect to the martensite habit plane trace, as expected when the austenite absorbs a significant proportion of the accommodation strain. Such extensive faulting can be expected to mechanically stabilise the residual austenite to further transformation.

(iv) Fe-0.31C-2.0Si

Since retained austenite could not be detected after direct quenching, an attempt was made to enhance the retention of austenite by thermal stabilisation. The specimen was austenitised at 1100°C for 5 min followed by a quench to 335°C (a temperature below the calculated M_s of 410°C) where it was held for 1 hour before finally quenching to room temperature. However, retained austenite

could not be detected and it was found that the martensite was in classical lath formation (figure VI.9) with alternate laths being twin related. The lath packets were extremely regular, as illustrated in figure VI.10. These results are again consistent with twin related martensite forming in a mutually compensating manner.

The above results are consistent with mechanical stabilisation being the operative mechanism for the problem at hand, but more direct evidence for the high degree of mutual accommodation between twin related martensite variants can be offered for the Fe-0.4C-4Ni alloy.

In chapter seven it will be demonstrated that the incipient twinning found in mainly dislocated low alloy martensites arises from accommodation effects. Such twins are not intrinsic transformation features. These kinds of twins can also be found in the Fe-0.4C-4Ni alloy. However, it is clear from figure VI.11 that the intensity and distribution of twinning depends critically on the local crystallography. In fig. VI.11, the twinning is extensive when adjacent units are twin related but is absent in the case of the laths marked 'A' and 'B' which are in the same crystallographic orientation. The nucleation of accommodation twinning and the transfer of slip across inter-lath boundaries would certainly be easiest when the adjacent lattices are twin related; this increases the scope for mutual accommodation. Additionally, it is hard to imagine how any retained austenite could exist between twin related laths when it is clear that their lattices are effectively interpenetrating because the twins nucleate in the same orientation as the adjacent lath. This matter will be dealt with in greater detail in chapter seven.

(VI.4) The Crystallography of Dislocated Martensites

In order to understand the operative deformation systems, accommodation modes and various other factors controlling the extent of transformation to martensite, it is necessary to completely define the crystallography with respect to the phenomenological theory of martensite. While it is noted that for ferrous martensites the theory provides fully satisfactory agreement in only a few cases, the elegance of such precise agreement despite the blatant complexities involved points towards the underlying truths of the theory.

Detailed comparison between experiment and theory requires a self consistent analysis involving more than just the prediction of the habit plane indices (120). However, the lack of adequate quantities of retained austenite in low alloy steels has rendered the determination of such data difficult, if not impossible. The following is a brief review of the available data on the habit plane of dislocated martensite.

(i) The Habit Plane of Dislocated Martensite - A Review

In 1929 Sauveur and Chou (121) identified the habit plane of martensite obtained by quenching 'pure' iron as $\{111\}_\gamma$, simply by comparing the optical microstructure with that of Widmanstätten ferrite. However, it is now established that far greater quench rates are necessary to obtain martensite in pure iron. In 1933 Mehl et. al. (122) found the $\{111\}_\gamma$ habit plane in quenched steels with carbon contents of 0.4-1.3 wt. pct. using single surface trace analysis (optical microscopy). The results are doubtful since it is now known that high carbon steels do not have a $\{111\}_\gamma$ habit plane. Mehl and Smith (123) quenched pure iron from 1300°C into a high pressure radial jet of water and identified the habit plane of the resulting martensite by two surface analysis (optical microscopy) to be $\{111\}_\gamma$. Greninger and Troiano (124) conducted a single experiment on a 0.35C steel and found a $\{111\}_\gamma$ habit plane using the method of twin band vestiges, which relies on the 'ghosts' of prior austenite twins to establish the austenite orientation. Wayman et. al. (125) fast quenched zone refined iron and showed that the relative angles of surface markings, as observed by optical microscopy, were consistent with a $\{111\}_\gamma$ habit plane although a pseudo $\{111\}_\gamma$ habit was not ruled out. The latter concept was first introduced by Bowles (126) and implies that the habit plane is in fact comprised of martensite needles which are parallel to directions of the form $\langle 10\bar{1}\rangle_\gamma$ within a given $\{111\}_\gamma$ plane. He further suggested that the transformation in low carbon steels is characterised by the degeneration of $\{225\}_\gamma$ martensite plates into needles. Kelly and Nutting (127) examined the morphology of martensite in several steels by means of thin film electron microscopy, and found martensite 'needles' parallel to $\langle 101\rangle_\gamma$ directions. Such pseudo-habits may exist in some cases (although confirmatory evidence would be useful), but genuine plates with a $\{111\}_\gamma$ habit must also exist (61).

A criticism that is common to all of the above work is that it fails to take account of the possibility that the lath and packet planes (as observed by optical microscopy) may differ.

Lagneborg (128) characterised the habit plane of lath martensite in 18Cr-8Ni-Fe alloys as $\{225\}_\gamma$. However, Kelly (129) subsequently criticised the crystallographic precision of this work and showed that the habit plane is in fact $\{112\}_\gamma$, using a pseudo-two surface analysis coupled with self consistent crystallography. The results of Kelly were obtained using transmission electron microscopy, and he further demonstrated that the data was consistent with the phenomenological theory of martensite (although a dilatation parameter of 1.8% had to be used).

Bell and Owen (130) implied that since the martensite plates obtained in Fe-N alloys were arranged in a Widmanstätten pattern, they could have formed by shear on $\{111\}_\gamma$ planes. Using single surface trace analysis and electron diffraction, Biswas and Codd (131) claimed that the lath habit in low nitrogen ferrous martensites could be characterised as the $\{110\}_{\alpha'}$ plane, consistent with the observation of (130) if a KS or NW orientation relationship is operative. The shortcomings of single surface trace analysis will be dealt with later, but it is clear that both of the above pieces of evidence are weak.

Schoen et. al. (132) transformed a large single crystal of Fe-Ni containing a nickel concentration gradient so that the transformation terminated at some point where the driving force became inadequate. At this point the martensite laths were embedded in austenite and three surface analysis proved that the unit of 'massive' martensite was a thin platelet with a habit plane within 3° from $\{111\}_\gamma$. It should be noted that the martensite unit concerned here is physically much larger (optically resolvable) than the 0.3μm width laths observed in the more common dislocated martensite found in low alloy steels. Byrans et. al. (133) found that the habit plane of 'massive' martensite in an Fe-22Ni alloy was near $\{111\}_\gamma$. This conclusion arose from the fact that the inter-lath angles measured always fell in a domain specified by the assumption of a $\{111\}_\gamma$ habit plane.

From electron microscopic analysis, McDougall (134) found that an Fe-24Ni-0.1C alloy had a structure of laths with habit planes

parallel to $\{111\}_\gamma$. However, Chilton et. al. (135) obtained a habit plane near $\{123\}_{\acute{\alpha}}$ for Fe-24Ni-0.1C, Fe-4Ni-0.05C and Fe-20Ni-0.03C alloys, using single surface trace analysis based on electron diffraction. These results are incompatible if it is assumed that the operative orientation relationship lies at or between KS and NW.

Bozic and Lucic (136) examined Fe-(0.22-1.68)As alloys, again by a single surface trace analysis/electron diffraction technique, and claimed clustering of the habit plane pole in the vicinity of $\{110\}_{\acute{\alpha}}$. They further considered that there was no systematic variation of habit plane pole with composition; this conclusion is unjustified since the technique cannot resolve such variations.

Similarly, Sarma et. al. (137) examined Fe-5Ni-0.5C, Fe-24Ni-2Mn and Fe-20Ni-6Ti alloys and claimed that the habit plane was $\{123\}_{\acute{\alpha}}$ in each case. These results can be severely criticised since they used only four sets of data (i.e. four great circles, each representing the locus of the habit plane pole on the stereogram) per alloy and it can be readily shown that their data is compatible with other possibilities. Furthermore, their interpretation that the $\{123\}_{\acute{\alpha}}$ habits could have arisen from either the $\{345\}_\gamma$ or $\{557\}_\gamma$ planes (depending on the orientation relationship) is confusing since this does not agree with the Bain correspondence.

Bolton and Petty (138) assumed that the habit plane of an Fe-Mn alloy martensite is $\{110\}_{\acute{\alpha}}$ by observing that the trace of the lath habit plane was parallel to that of ghosts of austenite twins; the lath traces were also parallel to the K2 twin plane on either side of the twin boundary.

In summary, it seems that the existence of a $\{111\}_\gamma$ habit plane in low alloy dislocated martensite has not been definitively demonstrated, particularly for carbon containing martensites. In some cases where the habit has been accurately identified to be near $\{111\}_\gamma$, the martensite is 'massive', and not representative of low alloy dislocated martensite in general.

(ii) Techniques for the Determination of Habit Planes

(a) The Significance of Habit Plane Multiplicity

The multiplicity of the form of the habit plane defines the number of independent habit plane traces observable in any given austenite grain. This kind of an analysis can only be used as a definitive method if the observed multiplicity uniquely

corresponds to a particular form of planes. An example would be the $\{111\}$ planes which are the only planes with a multiplicity of 8 in a cubic system. When optical microscopy is used, the observed multiplicity may be lower than the actual value if the habit plane lies sufficiently near a plane of low order, such that the difference cannot be resolved.

Considering further the example of the $\{111\}_\gamma$ plane, it should be noted that the observation of more than four independent traces rules out a $\{111\}_\gamma$ habit; however, when the observed multiplicity is less than four, this possibility cannot be discounted since there is no reason why all habit plane variants need be operative.

The above analysis is conditional on the existence of only one transformation product (or an easily distinguishable one) with a unique habit plane.

(b) The Measurement of Inter-Trace Angles

This method of defining the habit plane using optical microscopy was put forward by Crocker et. al. (139) and is limited to cases where the habit plane indices are of a low order. It involves the measurement of inter-trace angles formed in the arbitrary plane of section that intersects a set of three independent habit plane variants. Should all the measured angles fall within a domain specified by the indices of the postulated habit, the latter is confirmed. For best results, a sufficient number of critically distributed (eg. with respect to the domain boundaries) situations should be examined.

It was decided to extend the method so that the general case can be examined, bearing in mind that while conclusive results may not be obtained for complex cases, it may be useful to show that the measured angles are consistent with the postulated habit plane. The essentials of the method are presented in figure VI.12, and it should be noted that if the habit plane is known, the method can be iteratively used to calculate the plane of section.

(c) Two Surface Analysis

If the crystallographic orientation of the austenite is known, the observation of traces of the habit plane on two independent surfaces can yield accurate and unique habit plane data. When sufficient austenite is not retained (as is the case for most low alloy steels), the ghosts of prior austenite twins can be used to establish the austenite orientation. Even when the

austenite orientation cannot be determined, two surface analysis can be used to generate a set of data composed of the angles between habit plane variants. If sufficient data of this nature is accumulated, the habit plane indices can be iteratively determined by comparison with the set of angles produced between all 24 (maximum) variants of planes of the form $\{hkl\}_\gamma$, where $\{hkl\}_\gamma$ would be systematically varied (on a computer) until a match is obtained.

(d) Trace Normal Analysis using Electron Diffraction

Only a brief description of this technique is warranted since it is well established and is found in most standard textbooks on applied electron microscopy. The data obtained from electron diffraction and direct imaging are plotted as great circles on a convenient stereographic projection. The great circles represent the loci of the possible positions of the habit plane normal so that their common intersection point (after rotation into a unit stereographic triangle using symmetry operations) gives the actual habit plane normal. The purpose of the present section is to point out certain factors that can lead to misinterpretation and to further develop the method of analysis.

The technique is at its best when the great circles cover a fair range of orientations and are not just repetitive. However, most metallurgical samples are textured, and care must be exercised to avoid the clustering of great circles. When tilting is used, serious errors can arise (140) if the trace measurements are not corrected for projection effects. When a straightforward electron diffraction technique is used, it must be realised that the zone axis can deviate considerably ($\sim 5°$) from the electron beam direction, and care must be taken to use symmetrical diffraction patterns wherever possible.

The method becomes most difficult to interpret when the habit plane is irrational, as is the case for most ferrous martensites. This is because it requires the experimenter to spot the pole which is common to all the great circles, and often the pole concerned may not even be denoted on standard stereograms. In order to partly overcome these difficulties, a computer method was developed which allows the systematic testing of the experimental data such that the total amount of scatter of the great circles from the postulated habit plane pole is minimised. The additional advantage of this procedure is that all stereographic plotting errors are eliminated and the analysis becomes more objective.

The computing procedure involved can be outlined as follows:

The data input consists of $\underline{g}_1$, $\underline{g}_2$, θ_1 and θ_2 where

$\underline{g}_1$, $\underline{g}_2$ = two independent reciprocal lattice vectors obtained from the relevant diffraction pattern,

θ_1, θ_2 = the angles made by the trace normal to the habit plane with $\underline{g}_1$ and $\underline{g}_2$ respectively.

If all the vectors involved are normalised to give unit vectors, the operative zone axis ($\underline{Z}$) is given by

$$\underline{Z} = \hat{\underline{g}}_1 \times \hat{\underline{g}}_2 \quad \text{(The circumflex implies a unit vector)}$$

so that the trace normal vector ($\underline{t}$) can be calculated by the simultaneous solution of the following equations:

$$\hat{\underline{g}}_1 \cdot \hat{\underline{t}} = \cos(\theta_1)$$

$$\hat{\underline{g}}_2 \cdot \hat{\underline{t}} = \cos(\theta_2)$$

$$\hat{\underline{Z}} \cdot \hat{\underline{t}} = (\widehat{\hat{\underline{g}}_1 \times \hat{\underline{g}}_2}) \cdot \hat{\underline{t}} = 0$$

Hence the great circle representing the locus of the possible habit plane poles is given by

$$\hat{\underline{P}} = \hat{\underline{Z}} \times \hat{\underline{t}}$$

We then proceed to systematically guess the real pole of the habit plane, $\{hkl\}$ and calculate the angular deviation δ of the pole $\{hkl\}$ from the great circle whose pole is given by $\underline{P}$. This is repeated for all 24 variants of $\{hkl\}$, and that which gives a minimum departure δ_{min} from the great circle $\underline{P}$ is taken to be the best possibility for the particular guessed form. In this manner, a set D_{hkl} which represents the δ_{min} values for all the experimental data corresponding to the guessed pole $\{hkl\}$ is obtained.

In this way, the procedure is repeated systematically for as many guesses of $\{hkl\}$ as required, so that a new set consisting of values of (the sub-sets) D_{hkl} is generated. That value of D_{hkl} which is the minimum element of the new set then gives the 'best fit' habit plane $\{HKL\}$ consistent with the experimental data.

When a large amount of experimental data is available, the set D_{HKL} can be subjected to statistical analysis, to indicate whether its elements (the various values of δ_{min} corresponding to each set of experimental data) simply result from random measurement errors.

A precaution built into the program is that it does not

allow the habit plane to lie in the foil plane, since in such a case a habit plane trace would not be obtained.

The actual program is not included in this thesis because at the time of writing, it in fact consists of three separate programs (due to capacity limitations of the mini-computer used) which carry out different stages of the calculations. Thus large amounts of data have to be transferred between programs. In addition, the programs are written in BASIC, and no attempts have been made to optimise the computing time involved.

(iii) Experimental Habit Plane Determinations

(a) Fe-24Ni-0.16C

It is known that retained austenite can be found in this alloy despite its high calculated M_s temperature of 77°C, (134). Optical microscopy revealed the traces of only four different habit planes and it was confirmed that the optically observed habit corresponded to that found by transmission electron microscopy - dark field imaging (using an austenite reflection) revealed only four independent traces of the austenite-martensite interfaces when large areas were examined at low magnification.

Hence the method of Crocker et al. (139) was applied and inter-trace angles formed by the intersection of three habit plane variants (as observed by optical microscopy) with the plane of section were measured. These were then plotted on a ternary angle diagram (figure VI.13) whose sides represent the inter-trace angles. The angles almost completely fell within the domain specified for a $\{111\}_\gamma$ plane, confirming that the habit plane was near to $\{111\}_\gamma$, in agreement with (134). It is therefore thought that the results of Chilton et al. (135) who found a $\{123\}_\alpha$ habit may be ambiguously interpreted; they used single surface trace analysis coupled with electron diffraction to determine their habit planes, and the dangers of the simple form of such an analysis have been outlined earlier.

(b) Fe-25.2Ni-1.9Mn

This alloy has a calculated M_s temperature of 70°C, which compares well with the Fe-24Ni-0.16C alloy with an M_s of 77°C. Both these alloys gave lath martensite (figure VI.14) on water quenching from the austenitising temperature (1200°C for 5 min). Two surface analysis using optical microscopy provided values of inter-packet plane angles. These were found to best fit the set of angles formed between variants of $\{28\ 13\ 10\}_\gamma$, as given in

table VI.3. In one particular prior austenite grain, nine independent packet plane traces could be observed, and by measuring the angles between a reference trace and the other traces, it was possible to show that they were consistent with the above packet plane using the method given in (VI.4.ii.b). These results are presented in figure VI.15.

Single surface trace analysis using electron diffraction pattern/bright field image pairs and the computing technique of (VI.4.ii.d) gave the martensite lath habit plane with a best fit near $\{33\ 18\ 10\}_{\alpha'}$. The results are presented in figure VI.16. It is notable that after transforming all 24 independent variants of $\{28\ 13\ 10\}_{\gamma}$ through the KS orientation variant (1), we find that $\{10\ \bar{1}3\ 28\}_{\gamma}$ transforms to $\{18\ \bar{1}0\ 36\}_{\alpha'}$, indicating that once again the packet and lath planes are equivalent, and that the habit plane may more specifically be $\{10\ \bar{1}3\ 28\}_{\gamma}$ // $\{18\ \bar{1}0\ 33\}_{\alpha'}$.

X-ray analysis indicated that the Fe-25Ni-2Mn alloy contained 21% retained austenite at room temperature while the Fe-24Ni-0.16C alloy contained 16%; both the alloys had been water quenched following austenitisation at 1310°C for 20 min, when P_{111} was found to be zero in both cases. Allowing for an experimental error of 2%, the difference in the retained austenite contents is not large and is consistent with the small difference in M_s temperatures between the two alloys.

The above results suggest that not only is the cross-over point of the free energy surfaces of martensite and austenite similar for both the alloys (as manifested in their similar M_s temperatures), but their behaviour below M_s must also be similar since the amounts of austenite retained at room temperature are approximately the same. The latter point implies that the gradients of the free energy surfaces concerned (with respect to temperature) may be similar for both alloys.

We note that the likeness in behaviour noted above is not reflected in the crystallographic characteristics, since the habit planes of the two alloys have been demonstrated to be very different. It therefore appears that crystallography in itself does not control the extent of transformation, but is simply the route towards the achievement of the required degree of transformation.

The crystallographic characteristics of martensite are related to the operative shear systems for any given alloy so that the

specific crystallography may be expected to vary with the relative strengths of the austenite and martensite involved. This idea was originally proposed by Davies and Magee (141). In the present investigation, the strength of the martensite in the Fe-24Ni-0.16C alloy must be higher than that of the Fe-25Ni-2Mn alloy since the former contains carbon in interstitial solid solution. Since the flow stress of austenite is insensitive to the Ni, Mn and C contents (85,141), a difference in crystallographic behaviour can be expected between the above two alloys.

(c) Fe-0.4C-4Ni

Optical microscopy revealed that the martensite in this alloy had a habit plane multiplicity greater than four. Single surface trace analysis using electron diffraction (VI.4.ii.d) showed that the habit plane was near $\{123\}_{\alpha'}$, figure VI.17. Since a large set of data (60 electron diffraction pattern/bright field image pairs were analysed) had been obtained, the errors (i.e. the set of δ_{min} values obtained using the best fit computing technique) could be statistically analysed and were shown to follow the Normal cumulative distribution (fig.VI.18), implying that most of the departure of the great circles (fig.VI.17) from the $\{123\}_{\alpha'}$ pole may be due to random errors.

The detailed crystallography of this alloy has not yet been resolved.

(VI.5) General Summary

It seems that the thin films of retained austenite found between laths of low alloy martensite are mechanically stabilised, by the jamming of the austenite-martensite interface by transformation induced accommodation defects.

The stability and distribution of the films of austenite is a function of the local martensite-martensite crystallography. Inter-lath films of austenite are generally found to be absent when the adjacent variants of martensite form in a mutually accommodating manner, i.e. twin-related.

It has been shown that twin-related variants of martensite which are also variants of the austenite-martensite orientation relationship can only arise when the latter corresponds to the Kurdjumov-Sachs orientation relationship.

Initial results suggest that the behaviour of the transformation below the M_s temperature is not a sensitive function of the habit plane of the martensite, and it is thought that the crystallographic differences probably reflect variations in the relative strengths of the austenite and martensite concerned.

TABLE VI.1

The 24 Independent variants of the Kurdjumov and Sachs Orientation Relationship

Variant No.	Description		Group No.
1	$(011)_\alpha$ // $(111)_\gamma$	$[\bar{1}\bar{1}1]_\alpha$ // $[\bar{1}01]_\gamma$	1
2	(011) // (111)	$[\bar{1}\bar{1}1]$ // $[0\bar{1}1]$	1
3	(011) // (111)	$[\bar{1}\bar{1}1]$ // $[1\bar{1}0]$	1
4	(011) // (111)	$[1\bar{1}1]$ // $[\bar{1}01]$	1
5	(011) // (111)	$[1\bar{1}1]$ // $[0\bar{1}1]$	1
6	(011) // (111)	$[1\bar{1}1]$ // $[1\bar{1}0]$	1
7	(011) // $(\bar{1}\bar{1}1)$	$[\bar{1}\bar{1}1]$ // $[1\bar{1}0]$	2
8	(011) // $(\bar{1}\bar{1}1)$	$[\bar{1}\bar{1}1]$ // $[101]$	2
9	(011) // $(\bar{1}\bar{1}1)$	$[\bar{1}\bar{1}1]$ // $[011]$	2
10	(011) // $(\bar{1}\bar{1}1)$	$[1\bar{1}1]$ // $[1\bar{1}0]$	2
11	(011) // $(\bar{1}\bar{1}1)$	$[1\bar{1}1]$ // $[101]$	2
12	(011) // $(\bar{1}\bar{1}1)$	$[1\bar{1}1]$ // $[011]$	2
13	(011) // $(\bar{1}1\bar{1})$	$[\bar{1}\bar{1}1]$ // $[110]$	3
14	(011) // $(\bar{1}1\bar{1})$	$[\bar{1}\bar{1}1]$ // $[011]$	3
15	(011) // $(\bar{1}1\bar{1})$	$[\bar{1}\bar{1}1]$ // $[\bar{1}01]$	3
16	(011) // $(\bar{1}1\bar{1})$	$[1\bar{1}1]$ // $[110]$	3
17	(011) // $(\bar{1}1\bar{1})$	$[1\bar{1}1]$ // $[011]$	3
18	(011) // $(\bar{1}1\bar{1})$	$[1\bar{1}1]$ // $[\bar{1}01]$	3
19	(011) // $(1\bar{1}\bar{1})$	$[\bar{1}\bar{1}1]$ // $[110]$	4
20	(011) // $(1\bar{1}\bar{1})$	$[\bar{1}\bar{1}1]$ // $[101]$	4
21	(011) // $(1\bar{1}\bar{1})$	$[\bar{1}\bar{1}1]$ // $[0\bar{1}1]$	4
22	(011) // $(1\bar{1}\bar{1})$	$[1\bar{1}1]$ // $[110]$	4
23	(011) // $(1\bar{1}\bar{1})$	$[1\bar{1}1]$ // $[101]$	4
24	(011) // $(1\bar{1}\bar{1})$	$[1\bar{1}1]$ // $[0\bar{1}1]$	4

TABLE VI.2

The Axis-Angle pairs relating Martensite lattices which are variants of the Kurdjumov and Sachs Orientation Relationship

Variant No.	Rotation Axis			Rotation Angle/Degrees
2	.0000	.7071	.7071	60
3	.0000	.7071	.7071	120
4	.0000	.7071	.7071	-70.52
5	.0000	.7071	.7071	-10.5
6	.0000	.7071	.7071	49.5
7	.3568	-.1784	.9170	146.4
8	-.0750	-.1667	.9832	180
9	-.2901	-.1485	.9454	31.2
10	.8305	-.1384	.5396	116.7
11	.4331	-.1767	.8839	141.2
12	.0000	-.1710	.9853	173.9
13	-.8492	.4246	.3139	146.5
14	-.8563	-.0432	.5147	120
15	-.5774	-.5774	.5774	109.48
16	-.8304	-.1384	.5396	116.8
17	-.4990	-.6569	.5653	109.8
18	.0000	-.9200	.3919	124.3
19	-.7698	.1492	-.6206	120
20	-.4184	.6423	-.6422	109.47
21	.0862	.9030	-.4209	118.87
22	-.8414	-.3842	-.3821	152.04
23	-.8091	.0567	-.5849	121.8
24	-.4987	.5757	-.6480	121.48

Notes

1) Right-handed rotations are taken to be positive.
2) The rotations are relative to variant one (table VI.1) and refer to the martensite lattice.

Table VI.3

Two Surface analysis results on Fe-25.2Ni-1.9Mn alloy

$(hkl)_\gamma$	Computed angle between $(hkl)_\gamma$ and $(28\ 13\ 10)_\gamma$	Measured angle between $(hkl)_\gamma$ and $(28\ 13\ 10)_\gamma$
$\bar{2}8\ 13\ 10$	119.3	117
$\bar{2}8\ 10\ 13$	119.8	-
$\bar{1}0\ 28\ 13$	78.3	78
$10\ 13\ \bar{2}8$	80.8	81
$\bar{1}0\ 13\ 28$	80.8	-
$10\ \bar{1}3\ 28$	68.2	70
$13\ 28\ 10$	38.2	38
$13\ 28\ \bar{1}0$	53.4	51
$13\ \bar{2}8\ 10$	84.6	85
$\bar{1}3\ 28\ 10$	84.6	-

Notes

The experimentally measured angles quoted above are those found between the martensite habit plane variants by two surface analysis using optical microscopy. The computed angles are with reference to $(28\ 13\ 10)_\gamma$. The angles are quoted in degrees and the experimental error is probably $\pm 2°$, mainly due to the difficulty in precisely determining the habit plane trace.

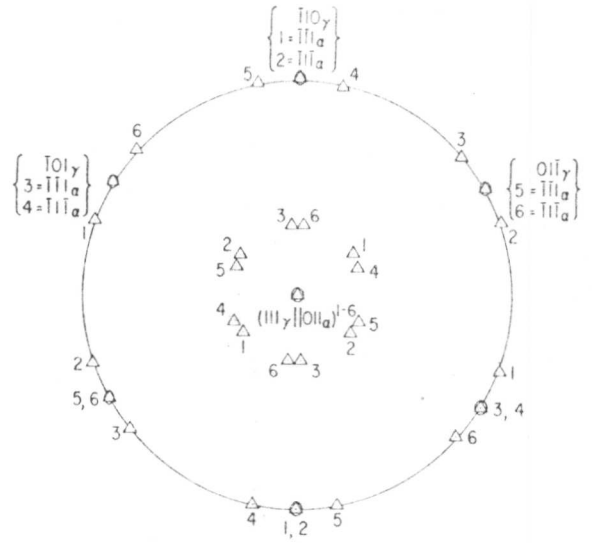

α_1 α_2	ORIENTATION RELATIONSHIP	
1-2, 3-4, 5-6	TWIN RELATED	(70° 32' ROTATION ABOUT $[0\bar{1}1]_\alpha$ OR 180° ROTATION ABOUT $[111]_\alpha$)
1-4, 2-5, 3-6	SMALL ANGLE	(10° ROTATION ABOUT $[0\bar{1}1]_\alpha$)
1-3, 1-5, 2-4, 2-6, 3-5, 4-6	LARGE ANGLE	(60° ROTATION ABOUT $[0\bar{1}1]_\alpha$)
1-6, 2-3, 4-5	LARGE ANGLE	(49° ROTATION ABOUT $[0\bar{1}1]_\alpha$)

Kurdjumov–Sachs variants from common $(111)_\gamma$

Figure VI.1

The Speich & Swann analysis (ref.115) of the Kurdjumov-Sachs orientation relationship.

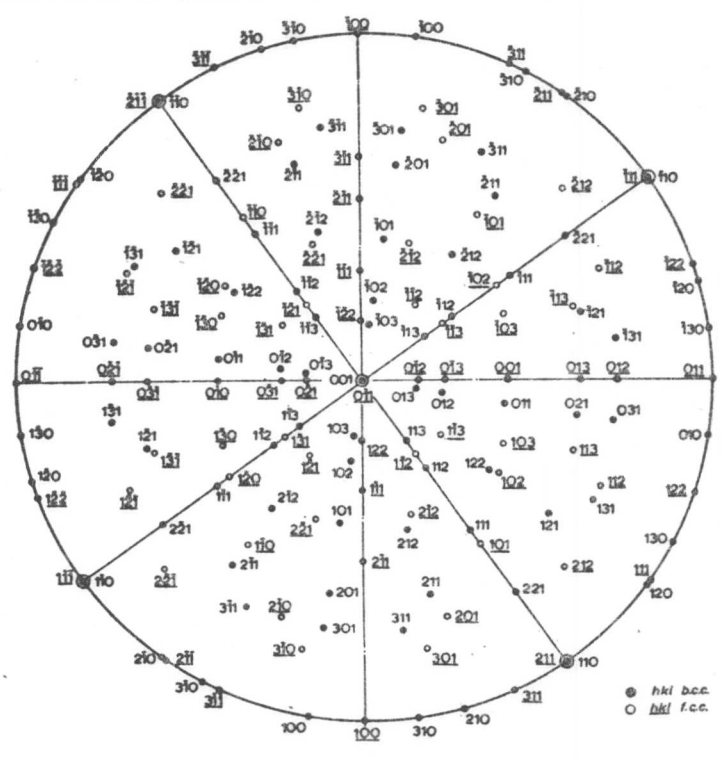

Stereographic projection representing the N–W orientation relationship between body- and face-centred cubic materials.
(001) b.c.c. //(011) f.c.c.
(1$\bar{1}$0) b.c.c. //(1$\bar{1}$1) f.c.c.
(110) b.c.c. //(2$\bar{1}$1) f.c.c.

Figure VI.2

Stereogram representing the Nishiyama-Wasserman orientation relationship.

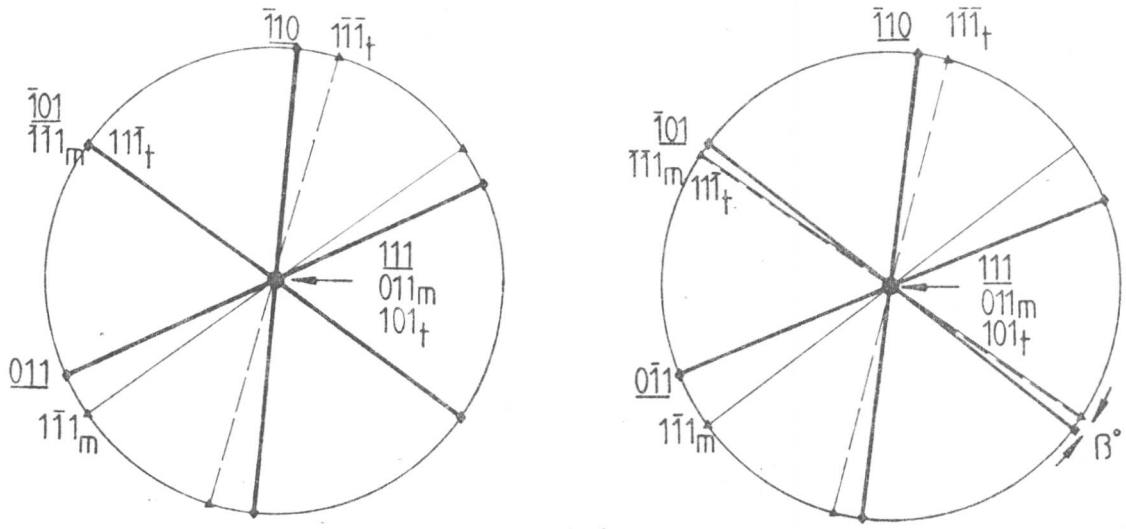

Figure VI.3

Stereograms illustrating how the slightest departure (β) from parallelism of the close packed directions of austenite and martensite leads to the nonexistence of twin-related martensite variants (assuming that the parallelism of the closest packed planes is maintained).

(a) Two twin-related martensite variants simultaneously in Kurdjumov-Sachs orientation with the austenite.

(b) The martensite variants in this case are still twin-related, but have crystallographically non-equivalent orientation relationships with the austenite.

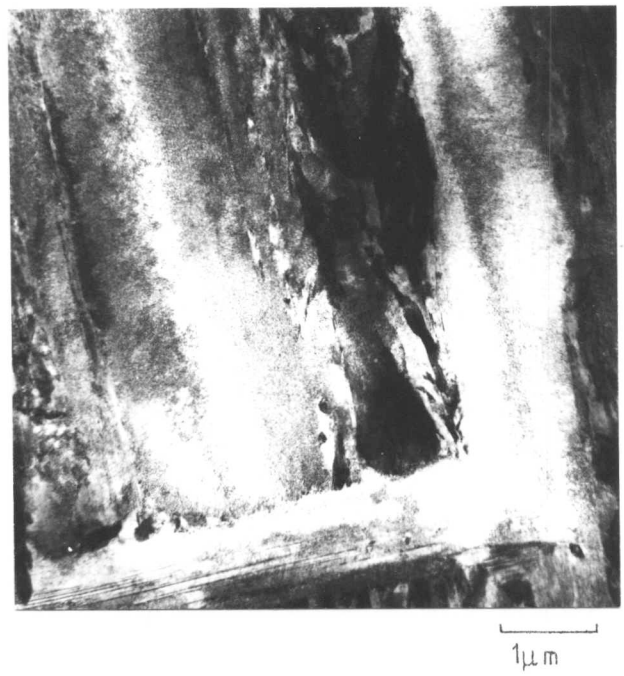

Figure VI.4

Transmission electron micrograph showing the partitioning behaviour of the martensite in Fe-4Ni-0.4C steel.

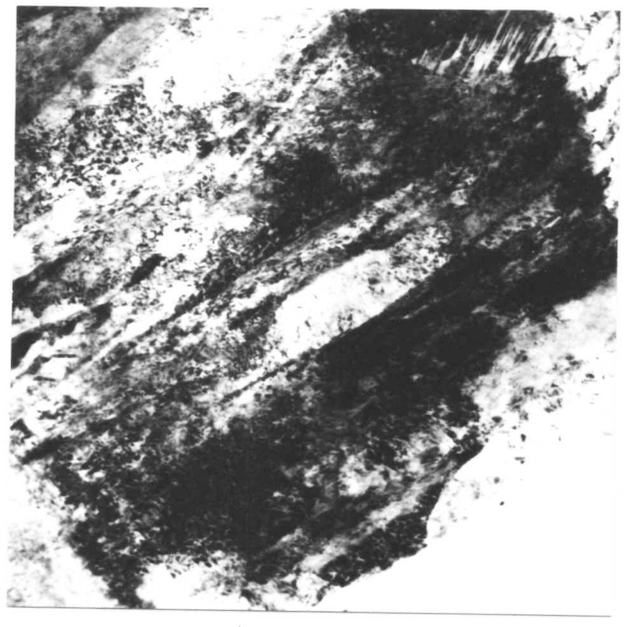

(a)

(b)

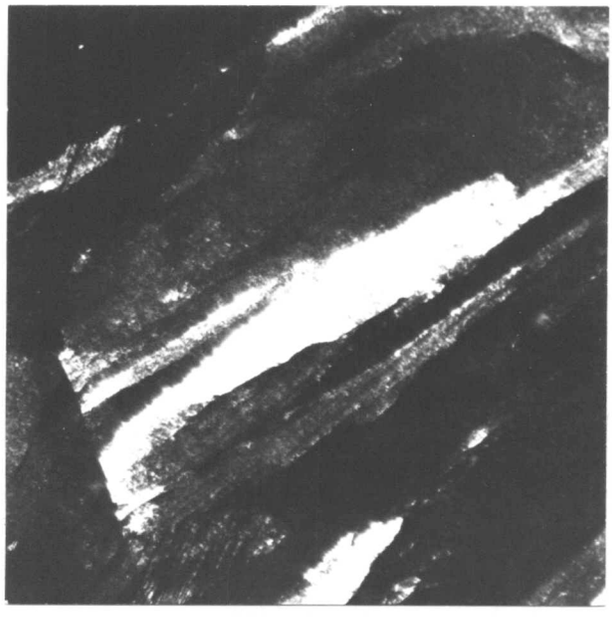

(c)

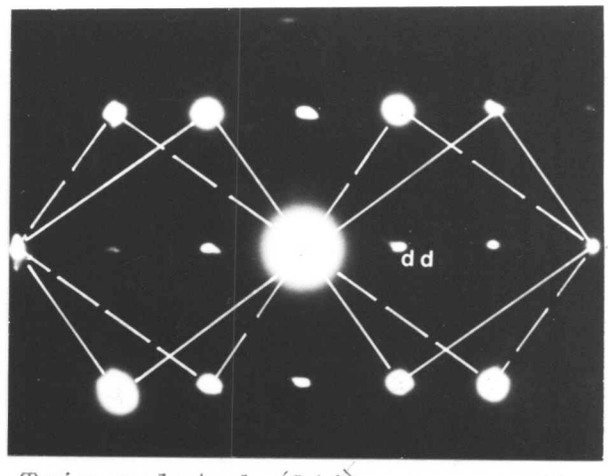

Twin related $\langle 011 \rangle_\alpha$ zones with a relative rotation of 70.52°. (dd = double diffraction)

(d)

Figure VI.5

Fe-4Ni-0.4C alloy, austenitised at 1200°C for 5 minutes and water quenched.

(a) Bright field image.

(b) & (c) Dark field images of twin related martensite variants.

(d) Corresponding diffraction pattern.

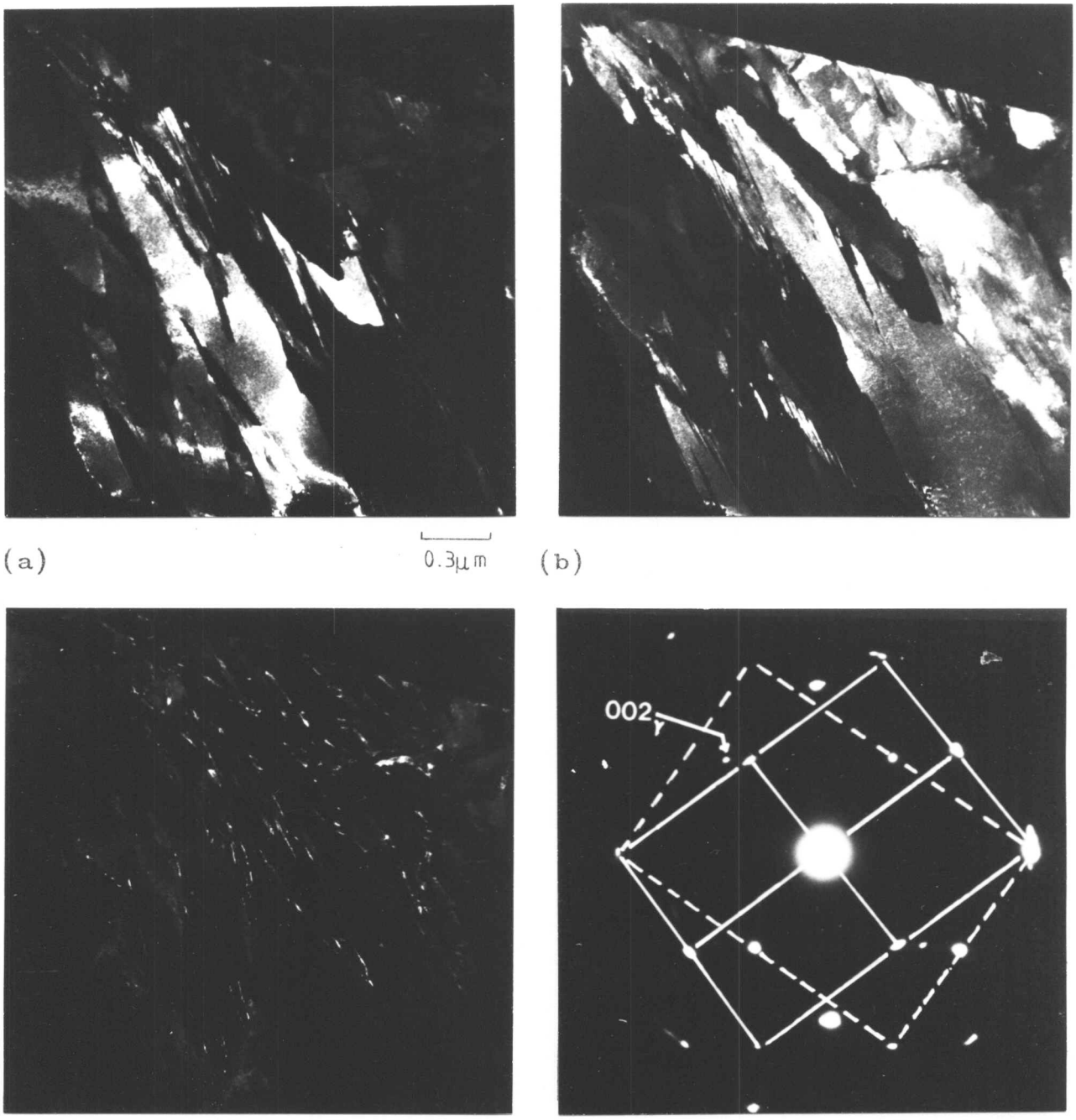

(a) (b)

(c) (d)

Figure VI.6

Fe-4Ni-0.4C alloy, austenitised at 1200°C for 5 minutes and water quenched.

(a) & (b) Dark field images of twin related martensite variants.

(c) Dark field image of retained austenite.

(d) Corresponding diffraction pattern, showing an $\{002\}_\gamma$ reflection in addition to twin-related $\langle 011 \rangle_{\alpha'}$ zones.

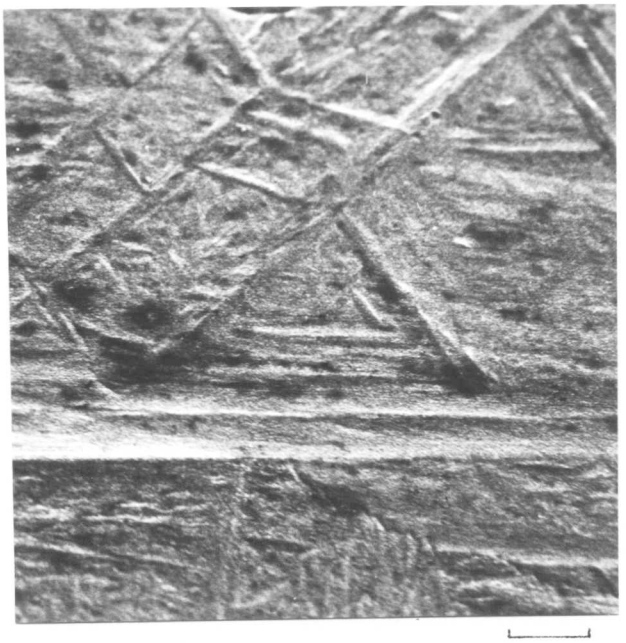

Figure VI.7
Scanning electron microscope image of surface relief due to martensite formation in Fe-4Ni-0.4C alloy.

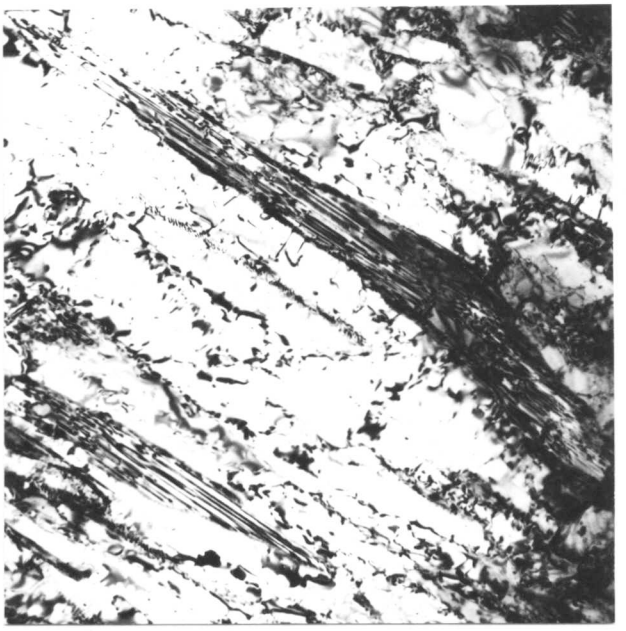

Figure VI.8a
Bright field image of martensite and retained austenite in a high alloy steel (described in the text).

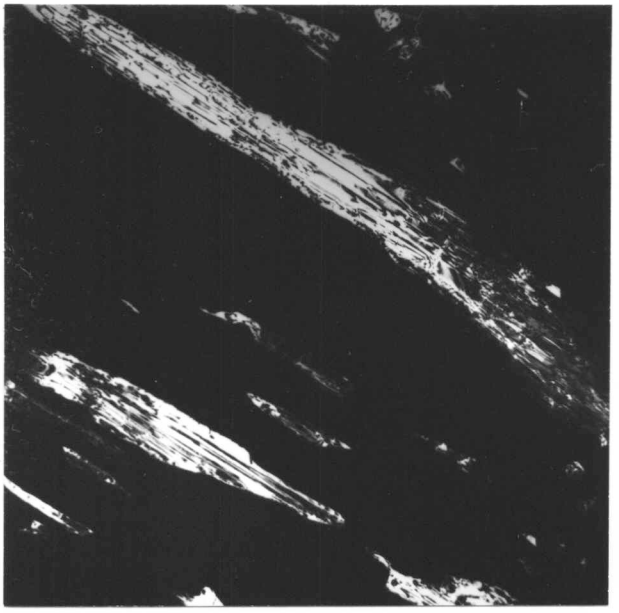

Figure VI.8b
Corresponging dark field image of retained austenite.

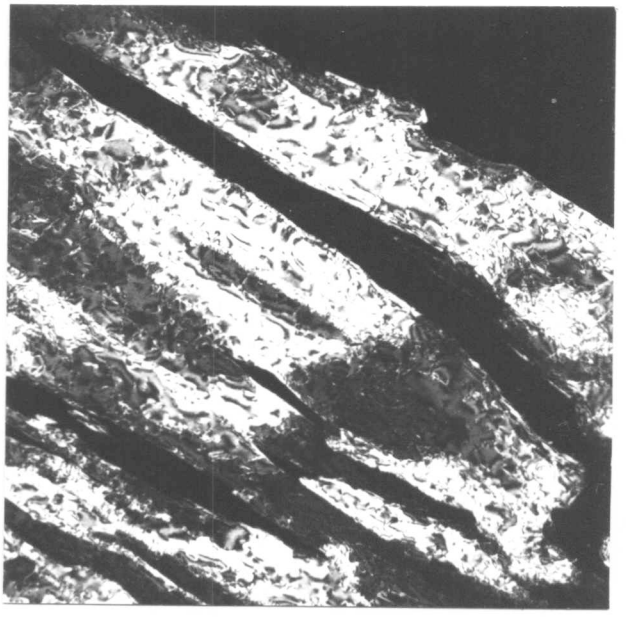

Figure VI.8c
Corresponding dark field image of martensite.

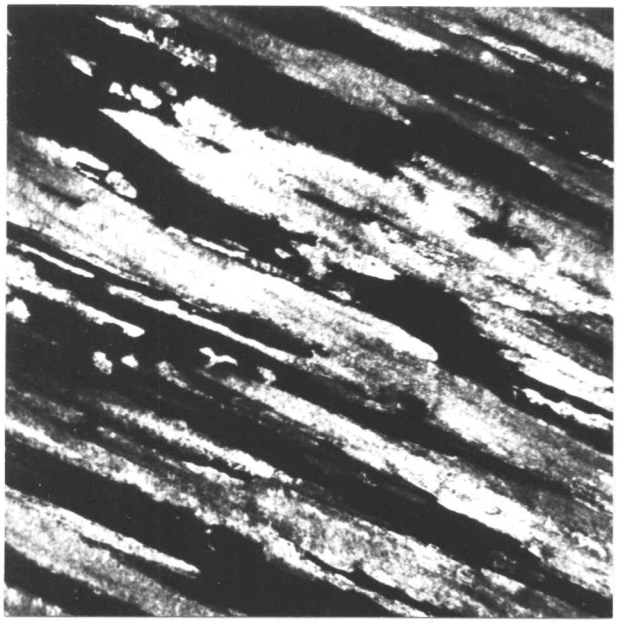

(a)

0.5μm

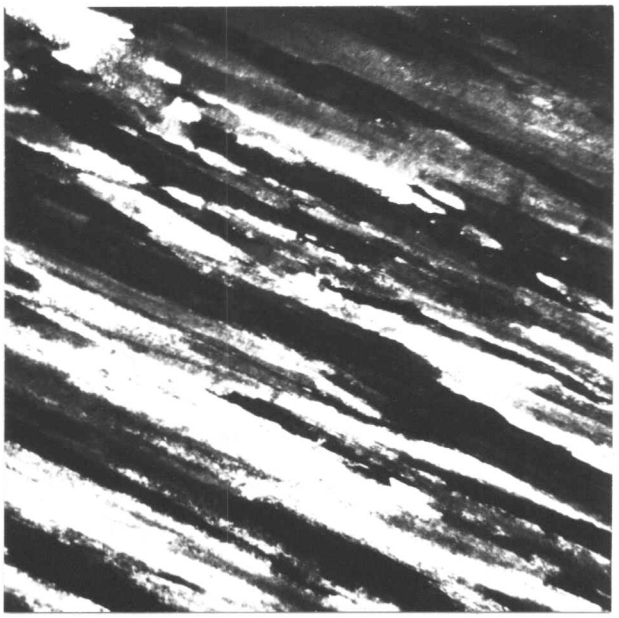

(b)

(c)

Figure VI.9

Fe-0.31C-2.0Si alloy, austenitised at 1100°C for 5 minutes, quenched to 334°C and held at this temperature for 1 hour before finally quenching to room temperature.

(a) & (b) Dark field images of twin-related martensite variants.

(c) Corresponding diffraction pattern showing twin-related $\langle 011 \rangle_{\alpha'}$ zones.

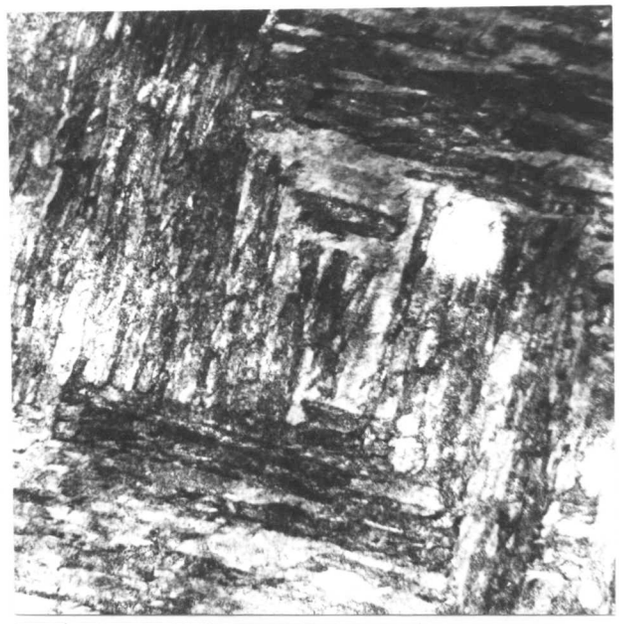

Figure VI.10
Electron micrograph illustrating the nature of twin-related martensite packets in Fe-0.31C-2.0Si alloy, heat treated as given in fig.VI.9.

1μm

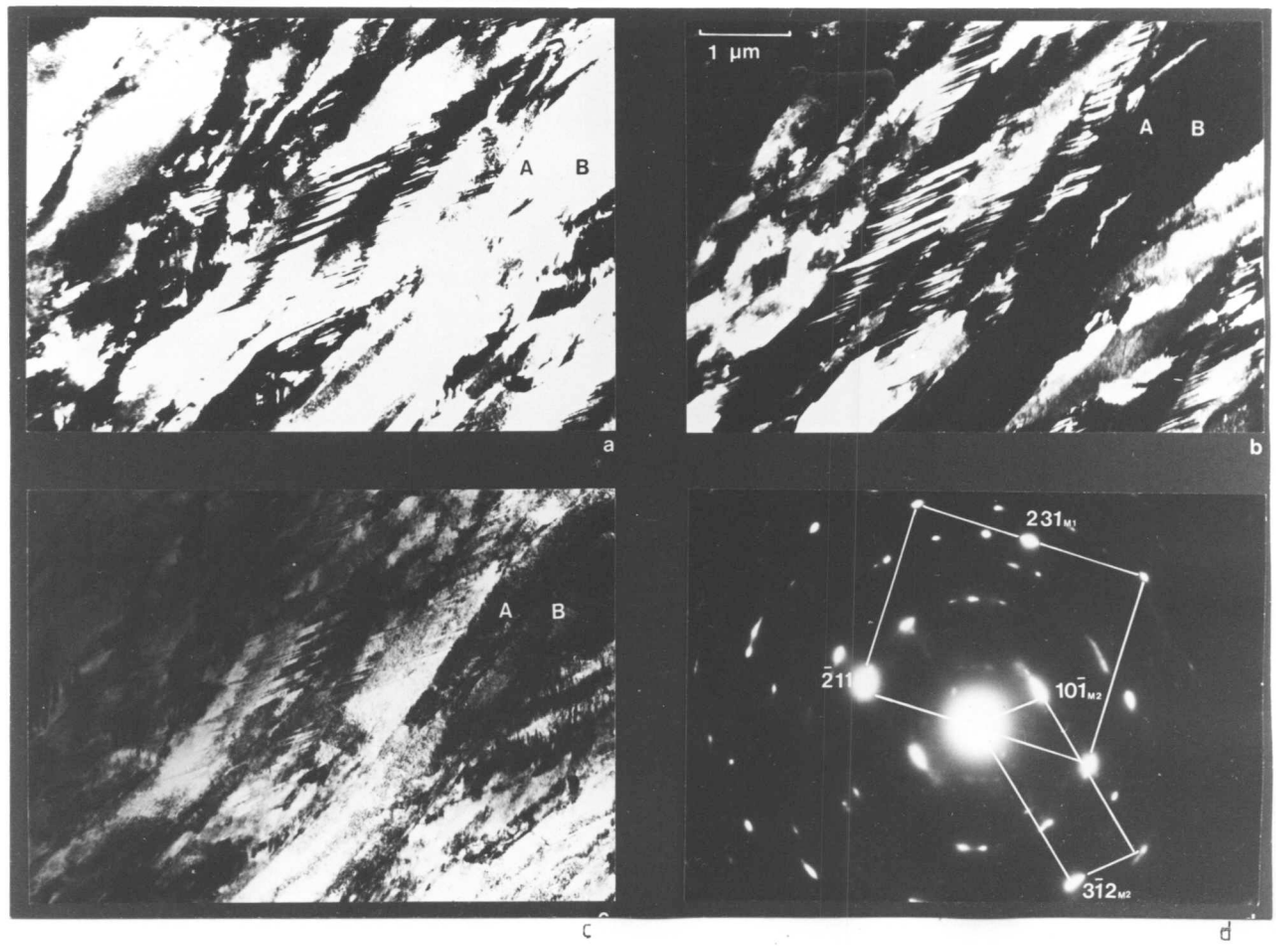

Figure VI.11.
Fe-4Ni-0.4C alloy, austenitised at 1200°C for 5 minutes and water quenched.

(a) & (b) Dark field images of twin-related martensite variants, and of internal twins within the martensite units.

(c) Bright field image. The laths marked 'A' and 'B' are in the same orientation and do not show any twinning.

(d) Corresponding diffraction pattern which can be shown to be consistent with twin-related lattices.

Figure VI.12

Diagram illustrating the solid geometry applicable to the method of inter-trace angle measurement (single surface) for habit plane determination. LMN represents the plane of section and the inter-trace angles are defined by the equations given below. One of the set of distances (a,b,c) can be taken to be unity.

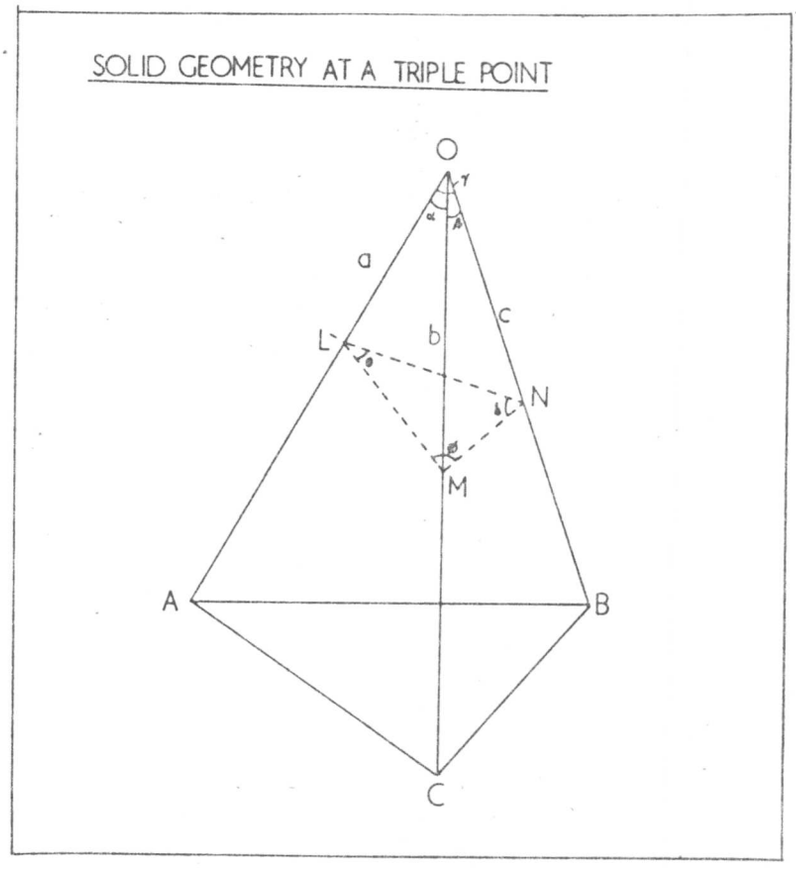

$$\cos\theta = \frac{a^2 - a\cos\alpha - ac\cos\gamma + c\cos\beta}{\left[(1 + a^2 - 2a\cos\alpha)(a^2 + c^2 - 2ac\cos\gamma)\right]^{1/2}}$$

$$\cos\phi = \frac{1 - a\cos\alpha - \cos\beta + ac\cos\gamma}{\left[(1 + a^2 - 2a\cos\alpha)(1 + c^2 - 2c\cos\beta)\right]^{1/2}}$$

$$\cos\delta = \frac{c^2 - c\cos\beta - ac\cos\gamma + a\cos\alpha}{\left[(1 + c^2 - 2c\cos\beta)(a^2 + c^2 - 2ac\cos\gamma)\right]^{1/2}}$$

For the above equations, (b) has been chosen to equal unity.

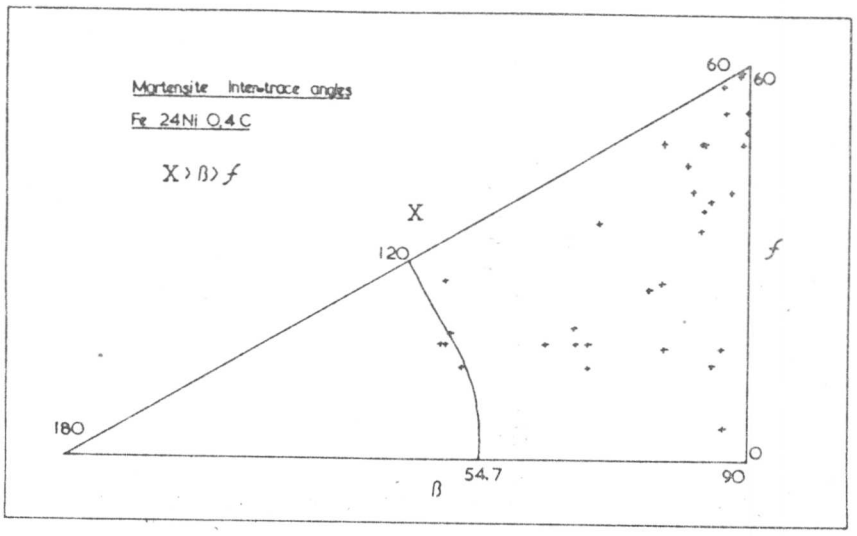

Figure VI.13
Ternary inter-trace angle diagram showing the experimental fit of the martensite habit plane in quenched Fe-24Ni-0.16C alloy with a $\{111\}_\gamma$ plane.

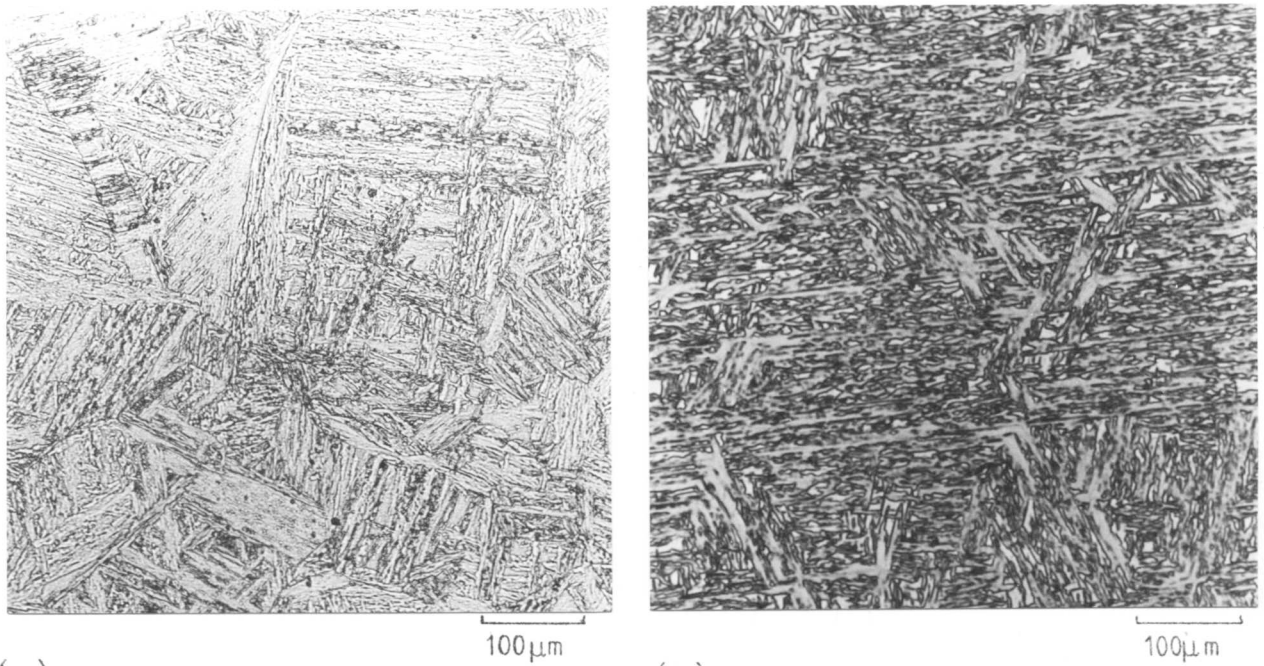

(a) (b)

Figure VI.14
Optical micrographs of lath martensite in (a) Fe-25.2Ni-1.9Mn
(b) Fe-24Ni-0.16C

(a)

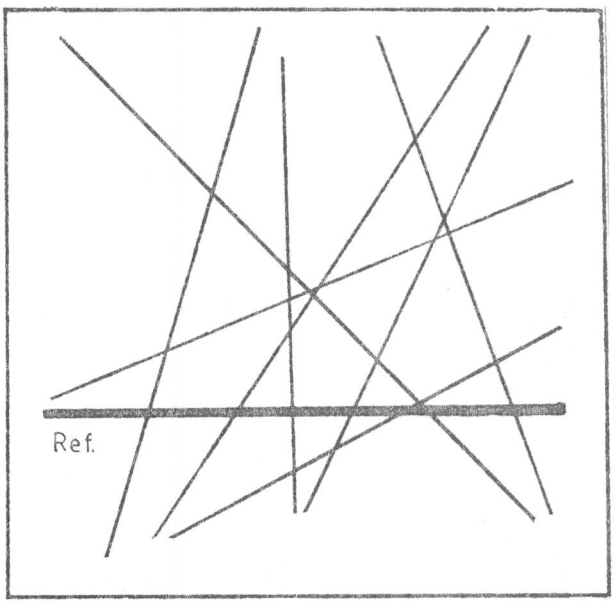

(b)

Figure VI.15

Experimental evidence to show that the inter-martensite trace angles within a prior austenite grain in Fe-25.2Ni-1.9Mn alloy are consistent with a $\{28\ 13\ 10\}_\gamma$ habit plane.

(a) Optical micrograph showing the prior austenite grain under examination.

(b) Diagram showing the relative dispositions of habit plane traces.

The following table lists the results obtained; the angles are quoted relative to the reference trace, which is arbitrarily taken to originate from a $(10\ 13\ 28)_\gamma$ plane.

Trace	Habit Plane Variant	Measured Angle	Computed Angle
1	$10\ 13\ 28$	-	-
2	$\bar{1}0\ 13\ 28$	47	47
3	$\bar{2}8\ 13\ 10$	89	83
4	$28\ \bar{1}3\ 10$	64	66
5	$13\ \bar{1}0\ 28$	23	23
6	$\bar{1}0\ \bar{2}8\ \bar{1}3$	29	33
7	$\bar{2}8\ 10\ 13$	71	76
8	$\bar{2}8\ \bar{1}0\ 13$	56	51
9	$\bar{1}3\ \bar{2}8\ \bar{1}0$	73	77

The approximate computed plane of section is $(21\ 39\ 28)_\gamma$

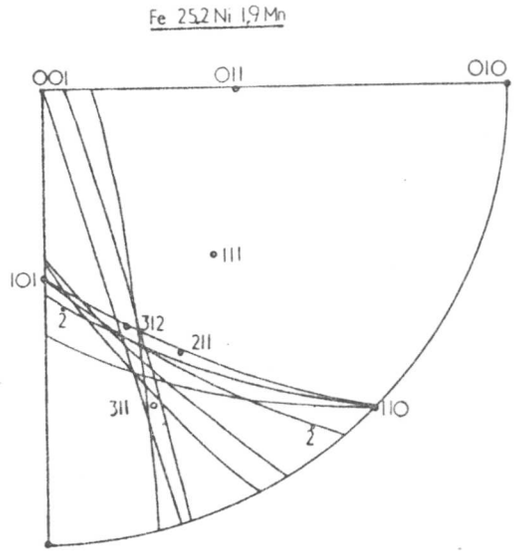

Figure VI.16
Trace analysis on the martensite in the Fe-25Ni-2Mn alloy.

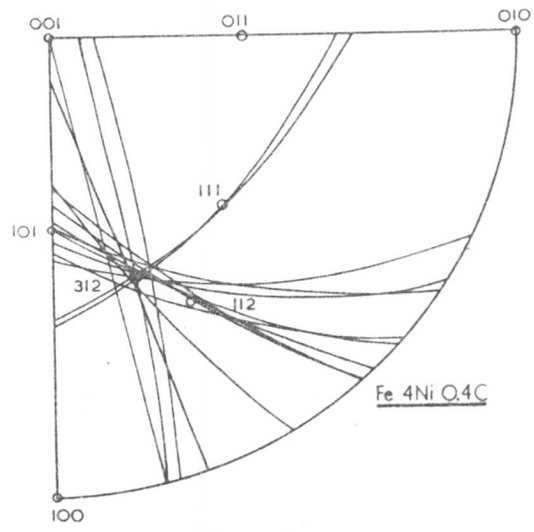

Figure VI.17
Trace analysis on the martensite in the Fe-4Ni-0.4C alloy.

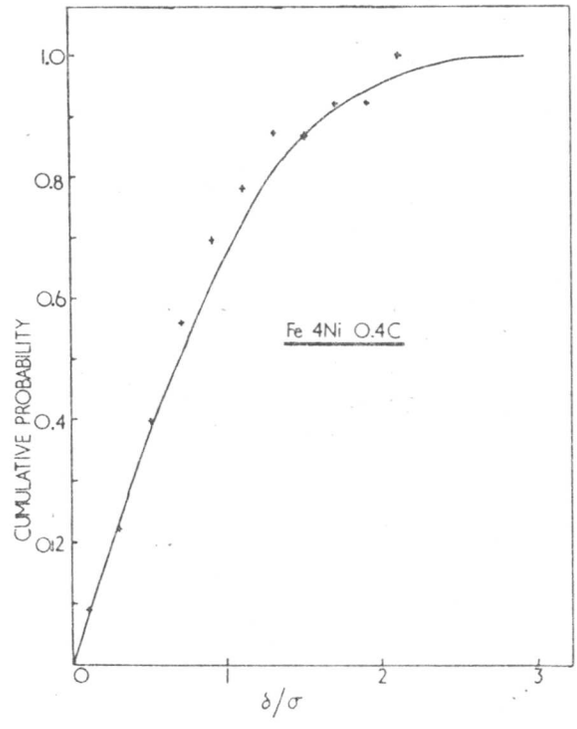

Figure VI.18
A plot of the experimental data (plotted as points) and computed cumulative probability (continuous line) of occurrance of error as a function of the normalised error δ/σ (where σ is the standard deviation of δ). The plot indicates that the observed errors could essentially be interpreted as measurement errors, of the 'Normal' type.

CHAPTER SEVEN

A DIRECT ANALYSIS OF TWINNING IN A LOW ALLOY MARTENSITE

(VII.1) Introduction

The deformation processes involved in the formation of low alloy martensites appear from microstructural observations to be essentially slip. However, extremely high dislocation densities are generally observed, such that the arrangement of the dislocations is very confused and does not give useful information on the slip systems involved. The fact that the dominant deformation process in low alloy martensite is slip is not surprising since the M_s temperatures concerned are relatively high when compared with fully twinned plate martensites. Despite the high M_s, however, incipient twinning can often be observed in low alloy martensites (142-5,Ch.VI). These twins sometimes extend only partially across the martensite units and the inter-twin spacings are generally larger and more variable than those intuitively expected from observations on well-defined plate martensites. It is not apparent whether these twins represent a mode of lattice invariant shear (and hence whether they can be useful in the application of the phenomenological theory of martensite formation) or whether they are simply manifestations of accommodation effects.

It is considered important to resolve the mechanism of formation of such twins, not only because this may lead to a better understanding of low alloy martensites (and their associated retained austenite), but also because they appear to influence the toughness of ultra-high strength steels (142-5). It has been suggested that the twins reduce toughness by reducing the available number of slip systems (142) although this idea is not firmly based since the yield strength does not appear to vary with the propensity of twinning in a given alloy (145). The situation is rather confusing, since the M_s temperature does not correlate with the presence or absence of twinning in mainly dislocated martensites (144). Furthermore, the intensity of twinning seems to vary with the austenitising conditions (145) although this evidence must be treated with caution since such determinations are based on rather qualitative observations from a limited amount of electron microscopy.

It seems important to resolve the mechanism of twin formation first, before attempting to study any interactions of twins with other properties. It was the purpose of the present work

to determine whether the twins can be described as intrinsic transformation features (similar to those found in plate martensites) or whether they result from high velocity impingements between martensite variants.

Unfortunately, it seems that the only method capable of distinguishing between the two cases entails detailed crystallographic analysis with respect to both the parent and the product phases. The lack of adequate quantities of the parent austenite phase, and the scale of the martensite microstructure in low alloy steels has excluded such an analysis in the past. In the present work, a novel method is used to enable the retention of experimentally expedient quantities of austenite, thus enabling a direct analysis of the twins in a low alloy martensite.

(VII.2) Experimental Method and Techniques

An experimental Fe-0.43C-3.00Mn-2.02Si steel of known transformation characteristics (Ch.1) was used in the present study. The M_s temperature of this alloy is 220°C and isothermal transformation at 350°C results in the formation of upper bainite (Ch.1). The upper bainite in this steel is exceptional in the sense that the high silicon content prevents the formation of carbides. Thus, the carbon which is partitioned into the residual austenite following the formation of bainitic ferrite stabilises the austenite and causes its retention following quenching to room temperature. This characteristic was exploited as described below.

A specimen was austenitised in a dynamic protective argon atmosphere at 1100°C for 20 mins and was then directly quenched into oil at 140°C. After holding at 140°C for 40 s, it was immediately up-quenched into a tin bath held at 350°C for isothermal transformation of some of the remaining austenite to upper bainite. After holding at 350°C for 25 mins, the specimen was finally water quenched. The direct quench to 140°C resulted in partial transformation to martensite, to an estimated extent of 50% by volume. This is because 140°C is below the M_s but well above the 'M_f' temperature of this alloy. The specimen was first transformed to martensite so that the carbon content of the martensite was the same as that of the alloy. The subsequent up-quench resulted in the transformation of some of the remaining austenite to upper bainite, with the accompanying carbon enrichment of the austenite between the martensite units,

and between the bainite sub-units. Thus, when the specimen was finally quenched to room temperature, the inter-martensite residual austenite was fully retained. Under normal circumstances this would have transformed to martensite.

Specimens for examination by transmission electron microscopy were prepared in the manner described in (I.2). A Philips EM300 transmission electron microscope operated at 100kV was used for this work.

(VII.3) Results and Discussion

The orientation relationship between the martensite and austenite was found by simple electron diffraction to be that of Kurdjumov and Sachs (110), (KS), i.e.

$$(111)_\gamma \;//\; (011)_{\alpha'}$$
$$[\bar{1}01]_\gamma \;//\; [\bar{1}\bar{1}1]_{\alpha'}$$

The above variant will be used as the standard variant in the analysis that follows. While it is noted that simple electron diffraction of this kind cannot give accurate orientation relationships, it will become clear later that the orientation has to be KS. This conclusion comes from the observation of twin-related martensite variants, a situation which has been shown to arise (VI.2) only with the KS orientation relationship.

Owing to the high silicon content of the alloy used, the formation of martensite is not accompanied by autotempering (I.3.i). However, due to the up-quench component of the heat treatment used for the present study, the martensite was found to be tempered, as shown in figures VII.1a,2a.

Single surface trace analysis was carried out to establish the twin plane and its relation to the austenite lattice. The analysis was always in terms of the standard correspondence stated above. The great circle representing the locus of the twin plane pole was plotted consistently and unambiguously with respect to the austenite, martensite and martensite twin lattices. The results are presented in figures VII.1,2.

For martensite twins to be transformation twins, certain symmetry requirements have to be satisfied (61). Assuming that the twins are of type 1 (involving a rotation of 180° about the pole of the twin plane), the twins have to relate adjacent martensite regions whose c-axes are variants of the c-axes of the Bain distortion. This means that the twin plane has to be

a plane of mirror symmetry with respect to the austenite lattice after transforming through the appropriate correspondence matrix. Furthermore, for the twinning system to be considered as an intrinsic transformation inhomogeneity, the twin plane must, in all cases, correspond to the same austenite mirror plane when the analysis is in terms of a standard correspondence. Thus specific Miller indices can be assigned to the twin plane (for the standard variant) and these indices have to be the same (not just of the same form) for every case examined if the twins are to be considered as transformation twins. Substitution into the phenomenological theory easily demonstrates that lattice invariant shears on different planes of the same form give different (crystallographically non-equivalent) solutions.

In figures VII.1,2 the evidence from the diffraction patterns is plotted on stereograms which also have the poles of the austenite and martensite matrix plotted in the standard KS variant. The great circles (A) and (B) represent the observed austenite and martensite matrix zones respectively, (D) represents the possible locus of the twin plane normal and (C) refers to the zone of coincidence. The zone of coincidence is defined as the zone obtained by superimposing the martensite matrix and twin stereograms in the correct relative orientation such that on this zone, twin and matrix poles of the same form are coincident. Furthermore, this zone must also contain all the coincident $\{110\}_{\alpha'}$ and $\{112\}_{\alpha'}$ poles. Assuming that the twin plane will either be $\{110\}_{\alpha'}$ or $\{112\}_{\alpha'}$ and that the twin boundary corresponds to the twinning plane, the intersection of (C) and (D) defines the twin plane. The former assumption takes account of the fact that the $\{110\}_{\alpha'}$ and $\{112\}_{\alpha'}$ planes are the most likely twin planes in BCC lattices (146) while the latter assumption is based on the fact that the energy of a twin boundary is a minimum when the composition plane coincides with the twin plane (147).

In figure VII.1 the twin plane is seen to be $(\bar{1}12)_{\alpha'} \equiv (011)_{\gamma}$ while that in figure VII.2 is $(112)_{\alpha'} \equiv (101)_{\gamma}$. This is despite the fact that they have both been plotted in the standard variant of the orientation relationship. In figure VII.1 the twin is not a variant of KS whereas in figure VII.2 it is. We can therefore conclude that since the twin plane does not uniquely correspond to a particular austenite mirror plane, the twins cannot be an intrinsic transformation feature and must be

attributed to accommodation effects.

Some rather spectacular physical evidence for this can be seen from the micrographs of figures VII.1,2. In fig.VII.1 the martensite matrices of the adjacent martensite plates are not twin related. The incidence of twinning is observed to be low and the twins are fine. On the other hand, in fig.VII.2, the adjacent martensite variants are twin related and dark field imaging shows extensive twinning; often large areas of the laths are twinned. In the latter case, since the two martensite variants are twin related, the nucleation of mechanical twins would be easier, and furthermore, the transmission of deformation across twin related lattices would be easier compared relative orientations. Hence accommodation of transformation strains would be easier for twin related martensite variants.

(VII.4) Summary

It has been found that the twinning observed in the martensite of an Fe-Mn-Si-C low-alloy steel is an accommodation phenomenon since the twin planes show inconsistent correspondence relative to austenite when analysed in terms of the standard variant of the orientation relationship.

The extent of twinning can be understood on the basis of the above conclusion and upon considering the inter-martensite orientations. It is possible that the intensity of twinning would be reduced if the martensite can be designed to adopt an orientation relationship other than KS.

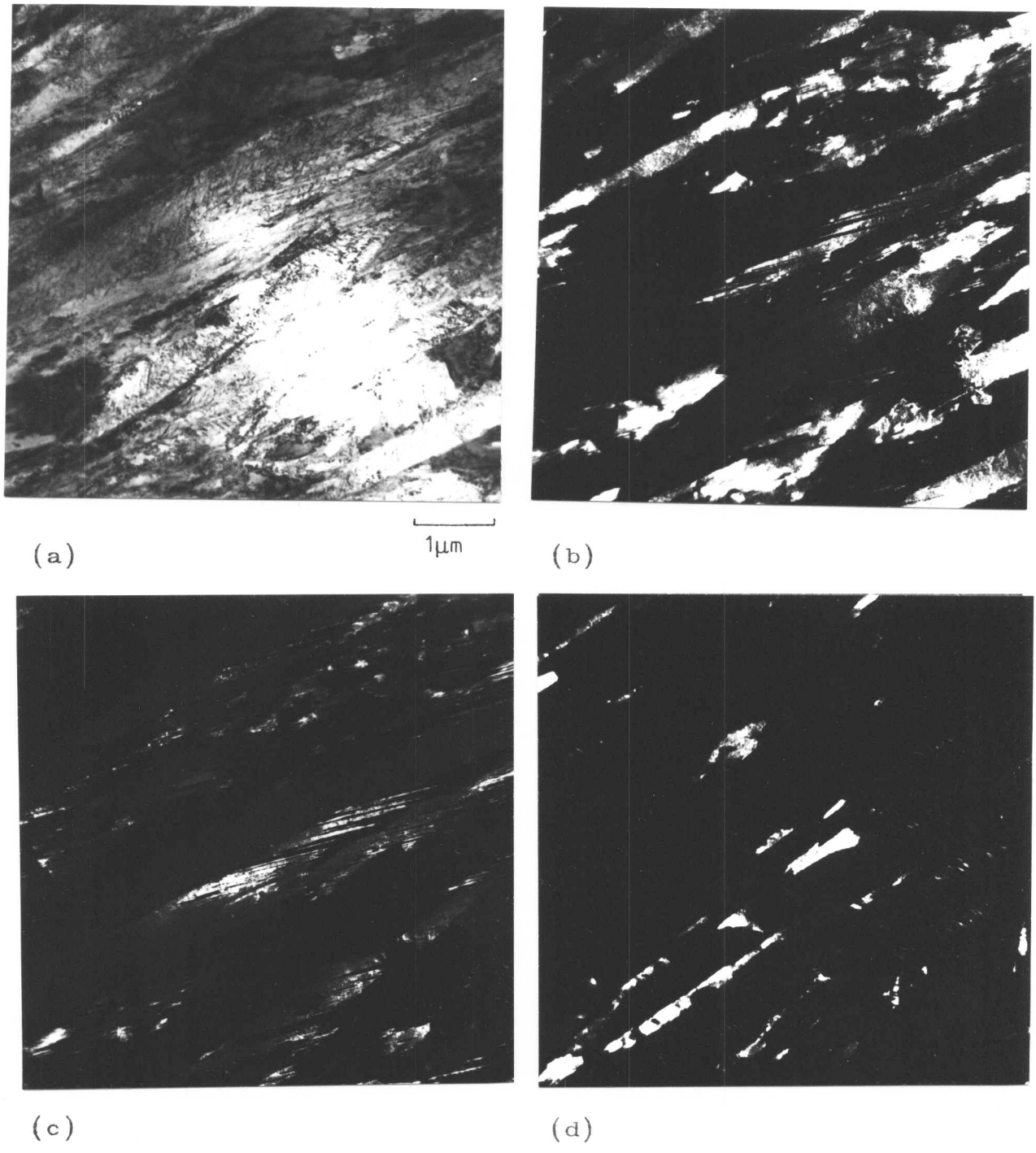

Figure VII.1

(a) Bright field image.

(b) Matrix martensite dark field image.

(c) Martensite twin dark field image.

(d) Retained austenite dark field image.

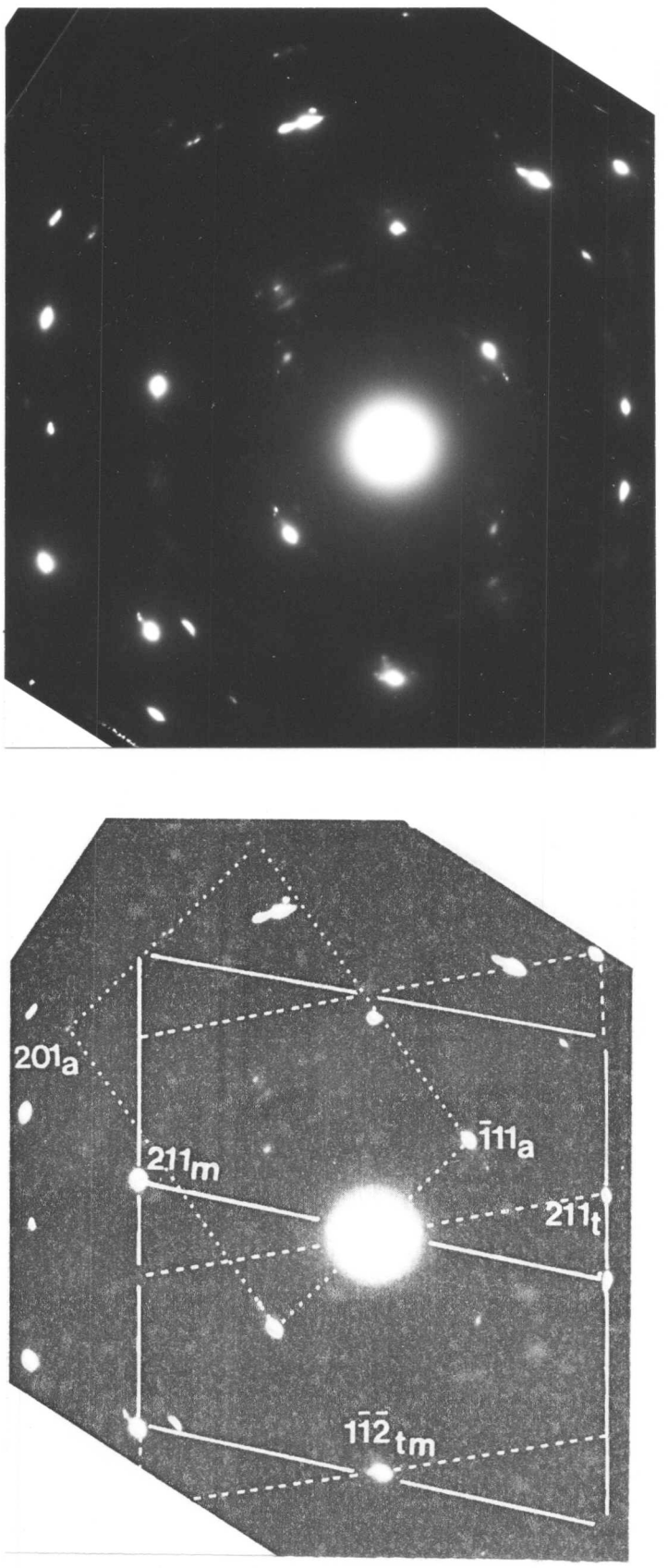

Figure VII.1e.i

Diffraction pattern showing twin-related $\langle 135 \rangle_\alpha$ zones and $[123]_\gamma$ zone.

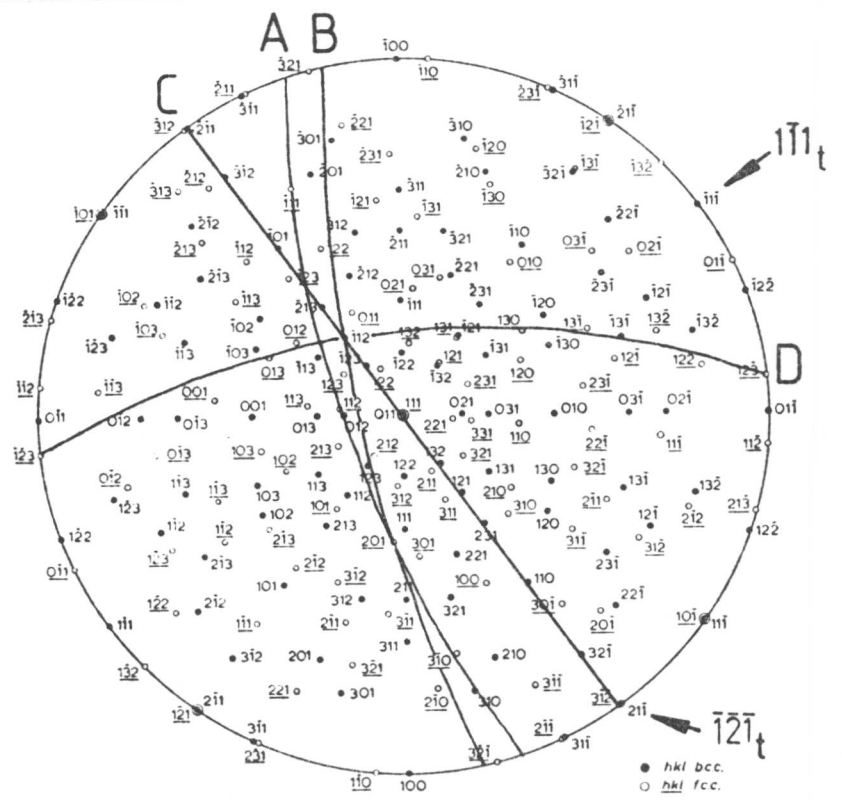

Figure VII.1e.ii

Corresponding stereographic analysis.

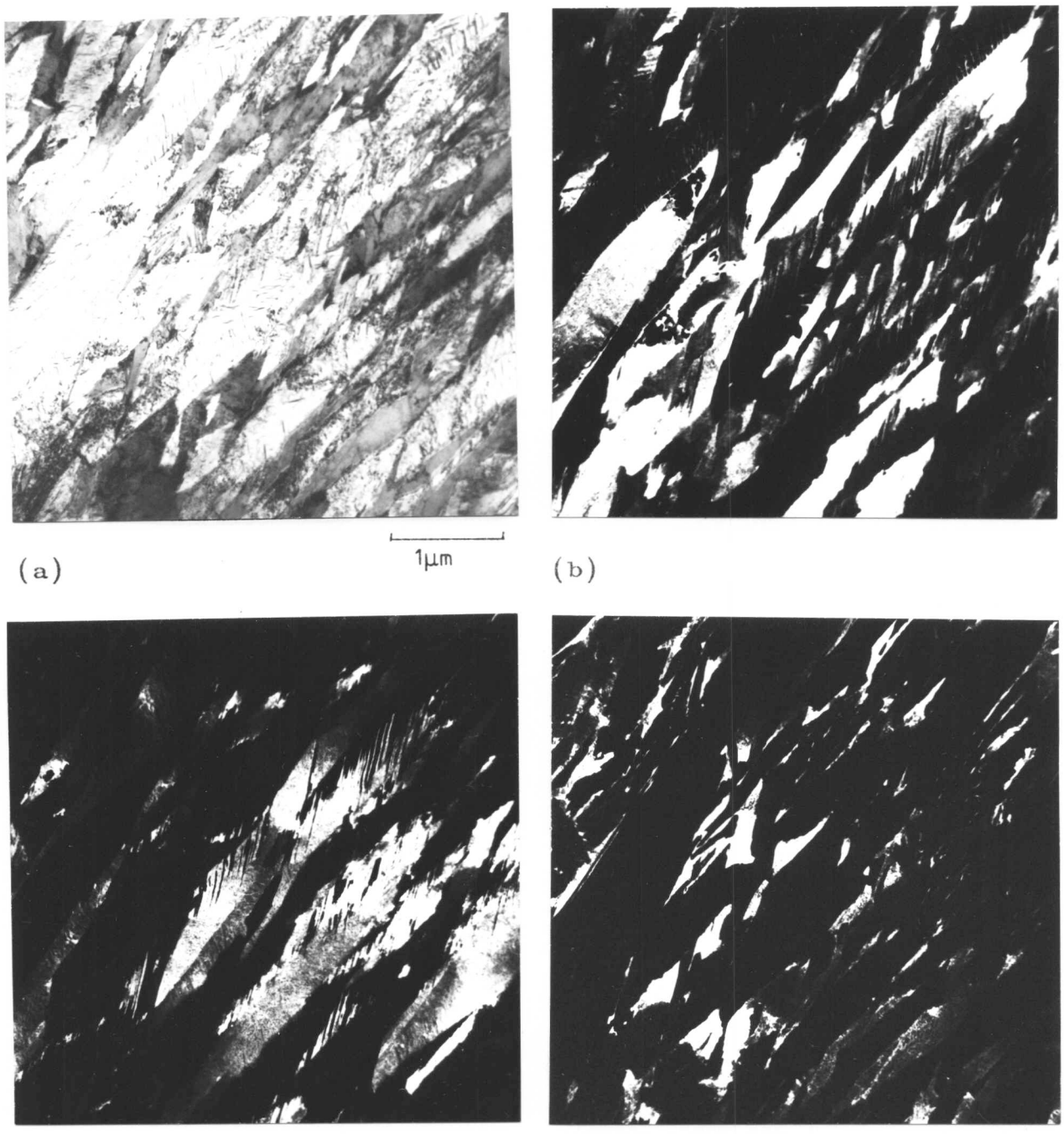

Figure VII.2

(a) Bright field image.

(b) Matrix martensite dark field image.

(c) Martensite twin dark field image.

(d) Retained austenite dark field image.

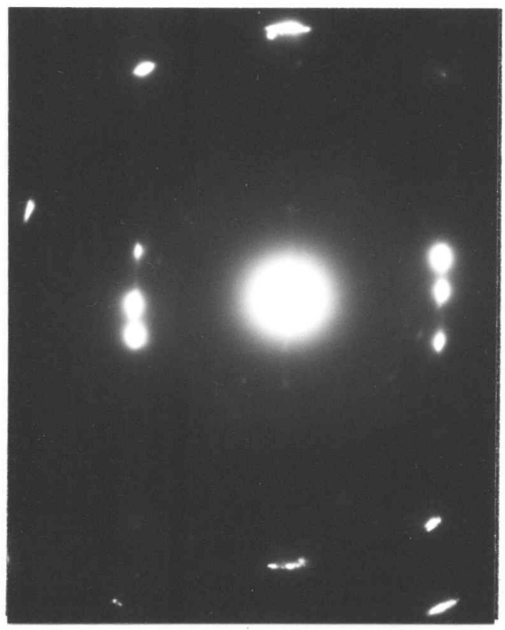

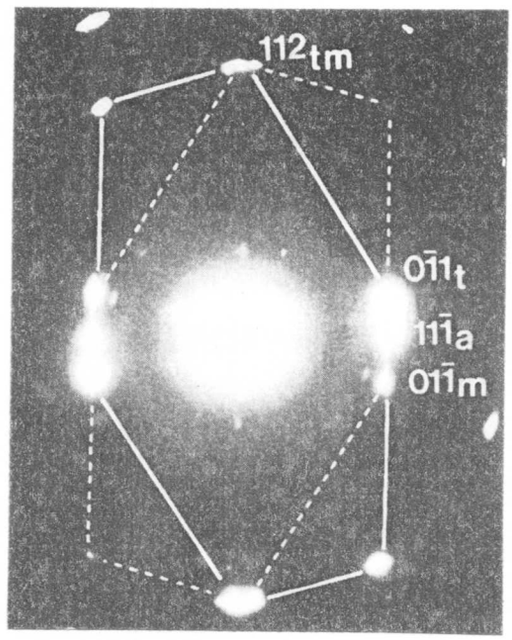

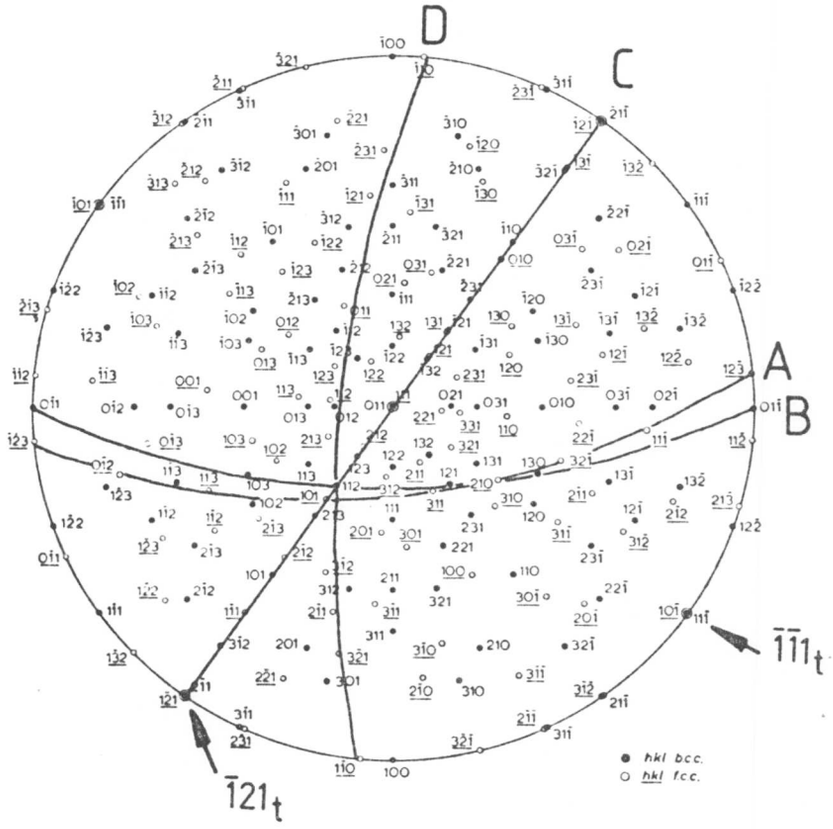

Figure VII.2e

Diffraction pattern showing twin-related $\langle 113 \rangle_{\alpha'}$ zones and corresponding stereographic analysis.

CHAPTER EIGHT

AN ANALYSIS OF THE MECHANICAL PROPERTIES AND MICROSTRUCTURE OF A HIGH-SILICON DUAL-PHASE STEEL

(VIII.1) Introduction

The simple method of mixtures analysis used to describe the strength variations of the silicon upper bainite was shown to be rather inadequate in (III.3.ii). The point was made that a more sophisticated model would be necessary in order to understand the interactions between the various components of the microstructure.

The aim of the present work was to evaluate two available deformation models. Such evaluation was considered necessary because there are some apparent discrepancies (which will become evident later) associated with the application of such models.

An additional difficulty is that such models require very detailed input data, of the type not yet available for the upper bainitic microstructure. Furthermore, for the purpose of model evaluation, it seemed expedient to use a simpler microstructure; since the dual-phase steel microstructure (to be described below) appears to be eligible in this respect and is at the same time of considerable industrial importance, it was chosen to be the test microstructure.

The term dual-phase steels has been used to describe the product of recent process/structure modifications to conventional HSLA steels. They can most conveniently be defined as low-carbon low-alloy ferritic steels with an aggregate microstructure of ferrite and a non-pearlitic hard phase (e.g. martensite). Their potential as superior strength and formability substitutes for current automotive steels in the USA was early realised (148-9) and has provided an incentive for their rapid development and acceptance in this role. This successful application has preceded the acquisition of a complete understanding of the detailed relationships between their process route, microstructure and mechanical properties, although considerable research has been carried out in order to optimise the variables in the strength and formability balance.

Steel composition has been one of the aspects studied, and it appears that the use of high silicon additions (2 wt. pct.) results in better combinations of strength and formability (150-3).

In solid solution, silicon not only increases strength, but its presence also raises the tensile stress to yield stress ratio, while at the same time eliminating discontinuous yielding (150). This last point is important in the avoidance of stretcher strain markings during forming operations. Relative to its capability to increase strength, silicon has a minimal detrimental effect on ductility (151). Silicon is also known to retard martensite tempering reactions (23-25) and often eliminates autotempering altogether (Ch.1). This effect should increase the strength of the martensitic component of dual-phase structures since carbon will then remain in interstitial solid solution in the martensite lattice.

The hardenability of dual-phase steels is generally critically balanced in order to achieve the necessary microstructure using continuous production processes, while at the same time being compatible with the weldability, strength and ductility requirements. However, little attention has been paid to the detailed microstructure of the hard phase, which is in turn a function of the hardenability of the residual austenite. In the case of high-silicon heat treatable steels, it has been shown that the best strength and toughness combination is achieved with a homogeneous upper bainitic microstructure (Ch.III). It should be noted that upper bainite in high-silicon steels consists of alternating layers of high-carbon retained austenite and 'interstitial free' dislocated bainitic ferrite (Ch.I). Furthermore, the properties of high-silicon steels are extremely structure sensitive (Ch.III). In the present study the mechanical properties and microstructure of an experimental high-silicon dual-phase steel are examined in detail.

The most important property characteristic of dual-phase steels, at least so far as their application in cold-pressing operations is concerned, is their high strain hardening coefficient. A high strain hardening coefficient, or n-value, stabilises tensile deformation against local instability and results in a greater degree of uniform elongation. In order to test the experimental behaviour of dual-phase steels, and eventually to achieve a predictive capability for structure-property relationships, a working model of the deformation of a composite consisting of two ductile components is required. Before the experimental results of the present work are considered, an evaluation is made of two available deformation models.

(VIII.2) Deformation Models

A model successfully used (154-5) to obtain the deformation parameters of dual-phase steels is that due to Mileiko (156). The use of Mileiko's theory has been stimulated by its capability to predict directly the strain hardening coefficient (the latter being equivalent to the true uniform elongation of a ductile phase) of the composite concerned. The relationship between the volume fraction, V, of the second phase and the mechanical properties of the composite and of the component phases is given by

$$V = \frac{1}{1 + \beta \frac{\varepsilon_c - \varepsilon_m}{\varepsilon_f - \varepsilon_c} \varepsilon_c^{\varepsilon_m} \varepsilon_f} \qquad \text{Equation VIII.1}$$

where $\beta = (\sigma_m \varepsilon_f^{\varepsilon_f} \exp \varepsilon_m) / (\sigma_f \varepsilon_m^{\varepsilon_m} \exp \varepsilon_f)$ Equation VIII.1a

and σ_m and σ_f are the true tensile strengths of the martensite (or any other hard phase) and ferrite respectively, and ε_c , ε_m and ε_f are the true uniform strains for the composite, martensite and ferrite respectively. The relationship is valid when the true stress/true strain behaviour of the composite and of the component phases can be represented by a power law of the form:

$$\sigma = K \varepsilon^n \qquad \text{Equation VIII.2}$$

where K is the strengthening coefficient.

However, the critical assumptions of this model require, firstly, equal strain distributions in both the hard and soft phases, and secondly, continuity of the phases in the tensile direction. Hence, the conclusions drawn by the application of Mileiko's theory to dual-phase steels have been criticised recently (157), especially as it has been shown (157) that different deductions, particularly with respect to strength/formability ratios, can be made by assuming non-uniform strain in the component phases.

Despite the above setbacks, it is apparent that Mileiko's theory does indeed give reasonable agreement with experimental data on the dual-phase steels examined thus far (154-5). The reasons for this agreement are not clear and it was felt that a more detailed analysis was necessary. The availability of a more general two-phase deformation theory developed by Tomota et al.(henceforth referred to as Tomota's theory, ref. 158)

where the internal stresses produced by inhomogeneous deformation are taken into account allows the detailed examination of the deformation behaviour involved. Furthermore, the latter theory applies to the case where the harder (or softer) phase is randomly distributed as grains of ellipsoidal shape (the random distribution ensures an effect approximating spherical grains) and is therefore more representative of dual-phase steel microstructures. Additionally, the stress and strain distributions can be followed at every stage of the deformation process. By this theory, the applied stress before the onset of plastic deformation in the hard phase is given as

$$\sigma_{33}^{A} = \sigma_f' \left| \frac{\bar{\varepsilon}_p}{1-f} \right| + \frac{f}{(1-f)} \bar{\varepsilon}_p \qquad \text{Equation VIII.3}$$

where $\bar{\varepsilon}_p = (1-f)\varepsilon_p'$ Equation VIII.3a

(Nomenclature listed in table VIII.1)

and the onset of plastic flow in the harder phase is represented by the following set of simultaneous equations:

$$Y(II) = \sigma_f' \left| \frac{\bar{\varepsilon}_{p(II)}}{1-f} \right| + \frac{f}{(1-f)} A\bar{\varepsilon}_{p(II)} \qquad \text{Equation VIII.4}$$

$$Y(II) = \sigma_y'' - A\bar{\varepsilon}_{p(II)} \qquad \text{Equation VIII.5}$$

Further deformation is calculated for small strain increments from the following simultaneous equations:

$$\sigma_f' \left| \varepsilon_{p(II)}' + \delta\varepsilon_p' \right| = \sigma_{33}^{A} - fA[\varepsilon_{p(II)}' + (\delta\varepsilon_p' - \delta\varepsilon_p'')] \qquad \text{Equation VIII.6}$$

$$\sigma_f'' |\delta\varepsilon_p''| = \sigma_{33}^{A} + (1-f)A[\varepsilon_{p(II)}' (\delta\varepsilon_p' - \delta\varepsilon_p'')] \qquad \text{Equation VIII.7}$$

Elastic deformation results in the term (σ_{33}^{A}/E) being added to the plastic strain of the alloy.

Thus the complete stress-strain curve can be computed and it follows that so can the strain hardening coefficient when the latter curve (or its segments) can be represented by the empirical equation, $\sigma = K\varepsilon^{n}$. In the analysis that follows, equations of the above form were used to represent the flow stresses of the individual components and of the composite. The strain increment $\delta\varepsilon_p'$ was taken as 0.01 and it was assumed that the modulus is the same for all phases. The yield stresses were taken as the true stress at $\varepsilon_t = 0.002$.

Mileiko's theory has been successfully applied to analyse the deformation of a zero-carbon ferrite/martensite structure in

Fe-3Ni-3Mo (154), and a ferrite/martensite structure in a vanadium HSLA steel, Fe-0.15C-1.5Mn-0.11V, (155). Considering first the data presented in reference (154) for the Fe-3Ni-3Mo alloy, the following deformation parameters can be listed:

σ_y'' = 705 MPa K_m = 1113 MPa

n_m = 0.06 K_f = 369 MPa

n_f = 0.24

The results of the inhomogeneous deformation analysis by Tomota's method are plotted in fig.VIII.1 and it is clear that the predictions are essentially the same as those of Mileiko's model. The reason for this becomes apparent from fig.VIII.2, which shows the plastic strain in the ferrite as a function of that in the martensite, calculated using Tomota's theory. It is clear that the plastic strain difference between the two components is very small, so that the equal strain model is applicable. This agreement with Mileiko's theory arises due to the relatively small amount of plastic strain in the ferrite prior to the onset of plastic flow in the martensite.

Similarly, application of the inhomogeneous deformation model to the data of ref.155 for the vanadium HSLA steel showed that the plastic strain difference between the ferrite and martensite components was also sufficiently small to give similar results to those predicted by Mileiko's theory, figs.VIII.3,4. In this analysis the following deformation parameters were used:

σ_y'' = 1500 MPa K_m = 2448 MPa

n_m = 0.08 K_f = 690 MPa

n_f = 0.31

The values of the strengthening coefficients were calculated from the tensile strength values quoted in (155), assuming failure by the ductile mode so that $\sigma_{uts} = K n^n$.

(VIII.3) Experimental Procedure

A 2kg melt of the experimental alloy was prepared from pure constitutents in a vacuum induction furnace, and the final analysis was Fe-0.04C-0.63Mn-2.01Si-0.1V. The ingot was hot worked down to 8 mm diameter rod by forging and swaging operations.

During austenitising treatments, the specimens were doubly protected by a dynamic argon atmosphere and a proprietary anti-decarburising compound. The heat treatments were carried out in

a resistance heated tube furnace.

Tensile specimens were machined [from heat treated blanks] with a 50 mm parallel length and a 3 mm diameter. They were tested on an Instron testing machine instrumented with a 25 mm gauge length linearly variable differential transformer extensometer. This was attached to the specimen for only a part of the test and the final uniform elongation was measured from 5 mm gauge lengths previously marked on the specimen parallel length, taking care that the measurement was well away from the position of the necked region.

Specimens for transmission electron microscopy were cut from the tensile specimen blanks as 3 mm diameter discs with a thickness of 0.25 mm. The discs were subsequently thinned and electropolished in a twin-jet polishing unit using a 25% glycerol, 5% perchloric acid and 70% ethanol mixture at room temperature and 55V. The foils were examined in a Philips EM300 microscope operating at 100 kV.

Quantitative metallography was carried out on a Quantimet image analysing computer.

(VIII.4) Results and Discussion

(i) Microstructural Observations

The volume fractions of hard phases obtained by various heat treatments are listed in table VIII.2. Using these data, and the fact that the formation of poreutectoid ferrite involves the partitioning of carbon into the residual austenite, the carbon content of the hard phase region was estimated on the assumption that the proeutectoid ferrite contained 0.02% carbon in solid solution. The latter assumption is approximate since the exact carbon content of the ferrite will depend on the cooling rate from the transformation temperature. The hardenability of the residual austenite, which is expected to be a sensitive function of its carbon content, will therefore also be a function of the volume fraction of transformation to ferrite. Hence, microstructural differences can be expected with varying ferrite volume fractions. This is particularly true for the present steel where the very low average carbon content imparts poor hardenability.

Air cooling from the austenitising temperature resulted in a microstructure of proeutectoid ferrite and extremely small islands of fine pearlite, the lamellae of which could be resolved by

transmission electron microscopy. The volume fraction of the pearlitic phase was approximately 0.03. (Fig.VIII.5).

Direct quenching into water or iced-brine from 1130°C (well above the Ae_3 temperature) gave up to 23% upper bainite.(Fig.VIII.6). This bainite was similar to that observed in higher carbon silicon containing steels (Ch.I) and consisted of dislocated bainitic ferrite laths separated by discontinuous films of carbon-enriched retained austenite. Additionally, it seemed that the islands of residual austenite transformed into a single crystallographic variant of upper bainite, rather than several variants (partitioning behaviour) as was the more usually observed mechanism in higher carbon steels. The latter observation is probably a manifestation of the fact that the kinetics of bainitic ferrite growth are markedly accelerated by a decrease in carbon content, so that in contrast to the higher carbon silicon steels, the first variant to nucleate will develop rapidly and consume the whole of the austenite region. Furthermore, the particular variant corresponding to the adjacent proeutectoid ferrite will find nucleation relatively easier and will therefore be favoured. This is illustrated in fig.VIII.6 where the bainitic ferrite plate (arrowed) has the same orientation as the adjacent proeutectoid ferrite. The morphology and discontinuous nature of the austenite films is probably due to the low carbon contents involved.

When the quench rate was increased by quenching into agitated iced-brine from a higher austenitising temperature (1310°C), the volume fraction of bainite increased to about 0.35 since there was less time available for the proeutectoid ferrite transformation during the quench, fig.VIII.7.

Quenching from lower austenitising temperatures (970-920°C) into agitated iced-brine resulted in a hard phase microstructure consisting of platelet martensite separated by films of retained austenite. Autotempering was not evident in the martensite, which was occasionally found to be twinned, fig.VIII.8.

The ferrite grain size was measured by lineal analysis and the intersections of test lines with the interfaces between hard phase and proeutectoid ferrite were included in the determinations. It is seen from table VIII.2 that the effective ferrite grain size does not vary markedly despite the wide variation in transformation conditions. In view of this, and the fact that uniform elongation is essentially unaffected by ferrite

grain size (152), the latter is not taken into account in the analysis of mechanical properties that follows.

(ii) Mechanical Properties

The deformation parameters obtained are listed in table VIII.3. The true stress-true strain curves were found to be accurately represented by equation VIII.2. These curves are plotted in fig.VIII.9 and the variations of the strain hardening and strengthening coefficients as a function of the volume fraction of hard phase are plotted in fig.VIII.10. In the case of the air-cooled specimen, use of eqn.VIII.2 is only approximate and leads to an underestimation of flow stress at high strains. However, the disagreement is sufficiently small for the purposes of the following calculations. The data from the air-cooled specimen was taken to be approximately representative of the deformation characteristics of pure ferrite in the present steel since it contained only 3% pearlite.

The first stage of deformation was analysed in terms of eqn.VIII.3 when it was assumed that at $\varepsilon_t = 0.002$, there was zero plastic strain in the hard phase, fig.VIII.11a. This assumption was necessary due to the absence of data for this alloy in the pure bainitic or martensitic states; 100% transformation to these microstructures was impossible due to the low hardenability of the alloy used. By systematically varying σ_y'', K_m, n_m, it proved possible to estimate the most likely values of these parameters by noting the set which gave best fit with the experimental composite stress-strain parameters. Thus, the following values were deduced:

Bainite	Martensite
$\sigma_y'' = 1000$ MPa	$\sigma_y'' = 1300$ MPa
$K_m = 5200$ MPa	$K_m = 6500$ MPa
$n_m = 0.300$	$n_m = 0.327$

The above values are considered to be realistic for the high-silicon microstructures, and compare well with the values obtained for an Fe-0.3C-3Cu-1Si alloy, isothermally transformed at 510°C to give a microstructure of silicon upper bainite and some martensite (this work was done by the present author during the early stages of the investigations of Ch.I, in order to establish a suitable experimental alloy for such investigations). The strain hardening coefficient in the latter microstructure was

found to be 0.48, the strengthening coefficient was 3130 MPa and the yield stress was 980 MPa.

Comparison of the experimental data with the values predicted by Tomota's theory using the above parameters, is illustrated in fig.VIII.11. Using the above deformation parameters, Mileiko's theory was found to overestimate considerably the composite strain hardening coefficients (at f = 0.1, n_c = 0.21, and at f = 0.2, n_c = 0.23). The reason for this can be understood from fig.VIII.12, which shows the variation of plastic strain in the two components. In the present steel, the deformation characteristics of the bainite and martensite on the one hand, and ferrite on the other, are sufficiently different to give extremely inhomogeneous strain distribution. Thus much of the deformation is concentrated in the ferrite. Since the intrinsic strain hardening coefficient of the latter is low, the general composite strain hardening coefficient will be lower than that predicted by an equal strain deformation model. The requirements of Mileiko's theory are clearly not justified with the present steel and agreement is poor.

Tomota's theory, however, gives good agreement with the experimental data and this reflects the more general applicability of the model to dual-phase steels. (It should be noted that while the failure to obtain 100% hard phase microstructures in the present experimental steel prevented the full predictive use of Tomota's theory, the calculated best fitting deformation parameters for the hard phases concerned are realistic.)

From table VIII.3 it is noted that the uniform elongation (as determined by measurements made on the gauge length well away from the necked region) does not in fact correspond to the magnitude of the strain hardening coefficient, but shows a negative correlation. This is attributed to the fact that the hard phases concerned fail prematurely in a non-ductile manner due to the rapid strain hardening.

(VIII.5) Summary

The applicability of Mileiko's theory to dual-phase steels has been compared with that of a more general two phase deformation model due to Tomota et al. Published data on dual-phase steels was found to be consistent with the latter model, with the predicted behaviour also being very similar to that found using Mileiko's theory. The apparently good agreement between the experimental results and the predictions using Mileiko's theory was shown to be due to the approximately homogeneous strain distribution (a necessary assumption of Mileiko's model) in the hard and soft phases of the steels whose data was analysed. The greater applicability of Tomota's theory is clear, not only from its less restrictive assumptions as far as dual-phase steels are concerned, but because by using an experimental steel it was demonstrated that Tomota's theory could be equally applied to situations of inhomogeneous strain distribution whereas that of Mileiko expectedly gave poor agreement.

The microstructure of the hard phases obtainable in the experimental high-silicon dual-phase steel used for the above analysis were also characterised in detail by transmission electron microscopy. Depending on the heat treatment condition the hard phase structures were identified either as martensitic plates separated by thin films of retained austenite, or as carbide-free upper bainitic ferrite plates, also associated with carbon-enriched retained austenite.

TABLE VIII.1

Symbol	Meaning
σ'_y	True yield stress for softer phase
σ''_y	True yield stress for harder phase
f	Volume fraction of harder phase
E	Young's modulus, taken to be 210 GPa
υ	Poisson's ratio, taken to be 0.33
ε'_p	True plastic strain in softer phase
ε''_p	True plastic strain in harder phase
$\varepsilon'_{p(II)}$	Critical plastic strain in soft phase to start yield in hard phase
$\varepsilon_{p(II)}$	Critical average plastic strain to start yield in hard phase
$\bar{\varepsilon}_p$	True average plastic strain
$Y(I)$	True average stress at the onset of flow in soft phase
$Y(II)$	True average stress at the onset of flow in hard phase
σ^A_{33}	True applied stress
$\delta\varepsilon'_p$	Strain increment in soft phase
$\delta\varepsilon''_p$	Corresponding strain increment in hard phase
σ'_f	True flow stress in soft phase
σ''_f	True flow stress in hard phase
A	$E(7 - 5\upsilon)/(10[1 - \upsilon^2])$
ε_t	Total true strain
n	Strain hardening coefficient
K	Strengthening coefficient
m	Subscript denoting hard phase

TABLE VIII.2**

Heat Treatment	(C)	Volume fraction of hard phase	Grain size μm
a) 10 min @ 1130°C, AC	.62	.03	23
b) 10 min @ 1130°C, WQ	.11	.22	16
c) 10 min @ 1130°C, IBQ	.11	.23	14
d) 5 min @ 1300°C, AIBQ	.08	.33	18
e) 10 min @ 920°C, AIBQ	.25	.09	30
f) 10 min @ 970°C, AIBQ	.16	.15	24
g) 10 min @ 935°C, AIBQ	.21	.11	22

**Notation

WQ = Water Quenched

AC = Air cooled

IBQ = Iced Brine Quench

AIBQ = Agitated Iced Brine quench

(C) = Carbon content of the hard phase region assuming that the carbon level in the proeutectoid ferrite is 0.02 wt.pct.

Specimen (a) contained pearlite, (b),(c), and (d) contained upper bainite and (e), (f) and (g) contained martensite.

TABLE VIII.3

	n	K/MPa	UTS/MPa	True uniform elongation	True stress at ε = 0.002/MPa
a)	0.066	504	529	0.153	337
b)	0.144	956	657	0.119	385
c)	0.153	1042	674	0.106	397
d)	0.174	1322	738	0.075	435
e)	0.132	839	629	0.142	372
f)	0.165	1041	659	0.102	368
g)	0.156	1005	656	0.102	383

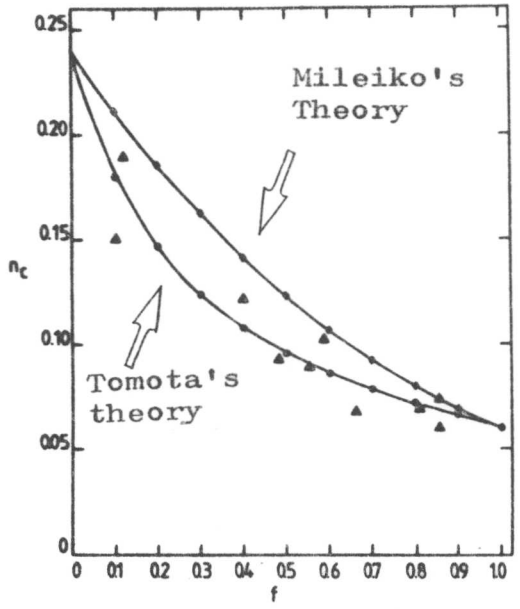

Figure VIII.1
Composite strain hardening coefficient vs. volume fraction of hard phase. The triangular points are from ref.154.

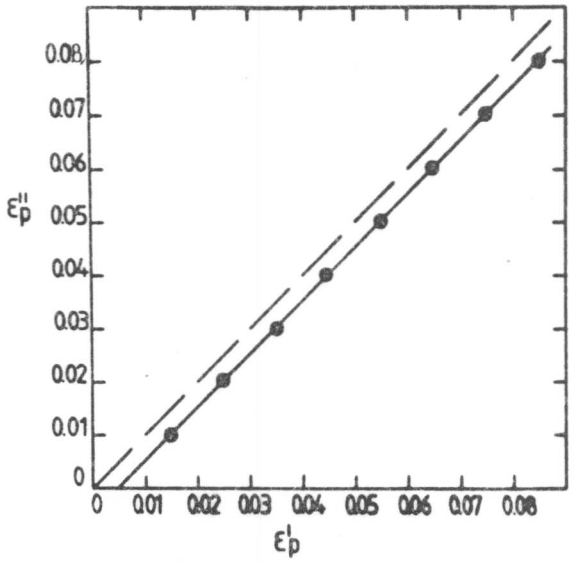

Figure VIII.2
Calculated cumulative plastic strain in the hard phase vs. that in the soft phase. The dashed line represents an equal strain situation.

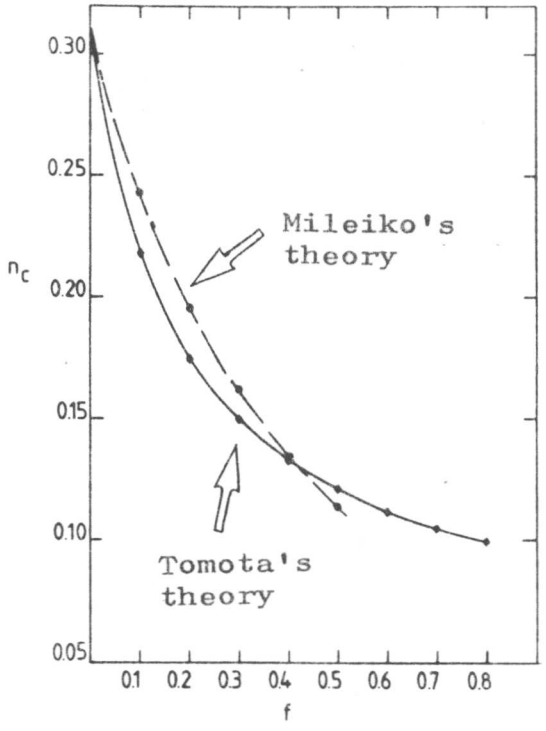

Figure VIII.3
Composite strain hardening coefficient vs. volume fraction of hard phase using the parameters listed in ref.155.

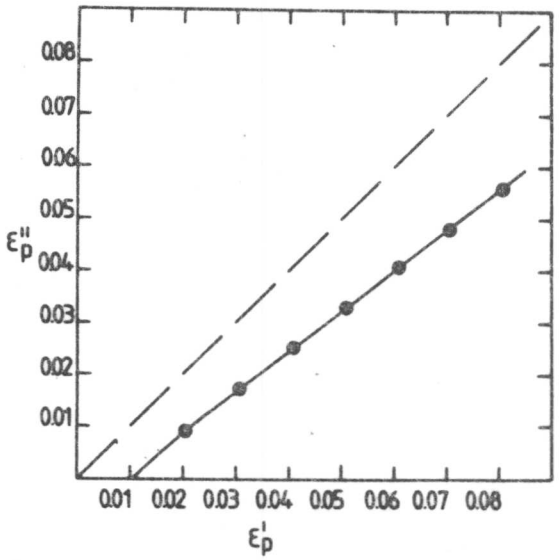

Figure VIII.4
Calculated cumulative plastic strain in the hard phase vs. that in the soft phase. The dashed line represents an equal strain situation.

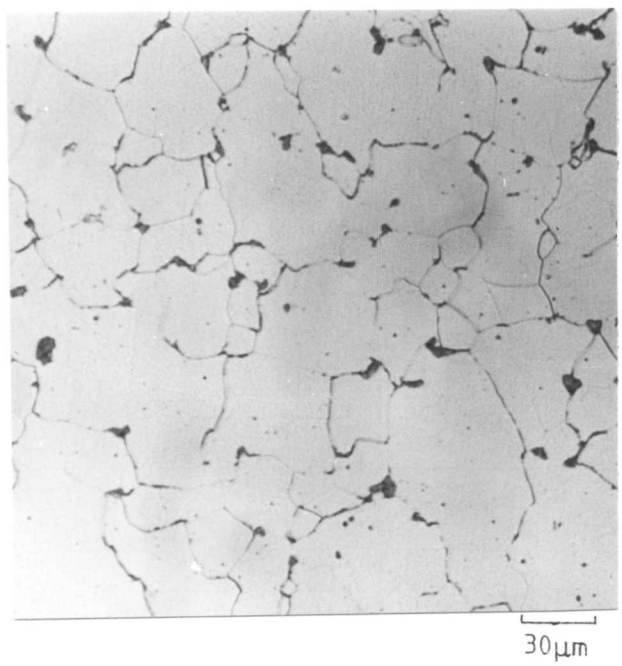

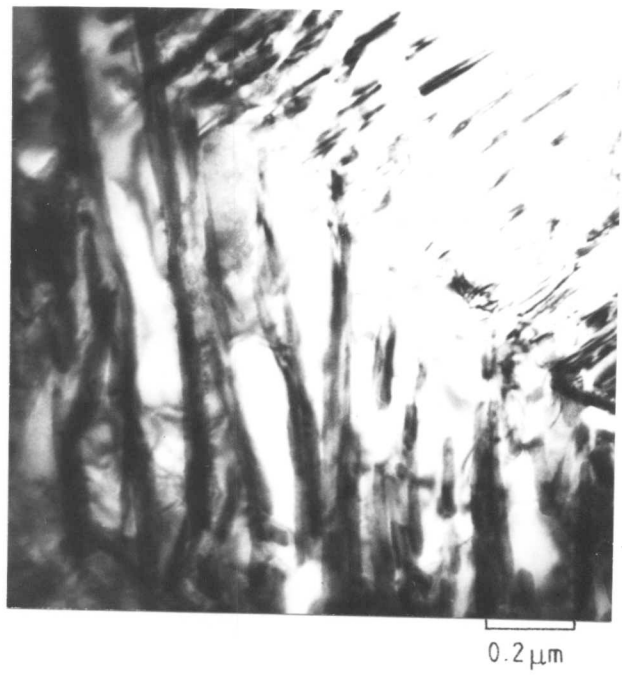

(a) (b)

Figure VIII.5

Air cooled following austenitisation at 1130°C for 10 minutes.

(a) Optical micrograph.

(b) Bright field transmission electron micrograph, showing an island of pearlite.

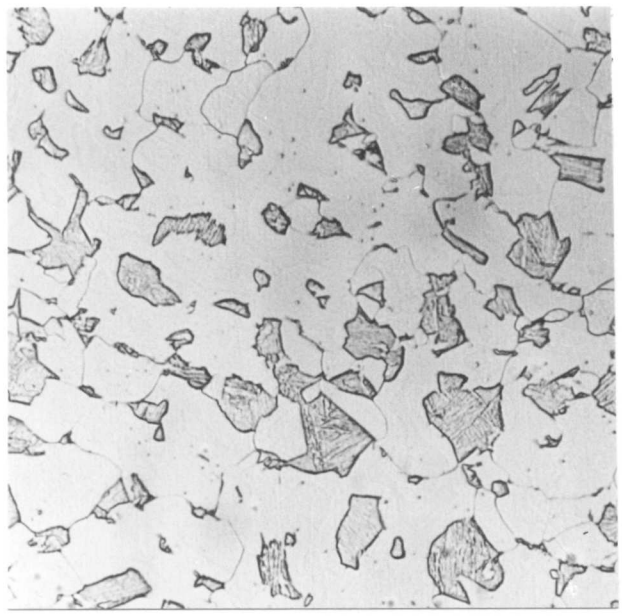

(a)

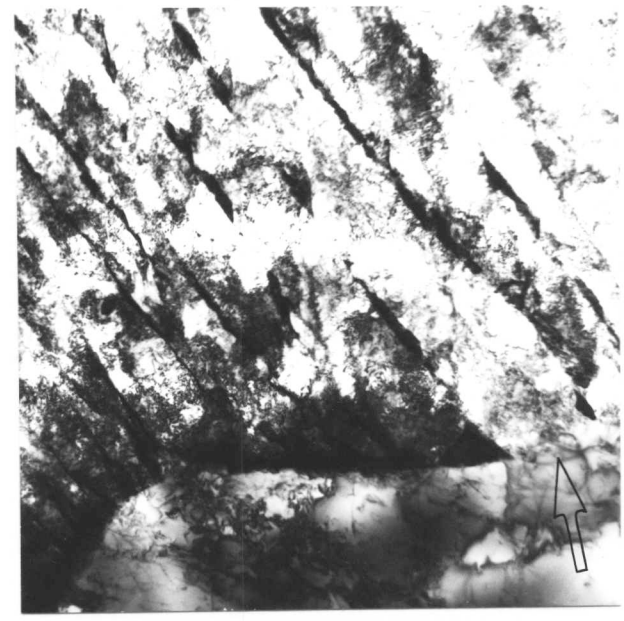

(b)

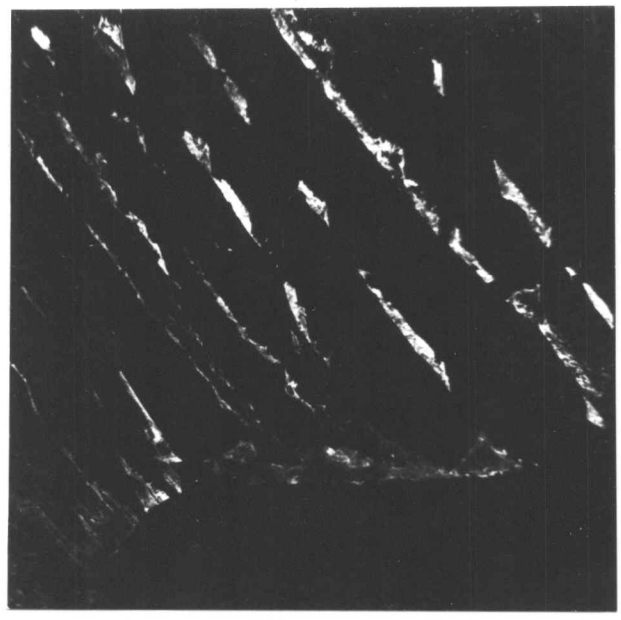

(c)

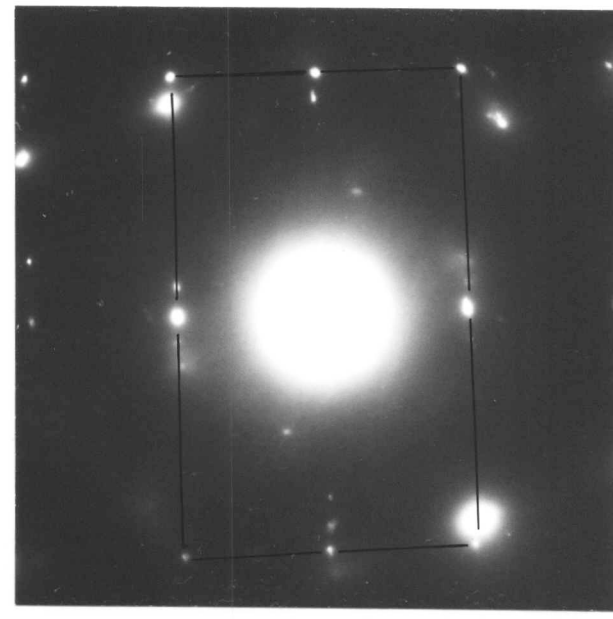

(d)

Figure VIII.6

Water quenched following austenitisation at 1130°C for 10 minutes.

(a) Optical micrograph.

(b) Bright field transmission electron micrograph.

(c) Corresponding retained austenite dark field image.

(d) Corresponding diffraction pattern: a $\langle\bar{1}12\rangle$ austenite zone is outlined.

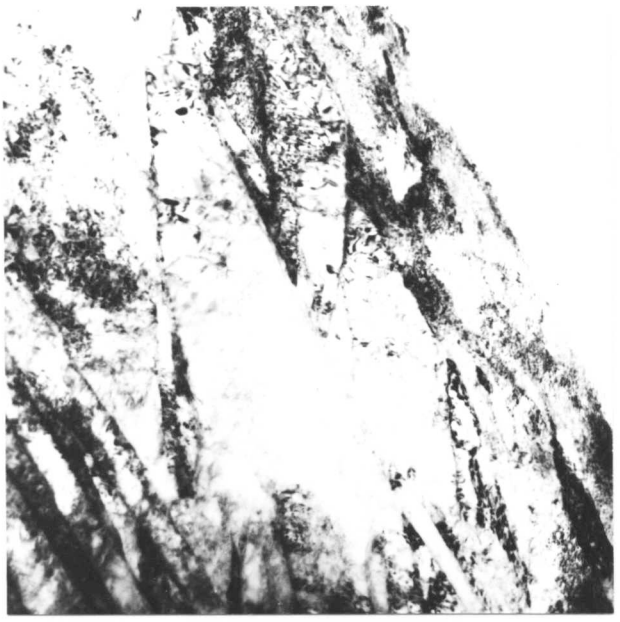

(8c)

(8d)

0.2μm

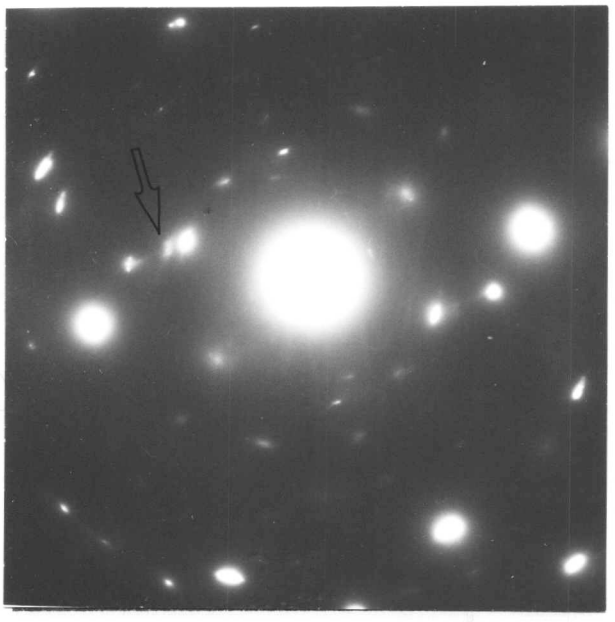

(8e)

Figure VIII.8

(c) Bright field image of an island of martensite.

(d) Corresponding retained austenite dark field image.

(e) Corresponding diffraction pattern. The arrowed spot is a {200} austenite reflection.

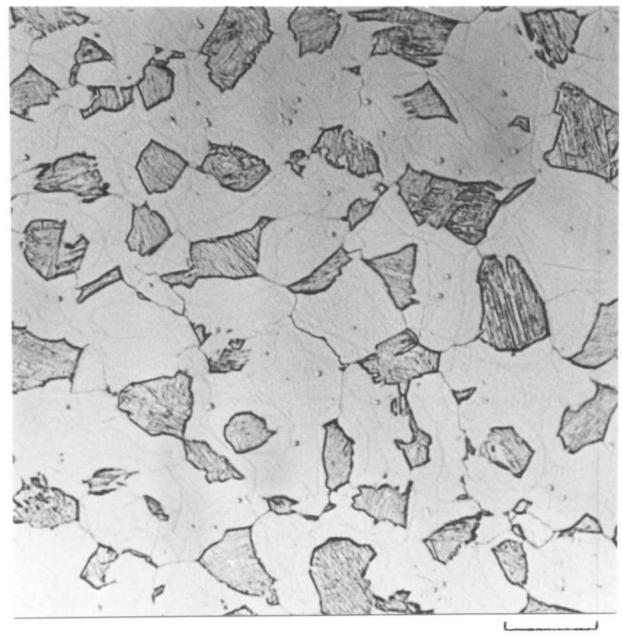

Figure VIII.7

Optical micrograph of specimen austenitised at 1300°C for 10 minutes and quenched into agitated iced brine.

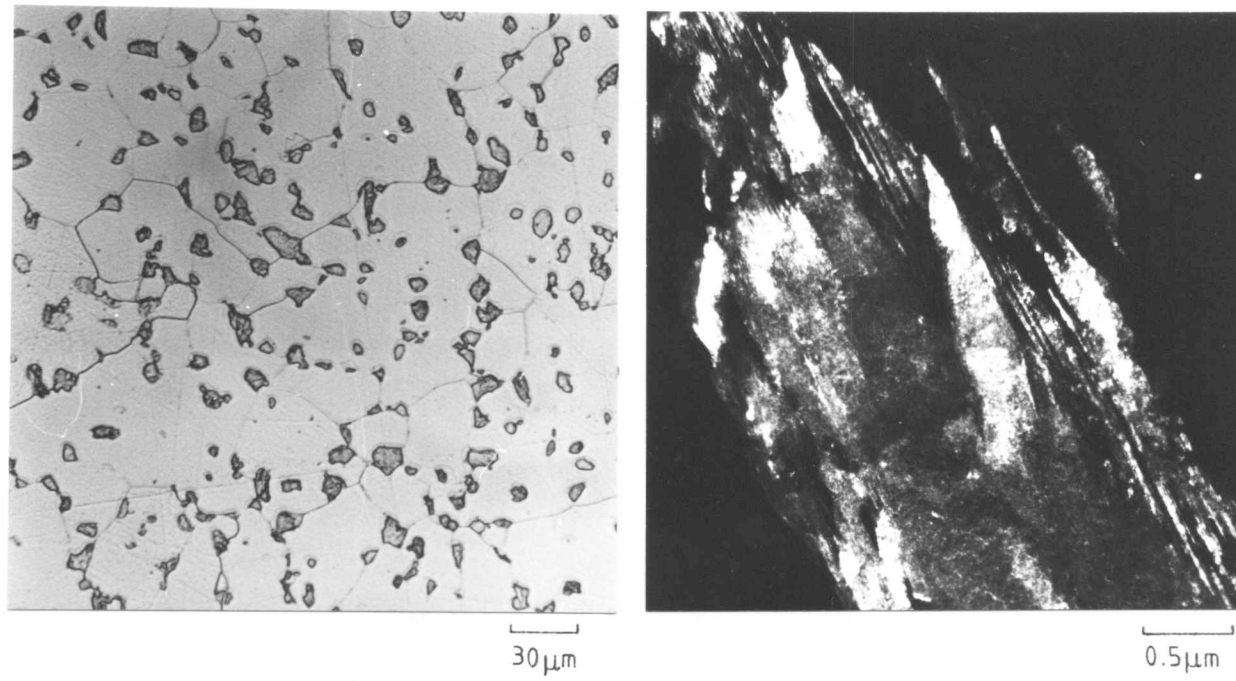

(a) (b)

Figure VIII.8a-e.

Austenitised at 935°C for 10 minutes followed by a quench into agitated iced brine.

(a) Optical micrograph.

(b) Dark field image of twins in martensite.

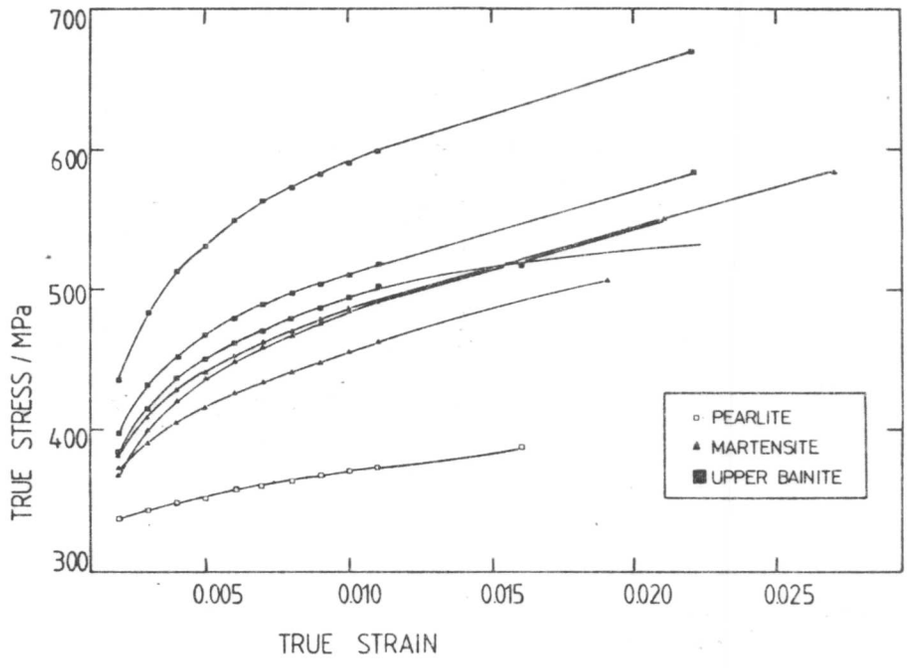

Figure VIII.9
True stress-true strain curves for the various microstructures examined.

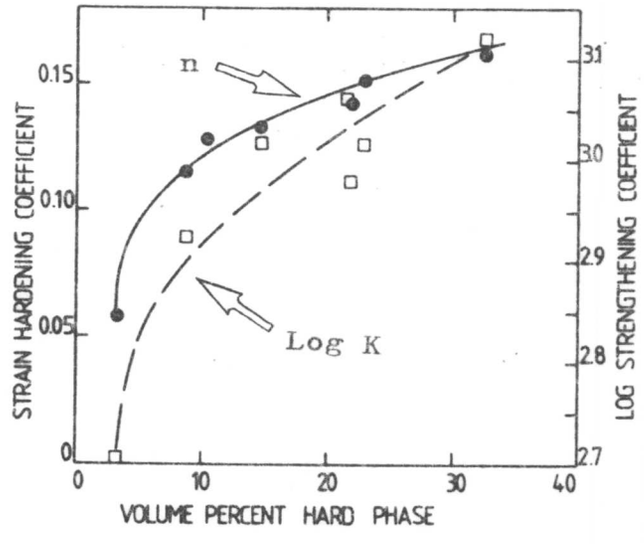

Figure VIII.10
The variations of strengthening and strain hardening coefficients as a function of the volume fraction of hard phase present. The dashed line represents the variation of the strengthening coefficient.

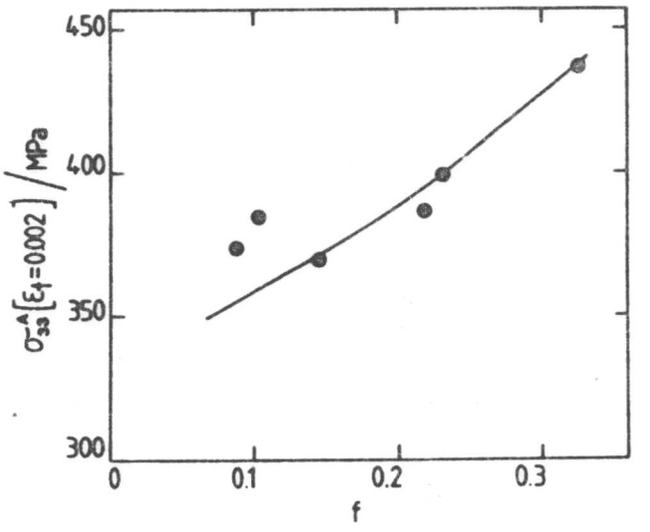

Figure VIII.11a

σ_{33}^{A} vs. volume fraction of hard phase. The line is calculated using Tomota's theory.

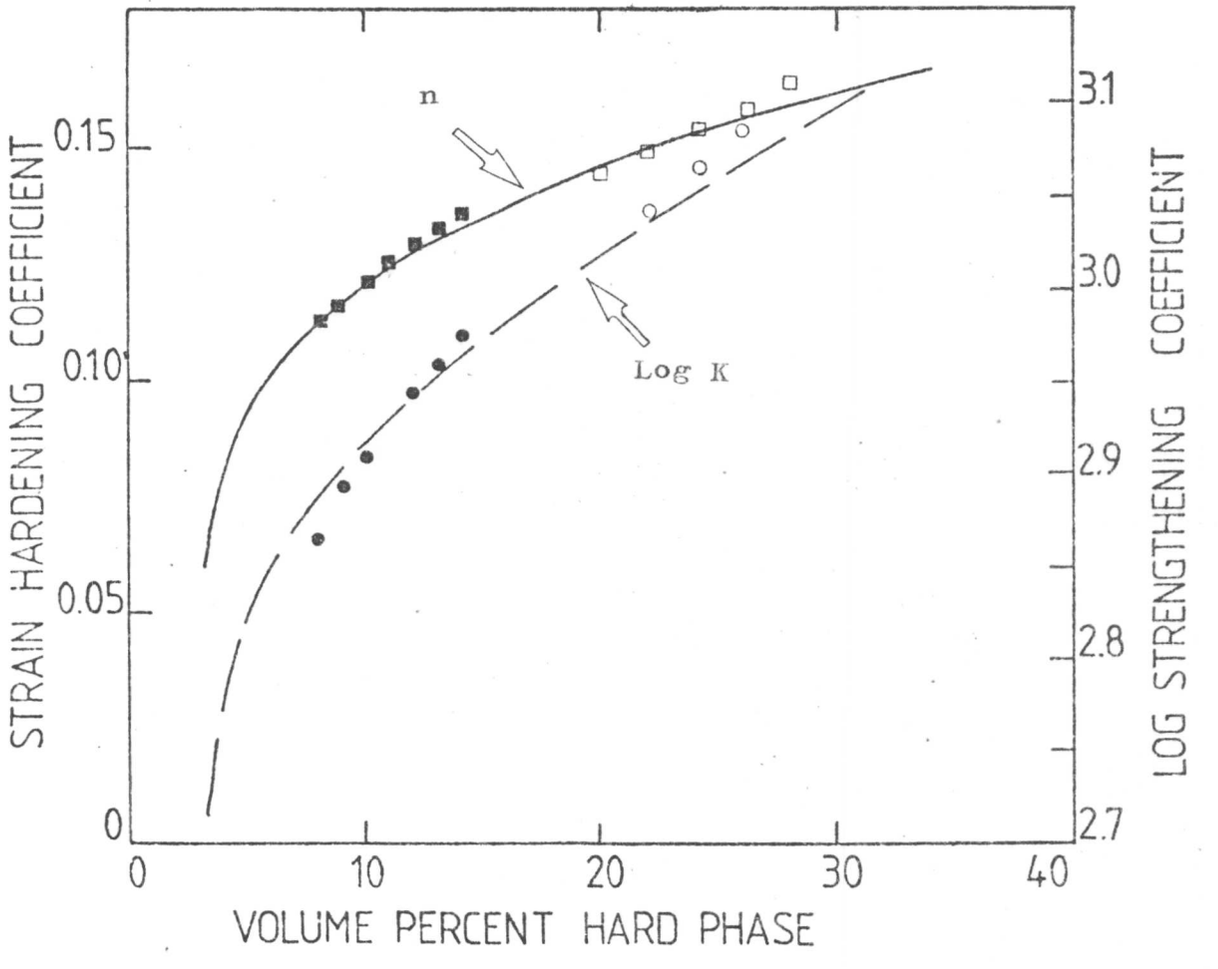

Figure VIII.11b

Best fit calculated values of strengthening and strain hardening coefficients obtained suing Tomota's theory vs. volume fraction of hard phase. The filled points refer to martensite, the open points to bainite and the lines represent the experimental curves from fig.VIII.10.

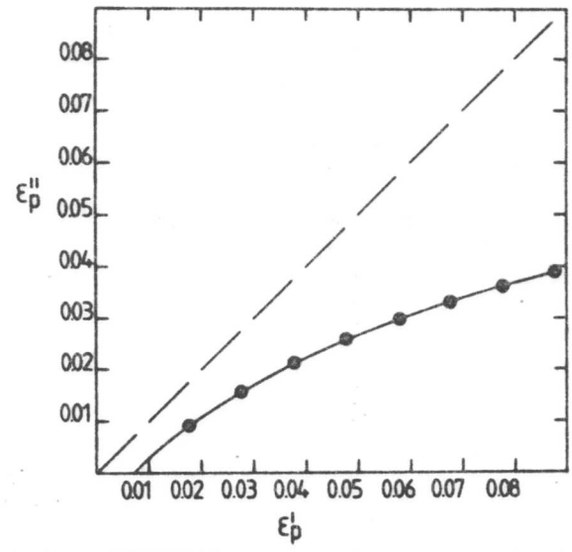

(a)

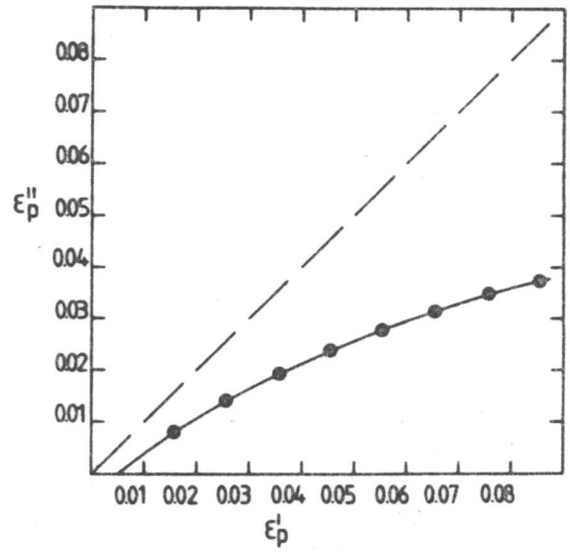

(b)

Figure VIII.12
Calculated cumulative plastic strain in the hard phase vs. that in the soft phase.
(a) Hard phase of martensite.
(b) Hard phase of bainite.

CHAPTER NINE

GENERAL CONCLUSIONS AND PROPOSED FURTHER RESEARCH

The bainite and martensite transformations in low alloy steels have been investigated, with the general aim of gaining a better understanding of the associated retained austenite. In this chapter, it is intended to summarise the results obtained and to discuss the implications of the conclusions reached, with respect to future work.

(IX.1) The Bainite Transformation

An experimental silicon steel was used in a detailed study of the bainite transformation, in an attempt to resolve the controversy surrounding the transformation mechanism, at least to the extent that the results may be usefully applied to the problem of retained austenite. The high silicon level in the experimental alloy ensured the retention of austenite since the post-bainitic partitioning of carbon into residual austenite dominated over reactions involving the precipitation of carbides.

The results obtained were found to be consistently in favour of a displacive transformation mechanism rather than one involving the diffusional migration of disordered ledges on the apparent habit plane (i.e. reconstructive mechanism).

Dilatometry and transmission electron microscopy showed the overlap of distinct ferrite-pearlite and upper bainite 'C' curves; the compatibility of kinetic and microstructural definitions of bainite was also demonstrated. The existence of a well defined B_s temperature and an incomplete reaction phenomenon was confirmed, and the verification of separate C-curves for upper and lower bainite not only indicated different modes of displacive transformation for upper and lower bainite, but also revealed two incubation bays, in addition to that at the B_s temperature, which cannot be explained by any solute drag model.

Microstructural examination indicated that the sheaf of upper bainite (which had the appearance of a plate on the scale of optical microscopy) in fact consisted of smaller displacive sub-units; these were, for the most part of their interfaces, separated by carbon enriched films of retained austenite. The morphology and distribution of the retained austenite, and the scale of the microstructure were found to be inconsistent with growth by the migration of ledges (of the type envisaged

by the reconstructive school) along the planar partially-coherent faces of bainitic ferrite platelets.

In contrast, the basic units of lower bainite were not found to be separated by retained austenite; each macroscopic plate appeared to consist of adjacently nucleated sub-units in parallel formation, such that they terminated at the plate tip in a set of spikes. Often, isolated 'sub-units' could also be found.

The cementite precipitate in the lower bainitic ferrite formed on many variants of the precipitation plane. This observation, together with other crystallographic evidence suggested that the precipitation occurred from a supersaturated ferrite matrix. At the same time, some partitioning of carbon also took place.

The sum of the evidence was subjected to a critical thermodynamic analysis which demonstrated that the results could only be rationalised in terms of a displacive mechanism, with partitioning of carbon occurring <u>after</u> the formation of fully supersaturated bainitic ferrite. It was possible not only to account for sympathetic nucleation, which seems to be a specific characteristic of the bainite transformation, but also to explain uniquely the nature of the incomplete reaction phenomenon. The limited size of the displacive sub-units in upper bainite was explained in terms of the friction stress associated with the motion of the transformation interface.

It seems therefore that the bainite transformation is a displacive transformation which can only occur at a certain degree of undercooling below the T_o temperature. The undercooling required is lower than that associated with the athermal martensite transformation, primarily due to the higher available thermal activation at the B_s temperature, and because of specific differences in nucleation behaviour - i.e. bainite initially nucleates at prior austenite grain boundaries, with subsequent nucleation being sympathetic. The relatively low driving force at the B_s temperature leads to a limited sub-unit size, the limitation coming into force when the chemical free energy change can no longer drive the transformation interface through the myriad of accommodation defects that are found to accompany the formation of bainite. The isothermal character of the bainite transformation arises since new sub-units can only sympathetically nucleate when the carbon concentration in the vicinity of the prior sub-unit (i.e. the carbon build-up resulting from post-

bainitic partitioning) is reduced by diffusion to a sufficiently low level such that displacive transformation is thermodynamically allowed. At a certain degree of transformation (depending on temperature and alloy composition), the carbon content of the austenite will reach a level such that the T_o condition is transgressed, and displacive transformation ceases. This is then the incomplete reaction phenomenon, assuming that carbon depletion by carbide precipitation is prevented. The partitioning of carbon and the precipitation of carbides seem to be competitive reactions in this respect.

The above considerations represent a summary of the current understanding of the bainite transformation. However, it is evident that certain points need clarification. While the upper and lower bainite reactions have been identified as separate reactions, both occurring in a displacive manner, the differences in the mechanisms of displacive transformation are not obvious. It is anticipated that such differences would be manifested in the lattice invariant shears involved, but before these can be deduced, the crystallography of both the transformations needs to be rationalised in terms of the phenomenological theory of martensite. It would also be valuable to characterise the nature of the transformation interfaces, in order to resolve whether an interface glide mechanism or a pole mechanism is operative.

Initial attempts to characterise the surface relief of bainite have proved to be encouraging, although the scale of the sub-units is such that conventional interference microscopy has failed to give definite results. However, the use of dimensionally stable replicas from pre-polished and transformed surfaces may help.

It would be interesting to quantitatively express the growth of an individual sheaf of upper bainite, and compare the theoretical and experimental values of its shape anisotropy.

Finally, the results need to be generalised to steels not containing silicon.

(IX.2) The Martensite Transformation

Retained austenite was detected in association with martensite in several low alloy steels examined by transmission electron microscopy and X-ray diffraction techniques. The austenite was present mainly as thin films between the martensite crystals.

However, the quantity and distribution of retained austenite varied between different steels. An examination of the inter-martensite crystallography indicated that the differences could be rationalised in terms of the relative orientations of martensite crystals bounding the austenite films. In steels with almost continuous films of inter-lath austenite, the degree of co-operative formation seemed limited in the sense that adjacent martensite units were of the same variant. When limited films of heterogeneously distributed austenite were observed, not only was the incidence of twin-related laths higher, but austenite was not in general observed between such laths. In a steel containing well organised packets of alternating twin-related laths, austenite could not be detected.

Some theoretical crystallography indicated that twin-related martensite orientations can only arise when the exact Kurdjumov and Sachs relationship is operative. However, the factors controlling the generation of any particular orientation relationship are not clear since the full crystallographic theory has not yet been successfully applied to dislocated martensites.

It thus appears that a high degree of mutual accommodation of transformation strains between adjacent variants reduces the propensity to retain inter-lath austenite, so that it is likely that mechanical stabilisation is a key factor controlling the stability of such films of austenite.

Initial results obtained using high alloy dislocated martensites suggest that for approximately the same M_s temperature, the behaviour of the martensite transformation below M_s is not a sensitive function of the habit plane crystallography despite the fact that the manner in which the prior austenite grain is geometrically partitioned depends on the habit plane multiplicity. This work was also found to be consistent with the idea that habit plane variations arise due to changes in the relative strengths of the austenite and martensite phases concerned.

A direct analysis of incipient twinning in a low alloy martensite indicated that such twinning originates from accommodation strains. The twins could not be described as intrinsic transformation features because the twin plane in the martensite was not found to uniquely correspond to a particular plane of mirror symmetry in the austenite, as required by the phenomenological theory. Furthermore, it was clear that the

intensity of twinning was highest when adjacent martensite units were twin-related; such a situation is expected to facilitate the nucleation of twins at the inter-martensite boundaries. Thus the earlier observation that austenite films cannot be readily detected between twin-related laths is not surprising since the lattices of such laths effectively interpenetrate. The interpenetration at the twin-related lath boundaries arises because the 'sympathetically nucleated' twins in a given variant adopt the lattice orientation of the adjacent variant.

The outstanding need as far as the martensite work is concerned is to define the detailed crystallography of low alloy martensites. The lack of adequate quantities of retained austenite and the fine scale of the microstructure have hindered the determination of such data. It is only when a complete set of crystallographic data becomes available that the phenomenological theory can be rigorously applied to obtain information on the transformation shears involved and to enable the calculation of parameters such as the degree of self-accommodation of shape strains as a function of crystallography. The up-quench technique (Ch.7) may help in this respect.

(IX.) Bainite - Mechanical Properties

It has been established that the silicon upper bainite microstructure can exhibit superior toughness compared with tempered martensites of equivalent or lower yield strengths. The better toughness seems to arise due to a number of factors, including the fact that the microstructure is free from carbides; the latter are generally responsible for enhancing the nucleation of voids and cleavage cracks at the expense of toughness. Retained austenite is found to be beneficial when it is in the more stable film morphology (rather than the blocky morphology). Its presence between bainitic ferrite sub-units is conducive to the periodic deflection of propagating cracks; it is also possible that a TRIP effect operates in the vicinity of the crack tip. The absence of any substantial amount of interstitial carbon in the bainitic ferrite and the ultra-fine 'grain size' resulting from the displacive character of the transformation optimise the overall toughness.

The strength of the silicon upper bainite originates from the transformation induced dislocation structure and the ultra-

fine grain size. The intimate dispersal of films of austenite between bainitic sub-units (in identical orientation) seems to additionally strengthen the overall microstructure by preventing the easy transfer of slip across sub-units within a given sheaf.

It was demonstrated that the toughness is at its best when the ratio of film austenite to blocky austenite is highest. Since this ratio is a function of the volume fraction of bainitic ferrite, it was possible to establish an empirical toughness criterion in which the only unspecified quantity is the volume fraction of bainitic ferrite. However, this quantity is calculable using thermodynamics, assuming that the reaction is allowed to terminate at the isothermal transformation temperature used. Thus the toughness behaviour could, in essence, be predicted from a knowledge of the composition of the steel. This principle was verified for two experimental steels.

While the silicon bainite microstructure seems to provide a viable, cheap and better alternative to the tempered martensite based ultra-high strength steels, it should be noted that the fatigue properties have not yet been examined, although the high ultimate strength to yield strength ratio engenders optimism. In principle, it should be possible to derive a steel composition where the blocky morphology is completely eliminated; such a steel would be expected to exhibit better properties than even the steels examined in the present work.

(IX.4) Martensite - Mechanical Properties

The microstructure and property changes accompanying the tempering of quenched low-alloy steels have been examined and correlated with the tempered martensite embrittlement (TME) phenomenon. TME was detected in an Fe-Mo-C steel and found to be controlled by the relatively coarser intralath cementite, rather than by the interlath cementite resulting from the decomposition of $<2\%$ retained austenite present as films between the martensite laths. In an Fe-V-C steel containing about 5% interlath retained austenite, TME was controlled by coarsening of the comparatively larger amount of interlath cementite resulting from thermal decomposition of the interlath retained austenite. In both cases fracture was translath, consistent with the crack nucleation role of cementite rather than that of providing an easy fracture path. In an Fe-Mn-Si-C steel containing

negligible retained austenite and fine carbides, TME was not found. Furthermore, embrittlement could not be associated with the transition from ε carbide to cementite.

It would be very interesting to quantify the relative coarsening rates of inter-and intra-lath carbides, as a function of the quantity of retained austenite and the potency of carbide inhibitors (such as silicon). This could then be directly related to the magnitude and shape of any TME troughs.

The extent of the TME effect with respect to tempering temperature is important since there are conflicting requirements of a low tempering temperature (consistent with high strength requirements) and the need to be beyond the TME trough. While ideally TME should be eliminated, another approach might involve modifications such that the TME trough would be extremely narrow and well defined. In this respect, the inter-lath dependence of TME is more desirable, as in the Fe-V-C steel.

APPENDIX I

THE IDENTIFICATION OF A NEW CARBIDE IN A SILICON CONTAINING STEEL

Isothermal transformation of an Fe-0.43C-3Mn-2.12Si alloy at 350°C gave a microstructure consisting of a lamellar aggregate of dislocated bainitic ferrite plates separated by films of carbon-enriched retained austenite (Ch.I). Tempering this structure at 500°C for 20 minutes led to the diffusional decomposition of the retained austenite to an unknown carbide phase and ferrite. This microstructure is illustrated in figure I.9a.

The carbide proved difficult to identify using conventional selected area electron diffraction due to the large number of crystallographic variants that contributed to the diffracted intensity from the area selected. The problem could not be simply overcome by using a smaller selected area aperture because the spherical aberration of the objective lens limits the size of such an aperture to approximately 0.5μm, at an operating voltage of 100 kV.

However, if the electron beam is condensed such that only the area of interest is illuminated, the diffracted intensity will arise mainly from that area. In principle, the spot size of the condensed beam is limited only by the resolution of the objective lens (159,160) although in practice the source of diffraction information will be larger due to beam spreading within the foil. For the present purposes, a spot size of 200 Å was found to be sufficient to resolve between the carbide particles (using a Philips EM300 electron microscope, operated at 100 kV).

One disadvantage of the above technique is that it leads to a broadening of the diffracted spots, as observed in the back focal plane of the objective lens. This is because a very small area is being illuminated, and the effect is directly analogous to the X-ray line broadening due to small crystallite size. Nevertheless, this setback did not deter the approximate determination of the crystal structure and parameters.

Some representative diffraction patterns are presented in figure AI.1. The camera constants were calibrated using ferrite reflections, and a set of 'd' spacings and angular relationships were obtained.

A literature search gave the following set of known iron carbides (which could also contain certain amounts of silicon or manganese):

Crystal Structure	Parameters	Reference
Hexagonal	a = 11.7 c = 10.8Å	161
Hexagonal	a = 9.81 c = 8.48	162
Hexagonal	a = 6.9 c = 4.8	163
Hexagonal	a = 6.4 c = 9.6	164
Hexagonal	a = 4.77 c = 4.35	165
Hexagonal	a = 2.75 c = 4.35	165
Hexagonal	a = 2.76 c = 4.36	165
Hexagonal	a = 6.27 c = 21.4	165
Orthorhombic	a = 8.8 b = 9 c = 14.4	166
Orthorhombic	a = 7.89 b = 4.6 c = 7.2	167
Orthorhombic	a = 4.525 b = 5.087 c = 6.743	165
Orthorhombic	a = 9.04 b = 15.66 c = 7.92	165
Orthorhombic	a = 3.82 b = 4.72 c = 12.5	165
Orthorhombic	a = 6.5 b = 7.7 c = 10.4	168
Orthorhombic	a = 14.8 b = 11.4 c = 8.5	168
Cubic	a = 3.88	165
Monoclinic	a = 11.563 b =4.573 c = 5.058 β = 97.44°	165
Hexagonal	a = 6.882 b = 4.54	(Source unknown)

Unsuccessful attempts were made to consistently index all available diffraction patterns to each of the above crystal structures. From the number of different low order reflections observed, it appeared that the crystal had a low symmetry, possibly monoclinic, if not worse. Since even the monoclinic structure is difficult to solve, the task was begun by assuming that the crystal had orthorhombic symmetry, but this proved futile, and a computer procedure was adopted with the assumption of monoclinic symmetry. In an attempt to simplify the calculations, it was assumed that the lowest order spacing observed by electron diffraction corresponded to one of the fundamental parameters of the unit cell (b). The other three parameters (a,c,β) were then systematically varied until a fit was obtained with all the available d-spacing and relative angle data.

The following parameters were thus deduced:

$a = 8.1\text{Å}$ $b = 10.4$ $c = 7.0$ $\beta = 107.2^{\circ}$

The agreement with experimental results is as follows:

Experimental	Calculated	Error %	Zone axis
(100) 7.73	7.73	-	011
$(01\bar{1})$ 5.54	5.62	1.4	
(100)*$(01\bar{1})$ 75°	75.6°		
(010) 10.41	10.41	-	$\bar{1}01$
(101) 4.22	4.44	5.25	
(010)*(101) 90°	90°		
(111) 4.15	4.09	1.6	$\bar{2}11$
$(0\bar{1}1)$ 5.74	5.62	2.2	
(111)*$(0\bar{1}1)$ 67°	64.3°		
(011) 5.774	5.62	2.7	$2\bar{1}1$
$(\bar{1}20)$ 4.18	4.31	3.1	
(011)*$(\bar{1}20)$ 69°	71.97°		
(011) 5.79	5.62	3.2	$2\bar{1}1$
$(\bar{1}20)$ 4.18	4.31	3.1	
(011)*$(\bar{1}20)$ 68°	71.97		
(011) 5.39	5.62	4.3	$2\bar{1}1$
$(\bar{1}20)$ 4.26	4.31	1.2	
(011)*$(\bar{1}20)$ 71°	71.97		

Note: All d-spacings are in Å, and (hkl)*(uvw) signifies the angle between the two planes indicated.

While further work would be useful to fully identify the carbide, it can be safely concluded that the above results represent a new carbide, whose detailed composition, relationship to the parent lattice and detailed crystal structure are as yet unknown. Furthermore, the errors involved in the above experiments and calculations are uncertain.

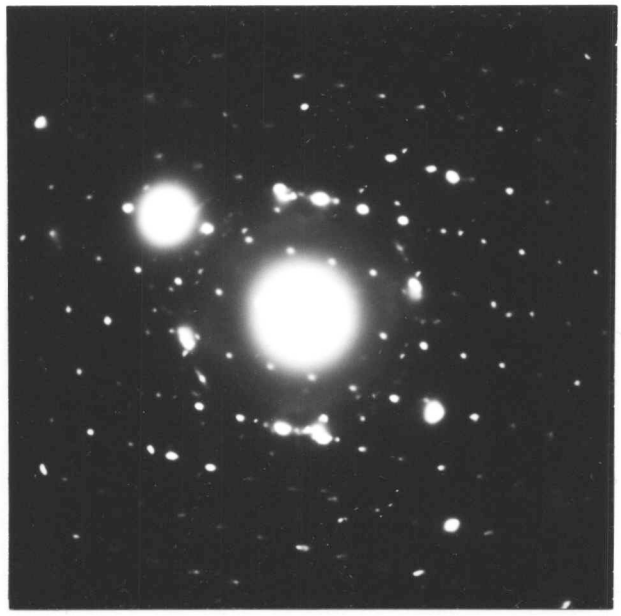

(a)

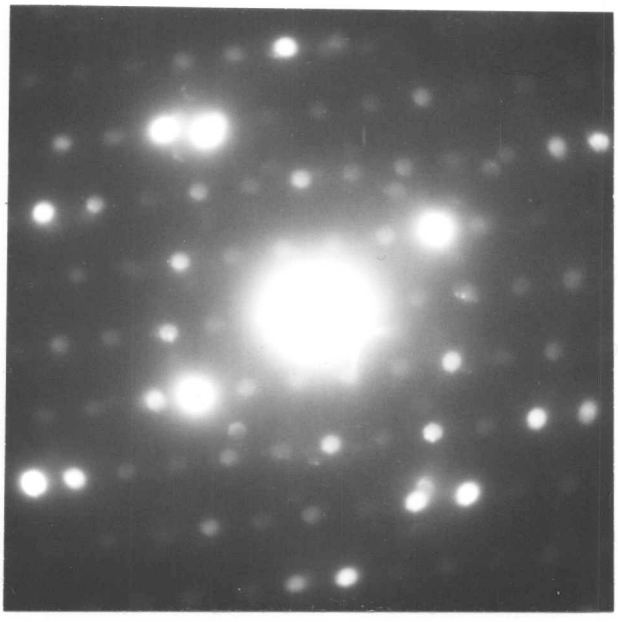

(b)

Figure A1.1

Convergent beam electron diffraction patterns from the carbide obtained after tempering silicon upper bainite at 500°C for 30 minutes.

(a) $[011]$ zone.

(b) $[2\bar{1}1]$ zone.

APPENDIX II

THERMODYNAMICS OF DISLOCATED MARTENSITES

Energy can be stored in polycrystalline martensitic specimens in the form of defects, interphase interfaces and coherency strains. Christian (169) considers that the calculated elastic coherency energy should give an approximate upper limit to the stored energy due to dislocations since the plastic deformation that leads to the formation of defects is driven by the coherency stresses.

It has recently been suggested that the energy stored in dislocated lath martensites is considerably greater than that in fully twinned plate martensites (170). The difference in stored enthalpy has been calorimetrically determined to be about 1150 J mol^{-1}, giving an absolute stored enthalpy of 1850 J mol^{-1} since that of twinned martensite amounts to 700 J mol^{-1} when both the twin interface energy (~ 100 J mol^{-1}, ref.170) and the elastic strain energy (600 J mol^{-1}, ref.169) are taken into account. This last value can be somewhat reduced if the plates form in some sort of a self accommodating manner (169), so that the stored enthalpy of lath martensite probably lies between 1250 and 1850 J mol^{-1} (possibly at the higher end of this range since the crystallography of ferrous martensites is incompatible with complete self-accommodation).

In general, martensite transformations involve a certain degree of undercooling below the T_o temperature (as discussed in Ch.II) prior to the onset of transformation at the M_s temperature. This seems to allow the build up of a sufficient amount of driving force to account for the various energy factors discussed above, and perhaps also to provide the activation energy needed to overcome any nucleation barrier**. However, it was intuitively

---

** Christian (171) suggests that we do not know enough about the nucleation process to reach any conclusion about whether an additional appreciable driving force is needed for the nucleation of martensite.

---

felt that the value of stored energy deduced above may be too high when considered in terms of the available driving force, since even for substitutional alloy martensites the latter amounts to about 1260 J mol^{-1} at the M_s temperature. It was therefore decided to scrutinise the available calorimetric data and the results are presented below.

Results and Discussion

Lee et al. (170) originally calculated the stored energy due to dislocations to be approximately consistent with the observed enthalpy difference between dislocated and twinned martensites. However, their calculations were found to be based on dislocation density values which were misquoted form the work of Kehoe and Kelly (172). Hence the stored energy due to the actual dislocation density was recalculated; additionally, the chemical driving force at M_s was estimated using the thermodynamic procedures of (38,40,41). The specific equations used for the latter calculations were based on the Lacher (42), Fowler and Guggenheim (43) statistics. The results are as follows:

Composition C	Mn	Si	M_s/°K	$-\Delta G$/J mol^{-1}	ρ/m^{-2}	E/J mol^{-1}	Ref.
0.01			830*	1034	5×10^{14}	10	172
0.04			815*	1060	8.9×10^{14}	18	172
0.06			806*	1070	1.1×10^{15}	21	172
0.10			787*	1061	1.6×10^{15}	31	172
0.022	4.3	0.95	738	586	3.9×10^{14}	8	86
0.035	4.6	0.29	703	680	4.6×10^{14}	9	86
0.058	4.8	0.30	698	630	7.1×10^{14}	14	86
(C = 0.02-0.18)			824-749*	1040-1140	1.5×10^{15}	30	173
0.43	3.0	2.12	493	1420	5.4×10^{15}**	108	

Notes

1) The compositions are expressed in wt. pct.
2) The M_s temperatures with asterisks are calculated using a regression equation from (174).
3) ΔG = The Chemical free energy change at M_s, calculated as indicated in the text.
   ρ = Dislocation density. The last figure marked (**) is obtained by extrapolating the graph of (172).
   E = Stored energy due to dislocations, assuming that when $\rho = 5\times10^{16}$ m^{-2}, E = 1000 J mol^{-1}, as in (174).
4) The last column refers to the source of the information.
5) The data from (173) gives the estimated ρ between lath boundaries, with the total being determined by resistivity measurements to be $0.3 - 0.9 \times 10^{16}$ m^{-2} (see Appendix to ref.173).

Before considering the implications of the above data, it is noted that Christian (171) considers that whilst 1260 J mol^{-1} is probably about right for the driving force at M_s for substitutional ferrous alloys, the data of (175-6) indicates an appreciably higher value for interstitial alloys. However, for the low interstitial contents being considered here, the discrepancy between the calculated values (for the Fe-C alloys) and the data of (175-6) amounts (at most) to about 200 J mol^{-1}.

After examining the above results, Argent (178) has reconsidered the procedure for the calculation of dislocation densities from stored energy measurements, as follows:

Case 1

Considering the dislocations in BCC iron to be dissociated as

$$\frac{a}{2}[\bar{1}\bar{1}1] \rightarrow \frac{a}{6}[\bar{1}\bar{1}1] + \frac{a}{3}[\bar{1}\bar{1}1]$$

and

$$\frac{a}{2}[111] \rightarrow \frac{a}{6}[11\bar{1}] + \frac{a}{3}[112]$$

and using the Moore and Khulmann-Wilsdorf (179) formula, i.e.

$$E = \frac{\rho\mu b^2}{4\pi K}\left(\ln \frac{R}{r_o} + 1.6n\right)$$

where E is as defined above,

- μ = Shear modulus, 8.3×10^{10} N m^{-2}
- b = Burgers vector, $a\sqrt{3}/6$ and $a\sqrt{3}/3$
- a = Ferrite lattice parameter, 2.861×10^{-10} m
- R = Outer radius of dislocation strain field, 10^{-6} m
- r_o = Inner radius of dislocation strain field, 10^{-10} m
- K = 1 for screw dislocations and $(1 - \upsilon)$ for edge dislocations, υ being the Poissons ratio.
- n = Number of dislocations in a pile up, taken to be 20.

The above parameters are more realistic than the ones used in the original calculation (170). Thus, for screw dislocations dissociated in the above manner, the energy per mole per unit dislocation density ($\varkappa$) is found to be 6.61×10^{-14} J mol^{-1} m^2 compared with the original value of 2×10^{-14} J $mol^{-1}m^2$. (Note: $\varkappa = E/\rho$)

Case 2

If the dislocations are not dissociated, but are all of screw character, the value of $\varkappa$ becomes 1.2×10^{-13} J $mol^{-1}m^2$, and for undissociated edge dislocations this amounts to 1.7×10^{-13} J $mol^{-1}m^2$.

It should be noted that the above formula yields the highest magnitude of dislocation energy for a given dislocation density

when compared with two other available equations (180,181) and hence is most compatible with the fact that the dislocations densities are lower than originally thought by Lee et al. If we now accept the highest value of $\varkappa$ from the above calculations, i.e. 1.7×10^{-13} J $mol^{-1} m^{2}$, all the 'E' values tabulated earlier would have to be multiplied by a factor of 8.5. On doing this, it was still found that the energy due to dislocations could not account for the excessive stored energy of lath martensites relative to fully twinned plate martensite. The results in fact strongly support Christian's (169) conclusion that any difference in stored energies of lath and plate martensites is likely to have its origin in the better elastic accommodation of the plates.

Despite this, there are a number of difficulties in accepting the magnitude of the excess stored enthalpy found by Lee et al. Assuming that the entropy of line defects may be neglected, the total stored enthalpy often exceeds the available driving force, as tabulated above. If much of the stored enthalpy (1250-1850 J mol^{-1}) is present as elastic energy (since the calculations suggest that the stored energy due to dislocations is rather low), then using the procedure and parameters given in (169), a shear component of the unconstrained invariant plane strain shape deformation of at least 0.26 can be calculated. It is most unlikely that this magnitude of strain can be elastically tolerated in the austenite, particularly since the austenite will have a low flow stress at the relatively high M_s temperatures associated with lath martensites.

It is possible that Lee et al. overestimated the stored energy values since they did not take account of carbide precipitation; many of their electron micrographs of high carbon plate martensites show significant amounts of carbide precipitation. While this would not apply to the Fe-30.3Ni alloy which they also studied, it should be noted that their estimate of stored energy was based on a regression analysis of all the results from many alloys, so that the influence of any one alloy may not be noticeable in the final result**.

**Argent (178) believes that for the particular transformation conditions used in the experiments of (169), fully twinned martensite was obtained in the Fe-30.3Ni alloy. The present author had suggested that this particular alloy does not give rise to fully twinned plates, in accordance with (182).

In conclusion it is suggested that the excess stored enthalpy of dislocated lath martensites may be lower than that found by Lee et al. (169), and that the dislocation substructure does not form a major part of the stored energy.

The present analysis does, however, suggest an interesting experiment. $\{225\}_\gamma$ plate martensite has a displacement vector which essentially lies in the habit plane, so that interaction between different variants is minimal, a fact which is reflected in the absence of a burst phenomenon. It would be extremely interesting to compare the stored energy of this martensite with say the fully twinned $\{3\ 10\ 15\}_\gamma$ type martensite which forms in a beautifully self-accommodating manner.

APPENDIX III

THE STRUCTURE OF TWINS IN Fe-Ni MARTENSITES

The martensite plates found in Fe-31Ni (wt.pct.) alloys are generally partially twinned (182). The twinned regions correspond to the midrib of the plate whereas the peripheral regions have a dislocated substructure consisting of two sets of screw dislocations aligned along $\langle 111 \rangle_{\alpha'}$ directions (183).

It is found that the composition plane of the twin is a plane of the form $\{112\}_{\alpha'}$, and corresponds to a plane of mirror symmetry in the austenite, as required by the phenomenological theory of martensite when type 1 twinning is involved (182). Additionally, if the composition plane is taken to be the twin plane, substitution into the phenomenological theory generates an invariant martensite habit plane that is consistent with the trace of the observed midrib plane (182).

However, the assumption that the composition plane corresponds to the twinning plane has recently been challenged (184). It has been proposed that the 'twin' in fact consists of a three dimensional stack of $\frac{a}{6}\langle 111 \rangle_{\alpha'}$ partial dislocations, such that the twinning plane (i.e. the plane on which the partials move), is a $\{11\bar{2}\}_{\alpha'}$ plane which is different from the composition plane although it belongs to the same $\langle 111 \rangle_{\alpha'}$ zone. However, the experimental evidence of (184) is based on the assumption that the twinning elements ($\langle 11\bar{1} \rangle_{\alpha'}$, $\{112\}_{\alpha'}$) can be determined from the observation of symmetry axes relating the twin and matrix lattices. Unfortunately, the intrinsic BCC twin/matrix symmetry allows three variants of $\{11\bar{2}\}_{\alpha'}$ planes, related by a common $\langle 111 \rangle_{\alpha'}$ axis, across which the twin and matrix are related by reflection.

This does not, however, rule out the basic hypothesis of (184) since the twinning elements are as yet undetermined. Nevertheless, any such model would have to explain a) the appearance of a single twin variant per plate, such that the composition plane is uniquely related to the specific martensite habit plane, and b) the driving force behind the formation of such twins.

The twinning element problem could, in principle, be resolved by measuring the shape deformation due to the twins, using dimensionally stable replicas taken from pre-polished and transformed specimens.

KEY REFERENCES

1. R.F. Hehemann, K.R. Kinsman, H.I. Aaronson: Met. Trans., 1970, vol.3, pp.1077-1093.
2. H.I. Aaronson: 'The Mechanism of Phase Transformations in Crystalline Solids, Institute of Metals Monograph 33, 1968, p.270.
3. 1st Progress Report of Sub-Committee XI, ASTM Committee E-4; Proc. ASTM, 1950, vol.50, p.444.
4. 2nd Progress Report of Sub-Committee XI, ASTM Committee E-4; ibid., 1952, vol.52, p.543.
5. 4th Progress Report of Sub-Committee XI, ASTM Committee E-4; ibid., 1954, vol.54, p.568.
6. L. Habraken: Proc. 4th Int. Conf. on Electron Microscopy, 1958, p.621, Berlin.
7. R.M. Fisher: ibid., p.579.
8. F. B. Pickering: ibid., p.626.
9. K. Shimizu, Z. Nishiyama: Mem. Inst. Sci. Ind. Res. Osaka Univ., 1963, vol.20, p.43.
10. J.M. Oblak, R.F. Hehemann: 'Transformations and Hardenability in Steels' p.15, Climax Molybdenum Company, Ann Arbor, 1967.
11. B.A. Leontyev, G.V. Kovalevskaya: Phys. Met. Metallogr., 1974, vol.38, p.139.
12. N.A. Snurenskaya, L.I. Kogan, R.I. Etin: Phys. Met. Metallogr., vol.41, pp.1019 - 1028.
13. Der-Hung Huang, G. Thomas: Met. Trans., 1977, vol.8, p.1661.
14. N.F. Kennon: J. Aust. Inst. Metals, 1974, vol.19, pp.3 -18.
15. K.R. Kinsman, H.I. Aaronson: Transformations and Hardenability in Steels, p.39, Climax Molybdenum Company, Ann Arbor, 1967.
16. R.F. Hehemann: 'Phase Transformations', p.397, ASM, Metals Park, Ohio, 1970.
17. R. Le Houiller, G. Begin, A. Dube: Met. Trans., 1971, vol.2 p.2645.
18. N.F. Kennon: Met. Trans., 1978, vol.9, pp.57 - 66.
19. G.R. Purdy: Acta Met., 1978, vol. 26, pp.477 - 486.
20. G.R. Purdy: Acta Met., 1978, vol. 26, pp.487 - 498.
21. B. Uhrenius: Scand. J. Met., 1977, vol.6, pp.83 - 89.
22. G.R. Speich: 'Decomposition of Austenite by Diffusional Processes', p.353, Interscience Publishers, New York, 1962.
23. W.S. Owen: Trans. ASM, 1954, vol.46, pp.812 - 829.
24. J. Gordine, I. Codd: J.I.S.I., 1969, vol. 207.1, p. 461.
25. R.M. Hobbs, G.W. Lorimer, N. Ridley: J.I.S.I., 1972, vol.210.2, p.757.

26. M.J. Dickson: J. App. Cryst., 1969, vol.2, p.176, also, Private Communication, Dr. L. Remy, Ecole Nationale Superireure Des Mines de Paris, 91003 Evry Cedex, France. 1977.
27. B.D. Cullity: 'Elements of X-ray Diffraction', 1st Edition, p.334, Addison-Wesley Publishing Co., 1956.
28. G.B. Olson, M. Cohen: Met. Trans., 1976, vol.7, p.1797.
29. Y. Ohmori, R.W.K. Honeycombe: Supp. Trans. ISIJ, 1971, vol.11, p.1160.
30. K.W. Andrews: Acta Met., vol.11, 1963, p.939.
31. B. Jacobson, A. Westgren: Zietschrift fur Physikalische Chemie, Badenstein Anniversary Volume, 1931, p.177.
32. N.C. Law: Ph.D. Thesis, University of Cambridge, England, 1977.
33. H.I. Aaronson, M.R. Plichta, G.W. Franti, K.C. Russell: Met. Trans., 1978, vol.9, p.368.
34. H.I. Aaronson: 'Decomposition of Austenite by Diffusional Processes', p.337, Interscience Publishers, New York, 1962.
35. W.L. Grube, S.R. Rouze: 'High Temperature - High Resolution Metallography', p.313, Gordon and Breach, New York, 1967.
36. S.R. Rouze and W.L. Grube: General Motors Corp., Warren, Mich., Private Communication toe H.I. Aaronson, referred to in (1).
37. K.R. Kinsman, E. Eichen, H.I. Aaronson: Met. Trans. A, 1975, vol.6A, p.303.
38. K.R. Kinsman, H.I. Aaronson: Discussion to ref.10.
39. C. Zener: Trans. AIME, 1946, vol.167, p.a50.
40. H.I. Aaronson, H.A. Domian, G.M. Pound: Trans. Met. Soc. AIME, 1966, vol.236, p.753.
41. H.I. Aaronson, H.A. Domian, G.M. Pound: Trans. Met. Soc. AIME, 1966, vol.236, p. 768.
42. J.R. Lacher: Proc. Cambridge Phil. Soc., 1937, vol.33, p.518.
43. R.H. Fowler, E.A. Guggenhiem: 'Statistical Thermodynamics', p.442 and preceeding, Cambridge Univ. Press, New York, 1939.
44. L. Kaufmann, E.V. Clougherty, R.J. Weiss: Acta Met., 1963, vol.11, p.323.
45. G.B. Olson, M. Cohen: Scripta Met., 1977, vol.11, p.345.
46. G.B. Olson, M. Cohen: Scripta Met., 1975, vol.9, p.1247.
47. A.T. Davenport: Republic Steel Research Centre, Project Report 12051, 1974.
48. L. Kaufmann, M. Cohen: Progress in Metal Physics, 1958, vol. 7, p.165.
49. G.B. Olson, M. Cohen: Met. Trans. A, 1976, vol.7A, p.1897.
50. G.B. Olson, M. Cohen: Met. Trans. A, 1976, vol.7A, p.1905.
51. G.B. Olson, M. Cohen: Met. Trans. A, 1976, vol.7A, p.1915.

52. M. Cohen: Met. Trans., 1972, vol.3, p.1095.
53. H. Knapp, U. Dehlinger: Acta Met., 1956, vol.4, p.289.
54. V. Raghavan, M. Cohen: Acta Met., 1972, vol.20, p.333.
55. D. Maclean: 'Mechanical Properties of Matter', John Wiley and Sons Inc., New York and London, 1962, p.8.
56. H.I. Aaronson, M.G. Hall, D.M. Barrett, K.R. Kinsman: Scripta Met., vol.9, 1975, p.705.
57. M. Shibata, L. Ono: Acta Met., 1977, vol.25, p.35.
58. J.W. Christian: 'Phase Transformations', York Conf., 1979, vol.1, No.11, Series 3, p.1, Inst. of Metallurgists, London.
59. M. Cohen, E.S. Machlin, E.V.G. Paranjpe: 'Thermodynamics in Physical Metallurgy', ASM, 1949, p.242.
60. E.S. Machlin: Trans. AIMME, 1954, vol.200, p.684.
61. J.W. Christian: 'The Theory of Transformation in Metals and Alloys', 1965, Pergamon Press, Oxford.
62. W.S. Owen, F.J. Schoen, G.R. Srinivasan: 'Phase Transformations', p.157, ASM, Metals Park, Ohio, 1970.
63. J.M. Rigsbee, H.I. Aaronson: Acta Met., 1979, vol.27, p.351.
64. J.M. Rigsbee, H.I. Aaronson: Acta Met., 1979, vol.27, p.365.
65. H.I. Aaronson, C. Laird, K.R. Kinsman: Scripta Met., 1968, vol.2, p.259.
66. F.B. Pickering: 'Phase Transformations', York Conf., 1979, vol.2, Series 3, No.11, p.VI.7.
67. D. Bhandarkar, V.F. Zackay, E.R. Parker: Met. Trans., 1972, vol.3, p.2619.
68. D. Fahr: Met. Trans., 1971, vol.2, p.1883.
69. W.W. Gerberich, P.L. Hemmings, V.F. Zackay: Met. Trans., 1971, vol.2, p.2243.
70. S.J. Matas, R.F. Hehemann: Trans. TMS-AIME, 1961, vol.221,p.179.
71. R.I. Entin: 'Decomposition of Austenite by Diffusional Processes', p.295, Interscience Pub., New York, 1962.
72. T. Lyman, A.R. Troiano: Trans. AIME, 1945, vol.162, p.196.
73. T. Lyman, A.R. Troiano: Trans ASM, 1946, vol. 37, p.402.
74. A.T. Davenport: AIME Abstracts - 5th Annual Spring Meeting, University of Pennsylvania, 1973.
75. E.R. Parker: Met. Trans., 1977, vol.8A, p.1025.
76. S.V. Radcliffe, M. Schatz: Acta Met., 1962, vol.10, p.201.
77. N. Ridley, H. Stuart, L. Zwell: Trans. TMS-AIME, 1969, vol. 245, p.1834.
78. R.C. Ruhl, M. Cohen: Trans. TMS-AIME, 1969, vol. 245, p.241.
79. C.S. Roberts: Trans.AIME, 1953, vol.197, p.203.
80. M.G. Lorinski, I.S. Simeonova: Acta Met., 1959, vol.7, p.709.

81. Y. Imai, M. Izumiyama, M. Tsuchiya: Sci. Rept. Res. Inst. Tohoku University, 1965, vol.A17, p.173.
82. D.J. Dyson, B. Holmes: J.I.S.I., 1970, vol.208, p.469.
83. J.M. Moyer, G.S. Ansell: Met. Trans., 1975, vol.6A, p.1785.
84. K.R. Kinsman, E. Eichen, H.I. Aaronson: Met. Trans., 1971, vol.2, p.346.
85. K.J. Irvine, D.T. Llewellyn, F.B. Pickering: J.I.S.I., 1961, vol. 199, p.153.
86. L. Norstrom: Scand. J. of Met., 1976, vol.5, p.159.
87. R.G. Davies: Met. Trans., 1979, vol.10A, p.113.
88. W.C. Leslie, A.S. Keh:'Mechanical Working of Steel II', pp.337-377, Gordon and Breach, New York, 1965.
89. E.R. Petty (Ed.): 'Martensite -- Fundamentals and Technology', Longmans, 1970.
90. T.K. Sanyal, R. Brook: Metal Science, 1975, vol. 9, p.135.
91. R.M. Horn, R.O. Ritchie: Met. Trans., 1978, vol.9A, p.1039.
92. G. Thomas: Met. Trans., 1978, vol.9A, p.439.
93. A.H. Cottrell: TMS - AIME, 1958, vol.202, p.192.
94. B.Uhrenius: Scand. J. Met., 1973, vol.2, p.177.
95. T. Wada, H. Wada, J.F. Elliott, J. Chipman: Met. Trans., 1977, vol.2, p.2199.
96. G.R. Chanani, S.D. Antolovich, W.W. Gerbriech: Met. Trans., 1972, vol.3, p.2661.
97. C.S. Roberts: Trans. AIME, 1953, vol.199, p.203.
98. J. McMahon, G. Thomas: 'Microstructure and Design of Alloys', vol.1, 1974, p.180, London (Metals Society).
99. B.V.N. Rao, G. Thomas: Int. J. Fracture, 1977, vol.13, p.705.
100. J.E. King, R.F. Smith, J.F. Knott: Fracture 77, vol.2, ICF4, Waterloo, Canada, 1977, pp.279 - 286.
101. R.A. Clark, G. Thomas: Met. Trans., 1975, vol.6, p.969.
102. J.E. King, R.F. Smith, J.F. Knott: Int. J. Fracture, 1977, vol.13, p.877.
103. U.H. Lindborg, B.L. Averbach: Acta Met., 1966, vol.14, p.1583.
104. R.E. Dolby, J.F. Knott: J.I.S.I., 1972, vol.210, p.857.
105. J.P. Naylor, P.R. Krahe: Met. Trans., 1975, vol.6A, p.594.
106. A.L.T. Azevedo, E.G. DaSilva: Scripta Met., 1978, vol.12, p.113.
107. N.C. Law, D.V. Edmonds, P.R. Howell: Unpublished research, University of Cambridge, England.
108. J.C. Bokros, E.R. Parker: Acta Met., 1963, vol.11, p.1291.
109. M. Shibata, K. Ono: Acta Met., 1975, vol.23, p.587.
110. G.V. Kurdjumov, G. Sachs : Z. Phys., 1930, vol.64, p.325.

111. A.B. Greninger, A.R. Troiano: Trans. AIME, 1949, vol.185, p.590.
112. Z. Nishiyama: Sci. Rept., Tohoku Univ., 1934, vol.23, p.325.
113. M. Watnabe, C.M. Wayman: Met. Trans., 1971, vol.2, p.2229.
114. J.S. Bowles, J.K. Mackenzie: Acta Met., 1954, vol.2, p.224.
115. G.R. Speich, P.R. Swann: J.I.S.I., 1965, p.480.
116. C.M. Wayman: 'Introduction to the Crystallography of Martensite Transformations', 1964, the Macmillan Co., New York.
117. P.M. Kelly: Acta Met., 1965, vol.13, p.635.
118. G. Thomas: Iron and Steel International, 1973, vol.46, p.2267.
119. B.V.N. Rao, R.W. Miller, G. Thomas: Proc. Int. Conf. Heat Treatment, 1976, the Metals Society, London.
120. D.P. Dunne, C.M. Wayman: Met. Trans., 1971, vol.2, p.2327.
121. A. Sauveur, C.H. Chou: Trans. AIME, 1929, vol.84, p.350.
122. R.F. Mehl, C.S. Barrett, D.W. Smith: Trans. AIME, 1933, vol.105, p.215.
123. R.F. Mehl, D.W. Smith: Trans. AIME, 1934, vol.113, p.203.
124. A.B. Greninger, A.R. Troiano: Trans. AIME, 1940, vol.140, p.307.
125. C.M. Wayman, C.J. Altstetter: Acta Met., 1962, vol.10,p.992.
126. J.S. Bowles: Acta Cryst., 1951, vol.4, p.162.
127. P.M. Kelly, J. Nutting: JISI, 1961, vol.197, p.199.
128. R. Lagneborg: Acta Met., 1964, vol.12, p.823.
129. P.M. Kelly: Acta Met., 1965, vol.13, p.635.
130. T. Bell, W.S. owen: JISI, 1967, p.428.
131. M.G.D. Biswas, I. Codd: JISI, 1968, p.494.
132. F.J. Schoen, J.C. Nilles, W.S. Owen: Met. Trans., 1971, vol.2, p.2489.
133. B.G.Byrans, T. Bell, V.M. Thomas: 'The Mechanism of Phase Transformations in Crystalline Solids', Institute of Metals Monograph 33, 1968, p.181, london.
134. P.G. McDougall: ISI Spec. Rept. 93, 1965, p.164.
135. J.M. Chilton, C.J. Barton, G.R. Speich: JISI, 1970, p.184.
136. B.I. Bozic, R.I. Lucic: Met. Sci. J., 1977, vol.12, p.751.
137. D.S. Sarma, J.A. Whiteman, J.H. Woodhead: Met. Sci. J., 1976, vol.10, p.391.
138. J.D. Bolton, E.R. Petty: Met. Sci. J., 1971, vol.5, p.166.
139. A.G. Crocker, F. Heckscher, M. Bevis: Phil. Mag., 1963, vol.8, p. 1863.
140. T.J. Patrician, H.M. Ledbetter, R.P. Reed: Met. Trans., 1973, vol.3, p.947.

141. R.G. Davies, C.L. Magee: Met. Trans., 1971, vol.2, p.1939.
142. S.K. Das, G. Thomas: Trans. ASM, 1969, vol.62, p.659.
143. G. Thomas, S.K. Das: JISI, 1971, vol.209, p.801.
144. M. Raghavan, G. Thomas: Met. Trans., 1971, vol.2, p.3433.
145. K.H. Khan, W.E. Wood: Met. Trans., 1978, vol.9A, p.899.
146. M. Bevis, P.C. Rowlands, A.F. Acton: Trans. TMS-AIME, 1968, vol.242, p.1555.
147. R. Clark, G.B. Craig: Prog. in Metal Phys., 1952, vol.3, p.115.
148. M.S. Rashid: SAE Preprint 760206, Feb.1976.
149. M.S. Rashid: SAE Preprint 770211, Feb. 1977.
150. P.E. Repas: Seminar on Vanadium Cold Pressing and Dual-Phase Steels, Paper no.2, 1978, West Berlin, Vanitec.
151. R.G. Davies, C.L. Magee: ibid., paper no.3.
152. R.G. Davies: Met. Trans., to be published.
153. R.G. Davies: 'On the Ductility of Dual-Phase Steels', Ford Motor Co., Dearborn, Michigan.
154. R.G. Davies: Met. Trans., 1978, vol.9A, p.451.
155. R.G. Davies: Met. Trans., 1978, vol.9A, p.41.
156. S.T. Mileiko: J. Mat. Sci., 1969, vol.4, p.974.
157. R. Lagneborg: Seminar on Vanadium Cold Pressing and Dual-Phase Steels, Paper no. 5, 1978, West Berlin, Vanitec.
158. Y. Tomota, K. Kuroki, T. Mori, I. Tamura: Mat. Sci. & Eng., 1976, vol.24, p.84.
159. J.M. Cowley: p.27, 'Practical Aspects of Electron Microscopy and Microbeam Analysis', Ed. B.M. Siegel, John Wiley and Sons, 1975.
160. W.D. Riecke: 'Electron Microscopy in Materials Science', 3rd Course of the International School of Electron Microscopy, Eltove Majorana, Int. Centre for Scientific Culture, Eds. V. Valdre, E. Rvedi, 1975, p.81.
161. J.G. Humphreys, W.S. Owen: JISI, 1961, vol.198, p.38.
162. P. Schwaab: Naturwiss: 1954, vol.51, p.356.
163. J. Pomey: Mem. Sci. Rev. Metallug., 1966, vol.63.6, p.509.
164. K.H. Jack: JISI, 1949, vol.163, p.384.
165. 'A Handbook of Lattice Spacings and Structures of Metals and Alloys', 1967, vol.2, p.1339, Pergamon Press.
166. G. Konoval, L. Zwell, L.A. Gorman, W.C. Leslie: Nature, 1959, vol.184, p.1862.
167. N.S. Owen, B.G. Street: JISI, 1962, vol.172, p.15.
168. J.M. Schissler, J. Arnould, G. Metauer: Mem. Sci. Rev. Metallug., 1975, p.779.

169. J.W. Christian: ICOMAT 79, June 1979, Boston, in press.
170. B. Lee, S. Millman, I.L. MacDougall, S.R. Keown, B.B. Argent Metal Science, 1977, vol.7, p.261.
171. J.W. Christian: Private Communication, July 1979.
172. M. Kehoe, P.M. Kelly: Scripta Met., 1970, vol.4, p.473.
174. B.B. Argent: Metal Science, 1976, vol.10, p.409.
175. R.A. Grange, H.M. Stewart: Trans. AIME, 1946, vol.167, p.467.
176. Y. Imai, M. Izumiyama, M. Tsuchiya: Sci. Rep. Res. Inst. Tohoku Univ., 1965, vol.A17, p.173.
177. T. Bell, W.S. Owen: TMS-AIME, 1967, vol.239, p.1944.
178. B.B. Argent: Private Communication, July 1979.
179. J.T. Moore, D. Kuhlman-Wilsdorf: Proc. 2nd Int. Conf. on Strength of Materials, ASM, 1970, p.484.
180. A. Seeger, H. Kronmuller: Phil. Mag., 1962, vol.7, p.897.
181. J.E. Bailey, P.B. Hirsch: Phil. Mag., 1960, vol.5, p.485.
182. R.L. Patterson, C.M. Wayman: Acta Met., 1966, vol.14, p.347.
183. R.L. Patterson, C.M. Wayman: Acta Met., 1964, vol.12, p.1306.
184. M. DeChamps, L.M. Brown: Acta Met., 1979, vol.27, p.1281.